

Copyright Undertaking

This thesis is protected by copyright, with all rights reserved.

By reading and using the thesis, the reader understands and agrees to the following terms:

- 1. The reader will abide by the rules and legal ordinances governing copyright regarding the use of the thesis.
- 2. The reader will use the thesis for the purpose of research or private study only and not for distribution or further reproduction or any other purpose.
- 3. The reader agrees to indemnify and hold the University harmless from and against any loss, damage, cost, liability or expenses arising from copyright infringement or unauthorized usage.

IMPORTANT

If you have reasons to believe that any materials in this thesis are deemed not suitable to be distributed in this form, or a copyright owner having difficulty with the material being included in our database, please contact lbsys@polyu.edu.hk providing details. The Library will look into your claim and consider taking remedial action upon receipt of the written requests.

SYNTHESIS AND STRUCTURE-ACTIVITY RELATIONSHIP STUDIES OF THIAZOLE DERIVATIVES AS INHIBITORS OF SARS-COV-2 MAIN PROTEASE

YIN WEILE

PhD

The Hong Kong Polytechnic University

2025

The Hong Kong Polytechnic University

Department of Applied Biology and Chemical Technology

Synthesis and Structure-Activity Relationship Studies of Thiazole Derivatives as Inhibitors of SARS-CoV-2 Main Protease

YIN Weile

A thesis submitted in partial fulfilment of the requirements for the degree of Doctor of Philosophy

March 2025

CERTIFICATE OF ORIGINALITY

I hereby declare that this thesis is my own work and that, to the best of my knowledge and belief, it reproduces no material previously published or written, nor material that has been accepted for the award of any other degree or diploma, except where due acknowledgement has been made in the text.

(Signed)

YIN WEILE

May 2025

ACKNOWLEDGEMENT

First and foremost, I express my profound gratitude to my supervisor, Prof. WONG Kwok-yin, for the life-altering opportunity and for the support, guidance, and encouragement throughout my academic pursuit.

My thanks go to Dr. KONG Wai Po for his expert assistance in conducting the experiments of X-ray cocrystal structures, which were fundamental to my research. I am also grateful to Dr. LEUNG Siu Lun for his valuable support in conducting the cytotoxicity experiment. I extend my appreciation to Dr. CHEN Yu Wai and Dr. LIANG Zhiguang for their thorough review and insightful feedback on my thesis draft. My thanks also go to Mr. HUNG Chueng Hin and all my other labmates for their assistance and companionship during my PhD study.

Last but not least, I dedicate my deepest thanks to my loving wife, Miss PEI Jiao, for her unwavering love and support, and to my parents and parents-in-law for their steadfast and unconditional support, which has been invaluable throughout my life.

TABLE OF CONTENTS

Abstract			I
List of Ta	ables		III
List of Fi	igures		IV
List of So	chemes	S	XI
List of A	bbrevia	ations	XV
Chapter 1	l. Int	roduction	1
1.1.	CC	OVID-19 pandemic and SARS-CoV-2	2
1.2.	SA	ARS-CoV-2 main protease in the viral replication	2
	1.2.1	The structure of SARS-CoV-2 main protease	2
	1.2.2	The function of SARS-CoV-2 main protease in the viral replicat	ion
	proces	ss	4
	1.2.3	The mutation of main proteases across coronaviruses	7
	1.2.4	SARS-CoV-2 M ^{pro} as a druggable target for the treatment of	
	COVI	ID-19	9
1.3.	Teo	chniques for discovery of SARS-CoV-2 M ^{pro} inhibitors	10
	1.3.1	Specificities of the catalytic site of main proteases and use of H	ΓS
			10
	1.3.2	The catalytic mechanism of M ^{pro} and its elucidation by mass	
	spectr	ometry	13

	1.4.	As	survey of existing SARS-CoV-2 M ^{pro} inhibitors	16
		1.4.1	Peptidomimetic SARS-CoV-2 M ^{pro} inhibitors	16
		1.4.2	Nonpeptidic small molecule SARS-CoV-2 M ^{pro} inhibitors	29
		1.4.3	Structural features of SARS-CoV-2 M ^{pro} inhibitors	45
	1.5.	Aiı	ms and Objectives of this project	46
Cha	pter 2	2. De	sign and Synthesis of New Main Protease Inhibitors	48
	2.1	Me	thods	49
		2.1.1	Materials and instruments	49
		2.1.2	Chemistry	49
	2.2	Soı	me background information of lead compounds	70
		2.2.1	Masitinib as inhibitor against SARS-CoV-2 M ^{pro}	70
		2.2.2	MAC-5576 against SARS-CoV-2 M ^{pro}	74
	2.3	De	sign of the compounds	78
		2.3.1	Introduction of Bioisosterism	78
		2.3.2	Strategy of Scaffold Fusion	80
		2.3.3	Strategy of Bioisosterism	82
		2.3.4	Other strategies	84
	2.4	Syı	nthetic routes to target compounds	86
		2.4.1	Thiazole-based analogues with phenyl and benzyl rings	86
		2.4.2	Oxazole-based analogues with phenyl rings	94
		2.4.3	Amide-linker analogues	96

2	2.4.4	Non-linker analogues	98
Chapter 3.	Det	termination of Structure Activity Relationship of the SARS	-CoV-2
M ^{pro} Inhib	itors		100
3.1	Me	thods	101
3	3.1.1	Materials and equipment	101
3	3.1.2	Cloning, expression, and purification of the recombinant SAR	RS-
(CoV-2	M ^{pro}	101
3	3.1.3	Measurement of SARS-CoV-2 M ^{pro} inhibitory activity	103
3	3.1.4	Evaluation of IC ₅₀ of compounds against SARS-CoV-2 M ^{pro}	106
3.2	The	e enzymatic FRET-based assay for SAR study	108
3.3	Res	sults of the inhibition on SARS-CoV-2 M ^{pro}	110
3.4	An	in-depth exploration of the structure of MC02	112
3	3.4.1	Effects of Part A	114
3	3.4.2	Effects of Part B and N-chain of Linker	120
3	3.4.3	Effects of Part C and amino group of Linker	123
3.5	Sur	mmary of Structure Activity Relationship	128
3.6	Insi	ight from the SAR study	130
3	3.6.1	The activity of Part A	130
3	3.6.2	The activity of Part B	131
3	3.6.3	The activity of Linker	131
3	3 6 4	The activity of Part C	132

3.7	Determination on the IC ₅₀ values against SASR-CoV-2 M ^{pro}	132
Chapter 4.	Biochemical Properties of the Compounds	135
4.1	Methods	136
4.	1.1 Materials and equipment	136
4.	1.2 Mass Spectroscopy of the covalent bond formation	136
4.1	1.3 Crystallization, data collection and structure determination	137
4.	1.4 Dilution assay	138
4.	1.5 Time-dependent assay	138
4.1	1.6 SARS-CoV and SARS-CoV-2 M ^{pro} Enzymatic assays	140
4.1	1.7 Cytotoxic assay	140
4.	1.8 Antiviral assay	141
4.2	Mechanistic studies of the target compounds against SASR-CoV-2	M ^{pro}
		144
4.2	2.1 X-ray crystal structure of SARS-CoV-2 M ^{pro} in complex with M	Л С12
		144
4.2	2.2 Mass Spectrometry of MC04-SASR-CoV-2 M ^{pro} complex form	ation
		146
4.2	2.3 Dilution assay of MC12 against SARS-CoV-2 M ^{pro}	151
4.2	2.4 Time-dependent assay of MC12 against SARS-CoV-2 M ^{pro}	153
4.3	Inhibition against SARS-CoV M ^{pro}	155
4.4	Cytotoxic studies of the target compounds	159

	4.4.1	Results after 1 day treatment
	4.4.2	Results after 2-day treatment
4.5	An	tiviral assays of the target compounds in Vero E6163
	4.5.1	Results of the antiviral assays
	4.5.2	Discussion on the antiviral results
Chapter :	5. Fui	rther Optimization on the Structure of Compounds168
5.1	Me	ethods
	5.1.1	Materials and equipment
	5.1.2	Chemistry
	5.1.3	Crystallization, data collection and structure determination194
	5.1.4	Antiviral assay195
5.2	Str	ategy I of the structural modification198
	5.2.1	Direction of the structural modification
	5.2.2	Strategy of the structural modification
	5.2.3	Synthetic route of new compounds
	5.2.4	Evaluation of the inhibitory activity against SASR-CoV-2 M ^{pro} 205
	5.2.5	Determination on the IC ₅₀ values against SASR-CoV-2 M ^{pro} 207
	5.2.6	Mechanistic studies of the target compounds against SASR-CoV-2
	M^{pro}	209
5.3	Alt	ternative strategy on the structural modification214
	531	Direction of the structural modification

5.3.2	2 Synthetic route of new compounds	6
5.3.3	B Evaluation of the inhibitory activity against SASR-CoV-2 M ^{pro} 22	20
5.3.4	4 Structural optimization of AD0222	24
5.3.	Determination on the IC ₅₀ values against SASR-CoV-2 M ^{pro} 22	26
5.3.0	Types of warheads and the effects of thiazole/oxazole22	29
5.3.	7 X-ray crystal structures of SARS-CoV-2 M ^{pro} in complex with AD0)5
and	AD0623	31
5.3.8	Summary of Structure Activity Relationship23	6
5.3.9	Antiviral assays of the target compounds in Vero E623	8
Chapter 6. C	Conclusion and Future Direction24	ŀ2
Appendices		
Declarati	on24	18
A1 Purifi	cation of recombinant SARS-CoV-2 M ^{pro}	18
A2 List o	f the structures of final compounds25	50
A3 ¹ H N	MR and mass spectra26	53
References	30)5

Abstract

Among the various potential drug targets in SARS-CoV-2, the main protease has emerged as a viable target for antiviral drug development. In this project, 42 thiazole and oxazole derivatives were designed and synthesized through a structure-based rational drug design approach. Biochemical screening and IC₅₀ assessments indicated that 5-chloropyridin-3-yl 2-(methyl(phenyl)amino)thiazole-4-carboxylate (compound MC12) is a potent SARS-CoV-2 Mpro inhibitor, with efficacy comparable to Nirmatrelvir. Compound MC12 also displayed the inhibitory activity against SARS-CoV M^{pro}. The structure-activity relationship of these compounds was further explored. The mechanism of inhibition was elucidated by mass spectrometry and X-ray crystal structure as covalent bond formation between the inhibitor and target. The compounds showed minimal cytotoxicity in MTT assays on mammalian cell lines and demonstrated antiviral activity against SARS-CoV-2 in Vero E6 cells. Structural modifications of MC12, such as the derivative 5-chloropyridin-3-yl 2-(((1H-benzo[d][1,2,3]triazol-1yl)methyl)(benzyl)-amino)thiazole-4-carboxylate (compound MC04BP01), were also explored. MC04BP01 exhibits inhibitory activity against SARS-CoV-2 M^{pro} similar to that used for MC12 and Nirmatrelvir. 2-Chloro-N-((S)-4-methyl-1-oxo-1-(((S)-1-oxo-3-((S)-2-oxopyrro-lidin-3-yl)propan-2-yl)amino)pentan-2-yl)thiazole-4-carboxamide (compound AD05) and 2-chloro-N-((S)-3-methyl-1-(((S)-4-methyl-1-oxo-1-(((S)-1oxo-3-((S)-2-oxo-pyrrolidin-3-yl)propan-2-yl)amino)pentan-2-yl)amino)-1-oxobutan-2-yl)thiazole-4-carboxamide (compound AD06), belonging to peptidomimetic derived from MC compounds, demonstrate inhibitory effects against the main protease. AD06 demonstrated an IC₅₀ value against SARS-CoV-2 M^{pro} that was similar to that of Nirmatrelvir. Furthermore, the analysis of X-ray crystal structures of SARS-CoV-2 M^{pro} in complex with AD05 and AD06 confirmed the covalent binding mechanism of the AD series of compounds. The antiviral assay results indicated that AD05 displayed the strongest potency (EC₅₀ = 3.264 μ M) against the SARS-CoV-2 virus. These findings highlight the potential of thiazole-based compounds as promising leads in the development of SARS-CoV-2 M^{pro} inhibitors.

List of Tables

- **Table 2.1** Examples of classical bioisosteres-groups in each row are equivalent.
- **Table 3.1** Inhibitory activities of MC02, Masitinib and MAC-5576 against SARS-CoV-2 M^{pro}.
- **Table 4.1** Results of inhibition of Nirmatrelvir and MC12 at 200 nM against SARS-CoV-2 M^{pro} and SARS-CoV M^{pro}.
- **Table 4.2** Evaluation of cytotoxicity in Vero E6 cells of the selected compounds.
- **Table 5.1** The lowest Rerank scores for MC04BP01, MC04, and MC12 calculated through Molegro Virtual Docker (MVD) docking.
- **Table 5.2** The IC₅₀ values of the selected compounds against SARS-CoV-2 M^{pro}
- **Table 5.3** Results of CPE assay of AD05, AD06, and AD06CN against SARS-CoV-2 M^{pro}.
- **Table A.1** List of the structures of the synthesized compounds.

List of Figures

- **Figure 1.1** The structure (PDB ID 7VTH) of SARS-CoV-2 M^{pro} dimer.
- Figure 1.2 A) The process of SARS-CoV-2 replication cycle and the druggable targets in the key steps. B) The genome of SARS-COV-2 and the corresponding proteins encoded by the genome frames.
- **Figure 1.3** Alignment of the sequences of three nonstructural polyproteins of SARS-CoV-2.
- Figure 1.4 A) The amino acids residues forming the subsites of M^{pro} catalytic site. B) Peptide sequences covering residues P4 to P1' recognized by SARS-CoV-2, SARS-CoV and MERS-CoV.
- Figure 1.5 The process of natural substrate hydrolysis by M^{pro} Cys145-His41 dyad.
- Figure 1.6 Chemical structures of PF-00835231, Nirmatrelvir and Nirmatrelvir-based scaffold.
- Figure 1.7 Chemical structure of N3.
- Figure 1.8 Chemical structure of 8a (YH-6).
- Figure 1.9 Chemical structures of 11a, 13a, 13b, boceprevir, GC376, UAWJ246, UAWJ247, and UAWJ248.

- Figure 1.10 Chemical structures of 11a, 11b, 18p,17w, 10a, 10b, MI-09 and MI-30.
- Figure 1.11 Chemical structures of MAC-5576, 7d, 1 and 3w.
- Figure 1.12 Chemical structures of 28, 31, 32, 20e, F8, E24, ebselen, disulfiram, carmofur, tideglusib, shikonin, PX-12, 18, 2j, 23 and 26.
- **Figure 1.13** Chemical structure of Ensitrelvir (S-217622).
- Figure 1.14 Chemical structure of Masitinib.
- Figure 1.15 Chemical structures of baicalin and baicalein.
- **Figure 1.16** Chemical structures of X77, ML188, 23R(Jun8-76-3A), 23S, Jun10541R, GC-14 and FD-9.
- Figure 1.17 Chemical structures of acriflavine (ACF), proflavine hemisulfate (PRF), walrycin B, LLL-12, 2j, 23 and 26.
- Figure 2.1 Chemical structure of Masitinib.
- Figure 2.2 A) X-ray crystal structure of Masitinib (carbons colored in purple) binding to SARS-CoV-2 M^{pro} (PDB ID 7JU7). B) The diagram showing the details of some interactions formed between the Masitinib (carbons colored in purple) and the active site of SARS-CoV-2 M^{pro}.
- Figure 2.3 Chemical structure of MAC-5576.
- Figure 2.4 A) X-ray crystal structure of MAC-5576 (colored in purple) binding to SARS-CoV-2 M^{pro} (PDB ID 7JT0). B) The diagram showing the

details of some interactions formed between the MAC-5576 (carbons colored in purple) and the active site of SARS-CoV-2 M^{pro}.

- Figure 2.5 Strategy of scaffold fusion utilized in the two lead compounds and the structure of one of the designed compounds, MC04.
- **Figure 2.6** Application of bioisosterism based on MC04.
- Figure 2.7 Structures of representative compounds for exploring the effects of other moieties.
- Figure 2.8 Structural features of the target compounds.
- **Figure 2.9** Route 1 of the retrosynthesis of MC04.
- **Figure 2.10** Route 2 of the retrosynthesis of MC04.
- A) Chemical structures of MCA/DNP; B) Chemical structure of the biosensor with sequence from P₄ to P1' residues recognized by SARS-CoV-2 M^{pro} (MCA-AVLQ\\$GFR-K(DNP)K; arrow indicates the cleavage site); C) Principle of the enzymatic FRET-based assay used to monitor M^{pro} activity.
- Figure 3.2 Structure of MC02 and the four components of the designed compound.
- Figure 3.3 Chemical structures and results of SAR exploration of effects of Part

 A when compounds at 150 nM.
- Figure 3.4 Results of SAR exploration of effects of Part A when compounds at 100 nM.

- Figure 3.5 Chemical structures and results of SAR exploration of effects of Part B and *N*-chain.
- Figure 3.6 The first set of chemical structures and results of SAR exploration of the importance of Part C and Part A.
- Figure 3.7 The second set of chemical structures and results of SAR exploration of the effects on Part C and Part A.
- **Figure 3.8** Summary of structure activity relationship.
- **Figure 3.9** Results of the evaluation of SARS-CoV-2 M^{pro} IC₅₀ and structures of Nirmatrelvir, MAC-5576, MC04, MC11, MC12 and MC10.
- Figure 4.1 A) X-ray crystal structure of MC12 binding to SARS-CoV-2 M^{pro}

 (PDB ID 9M2V) and B) Comparison of the binding mode of MC12

 with MAC-5576 (PDB ID 7JT0). Carbons of MC12 and MAC-5575

 are shown as purple and yellow, respectively.
- Figure 4.2 A) Mass spectrum of wild type SARS-CoV-2 M^{pro} (M⁺ = 33 795 Da),

 B) and C) Mass spectra of the complex of M^{pro} and MC04 (M⁺ = 33 997 Da) with different incubation time (B: without incubation; C: with 40-min incubation).
- **Figure 4.3** Mechanism of inhibition of SARS-CoV-2 M^{pro} by MC04.
- **Figure 4.4** Dilution assay of MC12 and Nirmatrelvir against SARS-CoV-2 M^{pro}.
- **Figure 4.5** Time-dependent inhibition of SARS-CoV-2 M^{pro} by MC12.

- Figure 4.6 A) Peptide sequences covering residues P4 to P1' recognized by SARS-CoV-2 M^{pro} and SARS-CoV M^{pro}; B) Chemical structure of the employed biosensor.
- **Figure 4.7** Results of MTT assays of MC04 for 1-day treatment to the cells.
- Figure 4.8 Results of MTT assays of MC04, MC10, MC11, MC1112, MC12, MC1210 and MAC-5576 for 2-day treatment to the cells.
- Figure 4.9 Antiviral activities against SARS-CoV-2 βCoV/Wuhan/WIV04 /2019 in Vero E6 cells of the selected compounds at 100 μM.
- Figure 4.10 Comparison of the binding mode of MC12 with Nirmatrelvir (PDB ID 8DZ2). Carbons of MC12 and Nirmatrelvir are shown as purple and green, respectively.
- Figure 5.1 A) Structures of MC04, MC12, MC12E01 and MC04BP; B) Results of inhibition of MC04, MC12, MC12E01 and MC04BP01 at 150 nM against SARS-CoV-2 M^{pro} and structures of MC04, MC12, MC12E01, MC04BP and MC04DN.
- Figure 5.2 A) Schematic of the binding mode of CCF0058981 (CCF981) orienting the binding site; B) Strategy of the structural modification
- Figure 5.3 Results of inhibition of MC12, MC12, MC04, MC04BP and MC04BP01 against SARS-CoV-2 M^{pro}.
- Figure 5.4 Results of the evaluation of SARS-CoV-2 M^{pro} IC₅₀ and structures of MC04BP01, MC12 and Nirmatrelvir.

- Figure 5.5 The predicted binding poses of MC04BP01 (carbons colored in purple) with the catalytic site of SARS-CoV-2 M^{pro} (PDB ID 7VTH).
- Figure 5.6 Time-dependent inhibition of SARS-CoV-2 M^{pro} by MC04BP01
- Figure 5.7 Alternative strategies for structural modification.
- Figure 5.8 Evaluation of the inhibitory activity of MC12, MC12D01 and AD01 against SARS-CoV-2 M^{pro}.
- Figure 5.9 Structural modification of AD01 and evaluation of their inhibitory activity against SARS-CoV-2 M^{pro}.
- **Figure 5.10** Structural modification of AD02 and evaluation of their inhibitory activity against SARS-CoV-2 M^{pro}.
- Figure 5.11 Results of the evaluation of IC₅₀ of the selected compounds against SARS-CoV-2 M^{pro}.
- **Figure 5.12** Evaluation of the effects of warhead and thiazole on inhibitory activity against SARS-CoV-2 M^{pro}.
- Figure 5.13 A) X-ray crystal structure of AD05 (carbons colored in purple) binding to SARS-CoV-2 M^{pro} (PDB ID 9M29). B) Mechanism of inhibition of SARS-CoV-2 M^{pro} by AD05.
- Figure 5.14 A) X-ray crystal structure of AD06 (carbons colored in purple) binding to SARS-CoV-2 M^{pro} (PDB ID 9M2U). B) Mechanism of inhibition of SARS-CoV-2 M^{pro} by AD06.

Figure 5.15 Comparison of the binding modes of A) AD06 with Nirmatrelvir (PDB ID 8DZ2) and B) AD06 with AD05 in SARS-CoV-2 M^{pro}. The major differences of AD06 from Nirmatrelvir and AD05 are marked with a dashed circle.

Figure 5.16 Five components of AD compounds.

Figure A.1 Result of the purified recombinant SARS-CoV-2 M^{pro} on SDS-PAGE

(M: marker, FT: flow through, NB: nonspecific binding, P1-P3: triple lanes of the same purified recombinant SARS-CoV-2 M^{pro}).

List of Schemes

- Scheme 2.1 Synthetic route to target compounds: (i) Benzoyl chloride, NH₄SCN, acetone, 60 °C, 45 min, 80%; (ii) 2 M aqueous NaOH, 100 °C, 1 h, 82 %; (iii) methyl bromopyruvate, methanol, 80 °C, 30 min, 70 %; (iv) 1 M aqueous NaOH/MeOH, room temperature, 1 h, 70%; (v) 3-Chloro-5-hydroxypyridine/3-chloro-2-fluoro-5-hydroxypyridine, 1-Hydroxybenzotriazole (HOBt), *N*,*N*'-Diisopropylcarbodiimide (DIC), *N*,*N*-Diisopropylethylamine (DIPEA), *N*,*N*-Dimethylformamide (DMF), room temperature, 24h, 53%.
- Scheme 2.2 Synthetic route to the oxazole-based compounds: (i) ethyl bromopyruvate, methanol, 80 °C, 30 min, 70 %; (ii) 1 M aqueous NaOH/MeOH, room temperature, 1 h, 80 %; (iii) 3-chloro-5-hydroxypyridine, 1-Hydroxybenzotriazole (HOBt), *N,N'*-Diisopropylcarbodiimide (DIC), *N,N*-Diisopropylethylamine (DIPEA), *N,N*-Dimethylformamide (DMF), room temperature, 24h, 66%.
- Scheme 2.3 Synthetic route to the amide-linker compounds: (i) 2-(7-Azabenzotriazol-1-yl)-*N*,*N*,*N'*,*N'*-tetramethyluronium

hexafluorophosphate (HATU), Triethylamine (TEA), *N*,*N*-Dimethylformamide (DMF), room temperature, overnight, 70%; (ii) 1 M aqueous LiOH/MeOH (v:v=1:1), room temperature, 1 h, 80%; (iii) 3-chloro-5-hydroxypyridine, 1-Hydroxybenzotriazole (HOBt), *N*,*N*'-Diisopropylcarbodiimide (DIC), *N*,*N*-Diisopropylethylamine (DIPEA), *N*,*N*-Dimethylformamide (DMF), room temperature, 24h, 64%.

- Scheme 2.4 Synthetic pathway to the non-linker compounds: (i) Sodium Hydrosulfide, Magnesium Chloride, *N,N*-Dimethylformamide (DMF), room temperature, 12 h, 70 %; (ii) methyl bromopyruvate, methanol, 80 °C, 30 min, 70%; (iii) 1 M aqueous NaOH/MeOH, 1 h, 80%; (iv) 3-chloro-5-hydroxypyridine/3-chloro-2-fluoro-5-hydroxypyridine, 1-Hydroxybenzotriazole (HOBt), *N,N*-Diisopropylearbodiimide (DIC), *N,N*-Diisopropylethylamine (DIPEA), *N,N*-Dimethylformamide (DMF), room temperature, 24h, 70%.
- Scheme 5.1 Synthetic route to MC04BP01: (i) methyl bromopyruvate, methanol, 80 °C, 30 min, 70%; (ii) NaH, *N*,*N*-Dimethylformamide (DMF), -20 °C to room temperature, 1 h, 80%; (iii) 1 M aqueous NaOH/MeOH, room temperature, 1 h, 80%; (iv) 3-chloro-5-

hydroxypyridine, HOBt, DIC, DIPEA, *N*,*N*-Dimethylformamide (DMF), room temperature, 24h, 53%.

- Scheme 5.2 Synthetic route to BP0101: (i) 3-(2-chloroacetyl)pyridine, methanol, 80 °C, 12 h, 70%; (ii) NaH, *N,N*-Dimethylformamide (DMF), -20 °C to room temperature, 1 h, 80%.
- Scheme 5.3 Synthetic routes to AD01: (i) 6 M HCl in 1,4-dioxane, room temperature, overnight; (ii) N,N,N',N'-tetramethylchloroformamidinium hexafluorophosphate (TCFH), N-methylimidazole (NMI), acetonitrile, room temperature, overnight, 70%; (iii) NaBH₄, THF, room temperature, overnight, 90%; (iv) Dess-Martin Periodinane, room temperature, overnight, 76%.
- Scheme 5.4 Synthetic routes to AD02, AD04, AD05 and AD06: (i) 6 M HCl in 1,4-dioxane, temperature, overnight; (ii) room 2-(7-Azabenzotriazol-1-yl)-*N*,*N*,*N*′,*N*′-tetramethyluronium hexafluorophosphate (HATU), Triethylamine (TEA), room temperature, overnight, 70%; (iii) 0.8 M aqueous LiOH, THF, room 2 80%; *N*,*N*,*N*′,*N*′temperature, h, (iv) tetramethylchloroformamidinium hexafluorophosphate (TCFH), N-methylimidazole (NMI), acetonitrile, room temperature, overnight, 70%; (v) NaBH₄, THF, room temperature, overnight,

90%; (vi) Dess-Martin Periodinane, room temperature, overnight, 70%.

List of Abbreviations

MERS-CoV Middle East respiratory syndrome coronavirus

BSL Biosafety level

PL^{pro} Papain-like protease

RdRP RNA-dependent RNA polymerase

ssRNA Single strand RNA

(BOC)₂O Di-tert-butyl dicarbonate

3CL^{pro} 3-Chymotrypsin like protease

ACE2 Angiotensin converting enzyme 2

ADMET Absorption, distribution, metabolism, excretion, and toxicity

CC Cell Control

CC₅₀ Median cytotoxic concentration

CoV Coronavirus

COVID-19 Coronavirus disease 2019

CPE Cytopathic Effect

DCM Dichloromethane

DIC *N,N'*-Diisopropylcarbodiimide

DIPEA *N,N*-Diisopropylethylamine

DMEM Dulbecco's Modified Eagle Medium

DMF *N,N*-Dimethylformamide

DMSO Dimethyl Sulfoxide

DNP 2,4-dinitrophenyl

DUB Deubiquitinating

E protein Envelope protein

EA Ethyl acetate

EC₅₀ the half-maximal effective concentration

EDTA Ethylenediaminetetraacetic acid

FBS Fetal Bovine Serum

FDA Food and Drug Administration

FRET Fluorescence resonance energy transfer

GFP Green Fluorescent Protein

HATU 2-(7-Azabenzotriazol-1-yl)-*N*,*N*,*N*′,*N*′-tetramethyluronium

hexafluorophosphate

HCV Hepatitis C virus

HEPES *N*-(2-hydroxyethyl)piperazine-*N*'-(3-ethanesulfonic acid)

HIV Human immunodeficiency virus

HOBt 1-Hydroxybenzotriazole

HTS High-throughput screening

IC₅₀ Half-maximal inhibitory concentration

m-CPBA 3-Chloroperbenzoic acid

M protein Membrane protein

MAb monoclonal antibodies

MC Medium Control

MCA 7-methoxycoumarin

MHV Hepatitis virus

mM Millimolar

MOI Multiplicity of Infection

M^{pro} Main protease

N protein Nucleocapsid protein

nM Nanomolar per liter

nsp Nonstructural proteins

ORF Open reading frame

PD Peptidase domain

PDB Protein Data Bank

PS Penicillin Streptomycin

RBD Receptor-binding domain

RBM Receptor-binding motif

RLU Relative Light Unit

RT Room temperature

S protein Spike protein

SARS Severe acute respiratory syndrome

SARS-CoV Severe acute respiratory syndrome coronavirus

SARS-CoV-2 Severe Acute Respiratory Syndrome Coronavirus 2

SI Selectivity index

TEA Triethylamine

TMRPSS2 Transmembrane protease serine 2

TOFMS Time-of-Flight Mass Spectrometry

Tris-HCl Tris(hydroxymethyl)aminomethane hydrochloride

VC Virus Control

WT Wild Type

ZIKV Zika virus

μM Micromolar per liter

SAR Structure-Activity Relationship

DMSO Dimethyl sulfoxide

PHEIC Public health emergency of international concern

E. coli Escherichia coli

MTT 3-(4,5-Dimethylthiazol-2-yl)-2,5-diphenyltetrazolium bromide

MVD Molegro Virtual Docker

pp1a Polyprotein chains 1a

pp1ab Polyprotein chains 1ab

Chapter 1. Introduction

1.1. COVID-19 pandemic and SARS-CoV-2

The COVID-19 pandemic, which was caused by SARS-CoV-2 and began in December 2019, quickly escalated to a global health crisis [1-4]. In response to the pandemic, global efforts have been placed on the discovery of specific antiviral treatments. A key strategy in antiviral therapy development is to disrupt the replication process at any stage of the virus life cycle [5]. This strategy aims to interfere with the ability of virus to replicate and propagate within the host, as this can effectively limit the spread of the virus. Among the SARS-CoV-2 targets, the main protease (M^{pro}) has been a focal point due to its crucial role in viral replication.

1.2. SARS-CoV-2 main protease in the viral replication

1.2.1 The structure of SARS-CoV-2 main protease

The main protease, also known as the 3-chymotrypsin-like protease, 3CL^{pro} or M^{pro} , is a crucial cysteine protease in the SARS-CoV-2 replication process. Its crystal structure indicates that M^{pro} exists as a dimer, with two protomers intersecting at right angles [5] (Figure 1.1). Each protomer is composed of three domains: domains I and II, which are structured with β -strands to form the chymotrypsin-like fold, and domain III, which is predominantly α -helical [6, 7]. A notable feature is the β -barrel domains that connect to domain III through an extended loop region [7]. The catalytic site of the enzyme, containing a Cys-His catalytic dyad, is located in the cleft between domains I and II of each protomer [8].

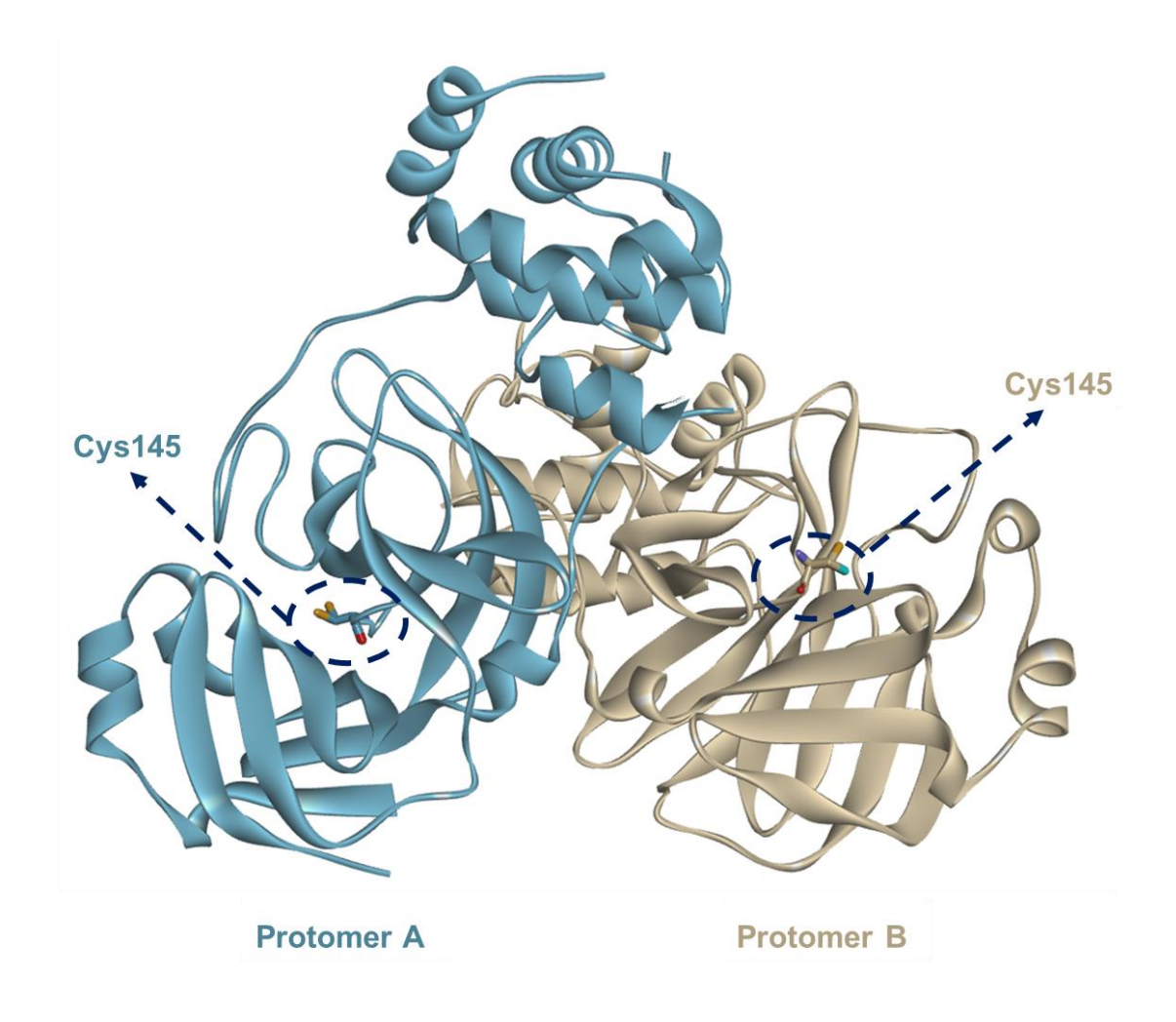


Figure 1.1 The structure (PDB ID 7VTH) of SARS-CoV-2 M^{pro} dimer.

1.2.2 The function of SARS-CoV-2 main protease in the viral replication process

1) The replication process of SARS-CoV-2

SARS-CoV-2 hijacks host cell machinery to complete its replication cycle. Upon entering the host cell, the viral single-stranded RNA (ssRNA) uses the host ribosome to produce viral proteins (Figure 1.2A). The open reading frame 1ab (ORF1ab) of SARS-CoV-2 viral genome was translated into two polyprotein chains, which are subsequently cleaved by the papain-like protease (PL^{pro}, also known as nsp3) and the main protease (M^{pro}, also known as 3CL^{pro} or nsp5) into 16 nonstructural proteins through autoproteolysis^[9, 10]. These proteins are crucial for viral assembly and the subsequent release of new virions from the host cell via exocytosis, continuing the infection cycle. If a host cell that was already engaged in viral replication cannot maintain homeostasis, it will ultimately be lysed by the virus, spreading the infection further ^[9, 10]. SARS-CoV-2 M^{pro} is located at the nsp5 site of the polyproteins pp1a and pp1ab (Figure 1.2B). Through autoproteolysis, M^{pro} releases itself from the nsp5 site and hydrolyzes eleven sites within the polyprotein chains ^[11].

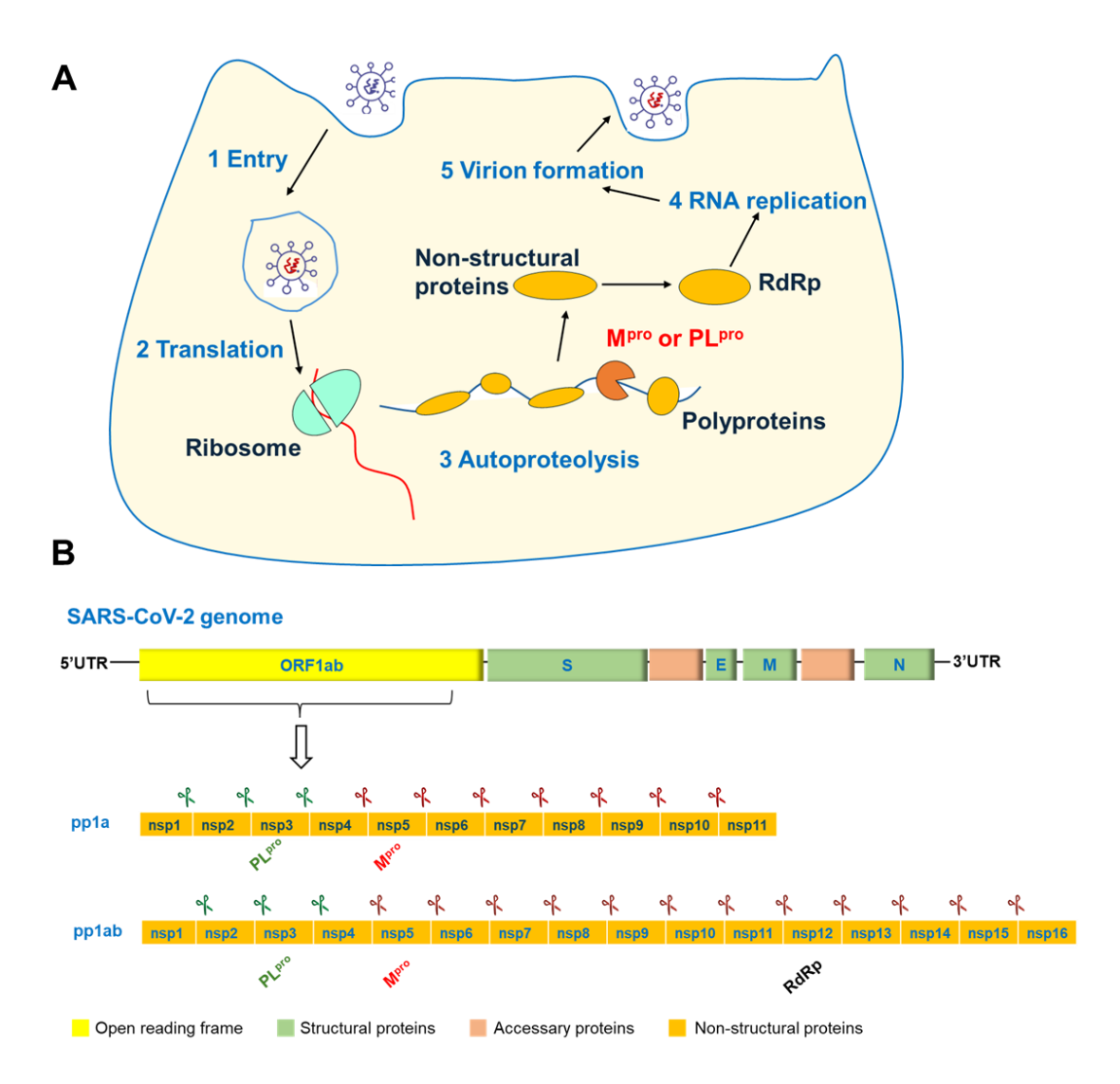


Figure 1.2 A) The process of SARS-CoV-2 replication cycle and the druggable targets in the key steps. B) The genome of SARS-COV-2 and the corresponding proteins encoded by the genome frames.

2) The function of SARS-CoV-2 Mpro

SARS-CoV-2 M^{pro} is essential for the viral replication cycle, responsible for hydrolyzing eleven conserved sites within the polyprotein chains 1a and 1ab. Specifically, M^{pro} cleaves at the junction between nsp5 and nsp16 [11]. This cleavage is critical for the production of individual nonstructural proteins required for the viral replication complex [11-13]. These nonstructural proteins include essential functional proteins such as the RNA-dependent RNA polymerase (RdRP, also known as nsp12) and helicase (nsp13), which play pivotal roles in viral assembly and modulation of the host immune response [10].

The active site, located in the cleft between domains I and II of each protomer of the main protease, is crucial for the proteolytic activity that facilitates the SARS-CoV-2 replication cycle. Importantly, the natural substrates of SARS-CoV-2 M^{pro} are not recognized by human cellular enzymes. Thus, inhibition on SARS-CoV-2 M^{pro} can in principle disrupt the viral replication process without affecting host cell functions. This unique characteristic positions M^{pro} as an attractive and highly specific target for the development of anti-coronavirus therapeutics, presenting a potential therapeutic strategy for COVID-19 [14].

1.2.3 The mutation of main proteases across coronaviruses

Figure 1.3 illustrates the sequence alignment of three nonstructural proteins (nsp) of SARS-CoV-2. Notably, the active site of the papain-like protease (PL^{pro}) is prone to mutations, particularly around the S543P site [15]. Similarly, the RNA-dependent RNA polymerase (RdRP) has been observed to mutate around the A423V site [15]. In contrast, mutations in the main protease (M^{pro}) have been specifically identified in the Clade 20B-T variant of the virus, which harbors the P108S mutation in M^{pro} [15]. The P108S mutation within Clade 20B-T is significant as it is associated with a decrease in substrate binding affinity, leading to a reduction in the enzymatic activity of SARS-CoV-2 M^{pro} [15]. This reduction in activity underscores the importance of M^{pro} in the viral replication process and suggests that even a single mutation can significantly impact the enzymatic function. Moreover, compared to the P108S mutation site, the surrounding residues in M^{pro} are highly conserved across different viral strains [15]. This conservation highlights the structural stability and functional integrity of M^{pro}, reaffirming its potential as a target for antiviral therapies.

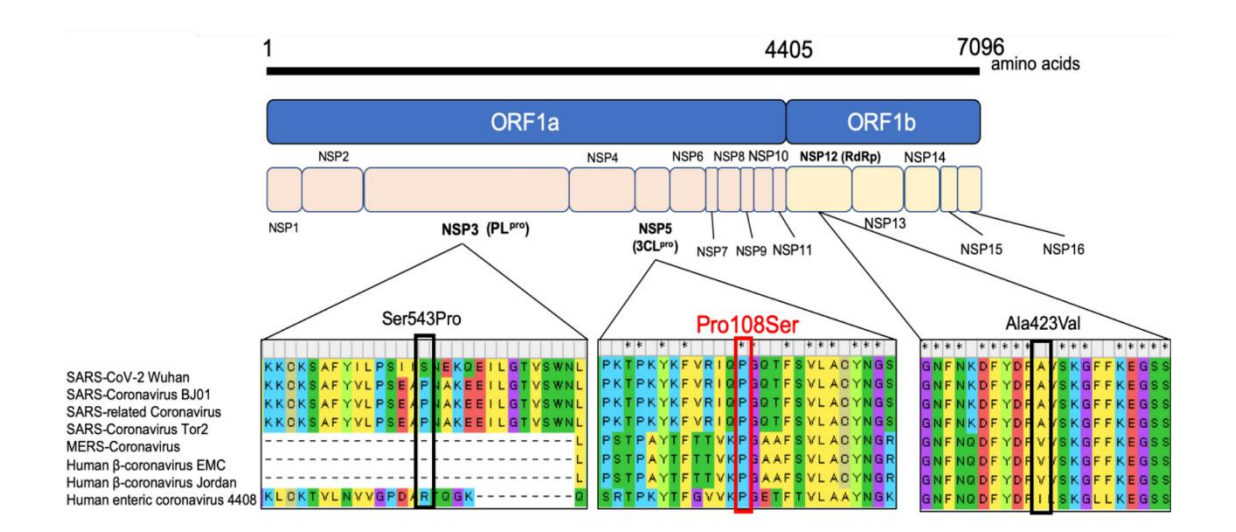


Figure 1.3 Alignment of the sequences of three nonstructural polyproteins of SARS-CoV-2. Reprinted with permission from the reference [15].

1.2.4 SARS-CoV-2 M^{pro} as a druggable target for the treatment of COVID-19

Upon analyzing the roles of three nonstructural proteins (nsp) in the viral replication process, the rationales for selecting M^{pro} as a target for antiviral intervention are multifaceted. In contrast to the PL^{pro} of SARS-CoV-2, which exhibits a high mutation rate [16, 17], M^{pro} maintains a highly conserved structure and function across different strains of SARS-CoV-2 [15]. Moreover, the catalytic sites of M^{pro} are remarkably similar across various coronaviruses [5, 18, 19]. This conservation makes M^{pro} an auspicious target for the creation of broad-spectrum antiviral inhibitors [5, 18, 19]. While the RdRP of SARS-CoV-2 is more conserved in structure than M^{pro} [5, 18, 19], its substrates, nucleoside triphosphates (NTPs), are also substrates for human enzymes. This similarity raises the risk of off-target effects with RdRP inhibitors [20-25]. Conversely, the substrates for SARS-CoV-2 M^{pro} are distinct from those of human proteases [5, 19], suggesting that M^{pro} inhibitors could be developed with a reduced risk of off-target effects. M^{pro} functions as an upstream protease relative to RdRP in the viral replication cascade [5, 18, 19]. In the absence of the initial proteolytic cleavage of the polyproteins pp1a and pp1ab by M^{pro}, RdRP cannot perform its role in viral replication effectively [5, 18, 19]. This positioning of M^{pro} early in the replication process implies that its inhibition could disrupt the entire downstream production of viral components.

In summary, the high conservation of M^{pro}, the distinct of its substrate from human counterparts, and its role as an early factor in the viral life cycle make it an attractive target for antiviral drug development, potentially leading to therapies with broad activity against coronaviruses.

1.3. Techniques for discovery of SARS-CoV-2 M^{pro} inhibitors

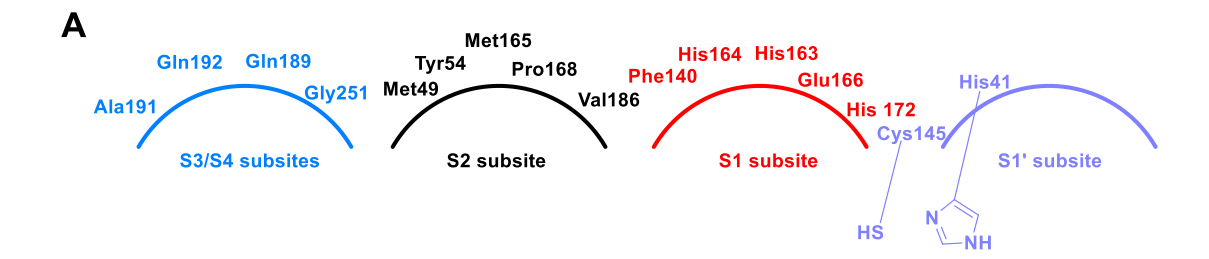
1.3.1 Specificities of the catalytic site of main proteases and use of HTS

High-throughput screening (HTS) is a widely used technique in lead identification and optimization in the drug discovery process [26]. In the context of identifying SARS-CoV-2 M^{pro} inhibitors, HTS has primarily employed two assay types: biochemical HTS and *in silico* HTS [26]. Among biochemical HTS methods, fluorescence resonance energy transfer (FRET)-based assays have emerged as particularly popular [27, 28].

A FRET-based biosensor for HTS consists of a recognition group and signal groups. In the specific application for screening SARS-CoV-2 M^{pro} inhibitors, the recognition group is an amino acid sequence modeled after the natural substrate of M^{pro}. The sequences are selected to align with the recognition profiles of M^{pro}. The catalytic site of M^{pro} is composed of five subsites, namely S4, S3, S2, S1, and S1' (Figure 1.4A), each corresponding to the substrate residues P4, P3, P2, P1 and P1', respectively [18,29] (Figure 1.4B).

A summary of the recognition profiles for each subsite is analyzed. Subsite S1' is where the Cys145-His41 catalytic dyad is located, recognizing P1' residues that are small in size, such as alanine and serine [18,29]. Subsite S1 is defined by the side chains of Phe140, His163, His164, Glu166, and His172, which show a strong preference for glutamine at the P1 position of the polyprotein substrates [18,29]. Subsite S2 is characterized by the hydrophobic side chains of Met49, Tyr54, Met165, Pro168, and Val186, which favor hydrophobic residues like leucine at the P2 position [18,29]. Subsites S3 and S4 consist of residues Gln189, Ala191, Gln192, and Gly251, which are solvent-exposed. The substrate residues at P3 and P4 are less conserved compared to those at P2, P1, and P1' [18,29]

Understanding the specificities of these subsites is crucial for the rational design of inhibitors that can effectively bind to and inhibit the activity of M^{pro}. SARS-CoV M^{pro} exhibits a high degree of structural and functional conservation with its SARS-CoV-2 counterpart, along with a similar recognition profile. This shared profile is crucial for the design of peptidomimetic M^{pro} inhibitors, as it allows the development of compounds that can potentially target both viruses with similar mechanisms of action.



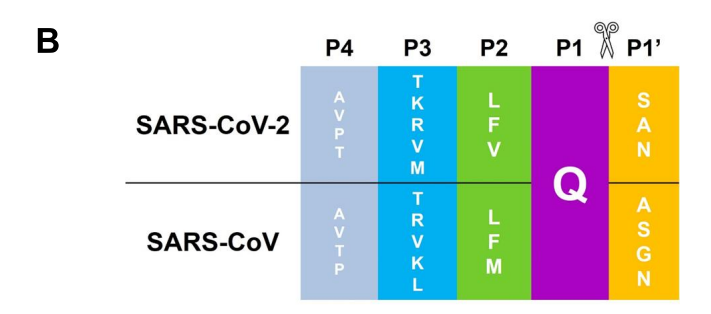


Figure 1.4 A) The amino acids residues forming the subsites of M^{pro} catalytic site. B) Peptide sequences covering residues P4 to P1' recognized by SARS-CoV-2, SARS-CoV and MERS-CoV.

1.3.2 The catalytic mechanism of M^{pro} and its elucidation by mass spectrometry

1) The catalytic mechanism of M^{pro}

The catalytic cycle initiates with the deprotonation of the thiol group of Cys145 by the basic residue His41. This step activates the cysteine, enabling its nucleophilic attack on the carbonyl carbon of the substrate (Figure 1.5). The reaction results in the release of an amine product and the formation of a thioester intermediate, which makes His41 return to its deprotonated state. Subsequently, the thioester intermediate is hydrolyzed under the catalytic influence of histidine, leading to the release of carboxylic acid. This final step culminates in the regeneration of the free enzyme, ready to engage in another catalytic cycle [30].

Figure 1.5 The process of natural substrate hydrolysis by M^{pro} Cys145-His41 dyad.

2) Mechanism elucidation by mass spectrometry

Mass spectrometry leverages the catalytic mechanism of SARS-CoV-2 M^{pro} by identifying covalent inhibitors. Covalent inhibitors of SARS-CoV-2 M^{pro} are designed to form covalent bonds with the active site cysteine (Cys145), thereby obstructing the enzymatic catalytic activity. The formation of covalent bond results in a complex between the enzyme and the inhibitor, which can be detected and confirmed by mass spectrometry [31, 32]. By monitoring the formation of covalent binding using mass spectrometry, the interactions between M^{pro} and potential covalent inhibitors researchers can be detected and characterized. This analytical technique provides a direct method to assess the formation of covalent bonds and offers evidence for the inhibitory mechanisms.

3) Combining FRET-based HTS and mass spectrometry

Furthermore, mass spectrometry can be integrated with high-throughput screening (HTS) to address the challenge of false positives that frequently arise in fluorescence-based enzymatic assays [33]. By employing mass spectrometry as a secondary validation tool, researchers can discern true covalent binding events from non-specific interactions or fluorescence interference, enhancing the accuracy and reliability of HTS in identifying potent and specific SARS-CoV-2 M^{pro} inhibitors.

1.4. A survey of existing SARS-CoV-2 Mpro inhibitors

Employing a variety of discovery strategies such as HTS, mass spectrometry, drug repurposing, and rational drug design, a number of compounds have been identified as inhibitors of SARS-CoV-2 M^{pro} and SARS-CoV M^{pro} [18]. These inhibitors can be categorized into two structural classes: peptidomimetics, which mimic the structure of the natural substrate, and nonpeptidic small molecules, which offer advantages such as improved stability and oral bioavailability. For example, peptidomimetic inhibitors have been reported to have a low half-life in plasma [34]. The identification of these diverse inhibitors underscores the multifaceted approach necessary to combat viral threats and highlights the potential of these compounds in developing effective treatments against SARS-CoV-2.

1.4.1 Peptidomimetic SARS-CoV-2 M^{pro} inhibitors

Peptidomimetic inhibitors are crafted to mimic the structures of the natural substrates with warhead that covalently bind to the enzyme. This ensures that these inhibitors can effectively fit into the corresponding subsites of the M^{pro} catalytic site [35].

1) Nitrile and hydroxymethylketone as warheads

PF-00835231 (Figure 1.6) is a compound identified through FRET-based screening as an inhibitor of the SARS-CoV M^{pro}. PF-00835231 also demonstrated inhibitory effects

on SARS-CoV-2 M^{pro} and exhibited antiviral efficacy in Vero E6 cells [13]. Despite its *in vitro* success, PF-00835231 faced challenges, such as poor oral absorption and low permeability *in vivo*. These limitations were addressed through the development of Nirmatrelvir.

Nirmatrelvir (PF-07321332 in Figure 1.6), derived from PF-00835231, stands as the first SARS-CoV-2 M^{pro} inhibitor to receive approval from the FDA and serves as a quintessential example of a peptidomimetic covalent inhibitor [36]. Nirmatrelvir has been optimized for improved pharmacological properties [36], which was developed as an orally available drug with favorable selectivity and toxicity profiles.

The antiviral efficacy of Nirmatrelvir is not only at SARS-CoV-2, but also shows broad-spectrum activity against several coronaviruses, including SARS-CoV and MERS-CoV [36]. Studies of structure-activity relationship (SAR) have been conducted on peptidomimetic analogues of Nirmatrelvir, featuring a variety of warheads (Figure 1.6). These studies revealed that, in comparison to the nitrile warhead of Nirmatrelvir, analogues with hydroxymethylketone and ketobenzothiazole warheads could match its inhibitory potency against SARS-CoV-2 M^{pro} and human coronavirus (HCoV) 229E [37]. This research underscores the importance of warhead optimization in the development of effective and selective M^{pro} inhibitors.

Nirmatrelvir (PF-07321332)-based scaffold

Figure 1.6 Chemical structures of PF-00835231, Nirmatrelvir and Nirmatrelvir-based scaffold.

2) Michael acceptor as warhead

Prior to the COVID-19 pandemic, N3 (Figure 1.7) was recognized as a covalent inhibitor for both SARS-CoV M^{pro} and MERS-CoV M^{pro}. N3 utilized a Michael acceptor as its reactive warhead [38]. With the emergence of SARS-CoV-2, N3 was repurposed and evaluated as an irreversible inhibitor against SARS-CoV-2 M^{pro}. It demonstrated effective inhibitory activity against the virus [12], illustrating the potential of repurposing existing compounds in response to new health threats.

Figure 1.7 Chemical structure of N3.

3) Chlorofluoroacetamide as warhead

Compound 8a, also known as YH-6 (Figure 1.8), incorporates a chlorofluoroacetamide (CFA) group as its warhead, which is designed to covalently bind to the cysteine residue 145 (Cys145) of SARS-CoV-2 M^{pro}. Studies conducted in 293T-ACE2-TMPRSS2 (293TAT) cells infected with SARS-CoV-2 have confirmed that the *R*-configuration of the CFA warhead is crucial for its antiviral efficacy [39]. Additionally, 8a (YH-6) has shown a high degree of specificity for the viral cysteine protease, underscoring its potential as a selective antiviral agent [39].

Figure 1.8 Chemical structure of 8a (YH-6).

4) α -ketoamide as warhead

Through the application of rational drug design principles, compounds 11r, 13a, and 13b (Figure 1.9), featuring an α -ketoamide warhead, were discovered. Compounds 13a and 13b were designed with a pyridione ring and a Boc group, respectively, as substitutes for the amide bond and cinnamoyl group present in 11r. These strategic modifications successfully increased the half-life of the α -ketoamide M^{pro} inhibitors, from 0.3 hours for 11r to 1.0 hour for 13a [34].

In a FRET-based high-throughput screening (HTS), boceprevir (Figure 1.9), a marketed hepatitis C virus (HCV) NS3-4A protease inhibitor, was identified for its inhibitory activity against SARS-CoV-2 M^{pro}. Boceprevir demonstrated its ability to inhibit SARS-CoV-2 viral replication in cellular assays [40].

GC376 (Figure 1.9) was identified as a SARS-CoV-2 M^{pro} inhibitor through a drug repurposing strategy. X-ray crystallographic analysis confirmed the formation of covalent bonds between GC376 and M^{pro}, existing in both *R*- and *S*-configurations. GC376 exhibited antiviral efficacy against SARS-CoV-2 [40], as well as against mouse hepatitis virus (MHV), murine norovirus, and MERS-CoV [41, 42]. Furthermore, a deuterated variant of GC376, along with GC376 analogues featuring various warheads

such as UAWJ246, UAWJ247, and UAWJ248 (Figure 1.9), were also validated as M^{pro} inhibitors $^{[43]}$ $^{[44]}$.

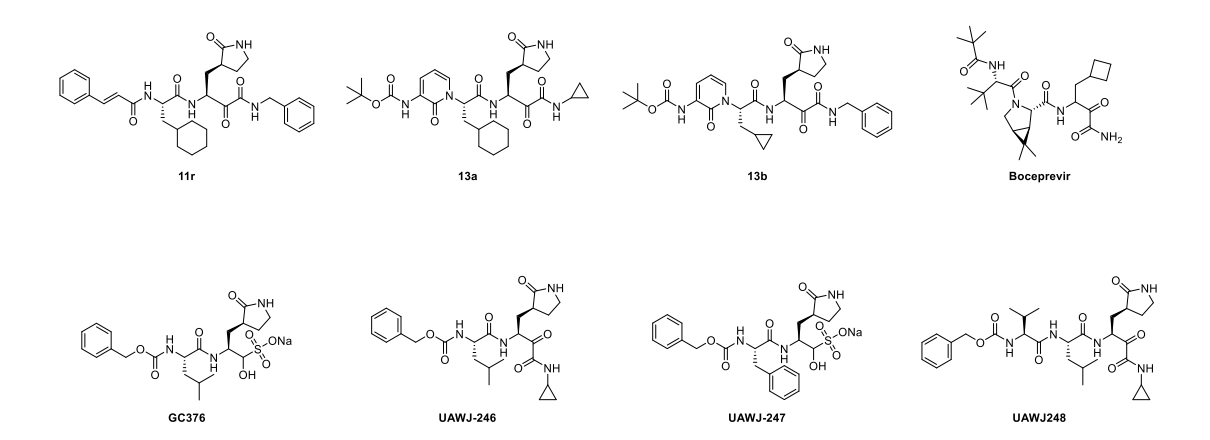


Figure 1.9 Chemical structures of 11a, 13a, 13b, boceprevir, GC376, UAWJ246, UAWJ247, and UAWJ248.

5) Aldehyde as warhead

11a and 11b (Figure 1.10) are two selective SARS-CoV-2 M^{pro} inhibitors with aldehyde warheads to form covalent bonds with Cys145 in the catalytic site. The cellular plaque assay revealed the excellent potency of 11a and 11b against SARS-CoV-2 [45, 46]. 18p (Figure 1.10) is a derivative of 11a and 11b and is also a covalent M^{pro} inhibitor with an aldehyde group. 18P exhibited antiviral activity against SARS-CoV-2 through inhibition against SARS-CoV-2 M^{pro} [47].

17w, 10a, and 10b (Figure 1.10) all have an aldehyde warhead. 10a showed weak SARS-CoV-2 M^{pro} inhibition. 17w and 10b were obtained from modification of hit compound 10a. 17w and 10b showed stronger inhibitory activities than 10a in the enzymatic and cellular assays [48].

MI-09 and MI-30 (Figure 1.10) were derived from boceprevir. X-ray crystallography confirmed the covalent bonds formed via aldehyde groups of MI-09 and MI-30 with Cys145 of SARS-CoV-2 M^{pro}. MI-09 and MI-30 showed excellent antiviral activity not only in the infected Vero E6 cells but also in mouse model where the lung viral loads were reduced when MI-09 and MI30 were administrated [49].

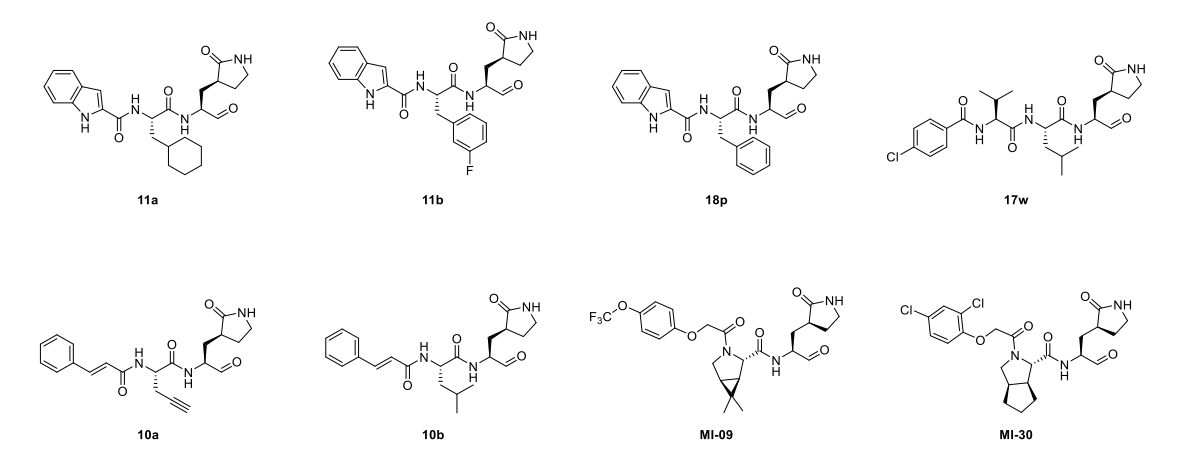


Figure 1.10 Chemical structures of 11a, 11b, 18p,17w, 10a, 10b, MI-09 and MI-30.

1.4.2 Nonpeptidic small molecule SARS-CoV-2 M^{pro} inhibitors

1) Covalent small molecule inhibitors

a) Specific covalent binding

MAC-5576 (Figure 1.11) represents the first generation of ester covalent inhibitors, identified through high-throughput screening (HTS) as an inhibitor against both SARS-CoV M^{pro} and SARS-CoV-2 M^{pro} [50-53]. Despite its promise *in vitro*, MAC-5576 did not demonstrate the anticipated potency in blocking viral replication in Vero E6 cells infected with SARS-CoV-2 [53]. However, indole-based derivatives of MAC-5576, including compounds 7d, 1, and 3W (Figure 1.11), have shown inhibitory effects against both SARS-CoV-2 M^{pro} and SARS-CoV-2 virus [54, 55]. Further details regarding the activity of MAC-5576 against SARS-CoV-2 M^{pro} will be elaborated in Chapter 2.

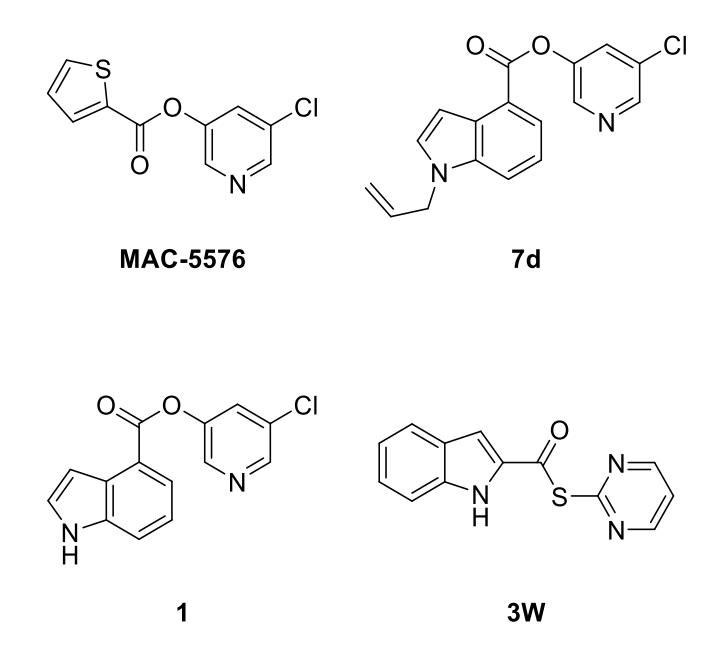


Figure 1.11 Chemical structures of MAC-5576, 7d, 1 and 3w.

b) Nonspecific covalent binding

Penicillin-based derivatives (compounds 28, 31, 32 and 20e in Figure 1.12), which are part of the β -lactam antibiotic class, have been identified as covalent inhibitors for cysteine and serine proteases. Crystallographic analysis has confirmed that the cysteine residue in M^{pro} can be acylated by a β -lactam compound [56].

Additionally, 2-(furan-2-ylmethylene)hydrazine-1-carbothioamide derivatives, such as F8 (Figure 1.12), have been found to possess weak inhibitory activity against M^{pro}. The covalent binding mode of F8 with M^{pro} was established through enzymatic assays and mass spectrometry [57].

In FRET-based screening, E24 (Figure 1.12) and ebselen were identified with nanomolar half-maximal inhibitory concentration (IC₅₀) values against SARS-CoV-2 M^{pro}. E24 demonstrated antiviral activity against SARS-CoV-2 in both Vero E6 cells and Calu-3 human lung epithelial cells [58].

Other covalent inhibitors have also been discovered through HTS, including disulfiram, carmofur, tideglusib, shikonin, and PX-12 [12] (Figure 1.12). Notably, ebselen, carmofur, and PX-12 are known to form nonspecific covalent bonds with the Cys145 residue of SARS-CoV-2 M^{pro} [12]. Carmofur, in particular, has been shown to release a hexylurea

moiety upon binding to Cys145 [59]. Furthermore, the benzoxaborole compound 18 has been identified as an active inhibitor of SARS-CoV-2 M^{pro}, exhibiting single-digit micromolar activity [60].

These findings highlight the diversity of covalent inhibitors that can target SARS-CoV-2 M^{pro}, offering a broad range of potential therapeutic agents for the treatment of COVID-19.

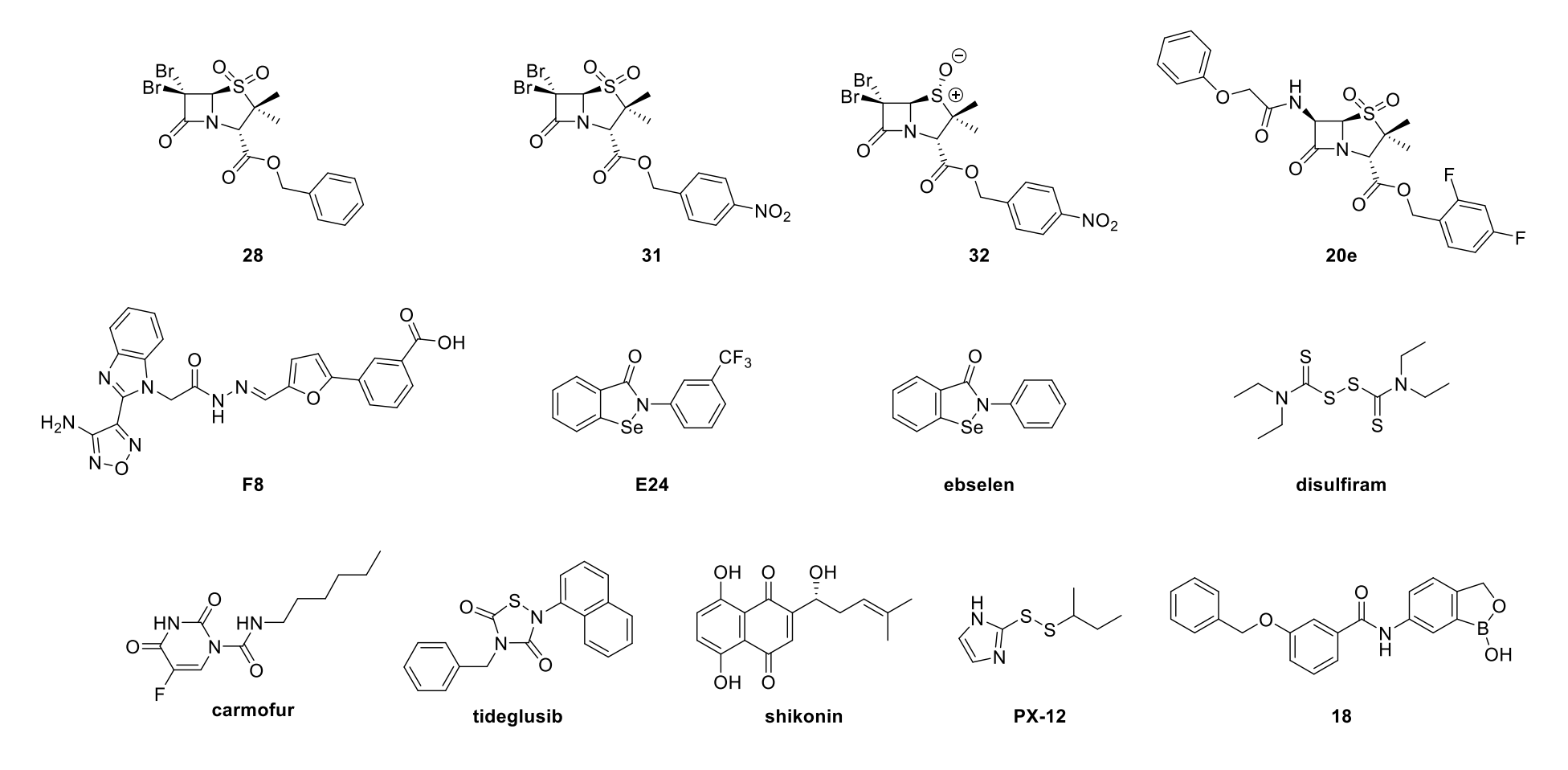


Figure 1.12 Chemical structures of 28, 31, 32, 20e, F8, E24, ebselen, disulfiram, carmofur, tideglusib, shikonin, PX-12, 18, 2j, 23 and 26.

2) Noncovalent small molecule inhibitors

a) Discovery based on de novo design

Ensitrelvir (S-217622 in Figure 1.13) marks a significant milestone as the first approved noncovalent inhibitor of SARS-CoV-2 M^{pro}, developed by Shionogi. This compound represents a *de novo* design strategy, a nonpeptidic inhibitor designed through an integrated approach of structure-based drug design. The discovery process involved virtual screening to identify potential candidates, which were then subjected to biological screening for validation. Ensitrelvir has demonstrated potent antiviral efficacy and exhibited favorable pharmacokinetic properties, making it suitable for once-daily oral administration [33]. Its approval underscores the success of modern drug design strategies in developing effective treatments against COVID-19.

Ensitrelvir (S-217622)

Figure 1.13 Chemical structure of Ensitrelvir (S-217622).

b) Discovery through drug repurposing

Masitinib (Figure 1.14), recognized as an oral *c*-kit inhibitor ^[61], has been successfully repurposed as an antiviral agent. Through the drug repurposing strategy, Masitinib has demonstrated its efficacy in significantly curtailing SARS-CoV-2 replication in mice. Notably, it achieved a remarkable reduction in viral titers by over 200-fold in the lungs and nose of the treated mice, along with a noticeable decrease in inflammation ^[62]. The antiviral activity of Masitinib is attributed to its noncovalent interaction with SARS-CoV-2 M^{pro [62]}. Further insights into the properties and effects of Masitinib will be provided in Chapter 2.

Figure 1.14 Chemical structure of Masitinib.

c) Discovery from natural products

Baicalein (Figure 1.15), a flavonoid derived from *Scutellaria baicalensis*, which is a plant with a long history of use in traditional Chinese medicine ^[63], has been studied through X-ray crystallography for its interaction with SARS-CoV-2 M^{pro}. The structural analysis revealed that baicalein binds noncovalently to M^{pro}, with its scaffold effectively occupying the critical S1/S2 subsites within the enzymatic catalytic pocket.

Additionally, baicalin (Figure 1.15), another natural product obtained from the same plant, has demonstrated inhibitory activity against SARS-CoV-2 M^{pro}. It has also shown antiviral potency in cellular assays ^[64], indicating the potential of these natural compounds as a source for the development of antiviral treatments against COVID-19.

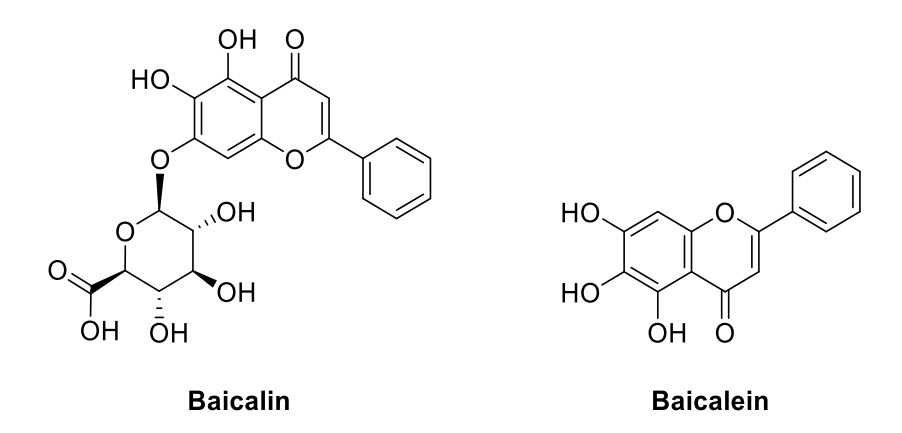


Figure 1.15 Chemical structures of baicalin and baicalein.

3) Transforming noncovalent small molecule inhibitors into covalent ones.

Certain noncovalent SARS-CoV-2 M^{pro} inhibitors can be modified to become covalent inhibitors by introducing a warhead at a strategic position within their chemical structure. Compounds X77, ML188, and 23R (Jun8-76-3A) (Figure 1.16) were all synthesized using the one-pot Ugi chemical reaction [35]. These compounds have been identified as potent noncovalent inhibitors of SARS-CoV-2 M^{pro} [35]. Notably, 23R demonstrated inhibitory activity against SARS-CoV-2 M^{pro} in both Vero E6 cells and Calu-3 cells [35]. These noncovalent inhibitors can be transformed into covalent ones by employing various warheads, such as vinyl sulfonamide, acrylamide, alkynylamide, α -chloramide, and α -ketoamide, which have shown promise in this context [65]. In Calu-3 cellular assays, Jun10541R exhibited antiviral potency against SARS-CoV-2, with cocrystal structures revealing that its nitrile warhead forms a covalent bond with Cys145

The conversion of GC-14 to GD-9 serves as another example of this transformation. GC-14 (Figure 1.16), featuring a 1,2,4-trisubstituted piperazine scaffold, was characterized as a noncovalent SARS-CoV-2 M^{pro} inhibitor ^[67]. By replacing the nicotinoyl group of GC-14 with a mono-halo acetamide, GD-9 (Figure 1.16) was developed and also showed inhibitory activity against SARS-CoV-2 M^{pro} ^[68].

This approach of converting noncovalent to covalent inhibitors expands the library of potential antiviral agents, offering more options for the development of effective treatments against COVID-19.

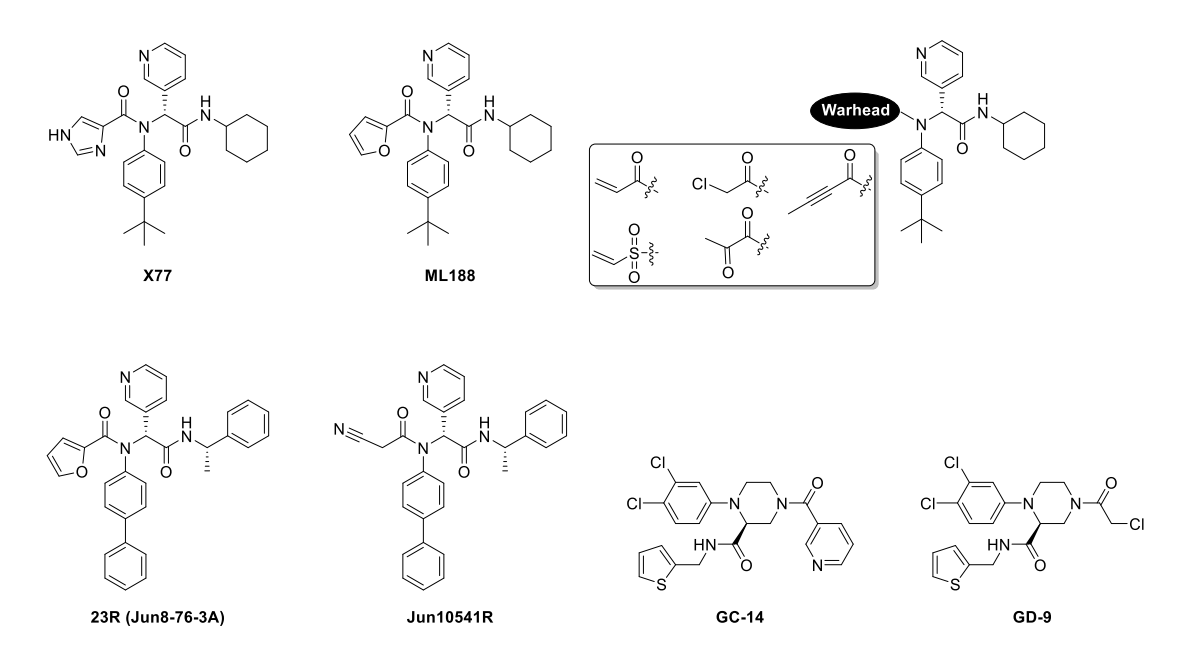


Figure 1.16 Chemical structures of X77, ML188, 23R(Jun8-76-3A), 23S, Jun10541R, GC-14 and GD-9.

4) Other repurposed small molecules against SARS-CoV-2 Mpro

Several compounds have been repurposed as noncovalent inhibitors of SARS-CoV-2 M^{pro}. Acriflavine (ACF) and proflavine hemisulfate (PRF) (Figure 1.17), both featuring acridine scaffolds, have shown dual inhibitory effects against SARS-CoV-2 M^{pro} and PL^{pro} [69]. Additionally, walrycin B and LLL-2 (Figure 1.17) were discovered through quantitative high-throughput screening (qHTS) [70]. The compound 2j (Figure 1.17), which contains a 3,7-diazabicyclo[3.3.1]nonan (bispidine) scaffold, has been reported to display submicromolar activity against SARS-CoV-2 M^{pro} in a FRET-based enzymatic assay [71]. Enzymatic assays have identified *N*-substituted isatin compounds, such as 23 and 26 (Figure 1.17), with inhibitory activity against SARS-CoV-2 M^{pro} [72].

These findings highlight the potential of repurposed compounds in inhibiting key viral enzymes, providing valuable insights for the development of novel antiviral therapies against COVID-19.

Figure 1.17 Chemical structures of acriflavine (ACF), proflavine hemisulfate (PRF), walrycin B, LLL-12, 2j, 23 and 26.

1.4.3 Structural features of SARS-CoV-2 M^{pro} inhibitors

Upon analyzing the structures of the identified SARS-CoV-2 M^{pro} inhibitors, the following conclusions can be drawn. Peptidomimetic inhibitors of SARS-CoV-2 M^{pro} have been developed using a structure-based strategy, designed to covalently bind to Cys145 of the catalytic site, thereby directly targeting the enzymatic active mechanism. Small molecule inhibitors of SARS-CoV-2 Mpro have been unearthed through highthroughput screening (HTS) and drug repurposing efforts. Their mechanisms of action can be divided into covalent binding, where they form a direct chemical bond with the enzyme, and noncovalent binding. For covalent SARS-CoV-2 M^{pro} inhibitors, active electrophilic groups are utilized as warheads to covalently bind to Cys145 [34, 73]. Noncovalent inhibitors can be modified to covalent inhibitors by introducing appropriate functional groups that enable such binding. The S1 subsite is a critical target for inhibitors aiming for selective binding to the catalytic site. The S2 subsite, on the other hand, tends to favor hydrophobic or small cyclopropyl groups. The nature of the moieties that bind to the S1 and S2 subsites is crucial for determining the selectivity of the inhibitors [74]. These insights into the structural requirements and binding preferences of SARS-CoV-2 Mpro inhibitors are vital for guiding the design and optimization of more potent and selective antiviral agents.

1.5. Aims and Objectives of this project

1) Design of SARS-CoV-2 M^{pro} inhibitors based on two lead compounds

Although approved SARS-CoV-2 Mpro inhibitors, such as Nirmatrelvir [75] and Ensitrelvir [33], have demonstrated high potency against the SARS-CoV-2 virus, the liver enzyme elevation associated with Ensitrelvir [33] and the requirement for Nirmatrelvir [75] to be used in combination with the CYP3A inhibitor Ritonavir limit their use in some patients. Therefore, the development of novel SARS-CoV-2 Mpro inhibitors to overcome these drawbacks is important and significant. In this project, we have developed a series of small molecule covalent inhibitors that take the scaffold of Masitinib while incorporating the reactive warhead of MAC-5576. As an approved drug, Masitinib has been proven to possess intrinsic activity and favorable pharmacokinetic properties. These characteristics are essential criteria for selecting lead compounds. The co-crystal structure [62] revealed that the N-phenyl-2-aminothiazole moiety of Masitinib can accommodate into the S2 subsite of the catalytic site of SARS-CoV-2 M^{pro}. In addition, MAC-5576 also exhibits inhibitory activity against SARS-CoV-2 M^{pro} and binds to the same subsite with Masitinib [53, 76]. Therefore, this project selected Masitinib and MAC-5576 as lead compounds. The design strategy in this project leverages the scaffold fusion approach in drug design, which facilitates the integration of pharmacophores from different sources to create a novel scaffold with potential therapeutic efficacy. Furthermore, the concept of bioisosterism was employed

to elucidate the structure-activity relationship (SAR) of the synthesized compounds. The methodology for the design and synthesis of these covalent inhibitors is reported in Chapter 2.

2) Identification of compounds against the main proteases of both SARS-CoV-2 and SARS-CoV

Given the high conservation in structure and function between SARS-CoV M^{pro} and SARS-CoV-2 M^{pro}, the development of effective inhibitors against SARS-CoV-2 M^{pro} can also be applicable to SARS-CoV M^{pro}. Thus, our research also aims to develop dual inhibitors targeting both proteases.

Chapter 2. Design and Synthesis of New Main Protease Inhibitors

2.1 Methods

2.1.1 Materials and instruments

All reagents and solvents were purchased from commercial sources without further purification. Chromatography was performed using 300 mesh silica gel. All reactions were monitored by thin-layer chromatography using silica gel plates with fluorescence F254 and UV light visualization.

2.1.2 Chemistry

1) ¹H and ¹³C Nuclear magnetic resonance (NMR) spectrometry

The purified samples were dried under vacuum and then dissolved in $600~\mu L$ of DMSO- d_6 in NMR sample tubes. The 1H and ^{13}C NMR spectra were characterized using a Bruker Advance-III 400 MHz FTNMR spectrometer or a Jeol ECZ500R 500 MHz NMR spectrometer.

2) Mass spectrometry (MS)

All final products were characterized using high-resolution mass spectrometry (HRMS). HPLC grade methanol was used to dissolve the final products. Then, a solution of the final products in methanol, at a concentration of approximately 1 μ M, was injected into an Agilent 6540 Liquid Chromatography-Electrospray Ionization Quadrupole-Time of Flight (HRMS) mass spectrometer at a flow rate of 200 μ L/min.

3) General procedures for synthesis of MC02-MC10, MC12-MC17, MC12S02-S04, MC1210, MC1210S01, MC12E01, MC12F, MC04F

5-Chloropyridin-3-yl 2-(phenylamino)thiazole-4-carboxylate (MC04)

Benzoyl chloride (3.00 g, 21.34 mmol) was slowly added to a freshly prepared solution of NH₄SCN (1.27 g, 16.68 mmol) in 20 mL of acetone. The *in situ* generated benzoyl isothiocyanate was then heated to reflux for 15 minutes. This benzoyl isothiocyanate then reacted with aniline (2.08 g, 21.49 mmol) in 20 mL of acetone. After being heated to reflux for an additional 30 minutes, the mixture was poured onto ice with vigorous stirring. The resulting solid, *N*-(phenylcarbamothioyl)benzamide 1-phenylthiourea, was collected and washed with H₂O, followed by cold acetone, with a yield of 4.58 g, (80%). [77].

A solution of N-(phenylcarbamothioyl)benzamide (2.00 g, 7.81 mmol) in a mixture of methanol and 2 M aqueous NaOH (v/v = 1:3, 10 mL) was heated to 100 °C for 1 hour. Then, the reaction mixture was poured onto ice water (50 mL) and extracted with Ethyl acetate (3 × 75 mL). The organic phase was combined and then evaporated under vacuum to yield the solid. 1-phenylthiourea was collected and washed with H₂O, with a yield of 2.0 g (81%). [77].

Methyl bromopyruvate (2.27 g, 12.61 mmol) was slowly added to a solution of 1-phenylthiourea (2.00 g, 13.16 mmol) in methanol (45 mL). The reaction solution was heated to 90 °C for 4 hours. After the reaction was complete, the mixture was poured onto ice with vigorous stirring. The resulting solid was collected and washed with H₂O to yield a pale-yellow solid, methyl 2-(phenylamino)thiazole-4-carboxylate, with a yield of 1.59 g (70%). [78].

Methyl 2-(phenylamino)thiazole-4-carboxylate (0.45 g, 9.70 mmol) was added to a mixture of methanol and 1 M aqueous NaOH (v/v = 1:3, 10 mL) at 0 °C and then warmed to reflux. After 2 hours of stirring, the reaction solution was cooled to room temperature, and a solid formed. The resulting solid was collected by filtration. The collected solid was dissolved in water, and the pH was adjusted to approximately 3 with 1 N HCl. The crude product was collected and washed with water to yield the pale-yellow solid, 2-(phenylamino)thiazole-4-carboxylic acid, with a yield of 1.65 g, 7.76 mmol (80%).

3-Chloro-5-hydroxypyridine (11.7 mg, 0.091 mmol), *N*,*N*-Diisopropylethylamine (DIPEA, 11.7 mg, 0.091 mmol), 1-Hydroxybenzotriazole (HOBt, 11.7 mg, 0.087 mmol), and *N*,*N*'-Diisopropylcarbodiimide (DIC, 12.2 mg, 0.096 mmol) were added to a solution of 2-(phenylamino)thiazole-4-carboxylic acid (20 mg, 0.091 mmol) in *N*,*N*-Dimethylformamide (DMF) (10 mL) at 0 °C. The resulting solution was stirred

overnight at room temperature. Then, the reaction mixture was quenched with water. The resulting solid was collected by filtration to yield a yellow crude solid product. Purification of the crude product by chromatography (Dichloromethane: Ethyl acetate = 20:1) afforded 5-chloropyridin-3-yl 2-(phenylamino)thiazole-4-carboxylate as a white solid, with a yield of 21 mg, 0.063 mmol (53%). 1 H NMR (400 MHz, DMSO- d_6) δ 12.05 (s, 1H), 8.63 (d, 1H), 8.60 (d, J = 2.3 Hz, 1H), 8.34 (d, J = 5.5 Hz, 1H), 8.30 (s, 1H), 8.14 (t, J = 2.2 Hz, 1H), 7.11 (dd, J = 5.5, 1.8 Hz, 1H), 7.07 (d, J = 1.8 Hz, 1H). MS (ESI) m/z 332.0260[M + H] $^{+}$; 354.0080 [M + Na] $^{+}$.

The other designed inhibitors were prepared using similar procedures but different starting compounds.

5-Chloropyridin-3-yl 2-((4-chloropyridin-2-yl)amino)thiazole-4-carboxylate (MC02) 2-Amino-4-chloropyridine was chosen as the starting compound. MC02 was prepared by following a similar procedure to that used for MC04. White solid (31 mg, 0.070 mmol, 65%, $R_f = 0.33$, Dichloromethane: Ethyl acetate = 20:1). ¹H NMR (400 MHz, DMSO- d_6) δ 12.05 (s, 1H), 8.63 (d, J = 2.1 Hz, 1H), 8.60 (d, J = 2.3 Hz, 1H), 8.34 (d, J = 5.5 Hz, 1H), 8.30 (s, 1H), 8.14 (t, J = 2.2 Hz, 1H), 7.11 (dd, J = 5.5, 1.8 Hz, 1H), 7.07 (d, J = 1.8 Hz, 1H). HRMS (ESI) m/z 366.9824 [M + H]⁺; 388.9644 [M + Na]⁺.

5-Chloropyridin-3-yl 2-((2,4-difluorophenyl)amino)thiazole-4-carboxylate (MC05)

2,4-Difluoroaniline was chosen as the starting compound. MC05 was prepared by following a similar procedure to that used for MC04. White solid (22 mg, 0.034 mmol, 70%, $R_f = 0.33$, Dichloromethane: Ethyl acetate = 20:1). ¹H NMR (400 MHz, DMSO- d_6) δ 10.97 (s, 1H), 8.63 (d, J = 2.1 Hz, 1H), 8.61 (d, J = 2.3 Hz, 1H), 8.29 (s, 1H), 8.16 (t, 1H), 7.43 (d, J = 2.3 Hz, 1H), 7.41 (d, J = 2.3 Hz, 1H), 6.83 (t, 1H). HRMS (ESI) m/z 368.0076 [M + H]⁺, 389.9901 [M + Na]⁺

5-Chloropyridin-3-yl 2-((3,5-dimethylphenyl)amino)thiazole-4-carboxylate (MC06) 3,5-Dimethylaniline was chosen as the starting compound. MC06 was prepared by following a similar procedure to that used for MC04. White solid (35 mg, 0.078mol, 74%, $R_f = 0.33$, Dichloromethane: Ethyl acetate = 20:1). ¹H NMR (400 MHz, DMSO-d₆) δ 10.39 (s, 1H), 8.63 (d, J = 2.1 Hz, 1H), 8.60 (d, J = 2.3 Hz, 1H), 8.15 (d, J = 1.6 Hz, 1H), 8.14 (s, 1H),7.25 (s, 2H), 6.66 (s, 1H), 2.25 (s, 6H). HRMS (ESI) m/z 360.0575 [M + H]⁺; 382.0394 [M + Na]⁺.

5-Chloropyridin-3-yl 2-((3,5-dimethoxyphenyl)amino)thiazole-4-carboxylate (MC07) 3,5-Dimethoxyaniline was chosen as the starting compound. MC07 was prepared by following a similar procedure to that used for MC04. White solid (36 mg, 0.080 mmol, 69%, R_f = 0.33, Dichloromethane: Ethyl acetate = 20:1). ¹H NMR (400 MHz, DMSO- d_6) δ 10.51 (s, 1H), 8.62 (d, J = 2.0 Hz, 1H), 8.59 (d, J = 2.3 Hz, 1H), 8.18 (s, 1H), 8.14

(t, J = 2.2 Hz, 1H), 6.91 (d, J = 2.2 Hz, 2H), 6.18 (t, J = 2.2 Hz, 1H), 3.73 (s, 6H). HRMS (ESI) m/z 392.0472[M + H]⁺; 414.0291 [M + Na]⁺.

5-Chloropyridin-3-yl 2-((4-methylpyridin-2-yl)amino)thiazole-4-carboxylate (MC08) 2-Amino-4-methylpyridinw was chosen as the starting compound. MC08 was prepared by following a similar procedure to that used for MC04. White solid (22 mg, 0.050 mmol 69%, $R_f = 0.33$, Dichloromethane: Ethyl acetate = 20:1). ¹H NMR (400 MHz, DMSO- d_6) δ 11.77 (s, 1H), 8.62 (d, J = 2.1 Hz, 1H), 8.59 (d, J = 2.3 Hz, 1H), 8.22 (s, 1H), 8.20 (d, 1H), 8.13 (t, 1H), 6.85 (s, 1H), 6.83 (s, 1H),2.31 (s, 3H). HRMS (ESI) m/z 347.0419[M + H]⁺; 369.0243 [M + Na]⁺.

5-Chloropyridin-3-yl 2-((4-methylpyridin-3-yl)amino)thiazole-4-carboxylate (MC09) 3-Amino-4-methylpyridinw was chosen as the starting compound. MC09 was prepared by following a similar procedure to that used for MC04. White solid (36 mg, 0.081 mmol, 80%, $R_f = 0.33$, Dichloromethane: Ethyl acetate = 20:1). ¹H NMR (400 MHz, DMSO- d_6) δ 9.81 (s, 1H), 9.12 (s, 1H), 8.62 (d, J = 2.1 Hz, 1H), 8.58 (d, J = 2.3 Hz, 1H), 8.22 (d, J = 4.8 Hz, 1H), 8.15 (s, 1H), 8.12 (t, 1H), 7.29 (d, J = 4.8 Hz, 1H), 2.31 (s, 3H). HRMS (ESI) m/z 347.0374 [M + H]⁺; 369.0190 [M + Na]⁺.

5-Chloropyridin-3-yl 2-((3-methoxyphenyl)amino)thiazole-4-carboxylate (MC10)

3-Methoxyaniline was chosen as the starting compound. MC10 was prepared by following a similar procedure to that used for MC04. White solid (28 mg, 0.063 mmol, 60%, R_f = 0.33, Dichloromethane: Ethyl acetate = 20:1). ¹H NMR (400 MHz, DMSO- d_6) δ 10.54 (s, 1H), 8.63 (s, 1H), 8.61 (s, 1H), 8.18 (s, 1H), 8.14 (s, 1H), 7.45 (s, 1H), 7.25 (t, 1H), 7.13 (d, J = 8.0 Hz, 1H), 6.59 (d, J = 8.0 Hz, 1H), 3.75 (s, 3H). HRMS (ESI) m/z 362.0368 [M + H]⁺; 384.0189 [M + Na]⁺.

5-Chloropyridin-3-yl 2-(methyl(phenyl)amino)thiazole-4-carboxylate (MC12) N-Methylaniline was chosen as the starting compound. MC12 was prepared by following a similar procedure to that used for MC04. White solid (29 mg, 0.066 mmol, 65%, $R_f = 0.33$, Dichloromethane: Ethyl acetate = 20:1). ¹H NMR (400 MHz, DMSO-d₆) δ 8.62 (s, 1H), 8.57 (s, 1H), 8.12 (s, 1H), 8.01 (s, 1H), 7.52 (s, 2H), 7.51 (s, 2H), 7.36 (s, 1H), 3.51 (s, 3H). HRMS (ESI) m/z 346.0419 [M + H]⁺; 368.0240 [M + Na]⁺.

5-Chloropyridin-3-yl 2-((3-(trifluoromethyl)phenyl)amino)thiazole-4-carboxylate (MC13)

3-(Trifluoromethyl)aniline was chosen as the starting compound. MC13 was prepared by following a similar procedure to that used for MC04. White solid (31 mg, 0.069 mmol, 59%, $R_f = 0.33$, Dichloromethane: Ethyl acetate = 20:1). ¹H NMR (400 MHz, DMSO- d_6) δ 10.89 (s, 1H), 8.62 (d, J = 9.1 Hz, 2H), 8.27 (d, J = 5.4 Hz, 2H), 8.16 (s,

1H), 7.84 (d, J = 8.3 Hz, 1H), 7.58 (t, J = 8.1 Hz, 1H), 7.33 (d, J = 7.7 Hz, 1H). HRMS (ESI) m/z 400.0138 [M + H]⁺; 421.9957 [M + Na]⁺.

5-Chloropyridin-3-yl 2-((3-chlorophenyl)amino)thiazole-4-carboxylate (MC14) 3-Chloroaniline was chosen as the starting compound. MC14 was prepared by following a similar procedure to that used for MC04. White solid (33 mg, 0.075 mmol 70%, $R_f = 0.33$, Dichloromethane: Ethyl acetate = 20:1). ¹H NMR (400 MHz, DMSO- d_6) δ 10.74 (s, 1H), 8.62 (d, J = 7.6 Hz, 2H), 8.24 (s, 1H), 8.16 (s, 1H), 7.96 (s, 1H), 7.50 (d, J = 7.9 Hz, 1H), 7.37 (t, J = 8.3 Hz, 1H), 7.04 (d, J = 7.9 Hz, 1H). HRMS (ESI) m/z 365.9869 [M + H]⁺; 387.9691 [M + Na]⁺.

5-Chloropyridin-3-yl 2-(pyridin-2-ylamino)thiazole-4-carboxylate (MC15)

2-Aminopyridine was chosen as the starting compound. MC15 was prepared by following a similar procedure to that used for MC04. White solid (31 mg, 0.069 mmol, 71%, $R_f = 0.33$, Dichloromethane: Ethyl acetate = 20:1). ¹H NMR (400 MHz, DMSO- d_6) δ 11.86 (s, 1H), 8.61 (d, J = 12.2 Hz, 2H), 8.35 (s, 1H), 8.25 (s, 1H), 8.14 (s, 1H), 7.77 (d, J = 6.6 Hz, 1H), 7.03 (d, J = 8.7 Hz, 1H), 6.99 (s, 1H). HRMS (ESI) m/z 333.0214 [M + H]⁺; 355.0028 [M + Na]⁺.

5-Chloropyridin-3-yl 2-((2-methyl-5-nitrophenyl)amino)thiazole-4-carboxylate (MC16)

2-Methyl-5-nitroaniline was chosen as the starting compound. MC16 was prepared by following a similar procedure to that used for MC04. White solid (40 mg, 0.090 mmol, 79%, $R_f = 0.33$, Dichloromethane: Ethyl acetate = 20:1). ¹H NMR (400 MHz, DMSO- d_6) δ 9.96 (s, 1H), 9.35 (s, 1H), 8.62 (d, J = 8.1 Hz, 2H), 8.28 (s, 1H), 8.16 (s, 1H), 7.84 (d, J = 8.2 Hz, 1H), 7.51 (d, J = 8.3 Hz, 1H), 2.44 (s, 3H). HRMS (ESI) m/z 391.0267 [M + H]⁺; 413.0082 [M + Na]⁺.

5-Chloropyridin-3-yl 2-((2-fluorophenyl)amino)thiazole-4-carboxylate (MC17) 2-Fluoroaniline was chosen as the starting compound. MC17 was prepared by following a similar procedure to that used for MC04. White solid (30 mg, 0.067 mmol, 66%, $R_f = 0.33$, Dichloromethane: Ethyl acetate = 20:1). ¹H NMR (400 MHz, DMSO- d_6) δ 10.34 (s, 1H), 8.61 (d, J = 9.8 Hz, 2H), 8.47 (t, J = 8.5 Hz, 1H), 8.21 (s, 1H), 8.14 (s, 1H), 7.28 (t, J = 9.9 Hz, 1H), 7.21 (d, J = 8.1 Hz, 1H), 7.06 (s, 1H). HRMS (ESI) m/z 350.0168 [M + H]⁺; 371.9983 [M + Na]⁺.

5-Chloropyridin-3-yl 2-(isopropyl(phenyl)amino)thiazole-4-carboxylate (MC12S02) N-Isopropylaniline was chosen as the starting compound. MC12S02 was prepared by following a similar procedure to that used for MC04. White solid (29 mg, 0.065 mmol, 60%, R_f = 0.33, Dichloromethane: Ethyl acetate = 20:1). ¹H NMR (400 MHz, DMSO- d_6) δ 8.62 (s, 1H), 8.57 (s, 1H), 8.11 (s, 1H), 7.88 (s, 1H), 7.59 (s, 2H), 7.53 (s, 1H),

7.38 (s, 2H), 4.90 (s, 1H), 1.16 (s, 6H). HRMS (ESI) *m*/z 350.26 [M + H]⁺; 348.09 [M - H]⁻.

5-Chloropyridin-3-yl 2-(phenyl(propyl)amino)thiazole-4-carboxylate (MC12S03) N-Propylaniline was chosen as the starting compound. MC12S03 was prepared by following a similar procedure to that used for MC04. White solid (24 mg, 0.053 mmol, 49%, $R_f = 0.33$, Dichloromethane: Ethyl acetate = 20:1). ¹H NMR (400 MHz, DMSO- d_6) δ 8.62 (s, 1H), 8.57 (s, 1H), 8.12 (s, 1H), 7.94 (s, 1H), 7.55 (s, 2H), 7.49 (s, 2H), 7.41 (s, 1H), 3.94 (s, 2H), 1.61 (s, 2H), 0.89 (s, 3H). HRMS (ESI) m/z 374.0729 [M + H]⁺; 396.0547 [M + Na]⁺.

5-Chloropyridin-3-yl 2-(butyl(phenyl)amino)thiazole-4-carboxylate (MC12S04) N-Butylaniline was chosen as the starting compound. MC12S04 was prepared by following a similar procedure to that used for MC04. White solid (25 mg, 0.057 mmol, 50%, R_f = 0.33, Dichloromethane: Ethyl acetate = 20:1). 1 H NMR (400 MHz, DMSO- d_6) δ 8.62 (d, J = 2.1 Hz, 1H), 8.57 (d, J = 2.3 Hz, 1H), 8.11 (t, J = 2.2 Hz, 1H), 7.94 (s, 1H), 7.55 (t, J = 7.7 Hz, 2H), 7.48 (d, J = 7.2 Hz, 2H), 7.41 (t, J = 7.2 Hz, 1H), 3.97 (t, J = 7.3 Hz, 2H), 1.57 (p, J = 8.1, 7.6 Hz, 2H), 1.32 (dt, J = 14.6, 7.4 Hz, 2H), 0.87 (t, J = 7.3 Hz, 3H). HRMS (ESI) m/z 388.0690 [M + H] $^+$; 410.0496 [M + Na] $^+$.

5-Chloropyridin-3-yl 2-((3-methoxyphenyl)(methyl)amino)thiazole-4-carboxylate (MC1210)

3-Methoxy-*N*-methylaniline was chosen as the starting compound. MC1210 was prepared by following a similar procedure to that used for MC04. White solid (29 mg, 0.065 mmol, 59%, R_f = 0.33, Dichloromethane: Ethyl acetate = 20:1). ¹H NMR (400 MHz, DMSO- d_6) δ 8.62 (s, 1H), 8.57 (s, 1H), 8.11 (s, 1H), 8.01 (s, 1H), 7.42 (s, 1H), 7.09 (s, 2H), 6.94 (s, 1H), 3.80 (s, 3H), 3.51 (s, 3H). HRMS (ESI) m/z 376.0520 [M + H]⁺; 398.0341 [M + Na]⁺.

5-Chloropyridin-3-yl 2-(benzyl(methyl)amino)thiazole-4-carboxylate (MC12E01) N-Methylbenzylamine was chosen as the starting compound. MC12E01 was prepared by following a similar procedure to that used for MC04. White solid (31 mg, 0.069 mmol, 66%, $R_f = 0.33$, Dichloromethane: Ethyl acetate = 20:1). ¹H NMR (600 MHz, DMSO- d_6) δ 8.61 (s, 1H), 8.56 (s, 1H), 8.11 (s, 1H), 8.03 (s, 1H), 7.38 (t, J = 7.6 Hz, 2H), 7.32 (s, 1H), 7.30 (d, J = 7.5 Hz, 2H), 4.76 (s, 2H), 3.10 (s, 3H). HRMS (ESI) m/z 360.0573 [M + H]⁺; 382.0386 [M + Na]⁺.

5-Chloro-6-fluoropyridin-3-yl 2-(methyl(phenyl)amino)thiazole-4-carboxylate (MC12F)

N-Methylaniline was chosen as the starting compound. 3-chloro-2-fluoro-5-hydroxypyridine was chosen to replace 3-chloro-5-hydroxypyridine. MC12F was

prepared by following a similar procedure to that used for MC04. White solid (32 mg, 0.072 mmol, 68%, R_f = 0.33, Dichloromethane: Ethyl acetate = 20:1). ¹H NMR (600 MHz, DMSO- d_6) δ 8.42 (d, 1H), 8.26 (s, 1H), 8.01 (s, 1H), 7.52 (s, 2H), 7.52 (s, 2H), 7.39 - 7.34 (m, 1H), 3.51 (s, 3H). HRMS (ESI) m/z 364.0316 [M + H]⁺; 386.0137 [M + Na]⁺.

5-Chloro-6-fluoropyridin-3-yl 2-(phenylamino)thiazole-4-carboxylate (MC04F) 3-Chloro-2-fluoro-5-hydroxypyridine was chosen to replace 3-chloro-5-hydroxypyridine. MC04F was prepared by following a similar procedure to that used for MC04. White solid (25 mg, 0.056 mmol,55%, $R_f = 0.33$, Dichloromethane: Ethyl acetate = 20:1). 1 H NMR (600 MHz, DMSO- d_6) δ 10.54 (s, 1H), 8.44 (d, J = 7.8 Hz, 1H), 8.29 (s, 1H), 8.17 (s, 1H), 7.67 (d, J = 8.0 Hz, 2H), 7.35 (t, J = 7.8 Hz, 2H), 7.00 (t, J = 7.4 Hz, 1H). HRMS (ESI) m/z 350.0165 [M + H]⁺; 371.9982 [M + Na]⁺.

5-Chloropyridin-3-yl 2-(dibenzylamino)thiazole-4-carboxylate (MC04BP)

Dibenzylamine was chosen as the starting compound. MC04 was prepared by following a similar procedure to that used for MC04. White solid (38 mg, 0.087 mmol, 68%, R_f = 0.33, Dichloromethane: Ethyl acetate = 20:1). ¹H NMR (600 MHz, DMSO- d_6) δ 8.61 (s, 1H), 8.56 (s, 1H), 8.10 (s, 1H), 8.01 (s, 1H), 7.37 (d, J = 7.5 Hz, 2H), 7.35 (s, 4H), 7.31 (d, J = 7.8 Hz, 4H), 4.78 (s, 4H). HRMS (ESI) m/z 436.0885 [M + H]⁺; 458.0705 [M + Na]⁺.

The NMR and mass spectra of the synthesized compounds are given in the A3 of Appendices.

4) General procedures for synthesis of MC11 and MC1112

5-chloropyridin-3-yl 2-(phenylamino)oxazole-4-carboxylate (MC11)

Methyl bromopyruvate (2.26 g, 12.56 mmol) was added to a solution of 1-phenylurea (2.00 g, 14.71 mmol) in methanol (45 mL) and stirred for 10 minutes. Then, the mixture was slowly added. The reaction mixture was heated to 90 °C for 4 hours. The completion of the reaction was monitored by TLC, and upon completion, the mixture was poured onto ice with vigorous stirring. The resulting solid was collected and washed with H₂O to yield a pale-yellow solid, methyl 2-(phenylamino)oxazole-4-carboxylate, with a yield of 2.24 g (70%).

Methyl 2-(phenylamino)oxazole-4-carboxylate (2.00 g, 9.17 mmol) was added to a mixture of methanol and 1 M aqueous NaOH (v/v = 1:3, 10 mL) at 0 °C and then warmed to reflux. After 2 hours of stirring, the reaction solution was cooled to room temperature. The resulting solid was collected by filtration. The collected solid was dissolved in water, and the pH was adjusted to approximately 3 with 1 N HCl. The crude product was collected and washed with water to afford the pale-yellow solid, 2-(phenylamino)oxazole-4-carboxylic acid, with a yield of 1.49 g (80%).

To a solution of 2-(phenylamino)oxazole-4-carboxylic acid (20 mg, 0.098 mmol) in N,N-Dimethylformamide (DMF) (10 mL) at 0 °C, 3-Chloro-5-hydroxypyridine (12.6 mg, 0.098 mmol), N,N-Diisopropylethylamine (DIPEA, 12.4 mg, 0.096 mmol), 1-Hydroxybenzotriazole (HOBt, 13.2 mg, 0.098 mmol), and N,N-Diisopropyl-carbodiimide (DIC, 12.4 mg, 0.096 mmol) were added. The mixture was stirred overnight at room temperature. Then, the reaction mixture was quenched with water. The resulting solid was collected by filtration to yield a yellow crude solid product. Purification of the crude product by chromatography (Dichloromethane: Ethyl acetate = 20:1) afforded 5-chloropyridin-3-yl 2-(phenylamino)oxazole-4-carboxylate as a white solid, with a yield of 27 mg, (0.061 mmol, 66%). 1 H NMR (400 MHz, DMSO- d_{0}) δ 10.53 (s, 1H), 8.74 (s, 1H), 8.63 (s, 1H), 8.59 (s, 1H), 8.13 (s, 1H), 7.65 (d, J = 7.9 Hz, 2H), 7.36 (t, J = 7.8 Hz, 2H), 7.01 (t, 1H). HRMS (ESI) m/z 316.0488 [M + H] $^{+}$; 338.0310 [M + Na] $^{+}$.

5-chloropyridin-3-yl 2-(methyl(phenyl)amino)oxazole-4-carboxylate (MC1112) methyl-1-phenylurea was chosen as the starting compound. MC1112 was prepared by following a similar procedure to that used for MC11. White solid (30 mg, 0.067 mmol, 70%, R_f = 0.33, Dichloromethane: Ethyl acetate = 20:1). ¹H NMR (400 MHz, DMSO- d_6) δ 8.67 (s, 1H), 8.62 (d, J = 2.1 Hz, 1H), 8.56 (d, J = 2.3 Hz, 1H), 8.11 (t, J = 2.2 Hz,

1H), 7.45 (d, J = 6.6 Hz, 4H), 7.25 (tt, J = 6.6, 1.9 Hz, 1H), 3.49 (s, 3H). HRMS (ESI) m/z 330.0642 [M + H]⁺; 352.0461 [M + Na]⁺.

The NMR and mass spectra of the synthesized compounds are given in the A3 of Appendices.

5) General procedures for synthesis of MC04AM

5-Chloropyridin-3-yl 2-benzamidothiazole-4-carboxylate (MC04AM)

To a solution of phenyl carboxylic acid (2.00 g, 16.39 mmol) in *N*,*N*-Dimethylformamide (DMF) (10 mL) at 0 °C, methyl 2-aminothiazole-4-carboxylate (2.59 g, 16.39 mmol), *N*,*N*-Diisopropylethylamine (DIPEA, 2.08 g, 16.39 mmol), and 2-(7-Azabenzotriazol-1-yl)-*N*,*N*,*N'*,*N'*-tetramethyluronium hexafluorophosphate (HATU, 6.23 g, 16.39 mmol) were added. The resulting solution was stirred overnight at room temperature. Then, the reaction mixture was quenched with water. The resulting solid was collected by filtration to yield a yellow crude solid, methyl 2-benzamidothiazole-4-carboxylate, with a yield of 3.00 g (70%).

Methyl 2-benzamidothiazole-4-carboxylate (2.50 g, 9.54 mmol) was added to a mixture of methanol and 1 M aqueous NaOH (v/v = 1:3, 10 mL) at 0 °C and then warmed to reflux. After 2 hours of stirring, the reaction solution was cooled to room temperature. The resulting solid was collected by filtration. The collected solid was dissolved in

water, and the pH was adjusted to approximately 3 with 1 N HCl. The crude product was collected and washed with water to afford the pale-yellow solid, 2-benzamidothiazole-4-carboxylic acid, with a yield of 1.89 g (80%).

To a solution of 2-benzamidothiazole-4-carboxylic acid (20 mg, 0.076 mmol) in *N,N*-Dimethylformamide (DMF) (10 mL) at 0 °C, 3-Chloro-5-hydroxypyridine (9.83 mg, 0.076 mmol), *N,N*-Diisopropylethylamine (DIPEA, 9.67 mg, 0.076 mmol), 1-Hydroxybenzotriazole (HOBt, 10.29 mg, 0.076 mmol), and *N,N'*-Diisopropylcarbodiimide (DIC, 9.68 mg, 0.076 mmol) were added. The resulting solution was stirred overnight at room temperature. Then, the reaction mixture was quenched with water. The resulting solid was collected by filtration to yield a yellow crude solid product. Purification of the crude product by chromatography (Dichloromethane: Ethyl acetate = 20:1) afforded 5-chloropyridin-3-yl 2-benzamidothiazole-4-carboxylate as a white solid, with a yield of 30 mg (0.067 mmol, 64%). ¹H NMR (600 MHz, DMSO- d_6) δ 13.16 (d, J = 78.4 Hz, 1H), 8.64 (d, J = 14.0 Hz, 1H), 8.17 (d, J = 6.1 Hz, 2H), 8.15 (d, J = 8.8 Hz, 1H), 7.68 (q, J = 7.7 Hz, 1H), 7.58 (q, J = 7.8 Hz, 2H), 3.85 (s, 1H). HRMS (ESI) m/z 381.2973 [M + Na]⁺.

The NMR and mass spectra of the synthesized compounds are given in the A3 of Appendices.

6) General procedures for synthesis of MC04DN, MC04DNF and MC04DN02

5-Chloropyridin-3-yl 2-phenylthiazole-4-carboxylate (MC04DN)

To the solution of benzonitrile (2.00 g, 19.42 mmol) in *N*,*N*-Dimethylformamide (DMF) at 0 °C was added sodium hydrosulfide (1.08 g, 19.27 mmol) with the catalysis of magnesium chloride hexahydrate (3.93 g, 19.36 mmol) as the catalyst. The resulting solution was stirred overnight at room temperature. Then the reaction mixture was quenched with water. Then the resulting solid thiobenzamide was collected by filtration to get a yellow crude solid product, with a yield of 1.86 g (70%).

Methyl bromopyruvate (1.34 g, 10.95 mmol) was added to thiobenzamide (1.50 g, 10.95 mmol) in methanol (45 mL). The reaction mixture was heated to 90 °C for 4 hours. The mixture was poured onto ice with vigorous stirring. The resulting solid was collected and washed with H_2O to yield a pale-yellow solid, methyl 2-phenylthiazole-4-carboxylate, with a yield of 1.12 g (70%).

Methyl 2-phenylthiazole-4-carboxylate (1.00 g, 4.57 mmol) was added to a mixture of methanol and 1 M aqueous NaOH (v/v = 1:3, 10 mL) at 0 °C and then warmed to reflux. After 2 hours of stirring, the reaction solution was cooled to room temperature. The resulting solid was collected by filtration. The collected solid was dissolved in water, and the pH was adjusted to approximately 3 with 1 N HCl. The crude product was

collected and washed with water to afford the pale-yellow solid, 2-phenylthiazole-4-carboxylic acid, with a yield of 0.79 g (80%).

To a solution of 2-phenylthiazole-4-carboxylic acid (20 mg, 0.096 mmol) in N,N-Dimethylformamide (DMF) (10 mL) at 0 °C, 3-Chloro-5-hydroxypyridine (12.48 mg, 0.096 mmol), N,N-Diisopropylethylamine (DIPEA, 12.39 mg, 0.096 mmol), 1-Hydroxybenzotriazole (HOBt, 13.17 0.096 mmol), and *N,N'*mg, Diisopropylcarbodiimide (DIC, 12.39 mg, 0.096 mmol) were added. The resulting solution was stirred overnight at room temperature. Then, the reaction mixture was quenched with water. The resulting solid was collected by filtration to yield a yellow crude solid product. Purification of the crude product by chromatography on silica gel (Dichloromethane: Ethyl acetate = 20:1) afforded 5-chloropyridin-3-yl 2phenylthiazole-4-carboxylate as a white solid, with a yield of 29 mg (0.065 mmol, 70%). ¹H NMR (600 MHz, DMSO- d_6) δ 8.95 (s, 1H), 8.65 (d, J = 2.2 Hz, 2H), 8.19 (t, J = 2.2 Hz, 1H), 8.05 (d, J = 2.6 Hz, 1H), 8.04 (d, J = 3.6 Hz, 1H), 7.58 (d, J = 2.9 Hz, 2H), 7.57 (s, 1H). HRMS (ESI) m/z 338.9967 [M + Na]⁺.

5-Chloro-6-fluoropyridin-3-yl 2-phenylthiazole-4-carboxylate (MC04DNF)

3-Chloro-2-fluoro-5-hydroxypyridine was chosen to replace 3-chloro-5-hydroxypyridine. MC04DNF was prepared by following a similar procedure to that used for MC04DN. White solid (30 mg, 0.068 mmol, 70%, R_f = 0.33, Dichloromethane:

Ethyl acetate = 20:1). 1 H NMR (600 MHz, DMSO- d_{6}) δ 8.95 (s, 1H), 8.48 (dd, J = 7.7, 2.6 Hz, 1H), 8.35 - 8.33 (m, 1H), 8.05 (d, J = 2.5 Hz, 1H), 8.04 (d, J = 3.7 Hz, 1H), 7.57 (d, J = 2.7 Hz, 2H), 7.57 (s, 1H). HRMS (ESI) m/z 335.0053 [M + H] $^{+}$; 356.9875 [M + Na] $^{+}$.

5-Chloropyridin-3-yl 2-(2,4-dichlorophenyl)thiazole-4-carboxylate (MC04DN02) Benzonitrile was taken as the starting compound. MC04DN02 was prepared by following a similar procedure to that used for MC04DN. White solid (30 mg, 0.068 mmol, 70%, $R_f = 0.33$, Dichloromethane: Ethyl acetate = 20:1). ¹H NMR (600 MHz, DMSO- d_6) δ 9.11 (s, 1H), 8.66 (s, 2H), 8.28 (d, J = 8.6 Hz, 1H), 8.20 (s, 1H), 7.94 (d, J = 2.1 Hz, 1H), 7.67 (dd, J = 8.6, 2.2 Hz, 1H). HRMS (ESI) m/z 384.9366 [M + H]⁺; 406.9187 [M + Na]⁺.

The NMR and mass spectra of the synthesized compounds are given in the A3 of Appendices.

7) General procedures for synthesis of MC10S01 and MC1210S01

5-Chloropyridin-3-yl 2-((3-hydroxyphenyl)amino)thiazole-4-carboxylate (MC10S01)

To a solution of MC10 (0.30 g, 0.83 mmol) in Dichloromethane at -78 °C, boron tribromide (0.22 g, 0.88 mmol) was added. The resulting solution was stirred overnight at room temperature. Then, the reaction mixture was poured onto ice water (50 mL)

and extracted with Dichloromethane (3 × 75 mL). The organic phase was combined and evaporated under vacuum to yield the solid. Purification of the crude product by chromatography on silica gel (Dichloromethane: Ethyl acetate = 20:1) afforded 5-chloropyridin-3-yl 2-((3-hydroxyphenyl)amino)thiazole-4-carboxylate as a white solid, with a yield of 0.15 g (0.43 mol, 53%). 1 H NMR (400 MHz, DMSO- d_6) δ 10.42 (s, 1H), 9.48 (s, 1H), 8.63 (d, J = 2.1 Hz, 1H), 8.60 (d, J = 2.3 Hz, 1H), 8.15 (s, 1H), 8.14 (t, J = 2.2 Hz, 1H), 7.13 (t, J = 2.1 Hz, 1H), 7.10 (d, J = 8.0 Hz, 1H), 7.04 (d, J = 7.9 Hz, 1H), 6.42 (dd, J = 7.9, 2.3 Hz, 1H). HRMS (ESI) m/z 348.0207 [M + H] $^{+}$; 370.0027 [M + Na] $^{+}$.

5-Chloropyridin-3-yl 2-((3-hydroxyphenyl)(methyl)amino)thiazole-4-carboxylate (MC1210S01)

MC1210 was chosen as the starting compound. MC1210S01 was prepared by following a similar procedure to that used for MC10S01. White solid (0.19 g, 0.53 mmol, 65%, $R_f = 0.33$, Dichloromethane: Ethyl acetate = 20:1). ¹H NMR (400 MHz, DMSO- d_6) δ 9.84 (s, 1H), 8.62 (d, J = 2.1 Hz, 1H), 8.57 (d, J = 2.3 Hz, 1H), 8.11 (t, J = 2.2 Hz, 1H), 7.99 (s, 1H), 7.30 (t, J = 8.0 Hz, 1H), 6.91 (d, J = 10.4 Hz, 1H), 6.86 (t, J = 2.2 Hz, 1H), 6.76 (d, J = 8.1 Hz, 1H), 3.47 (s, 3H). HRMS (ESI) m/z 362.0364 [M + H]⁺; 384.0194 [M + Na]⁺.

The NMR and mass spectra of the synthesized compounds are given in the A3 of Appendices.

2.2 Some background information of lead compounds

2.2.1 Masitinib as inhibitor against SARS-CoV-2 M^{pro}

Masitinib (Figure 2.1), a selective tyrosine kinase inhibitor developed by AB Science, is approved for canine mast cell tumor treatment [79,80]. It is currently under investigation for its potential in treating human inflammatory, neurological, and oncological conditions [61,62,79]. During the pandemic, Masitinib was repurposed as an antiviral agent, demonstrating *in vivo* efficacy against SARS-CoV-2 by inhibiting the main protease, thereby impeding viral replication *in vitro* [62]. In SARS-CoV-2-infected mice, Masitinib significantly reduced viral loads in the lungs and nasal passages and mitigated lung inflammation. By day 6 of treatment, a 200-fold decrease in viral titers was observed, accompanied by a reduction in proinflammatory cytokines like interferon-γ (IFN-γ) and interleukin-1β (IL-1β), leading to improved survival rates and reduced weight loss [62]. *In vitro* cellular assays confirmed the activity of Masitinib against various SARS-CoV-2 variants, including B.1.1.7, B.1.351, and P.1 [62]. Enzymatic assays revealed that Masitinib specifically inhibits SARS-CoV-2 M^{pro} without affecting the activity of PL^{pro}

Generic name: Masitinib

Chemical name: N-(4-methyl-3-((4-(pyridin-3-yl)thiazol-2-yl)amin

o)phenyl)-4-((4-methylpiperazin-1-yl)methyl)benzamide

Chemical Formula: $C_{28}H_{30}N_6OS$

Molecular Weight: 498.65

CAS Number: 790299-79-5

Figure 2.1 Chemical structure of Masitinib.

Crystallographic studies have revealed that Masitinib occupies the catalytic site of SARS-CoV-2 M^{pro} through non-covalent interactions [62]. Specifically, the pyridinyl nitrogen forms a hydrogen bond with the imidazole ring of His163 (Figure 2.2), while the pyridinyl ring itself engages in hydrophobic interactions with the S1 subsite. The amino group of aminothiazole is hydrogen-bonded to the main chain of His164. The catalytic dyad, consisting of Cys145 and His41, is effectively blocked by the thiazole and phenyl groups. The nitrogen atom of thiazole forms a hydrogen bond with the thiol group of Cys145. Meanwhile, the toluene ring connecting to the aminothiazole group is perfectly stacked in a π - π interaction with the side chain of His41. The benzamide moiety of Masitinib is oriented away from the S4 subsite, with its amino group forming a hydrogen bond with a water molecule within the binding pocket. The remainder of the benzamide interacts with the main chain of protein between Cys44 and Ser46. The N-methylpiperaze group, which lacks direct interaction with M^{pro}, extends outward from the pocket. This detailed description underscores the precise molecular interactions that underline the inhibitory effect of Masitinib on SARS-CoV-2 M^{pro}.

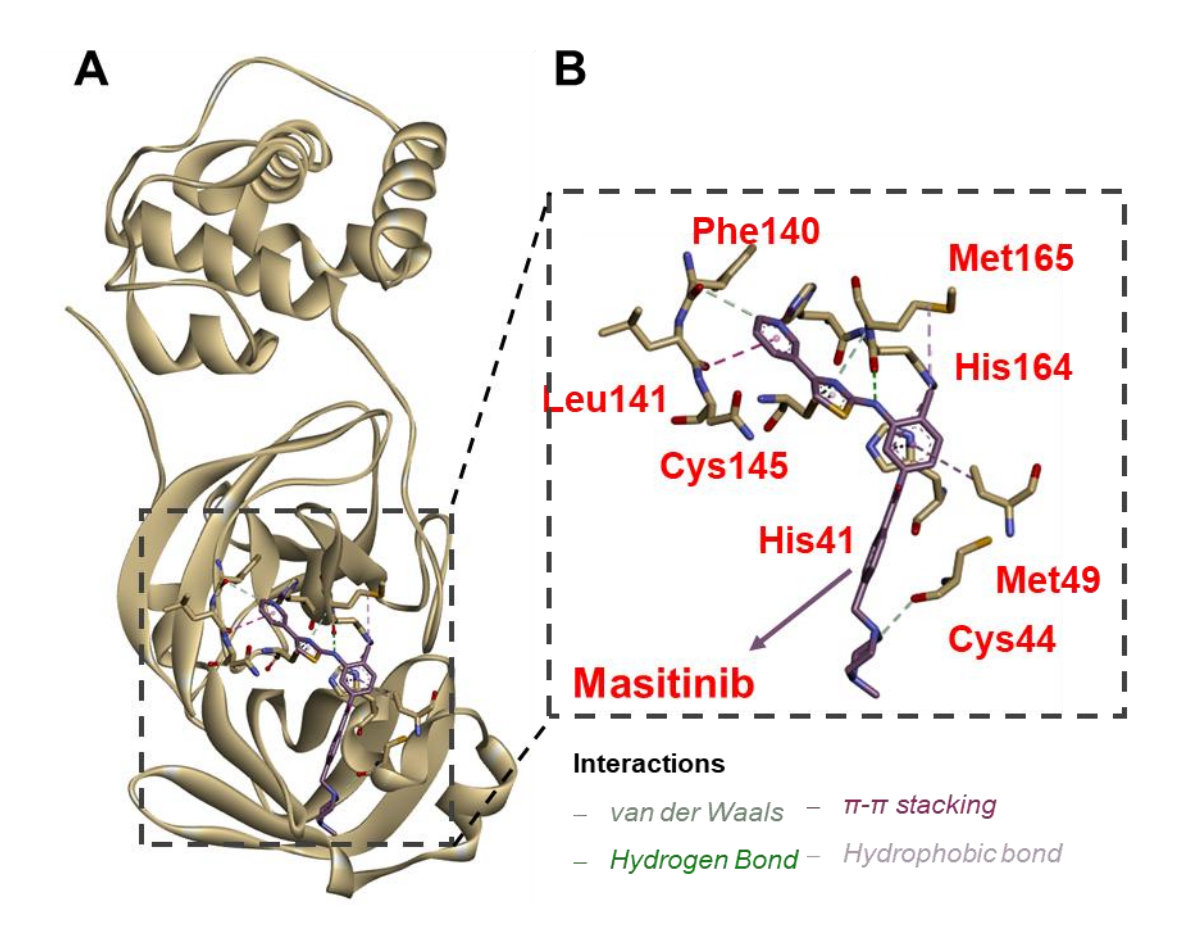


Figure 2.2 A) X-ray crystal structure of Masitinib (carbons colored in purple) binding to SARS-CoV-2 M^{pro} (PDB ID 7JU7). B) The diagram showing the details of some interactions formed between the Masitinib (carbons colored in purple) and the active site of SARS-CoV-2 M^{pro}.

2.2.2 MAC-5576 against SARS-CoV-2 M^{pro}

MAC-5576 (Figure 2.3) is a nonpeptidic small molecule identified two decades ago through high-throughput screening (HTS) of 50,000 drug-like compounds for its activity against SARS-CoV M^{pro} [50]. It exhibited selectivity for proteases with a chymotrypsin-like fold, including SARS-CoV M^{pro}, HAV 3C^{pro}, and chymotrypsin, while showing no inhibitory effect on PL^{pro}, which lacks this fold [50]. Mass spectrometry of the complex between wild-type SARS-CoV M^{pro} and a MAC-5576 derivative revealed a covalent bond formation mechanism involving the acylation of M^{pro} and release of the 3-halo-5-hydroxypyridine group [51].

Compound Code: MAC-5576, MAC5576

Chemical Name: 5-chloropyridin-3-yl thiophene

-2-carboxylate

 $\textbf{Chemical Formula:} \ \ C_{10} H_6 CINO_2 S$

Molecular Weight: 239.67

CAS Number.: 219929-01-8

Figure 2.3 Chemical structure of MAC-5576.

MAC-5576 has also emerged as a potential inhibitor of SARS-CoV-2 M^{pro} [53]. The cocrystal structure with SARS-CoV-2 M^{pro} demonstrated that, following the departure of the pyridinyl group, the thiophene moiety of MAC-5576 forms a covalent bond with Cys145, thereby blocking the catalytic site by occupying the S2 subsite (Figure 2.4). Additionally, the imidazole in His41 rotates to engage in π - π stacking with the thiophene of MAC-5576, further stabilizing the inhibitory complex [53,76].

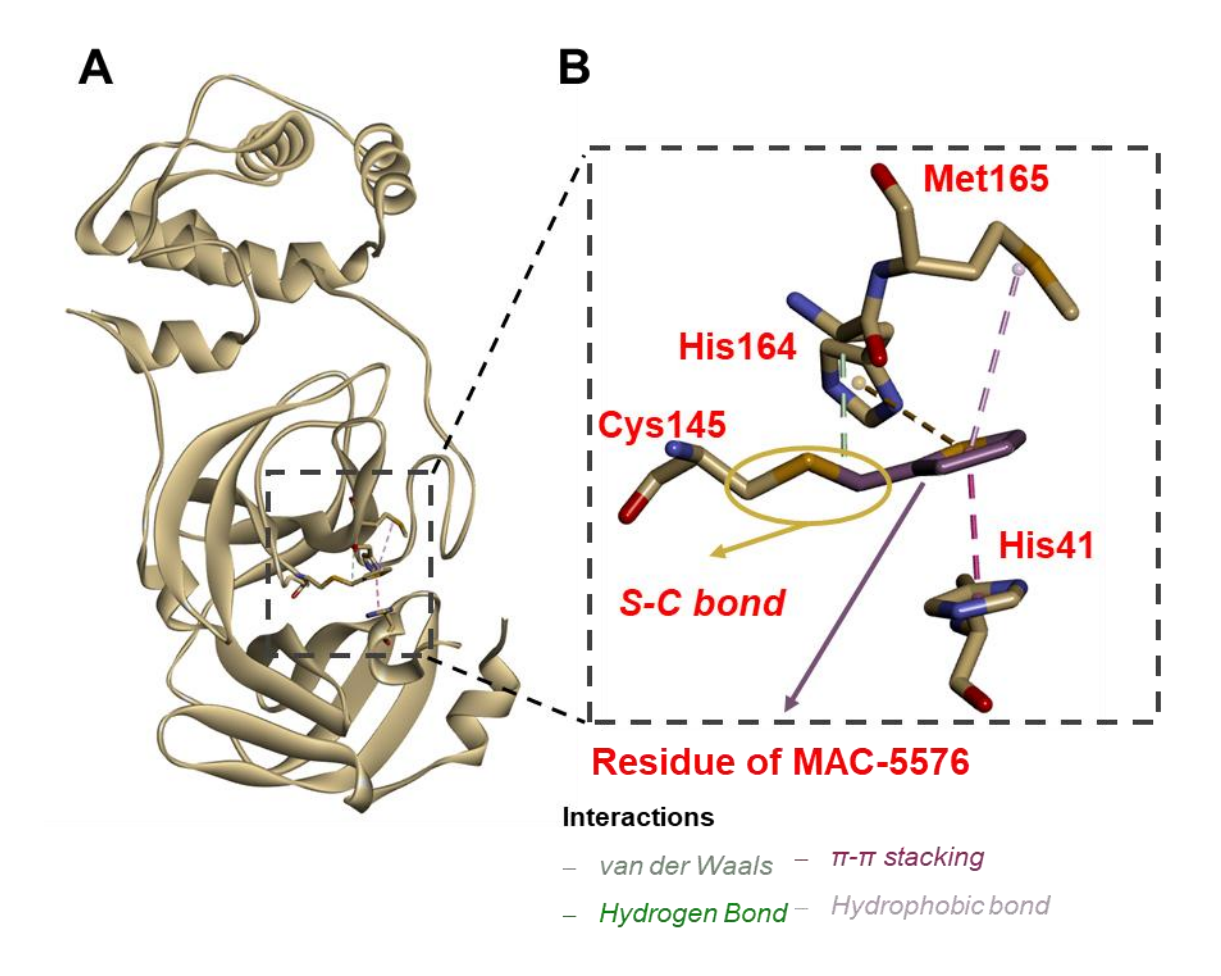


Figure 2.4 A) X-ray crystal structure of MAC-5576 (colored in purple) binding to SARS-CoV-2 M^{pro} (PDB ID 7JT0). B) The diagram showing the details of some interactions formed between the MAC-5576 (carbons colored in purple) and the active site of SARS-CoV-2 M^{pro}.

2.3 Design of the compounds

2.3.1 Introduction of Bioisosterism

Bioisosterism plays a pivotal role in the evolution of hit compounds into leads and the subsequent optimization of lead compounds into drug candidates with favorable pharmacological attributes [81]. It is a fundamental strategy for enhancing compound potency and selectivity, minimizing adverse effects, and refining pharmacokinetic profiles [81]. Bioisosteres are categorized into classical and nonclassical types. Classical bioisosteres, as detailed in Table 2.1, include monovalent, bivalent, trivalent, tetravalent, and ring equivalences. The nonclassical bioisosteres comprise a diverse range of functional groups, including carbonyl, carboxylic acid, hydroxyl, catechol, halogens, amides, esters, thiourea, pyridine, and the distinction between cyclic and acyclic structures [82]. This systematic classification facilitates the strategic modification of chemical entities to achieve desired pharmaceutical properties.

Table 2.1 Examples of classical bioisosteres-groups in each row are equivalent.

Bioisosteres	Sample structures			
Monovalent	OH, NH			
	OH, NH or CH ₃ for H SH, OH			
	Divalent	C=S	C=O	C=NH
Trivalent atoms or		—С-H	$-\stackrel{N}{O}$	
groups		P	As	
Tetrasubstituted		-C-	$-\stackrel{\mid}{N}^{+}$	
		P+	-As ⁺	
Rings		N		

2.3.2 Strategy of Scaffold Fusion

In molecular docking studies, the nitrogen atom of pyridine ring of MAC-5576 forms a hydrogen bond with the imidazole of the M^{pro}, akin to the interaction between the pyridine-3-yl ring of Masitinib and His163 in SARS-CoV-2 M^{pro} [32, 51]. Co-crystal structures[53, 62] of SARS-CoV-2 M^{pro} with both Masitinib [62] and MAC-5576 [53] reveal that the *N*-phenylthiazol-2-amine of Masitinib occupies the same subsite as the thiophene of MAC-5576, suggesting a common binding mode.

Given that thiazole and thiophene are bioisosteric, the thiazole of Masitinib was rationally replaced with the thiophene of MAC-5576 to create a novel scaffold [83]. This design strategy, involving the fusion of scaffold, preserves the pyridinyl-ester moiety of MAC-5576 as the active warhead. The *N*-phenylthiazol-2-amine group from Masitinib replaces the thiophene of MAC-5576, while the amide part of Masitinib, which is oriented away from the S4 subsite, is omitted for structural simplicity. The resulting structure, exemplified as MC04, represents a new class of inhibitors with a redesigned scaffold for potential antiviral activity (Figure 2.5).

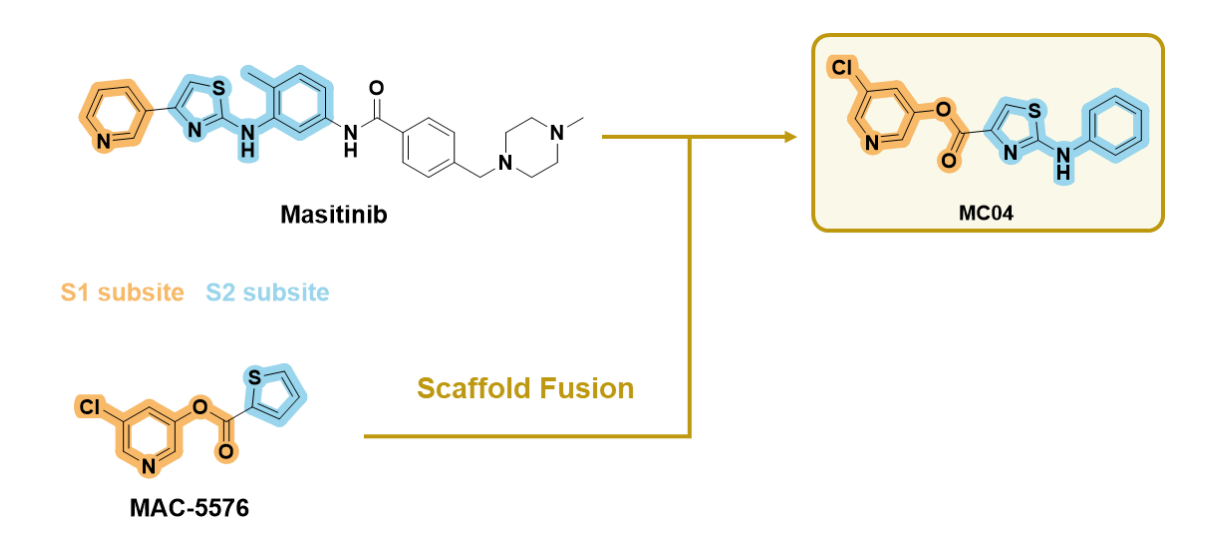


Figure 2.5 Strategy of scaffold fusion utilized in the two lead compounds and the structure of one of the designed compounds, MC04.

2.3.3 Strategy of Bioisosterism

Thiazole and oxazole, as ring equivalents, are aromatic cyclic compounds distinguished by their heteroatoms. The oxazole ring has garnered significant interest in drug discovery due to its diverse pharmaceutical applications, including antifungal, antiparasitic, anti-inflammatory, and anticancer properties [84]. Despite their differences, the oxygen in oxazole and the sulfur in thiazole are both members of the same family in the periodic table, suggesting a degree of chemical similarity. In this project, bioisosterism as a rational design strategy was used, such as replacing the thiazole ring with an oxazole ring to develop a series of oxazole-based compounds (Figure 2.6). These compounds retain the pyridinyl-ester warhead and the *N*-phenyl rings in this series.

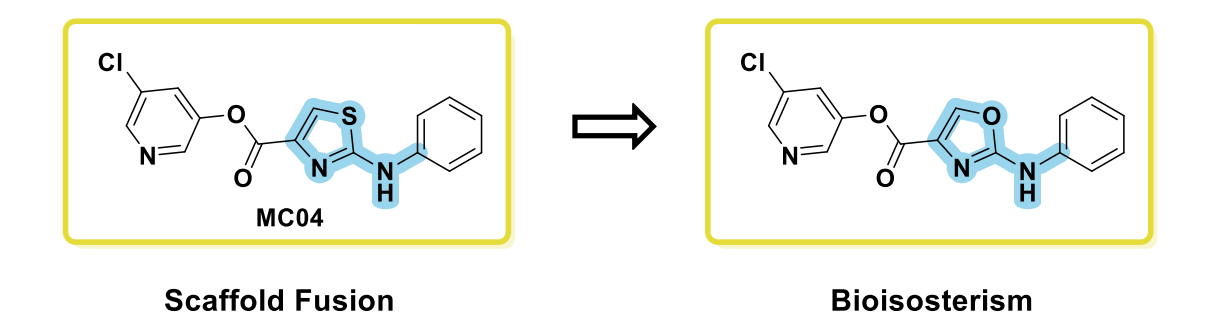


Figure 2.6 Application of bioisosterism based on MC04.

2.3.4 Other strategies

The introduction of a new warhead could potentially alter the orientation or position of the compounds within the catalytic site of SARS-CoV-2 M^{pro}, necessitating an exploration of these effects on inhibitory activity. This project underscored the significance of the pyridinyl ester and a thorough examination of the role of aminothiazole was conducted (Figure 2.7). Specifically, we investigated the impact of replacing aminothiazole with thiazole to directly link to the phenyl ring. The use of an amide group to acylate aminothiazole was also explored. Additionally, it was scrutinized that the spatial relationship between the amino group of aminothiazole and the benzene ring, including the influence of the size and length of substituents on the amino group. These investigations aim to elucidate the structural factors that contribute to the inhibitory potency of the compounds.

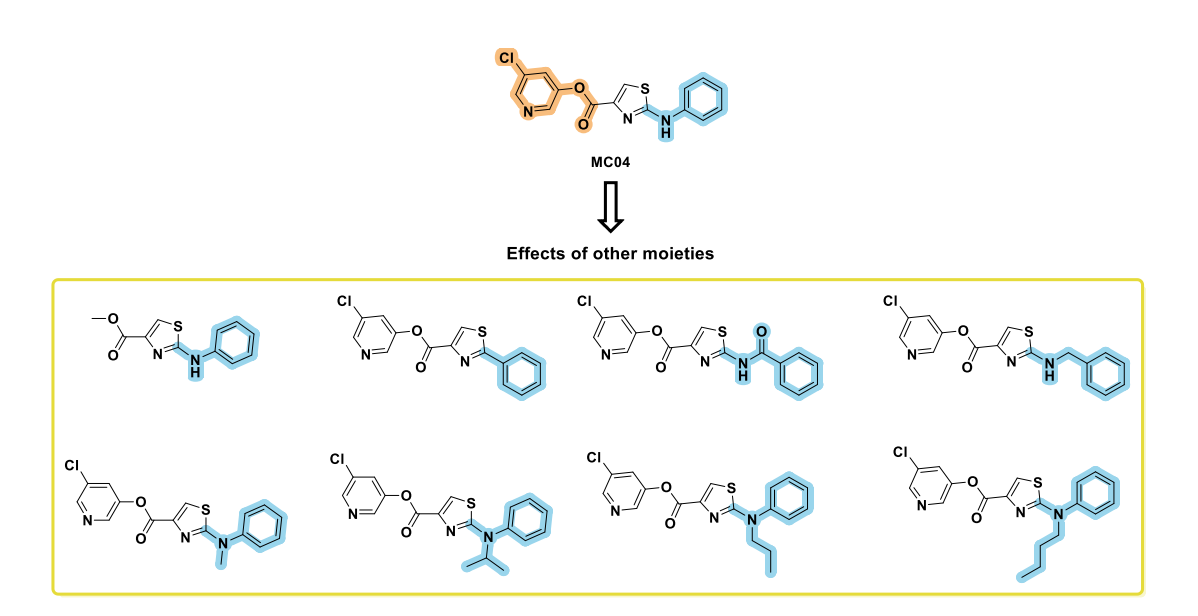


Figure 2.7 Structures of representative compounds for exploring the effects of other moieties.

2.4 Synthetic routes to target compounds

2.4.1 Thiazole-based analogues with phenyl and benzyl rings

Based on retrosynthetic analysis, the thiazole-based structure can be conceptually divided into three distinct components: the phenyl ring, the 2-aminothiazole ring, and the pyridinyl ring. The linkage between the pyridinyl and thiazole rings is facilitated through an ester bond, derived from 3-hydroxypyridine and carboxylic acid (Figure 2.8).

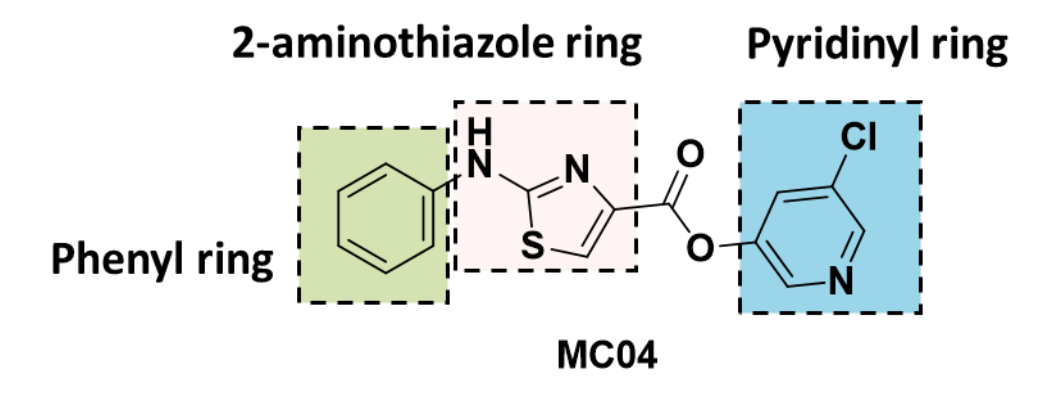


Figure 2.8 Structural features of the target compounds.

1) Analysis on the preparation of the N-phenyl-2-aminothiazole moieties

One of the synthetic challenges lies in the preparation of the *N*-phenyl-2-aminothiazole moieties. Two synthetic routes are available for this purpose: The first involves a Chan-Lam coupling reaction between 2-aminothiazole and phenyl boronic acid [85,86] (Figure 2.9). This coupling reaction is a versatile method for the formation of aryl amines or ethers from the reaction of an amine or alcohol with an aryl boronic acid. It can be performed under ambient conditions and does not require an inert atmosphere. However, the Chan-Lam coupling requires copper catalysts, which can be challenging to remove completely and may pose issues due to their toxicity to proteins if residues remain post-reaction. Given these considerations, we opted against using the Chan-Lam coupling for the synthesis of the *N*-phenyl-2-aminothiazole moiety in this project.

Figure 2.9 Route 1 of the retrosynthesis of MC04.

An alternative synthetic pathway for the *N*-phenyl-2-aminothiazole moiety involves a cyclization reaction starting from phenylthiourea (Figure 2.10) [77, 78]. This process involves the cyclization of phenylthiourea with methyl bromopyruvate to yield methyl 2-(phenylamino)thiazole-4-carboxylate, which can then be hydrolyzed to obtain the carboxylic acid necessary for the final ester linkage. The cyclization workup is straightforward: after refluxing, the reaction mixture is cooled and stirred, and the *N*-phenyl-2-aminothiazole moiety is precipitated to form upon the addition of water. The solid intermediate is then isolated by filtration. The utilization of environmentally friendly solvents like methanol or ethanol in the cyclization reaction is a notable advantage.

Figure 2.10 Route 2 of the retrosynthesis of MC04.

2) Review on the preparation of the phenylthiourea intermediates

In the aforementioned second synthetic pathway for the *N*-phenyl-2-aminothiazole moiety, obtaining phenylthiourea intermediates presents another challenge. Two methods are available: One is a direct reaction between anilines and ammonium thiocyanate under acidic conditions, which, although simpler, requires product purification via silica gel chromatography. The second method involves the reaction of benzoyl chloride with anilines in the presence of ammonium thiocyanate in acetone, followed by debenzoylation under basic conditions [77]. This method, despite being more complex, typically yields purer products.

3) Synthetic route to the target compounds

The synthesis of thiazole-based final compounds is outlined in Scheme 2.1 and begins with aniline or benzylamine derivatives as the starting materials. These amines react with potassium thiocyanate in the presence of benzoyl chloride to form phenylthioureas or benzylthioureas, which are subsequently hydrolyzed under basic conditions. The resulting phenylthioureas or benzylthioureas undergo cyclization with methyl bromopyruvate or its analogs, yielding methyl 2-(benzylamino)thiazole-4-carboxylate derivatives. These methyl esters are then hydrolyzed to produce the corresponding thiazol-4-carboxylic acids. In the final step, these carboxylic acids are reacted with pyridin-3-yl derivatives to form the desired thiazole-core ester compounds.

Scheme 2.1 Synthetic route to target compounds: (i) Benzoyl chloride, NH₄SCN, acetone, 60 °C, 45 min, 80%; (ii) 2 M aqueous NaOH, 100 °C, 1 h, 82 %; (iii) methyl bromopyruvate, methanol, 80 °C, 30 min, 70 %; (iv) 1 M aqueous NaOH/MeOH, room temperature, 1 h, 70%; (v) 3-Chloro-5-hydroxypyridine/3-chloro-2-fluoro-5-hydroxypyridine, 1-Hydroxybenzotriazole (HOBt), *N,N'*-Diisopropylcarbodiimide (DIC), *N,N*-Diisopropylethylamine (DIPEA), *N,N*-Dimethylformamide (DMF), room temperature, 24h, 53%.

2.4.2 Oxazole-based analogues with phenyl rings

Some oxazole-based analogues of thiazole derivatives were also prepared. The synthetic approach for oxazole-based compounds is similar to that of the thiazole-based counterparts, with a key difference in the preparation of phenylurea. As depicted in Scheme 2.2, the synthesis of oxazole-based analogues initiates with aniline derivatives reacting directly with potassium thiocyanate under acidic conditions to yield phenylureas. Subsequently, phenylureas undergo cyclization upon treatment with methyl bromopyruvate or its analogs, resulting in the formation of methyl 2-(phenylamino)oxazole-4-carboxylate derivatives. These esters are then subjected to hydrolysis to obtain oxazol-4-carboxylic acid. The final step involves coupling the oxazol-4-carboxylic acids with pyridin-3-yl analogs to synthesize the ultimate ester compounds featuring an oxazole core.

$$H_{2}N$$
 $H_{2}N$
 H

Scheme 2.2 Synthetic route to the oxazole-based compounds: (i) ethyl bromopyruvate, methanol, 80 °C, 30 min, 70 %; (ii) 1 M aqueous NaOH/MeOH, room temperature, 1 h, 80 %; (iii) 3-chloro-5-hydroxypyridine, 1-Hydroxybenzotriazole (HOBt), *N,N'*-Diisopropylcarbodiimide (DIC), *N,N*-Diisopropylethylamine (DIPEA), *N,N*-Dimethylformamide (DMF), room temperature, 24h, 66%.

2.4.3 Amide-linker analogues

Starting from methyl 2-aminothiazole-4-carboxylate, the synthesis proceeds by reacting it with benzoic acid to form methyl 2-benzamidothiazole-4-carboxylate. This intermediate is then hydrolyzed to produce the corresponding carboxylic acid. The final step involves a reaction with pyridin-3-yl analogs, leading to the formation of the target compounds (Scheme 2.3).

Scheme 2.3 Synthetic route to the amide-linker compounds: (i) 2-(7-Azabenzotriazol-1-yl)-*N*,*N*,*N*',*N*'-tetramethyluronium hexafluorophosphate (HATU), Triethylamine (TEA), *N*,*N*-Dimethylformamide (DMF), room temperature, overnight, 70%; (ii) 1 M aqueous LiOH/MeOH (v:v=1:1), room temperature, 1 h, 80%; (iii) 3-chloro-5-hydroxypyridine, 1-Hydroxybenzotriazole (HOBt), *N*,*N*'-Diisopropylcarbodiimide (DIC), *N*,*N*-Diisopropylethylamine (DIPEA), *N*,*N*-Dimethylformamide (DMF), room temperature, 24h, 64%.

2.4.4 Non-linker analogues

In this project, non-chain analogs feature a 2-phenylthiazole core, replacing the *N*-phenyl-2-aminothiazole. The synthesis of these analogues hinges on the formation of benzothioamide, which presents the main challenge in this series. The process begins with benzonitrile, which reacts with sodium hydrosulfide in the presence of magnesium chloride hexahydrate as a catalyst in *N*,*N*-Dimethylformamide (DMF). The benzothioamide intermediates obtained are then cyclized using methyl bromopyruvate analogs, leading to the formation of methyl 2-(phenyl)thiazole-4-carboxylate analogs. Following hydrolysis of these esters under basic conditions, the resulting carboxylic acids are coupled with pyridin-3-ol analogs to produce the final ester products lacking the *N*-chain (Scheme 2.4).

Scheme 2.4 Synthetic pathway to the non-linker compounds: (i) Sodium Hydrosulfide, Magnesium Chloride, *N,N*-Dimethylformamide (DMF), room temperature, 12 h, 70 %; (ii) methyl bromopyruvate, methanol, 80 °C, 30 min, 70%; (iii) 1 M aqueous NaOH/MeOH, 1 h, 80%; (iv) 3-chloro-5-hydroxypyridine/3-chloro-2-fluoro-5-hydroxypyridine, 1-Hydroxybenzotriazole (HOBt), *N,N'*-Diisopropylcarbodiimide (DIC), *N,N*-Diisopropylethylamine (DIPEA), *N,N*-Dimethylformamide (DMF), room temperature, 24h, 70%.

Chapter 3. Determination of Structure Activity Relationship of the SARS-CoV-2 M^{pro} **Inhibitors**

3.1 Methods

3.1.1 Materials and equipment

All tested compounds were synthesized in the laboratory. The FRET-based biosensor (MCA-AVLQ↓SGFR-Lys(DNP)-Lys-NH₂) was purchased from GL Biochem (Shanghai). The kinetics of enzymatic activity were measured using a TECAN Freedom EVO 100.

3.1.2 Cloning, expression, and purification of the recombinant SARS-CoV-2 Mpro

The method of cloning and producing recombinant SARS-CoV-2 M^{pro} followed the protocol published previously ^[34]. The full-length gene that encodes SARS-CoV-2 Mpro (NC_045512) fused with a C-terminal PreScission cleavage site and His tag was cloned into pGEX-6P-1 (Bio-Gene). At the *N*-terminus, the construct designed for SARS-CoV-2 M^{pro} contains the M^{pro} cleavage site (SAVLQ\$SGFRK; the arrow indicates the cleavage site) corresponding to the cleavage site between nsp4 and nsp5 in the polyprotein of this virus. At the C-terminus, the construct codes for a modified PreScission cleavage site (SGVTFQ\$\$\dagger\$GP\$; the six-residue sequence at the C-terminus of SARS-CoV-2 M^{pro} was used as P6-P1 for PreScission cleavage) connected to a His6-tag. An authentic *N*-terminus was generated during gene expression by auto-cleavage of the M^{pro} itself, and the authentic C-terminus was generated after treatment with

PreScission protease. The sequence-verified SARS-CoV-2 M^{pro} construct was transformed into the Escherichia coli (E. coli) strain BL21-Gold (DE3) (Novagen). Transformed clones were pre-cultured at 37°C in 50 mL of 2x Yeast Extract Tryptone (2x YT) medium with ampicillin (100 μg/mL) for 3 hours, and the incubated culture was inoculated into 4 L of 2x TY medium supplemented with 100 μg/mL ampicillin. 0.5 mM isopropyl-D-thiogalactoside (IPTG) was added for the induction of the overexpression of the M^{pro} gene at 37°C when the OD600 reached 0.8. After 5 hours, cells were harvested by centrifugation at 10,000 x g, 4°C for 15 minutes. The pellets were resuspended in 30 mL of buffer A (20 mM Tris, 150 mM NaCl, pH 7.8; the pH of all buffers was adjusted at room temperature) and then lysed by sonication on ice. The lysate was clarified by ultracentrifugation at 10,000 x g at 4°C for 2 hours. The HisTrap FF column was washed with 150 mL of buffer A to remove unspecific binding proteins, followed by elution using buffer B (20 mM Tris, 150 mM NaCl, 500 mM imidazole, pH 7.8) with a linear gradient of imidazole ranging from 0 mM to 500 mM over 20 column volumes. The fractions containing the target protein were pooled and mixed with PreScission protease (GenScript) at a molar ratio of 5:1 and dialyzed into buffer C (20 mM Tris, 150 mM NaCl, 1 mM DTT, pH 7.8) at 4°C overnight, resulting in the target protein with authentic N- and C-termini. The PreScission-treated M^{pro} was applied to connected GSTtrap FF (GE Healthcare) and nickel columns to remove the GST-tagged PreScission protease, the His-tag, and any protein with an uncleaved Histag. The His-tag-free M^{pro} in the flow-through was subjected to buffer exchange with

buffer D (20 mM Tris, 1 mM DTT, pH 8.0) using Amicon Ultra 15 centrifugal filters (10 kD, Merck Millipore) at 2,773 x g, and 4°C. The protein was loaded onto a HiTrap Q FF column (GE Healthcare) equilibrated with buffer D for further purification. The column was eluted with buffer E (20 mM Tris, 1 M NaCl, 1 mM DTT, pH 7.8) with a linear gradient ranging from 0 to 500 mM NaCl over 20 column volumes. Fractions eluted from the HiTrap Q FF column containing the target protein with high purity were pooled and subjected to buffer exchange (buffer A: 20 mM Tris, 150 mM NaCl, pH 7.8). The quality of the purified M^{pro} was checked by sodium dodecyl-sulfate polyacrylamide gel electrophoresis (SDS-PAGE).

3.1.3 Measurement of SARS-CoV-2 M^{pro} inhibitory activity

The *in vitro* inhibitory activity of the recombinant SARS-CoV-2 M^{pro} was measured as previously described ^[53] with modifications. The FRET-based biosensor was purchased from GL Biochem in Shanghai. The recombinant SARS-CoV-2 M^{pro} in the buffer (20 mM Tris-HCl, pH 8.0, and 150 mM NaCl) was preincubated with compounds in 100% DMSO for 10 minutes at 37°C. After the FRET-based biosensor in dimethyl sulfoxide (DMSO)/buffer (v/v = 1/1) was added to each well to achieve final concentrations of SARS-CoV-2 M^{pro}, compounds, and the biosensor at 200 nM, 150 nM, and 20 μ M, respectively, fluorescence (excitation wavelength: 320 nm; emission wavelength: 405 nm) was continuously measured on a plate reader for 5 minutes to analyze the inhibitory activity of the compounds. For calculation of the percentage inhibition, a 100% active

enzyme was assumed. The experimental errors were estimated from triplicate measurements.

The inhibitory activity of the compounds was expressed as % Inhibition and was calculated using the following formula:

Inhibition (%) = $(1 - Raw \ data \ compound / Average \ DMSO)*100$

Where:

Raw data compound is the values of fluorescence intensity measured in the wells treated with the compound.

Average DMSO is the average value of fluorescence intensity measured in the wells treated with DMSO.

The Z score compares the separation between the mean signals of positive and negative controls relative to the variability (standard deviation) of the data. It is calculated as:

$$Z = (\mu_{positive} - \mu_{negative}) / \sigma_{negative}$$

Where:

- $\mu_{positive}$: Mean signal of positive controls (e.g., molecules with strong FRET).
- $\mu_{negative}$: Mean signal of negative controls (e.g., molecules with no/low FRET).
- $\sigma_{negative}$: Standard deviation of negative controls.

Interpretation of Z Scores

• Z-score < 2: The difference between the experimental and control groups is likely not significant. The FRET effect may be due to random error. Results are unreliable and need further validation.

2 ≤ Z-score < 3: The difference has some significance, but uncertainty remains.
 The FRET effect may be real but needs more experiments to confirm. Results have limited credibility.

• Z-score ≥ 3: The difference is highly significant. The FRET effect is almost certainly due to experimental changes, not random error. Results are reliable and indicate a real FRET event.

The calculation of "MC12 and MC12S03" was taken as an example, with MC12 as positive control and MC12S03 as negative control.

The positive control MC12 values were 98.404010, 97.039760, 98.095140, and 97.992180, with a mean (μ positive) of 97.8828. The negative control MC12S03 values were 95.365270, 92.793070, 94.695890, and 92.895010, with a mean (μ negative) of 93.9373 and a standard deviation (σ negative) of 1.2923. The Z-score for MC12 and MC12S03 was calculated as follows:

Z MC12 & MC12S03

= (97.8828-93.9373)/1.2923

= 3.053084

Since the Z-score between MC12 and MC12S03 was over 3, the difference between MC12 and MC12S03 was significant.

3.1.4 Evaluation of IC₅₀ of compounds against SARS-CoV-2 M^{pro}

The IC₅₀ of the inhibitors against recombinant wild-type SARS-CoV-2 M^{pro} was quantified as previously described [34], with modifications. A serially diluted solution of the tested compounds was prepared in 100% DMSO. This serially diluted solution of compounds was then added to a 96-well plate, followed by the addition of the protease to achieve a final concentration of SARS-CoV-2 Mpro at 100 nM. After incubating SARS-CoV-2 M^{pro} with the compounds for 10 minutes at 37°C, the FRET-based biosensor was added to each well to a final concentration of 20 µM. Fluorescence (excitation wavelength: 320 nm; emission wavelength: 405 nm) was continuously measured on a plate reader for 5 minutes. For calculations, a 100% active enzyme was assumed [53]. The experimental errors were estimated from triplicate measurements. The inhibitory activity of the compounds was expressed as % Inhibition and calculated using the formula provided in section 3.6.3. IC₅₀ values were calculated using GraphPad Prism software (Version 8.0) with the equation log(inhibitor) vs. response with variable slope, where the R^2 values were as follows: 0.9644 for Nirmatrelvir, 0.9810 for MAC-5576, 0.9653 for MC04, 0.9776 for MC11, 0.9838 for MC12, and 0.9880 for MC10.

The Ki value of the compounds was calculated using the following formula:

$$Ki = IC_{50} / (1 + [S]/Km)$$

Where:

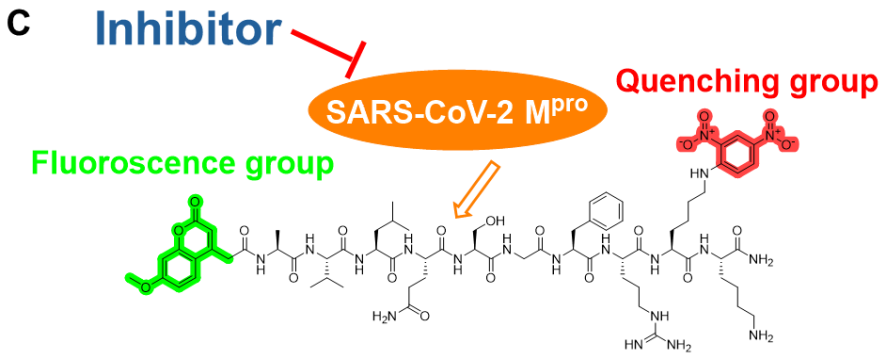
[S] is the substrate concentration.

Km is the Michaelis constant. In this assay K_m was $7.22 \pm 2.48 \,\mu M^{\,[53]}$.

3.2 The enzymatic FRET-based assay for SAR study

FRET-based biosensor procured from GL Biochem Ltd was utilized as an assay for M^{pro} activity. The biosensor employs a donor-acceptor pair consisting of 7-methoxycoumarin (MCA) as the fluorophore and a 2,4-dinitrophenyl group (DNP) as the quencher. The substrate peptide sequence, AVLQ\SGFRKK, is designed to match the cleavage site recognized by SARS-CoV-2 M^{pro [18]} (Figure 3.1). The principle behind the FRET mechanism is that when the distance between MCA and DNP is short (fewer than eight amino acid residues apart), the fluorescence emitted by MCA is quenched by DNP [87]. Upon interaction with SARS-CoV-2 M^{pro}, the biosensor undergoes cleavage at the amide bond between Glutamine (Q) and Serine (S), resulting in an increased distance between MCA and DNP. This increase in distance disrupts the energy transfer, causing a measurable change in fluorescence intensity [88, 89]. When an inhibitor binds to the catalytic site of SARS-CoV-2 Mpro, the biosensor cannot be hydrolyzed by the enzyme. This means the distance between MCA and DNP remains unchanged, preventing the signal of MCA from being measured. This principle can serve as a quantitative indicator of M^{pro} activity.





Sequence of the biosensor: MCA-AVLQ↓SGFR-K(DNP)K

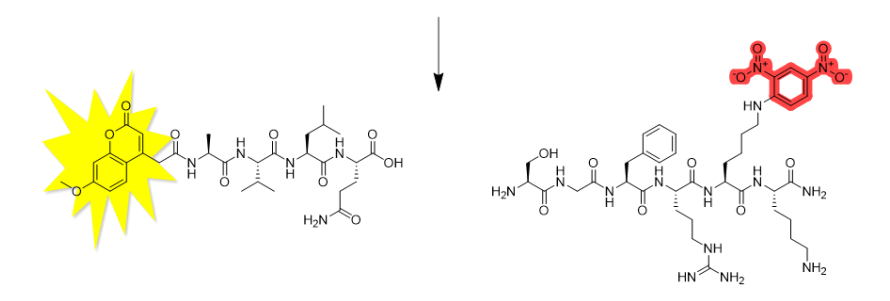


Figure 3.1 A) Chemical structures of MCA/DNP; B) Chemical structure of the biosensor with sequence from P₄ to P1' residues recognized by SARS-CoV-2 M^{pro} (MCA-AVLQ\SGFR-K(DNP)K; arrow indicates the cleavage site); C) Principle of the enzymatic FRET-based assay used to monitor M^{pro} activity.

3.3 Results of the inhibition on SARS-CoV-2 Mpro

Following the design strategies outlined in Chapter 2, we have developed and synthesized four distinct scaffolds: thiazole-based, oxazole-based, amide-linker-based, and non-chain-based. The initial compounds synthesized feature a *N*-phenyl-2-aminothiazole core. The scaffold fusion approach was applied to create the first compound, MC02, which integrates the pyridinyl ester from MAC-5576 with the aminothiazole moiety found in Masitinib. In MC02, the *N*-phenyl ring of Masitinib is substituted by a 4-chloropyridin-2-yl group.

Table 3.1 presents the inhibitory activity of MC02 against the recombinant SARS-CoV-2 M^{pro}. In these assays, Masitinib and MAC-5576 served as positive controls, and the FRET-based biosensor described in section 3.2 was utilized to measure enzymatic activity. MC02 demonstrated significantly greater inhibitory activity against SARS-CoV-2 M^{pro} compared to Masitinib, with Masitinib showing approximately 72% inhibition and MC02 achieving up to 98% inhibition. The activity of MAC-5576 was comparable to that used for MC02. These results suggest that the scaffold fusion strategy is effective for designing new compounds targeting SARS-CoV-2 M^{pro}, and the 2-aminothiazole scaffold warrants further investigation as a promising moiety for the development of SARS-CoV-2 M^{pro} inhibitors

Table 3.1 Inhibitory activities of MC02, Masitinib and MAC-5576 against SARS-CoV- $2\ M^{pro}$.

Compounds	%inhibition at 3 µM
MC02	98.7 ± 0.8
Masitinib	72.8 ± 7.7
MAC-5576	94.7 ± 0.6

3.4 An in-depth exploration of the structure of MC02

The structure of MC02 was dissected into four components for detailed SAR analysis (Figure 3.2): the 4-chloropyridin-2-yl moiety was designated as Part A; the amino group acts as a linker; the thiazole ring was referred to as Part B; and the 3-chloropyridin-5-yl group was identified as Part C. The individual contributions and modifications of these components were examined to elucidate their impact on the inhibitory activity against SARS-CoV-2 M^{pro}. The findings regarding the efficacy of compound are detailed across in section 3.4.1 to 3.4.3, providing a comprehensive overview of the SAR study and its implications for the design of potent and selective inhibitors targeting SARS-CoV-2 M^{pro}.

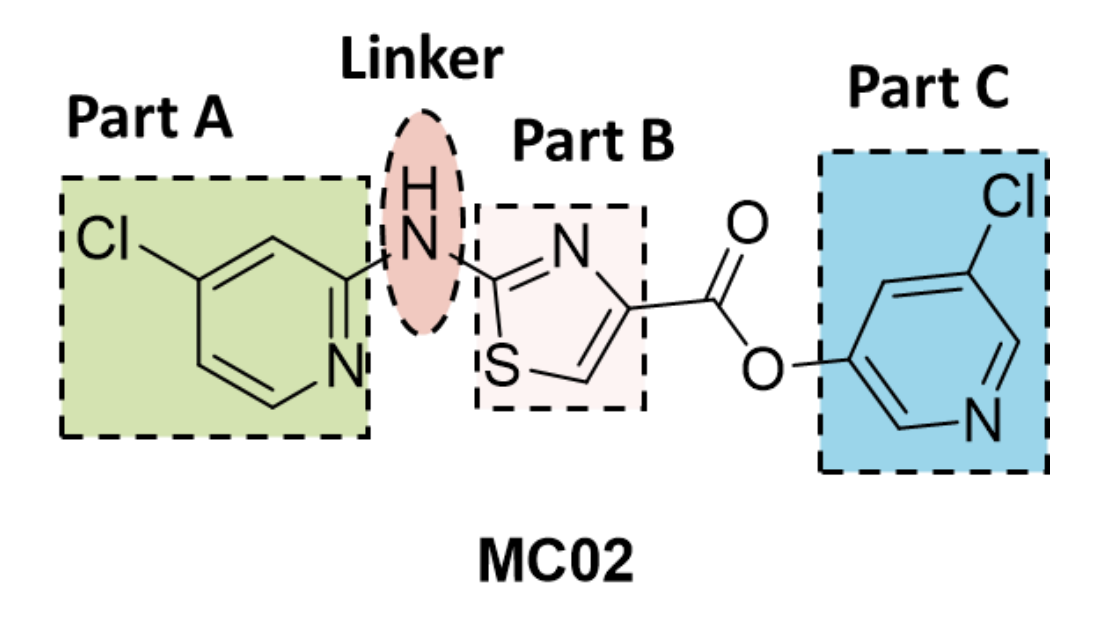


Figure 3.2 Structure of MC02 and the four components of the designed compound.

3.4.1 Effects of Part A

The assays were conducted with a fixed concentration of 200 nM for the purified recombinant SARS-CoV-2 Mpro and 150 nM for the tested compounds. In our investigation, Part A of the molecule, comprising pyridine and phenyl rings, was modified with various substituents categorized by their electronic effects into electronwithdrawing and electron-donating groups. The influence of these substituents, along with their size, was scrutinized in a series of assays. It was observed that the nature of the substituents on the phenyl ring significantly affected the inhibitory potency of compounds. Electron-donating groups, such as methyl, methoxy, and hydroxyl, consistently enhanced the inhibitory activity against SARS-CoV-2 Mpro, with compounds like MC04, MC06, MC07, MC09, MC10, and MC12 demonstrating over 80% inhibition. In contrast, MC14, bearing a chloro group at the *meta* position, showed less than 50% inhibition, while MC13, with a meta-trifluoromethylphenyl group, exceeded 80% inhibition. This contrast underscores the sensitivity of inhibitory activity to the type and position of substituents on the phenyl ring (Figure 3.3).

When comparing phenyl to pyridine rings as Part A, pyridine-containing compounds generally showed reduced inhibitory effects. For instance, MC15, with an unsubstituted pyridine ring, exhibited only about 30% inhibition as compared to MC04 with a benzene ring, which showed nearly 90% inhibition. The position at which the

pyridinyl ring is connected to the aminothiazole also played a crucial role. Compounds with pyridin-2-yl moieties (MC02, MC08, and MC15) showed lower activity than MC09, which has a pyridin-3-yl group attached to aminothiazole. Notably, the presence of electron-donating or electron-withdrawing substituents on the pyridin-2-yl ring, such as in the 4-chloropyridin-2-yl or 4-methylpyridin-2-yl groups, did not significantly alter the inhibitory activity against the protease. This indicates that the position of the attachment of pyridine ring to aminothiazole is more influential in determining the inhibitory effect than the nature of the substituents on the pyridine ring itself (Figure 3.3).

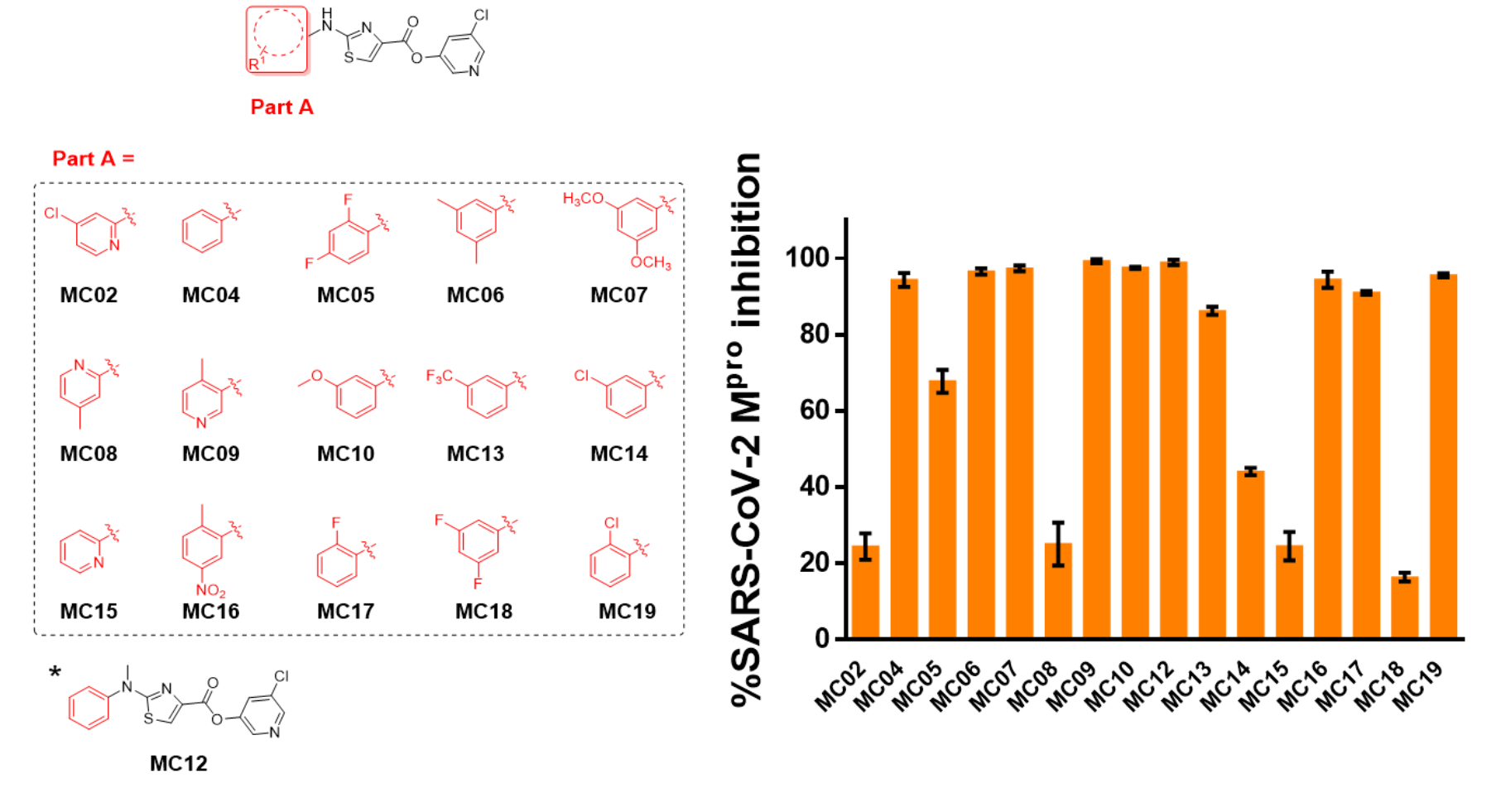


Figure 3.3 Chemical structures and results of SAR exploration of effects of Part A when compounds at 150 nM.

Selected compounds that demonstrated over 80% inhibition in the initial assays were further evaluated at a reduced concentration of 100 nM to delineate their inhibitory effects on SARS-CoV-2 M^{pro} with greater precision. MC12, which has a methyl group at the amino moiety of aminothiazole, displayed enhanced inhibition compared to the non-substituted MC04. MC06 and MC07, both featuring two electron-donating groups at *meta* positions on phenyl rings, showed a notable difference in activity (Figure 3.4). MC07, with methoxy groups, exhibited nearly twice the inhibitory effect of MC06, which has methyl groups. This disparity underscores the impact of the type of electrondonating group on potency. MC10, bearing a meta-methoxy group, showed comparable inhibition to MC07, further validating the enhancing effect of electron-donating groups. In contrast, MC13 exhibited significantly lower activity than MC10, reinforcing the positive contribution of these groups to inhibitory activity. MC09 and MC16, each with an ortho-methyl group on their pyridinyl or phenyl ring, achieved nearly 90% inhibition. Additionally, both MC17 and MC19, each with an ortho-halo atom on their phenyl rings, showed inhibitory activity against SARS-CoV-2 M^{pro} that was as potent as MC04. This suggests that *ortho* substituents on these groups may facilitate the active conformation of the compounds.

The analysis of the aforementioned results indicates that the presence of a phenyl group as Part A likely contributes positively to the inhibitory activity against SARS-CoV-2

M^{pro}. Furthermore, the introduction of electron-donating groups on the benzene rings appears to enhance this inhibitory effect. This suggests that the phenyl group and electron-donating substituents play a significant role in optimizing the interaction of the compounds with the target enzyme, indicating that both the type and position of these groups are critical in optimizing their effectiveness against SARS-CoV-2 M^{pro}.

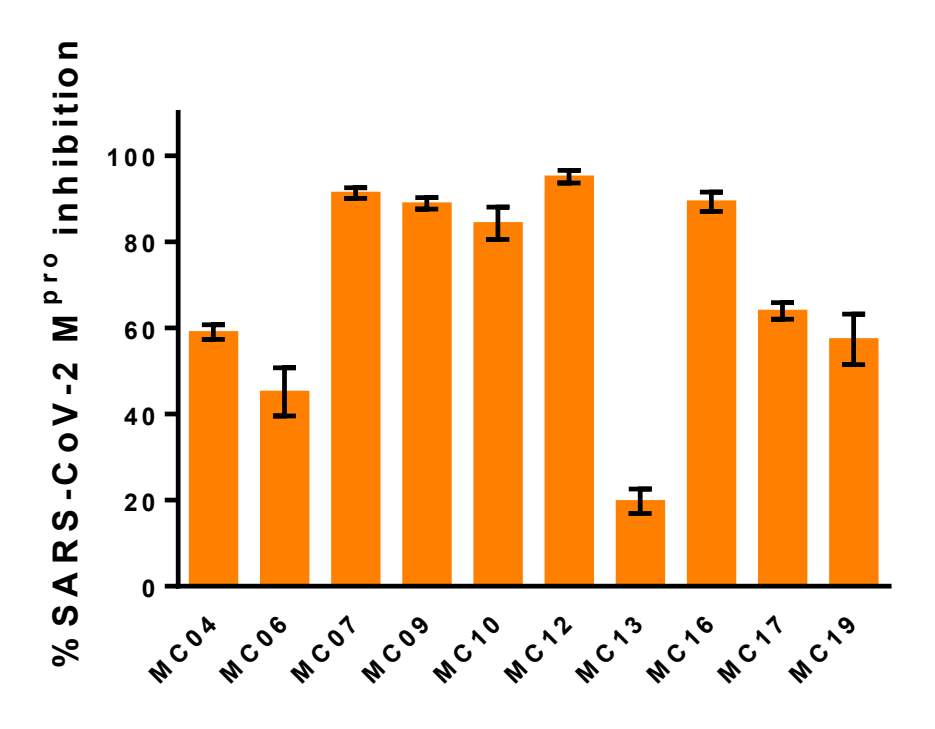


Figure 3.4 Results of SAR exploration of effects of Part A with compounds at 100 nM.

3.4.2 Effects of Part B and N-chain of Linker

The second set of compounds focused on two directions. The first was the bioisosteric replacement of the thiazole core with an oxazole core, while the second focused on the optimization of the *N*-chain at the amino group of aminothiazole to ascertain the ideal chain length and size.

In these assays, the final concentration for SARS-CoV-2 Mpro was maintained at 200 nM, with the compounds tested at 150 nM (Figure 3.5). Compounds MC11 and MC1112, featuring the oxazole core, were synthesized as analogs of the parent compounds MC04 and MC12. MC11 lacked any substituent on its phenyl group, whereas MC1112 had a N-methyl group at the amino group of aminooxazole. The inhibitory activities of the oxazole-based MC11 and MC1112 were found to be as potent as those of the thiazole-based MC04 and MC12, indicating that the core structure does not significantly affect the inhibitory efficacy against SARS-CoV-2 M^{pro}. Additionally, the data from MC11 and MC1112 confirmed that the N-methyl group enhances the inhibitory activity in both thiazole- and oxazole-based compounds. Further investigation into the impact of the N-chain length and size on inhibitory activity was conducted with compounds MC12, MC12S02, MC12S03, and MC12S04. The results indicated that a methyl group and a n-propyl group at the amino moiety of aminothiazole were more effective than iso-propyl and n-butyl groups. In section 3.4.1,

MC10 and MC12 exhibited significantly stronger inhibition against SARS-CoV-2 M^{pro} compared to other compounds. Consequently, a hybrid compound, MC1210, was synthesized by combining the structures of MC10 and MC12. MC1210 features a methyl group at the amino group and a meta methoxy group on the phenyl ring. To explore the effects of hydroxyl substitution, MC10S01 and MC1210S01 were also synthesized. It was observed that the *meta*-hydroxy groups in MC10S01 and MC1210S01 resulted in marginally reduced inhibition compared to the *meta* methoxy groups present in MC10 and MC1210.

The assay outcomes highlighted that *meta*-substituted phenyl groups and *N*-chains at the amino group of aminothiazole significantly bolstered the inhibitory effects against SARS-CoV-2 M^{pro}. Notably, the presence of an *N*-methyl group correlated with more potent inhibition compared to the presence of larger or more extended *N*-chains. However, even when both an *N*-chain and a *meta*-methoxy group were present, their combined effect did not result in a synergistic enhancement of inhibition. This observation suggests that while both factors are influential, their contributions to the overall inhibitory activity are not multiplicative or additive but rather independent.

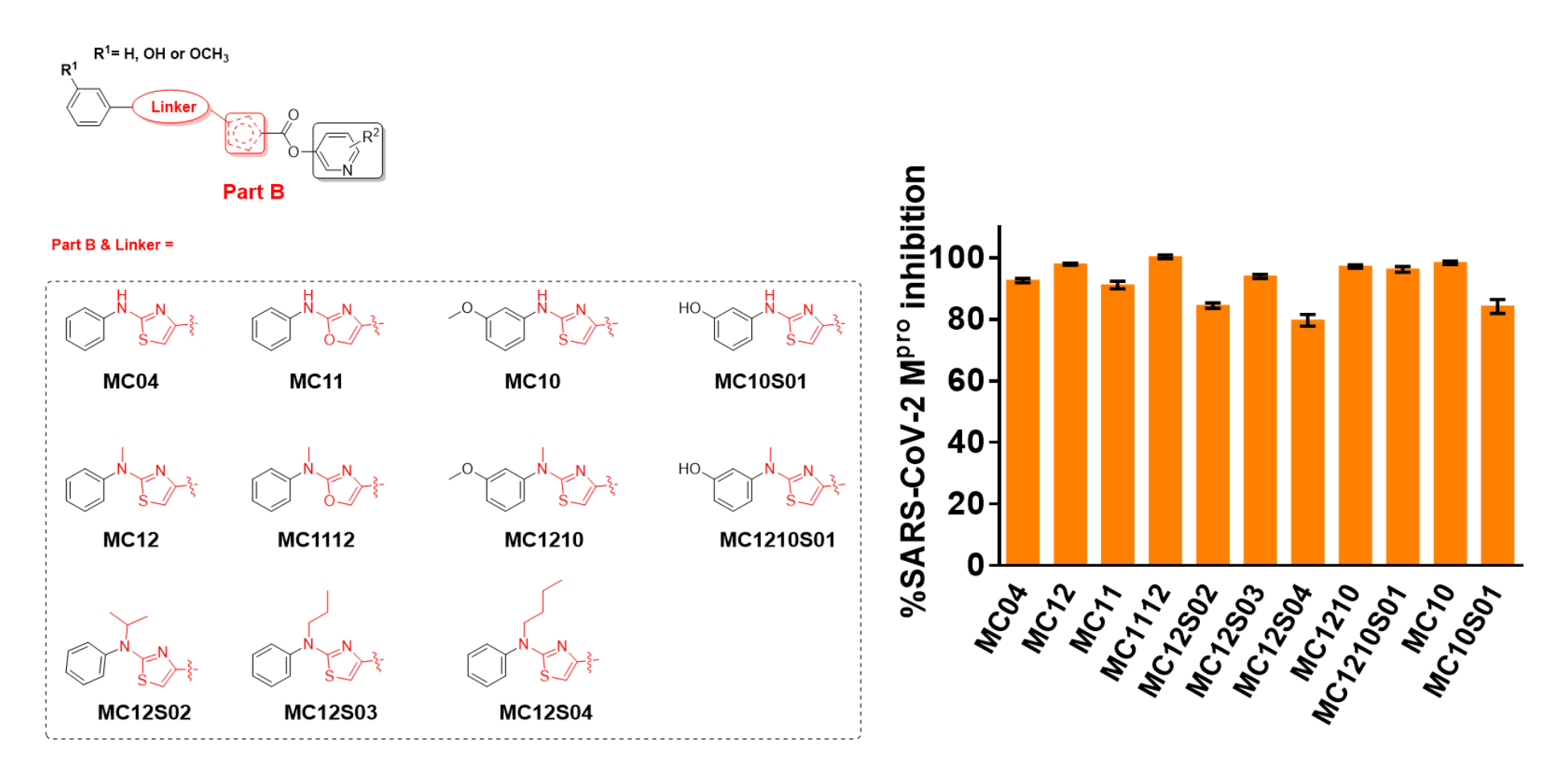


Figure 3.5 Chemical structures and results of SAR exploration of effects of Part B and N-chain.

3.4.3 Effects of Part C and amino group of Linker

1) The importance of moiety of pyridinyl ester

The hypothesis entertained in this study is that the designed compounds are capable of acylating the Cys145 residue within the catalytic site of SARS-CoV-2 M^{pro}, with the concurrent release of 3-chloro-5-hydroxypyridine. A04-01 and A12-01, at a concentration of 150 nM, exhibited less than 10% inhibition against the protease, whereas MC04 and MC12, at the same concentration, demonstrated over 80% inhibition (Figure 3.6). These findings underscore the pivotal role of the pyridinyl ester as the essential pharmacophore for the inhibitory activity of these compounds against SARS-CoV-2 M^{pro}. To evaluate the impact of 3-chloro-5-hydroxypyridine (CHP), its effect on SARS-CoV-2 M^{pro} was examined (Figure 3.6). It was found that CHP did not inhibit SARS-CoV-2 M^{pro}. The stark contrast in inhibitory efficacy between CHP and the pyridinyl ester-containing compounds confirms that the pyridinyl ester is crucial for the inhibitory effectiveness.

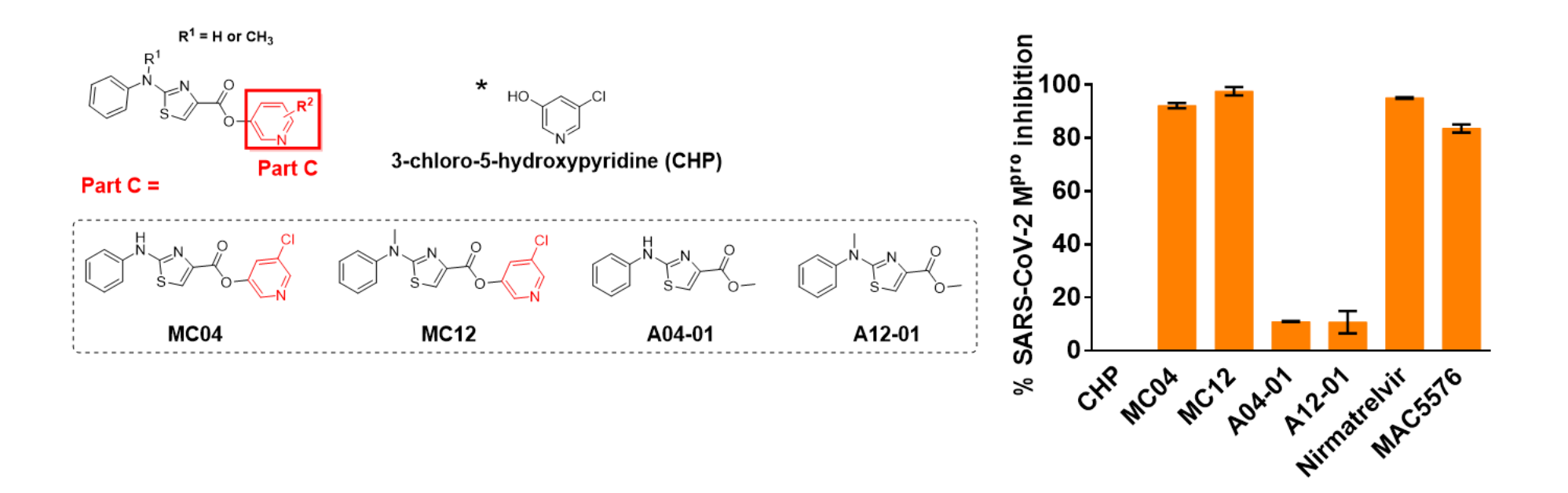
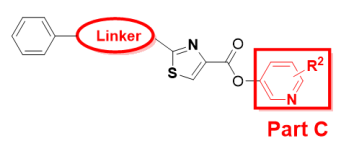


Figure 3.6 The first set of chemical structures and results of SAR exploration of the importance of Part C and Part A.

2) Substitutions of the pyridinyl ring and the significance of linker

The influence of a fluoride atom on the pyridinyl ring was probed using 3-chloro-2fluoro-5-hydroxypyridine. The introduction of a fluoride atom in MC12F, MC04F, and MC04DNF did not compromise their inhibitory activities, which were found to be on par with those of MC12, MC04, and MC04DN, respectively (Figure 3.7). Additionally, the role of the amino group in aminothiazole was scrutinized through the synthesis and testing of MC04DN, a compound lacking the amino group, resulting in a direct linkage between the phenyl ring and thiazole. Assay outcomes for MC04DN and MC04DN02 indicated that the presence of two chloro-substituted phenyl groups diminished the inhibitory efficacy against SARS-CoV-2 M^{pro} (Figure 3.7). Further modifications involved the substitution of a phenyl ring with a benzyl group in MC12E01 and MC04BP, which features two benzyl rings. When comparing these modified compounds with their phenyl ring-containing counterparts, MC12 and MC04, the presence of benzyl rings in MC12E01 and MC04BP did not significantly alter their inhibitory activities against SARS-CoV-2 M^{pro} (Figure 3.7). MC04AM was synthesized by replacing the phenyl ring of MC04 with a benzoyl group. MC04AM exhibited significantly reduced inhibitory activity, suggesting that the type of aryl group linked to the thiazole core is a critical determinant of the effectiveness of the compounds against the protease (Figure 3.7).

The findings from the assays underscore the critical role of Part C in the inhibitory mechanism against SARS-CoV-2 M^{pro}. Furthermore, the removal of the amino group from the aminothiazole structure was found to significantly diminish the inhibitory potency. This suggests that the integrity of the phenyl aminothiazole moiety is essential for optimal interaction with the target protease.



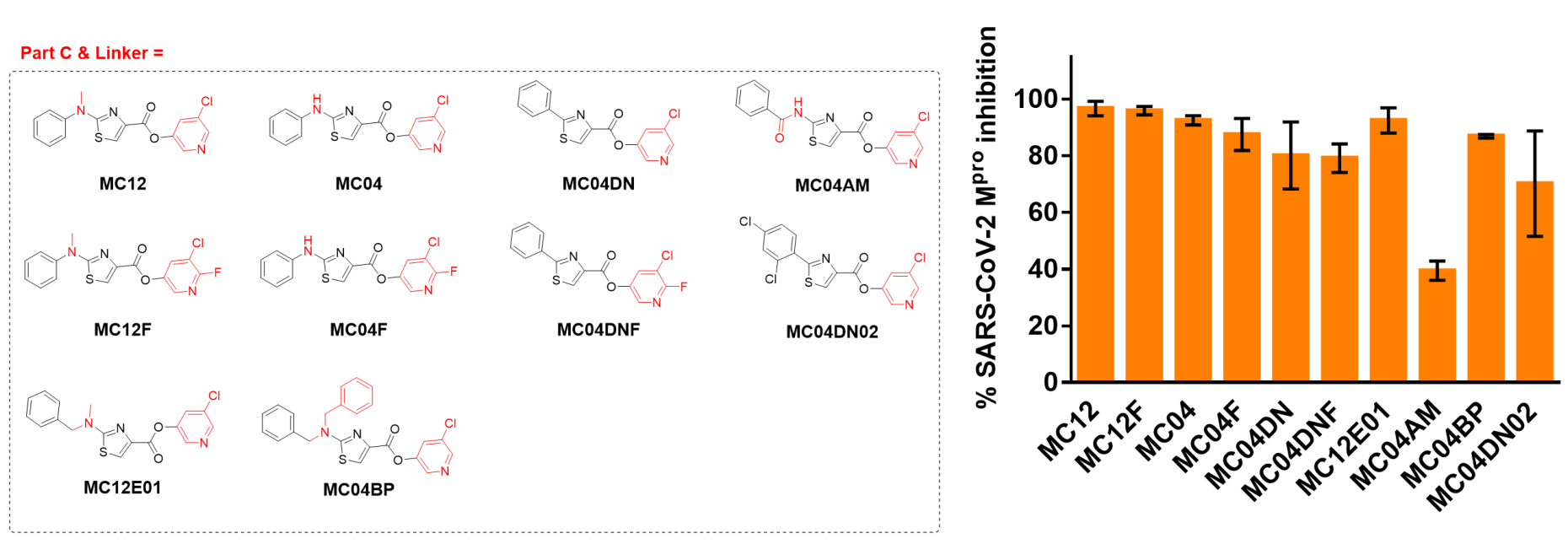


Figure 3.7 The second set of chemical structures and results of SAR exploration of the effects on Part C and Part A.

3.5 Summary of Structure Activity Relationship

The chemical structure depicted in Figure 3.8 is dissected into five key components: Part A, the Linker, Part B, the ester group, and Part C. The subsequent summary consolidates the structure-activity relationship (SAR) findings for these components, highlighting how each element contributes to the overall inhibitory effect on SARS-CoV-2 M^{pro}.

N-methyl compounds showed higher potency than no substituent at N-position.

The size and length of *N*-chain affects the inhibitory activity. The removal of amino group of aminothiazole obviously reduces the inhibitory ability.

- · Bioisosterism is investigated.
- Thiazole core showed slightly higher potency than oxazole.

Phenyl group:

- m-position of phenyl ring
- Methoxy groups enhance the inhibitory activity
- · Halo atoms decrease the potency
- · Size of substitutes affects the bioactivity.

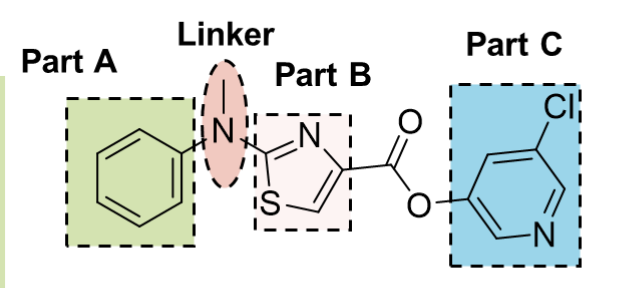
Pyridinyl group:

- · m-position of pyridinyl ring
- · Pyridinyl ring has negative effect.
- Pyridin-3-yl or pyridine-5-yl showed stronger than pyridine-2-yl.

Benzoyl group:

 Replacement of phenyl ring with benzoyl group decreases the inhibitory activity.

Figure 3.8 Summary of structure activity relationship.



- 3-chloropyridin-5-yl is essential to the bioactivity.
- A fluoride atom at pyridinyl ring had comparable inhibitory activity with no fluoride.

3.6 Insight from the SAR study

3.6.1 The activity of Part A

The investigation into Part A of the compounds, which includes both phenyl and pyridinyl groups, yielded the following insights into their inhibitory effects on SARS-CoV-2 M^{pro}. When Part A is a phenyl ring, both *meta* and *ortho* substituents on the phenyl ring enhance the inhibitory activity of compounds. A *meta*-methoxy group is more beneficial than methyl groups or the absence of substitution. Electron-withdrawing groups, particularly halogens on the phenyl ring, reduce the inhibitory potency compared to electron-donating groups. Compounds with pyridinyl groups generally exhibit lower inhibitory activity than those with phenyl groups. The presence of *meta* substituents on the pyridinyl ring can partially restore the inhibitory capability. Variations among different pyridinyl rings are observed, with pyridin-3-yl and pyridine-5-yl showing stronger activity than pyridine-2-yl. In addition, compounds containing benzyl groups as Part A maintain comparable inhibitory activity to those with phenyl groups. The benzoyl group was found to decrease the inhibitory activity against SARS-CoV-2 M^{pro}.

These findings provide a clear direction for the optimization of Part A in the design of more potent SARS-CoV-2 M^{pro} inhibitors, emphasizing the importance of both the type of aromatic group and the nature and position of its substituents.

3.6.2 The activity of Part B

The exploration of Part B focused on the application of bioisosterism, comparing the inhibitory effects of compounds with a thiazole core to those with an oxazole core. The results indicated that compounds centered around the thiazole core demonstrated a marginally greater inhibition against SARS-CoV-2 M^{pro} compared to their oxazole counterparts. This subtle difference suggests that while both cores are viable, the thiazole core may offer a slight advantage in the context of SARS-CoV-2 M^{pro} inhibition.

3.6.3 The activity of Linker

The examination of the Linker segment concentrated on the impact of the *N*-chain and the significance of the amino group within the aminothiazole structure. The presence of an *N*-methyl group as a linker between Part A and Part B resulted in higher inhibitory activity against SARS-CoV-2 M^{pro} compared to compounds lacking an *N*-substituent. The size and length of the *N*-chain were found to influence the inhibitory potency of compounds, with *iso*-propyl and *n*-butyl groups exhibiting less effectiveness than the *n*-propyl group. The elimination of the amino group from aminothiazole significantly diminished the efficacy in obstructing the catalytic site of SARS-CoV-2 M^{pro}.

3.6.4 The activity of Part C

The screening assay outcomes confirm that the pyridinyl ester functions as a pharmacophore, with specific characteristics of Part C being crucial for biological activity. The 3-chloropyridin-5-yl group as Part C is indispensable for maintaining bioactivity. The substitution of the pyridinyl ester with a methyl ester led to a loss of inhibitory capability against SARS-CoV-2 M^{pro}. The 2-fluoro-3-chloropyridin-5-yl ester was found to contribute to the inhibitory activity against SARS-CoV-2 M^{pro} to a similar extent as the 3-chloropyridin-5-yl ester.

3.7 Determination on the IC₅₀ values against SASR-CoV-2 M^{pro}

MC12 emerged as the most potent inhibitor against SARS-CoV-2 M^{pro} in the enzymatic screening assays, prompting its selection for half-maximal inhibitory concentration (IC₅₀) determination. The structure-activity relationship analysis highlighted that electron-donating substituents at the *meta*-position of Part A enhance the potency against the protease. Consequently, MC10 was also chosen for IC₅₀ evaluation. Recognizing the successful application of bioisosterism in structural modification, MC11, with its oxazole core, was selected for IC₅₀ measurement. MC04, as a reference compound, underwent IC₅₀ determination as well. As depicted in Figure 3.9, MC10 and MC12 exhibited inhibition levels comparable to Nirmatrelvir, with IC₅₀ values lower than those of MAC-5576, MC04, and MC11. This affirms the beneficial impact of the

N-methyl group and meta-position electron-donating substituents on the phenyl ring in enhancing the inhibitory activity against SARS-CoV-2 M^{pro} . The IC₅₀ values obtained offer quantitative insights into the relative strengths of these compounds as potential M^{pro} inhibitors.

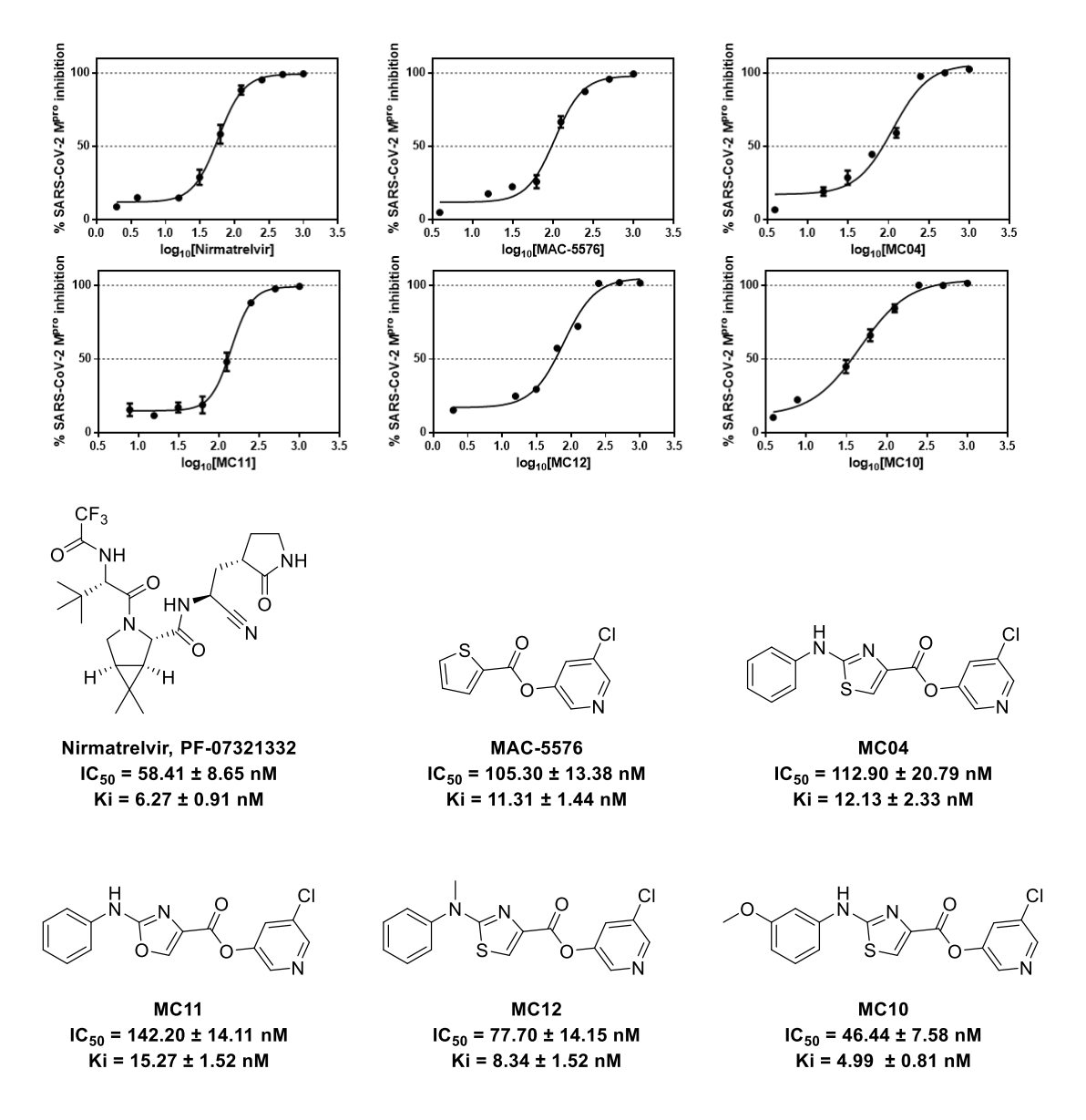


Figure 3.9 Results of the evaluation of SARS-CoV-2 M^{pro} IC₅₀ and structures of Nirmatrelvir, MAC-5576, MC04, MC11, MC12 and MC10.

Chapter 4. Biochemical Properties of the Compounds

4.1 Methods

4.1.1 Materials and equipment

All the tested compounds were synthesized as described in Chapter 3, and the SARS-CoV-2 M^{pro} was expressed in the laboratory. The SARS-CoV M^{pro} protein was purchased from Gene Company Limited, and all other reagents and solvents were used as received from commercial sources without further purification. The kinetics of enzymatic activity were measured using a TECAN Freedom EVO 100. The mass of the enzyme in complex with the tested compound was measured using a Bruker UltrafleXtreme MALDI-TOF-TOF Mass Spectrometer. The antiviral assays in Vero E6 cells were conducted by the collaborator lab at Wuxi AppTec.

4.1.2 Mass Spectroscopy of the covalent bond formation

The recombinant SARS-CoV-2 M^{pro} (approximately 20 µM) was mixed with 10 equivalents of inhibitor at room temperature, either without any preincubation or with a 40-minute preincubation. In addition, a control parallel experiment was performed on the enzyme alone without any inhibitor. Liquid Chromatography-Mass Spectrometry (LC-MS) was performed in positive-ion mode with Agilent 6540 QTOF mass spectrometer coupled with Agilent 1290 Infinity UHPLC system. Protein samples were injected into a C4 LC column (Waters) and eluted with a 14-min linear gradient from 95% solvent A:5% solvent B to 5% solvent A:95% solvent B, where solvent A is 0.1%

formic acid in milliQ water and solvent B is acetonitrile with 0.1% formic acid. Positive ion mode was used to acquire a m/z range of 100-2500. The molecular mass of the protein or protein-inhibitor complexes was obtained by deconvoluting by the MassHunter (Agilent) BioConfirm program. In this study, three replicates of each sample were analyzed [51].

4.1.3 Crystallization, data collection and structure determination

The protein-substrate complexes were generated by mixing SARS-CoV-2 M^{pro} with the compound MC12, respectively, in a 1:10 molar ratio overnight at 4 °C. The complexes were then concentrated to 10 mg/mL and crystallized by hanging drop vapor diffusion method at 20 °C. Plate-like crystal of SARS-CoV-2 M^{pro} in complex with MC12 was grown with well buffer containing 0.1 M Bis-Tris pH 5.8, 30% (v/v) polyethylene glycol (PEG) 3350 at a 1:2 ratio. The crystal was cryoprotected in the same crystallization buffer with an additional 10% DMSO.

The diffraction data were collected inhouse on a Rigaku MicroMax-007 HK generator with a Dectris PILATUS3 R 200K detector at 100 K. The diffraction images were processed with IMOSFLM [90], and data were reduced by AIMLESS [91] from the CCP4 suite [92]. The structure was determined by molecular replacement with Phaser [93] in CCP4 using the native SARS-CoV-2 M^{pro} structure (PDB ID: 7K3T) [94] as a search model. The output model was subsequently subjected to iterative cycles of manual

adjustment with Coot [95] and refinement with REFMAC [96]. The inhibitors were built according to the omit map along with the refinement cycle.

4.1.4 Dilution assay

Dilution experiments for SARS-CoV-2 M^{pro} were conducted by adjusting the compound concentrations from 1000 nM (approximately 10-fold the IC50) to 50 nM (approximately 10-fold the IC₅₀), as described in the references [97, 98]. MC12 and Nirmatrelvir at 1000 nM were incubated with the recombinant SARS-CoV-2 M^{pro} (to a final concentration of 800 nM) for 10 minutes in enzymatic buffer to ensure complete inhibition. The reaction solution (5 μL) was then diluted 20-fold with enzymatic reaction buffer (93 μL, 50 mM Tris-HCl, pH 7.5, 1 mM EDTA) containing a fluorogenic substrate (10 μL) to achieve a final inhibitor concentration of 50 nM. Recovery of enzyme activity was measured immediately using a multifunctional microplate reader for 10 minutes with filters for excitation at 320 nm and emission at 405 nm.

4.1.5 Time-dependent assay

The time-dependent inhibition of MC12 against SARS-CoV-2 M^{pro} was conducted similarly to the SARS-CoV-2 M^{pro} inhibition assay. The fluorogenic peptide MCA-AVLQ\SGFR-Lys(DNP)-Lys-NH₂ was purchased from GL Biochem in Shanghai. The fluorogenic peptide was resuspended in DMSO to serve as the substrate. The final concentration of the protease was prepared to be 100 nM in the enzymatic reaction

buffer (50 mM Tris-HCl, pH 7.5, 1 mM EDTA) in a 96-well plate. The recombinant SARS-CoV-2 M^{pro} was preincubated with different concentrations of MC12 or DMSO in the enzymatic reaction buffer at 37°C for 0, 10, 20, 30, and 60 minutes. At each time point, the FRET-based substrate was added to each well, after which the concentration of the substrate in each well was 20 μ M. Then, fluorescence was continuously measured on a plate reader for 5 minutes. For calculations, a 100% active enzyme was assumed. All experiments were performed in triplicate.

4.1.6 SARS-CoV and SARS-CoV-2 M^{pro} Enzymatic assays

The fluorogenic peptide MCA-AVLQ↓SGFR-Lys(DNP)-Lys-NH₂ was purchased from GL Biochem (Shanghai). The fluorogenic peptide was resuspended in DMSO to serve as a substrate. A final concentration of the protease at 100 nM was prepared in the enzymatic reaction buffer (50 mM Tris-HCl, pH 7.5, 1 mM EDTA) in a 96-well plate. After incubating the main protease with the tested compounds for 10 minutes, the FRET-based substrate was added to each well, resulting in a final substrate concentration of 20 μM in each well. Subsequently, fluorescence was continuously measured on a plate reader for 5 minutes. For calculations, a 100% active enzyme was assumed. All experiments were performed in triplicate.

4.1.7 Cytotoxic assay

The HFF-1 cell line was taken as an example. The normal human cell line HFF-1 (ATCC SCRC-1041) was cultured in a medium following ATCC recommendations. All cultured cell lines were maintained in a humidified incubator at 37°C and 5% CO₂. Initially, the cell lines were seeded in a 96-well plate at a density of 5 × 10³ cells/well. After incubation for 1 day, the cells were treated with media containing different concentrations of the compounds. Following drug treatment for 24 hours, the culture medium was replaced with an MTT solution (1 mg/mL) (Invitrogen) and incubated at 37°C for 4 hours. After incubation, the MTT solution was replaced with dimethyl

sulfoxide (DMSO), and the absorbance at 570 nm was measured with a reference wavelength at 650 nm. Cell viability was determined by dividing the absorbance of treated cells by the average absorbance of untreated cells. The CC₅₀ values of the compounds (with a 95% confidence interval) were analyzed using GraphPad Prism software (Version 8.0). All experiments were performed in triplicate.

4.1.8 Antiviral assay

Antiviral assay was conducted by the collaborator biosafety level 3 (BSL-3) lab of WuXi AppTec (HongKong) Limited. Vero E6 cells were provided by the Wuhan Institute of Virology and maintained in Dulbecco's Modified Eagle Medium (DMEM, Gibco#C11995500BT) supplemented with 10% fetal bovine serum (FBS) and 1% penicillin-streptomycin (PS). DMEM supplemented with 2% FBS and 1% PS was used as the assay medium. The SARS-CoV-2 βCoV/Wuhan/WIV04/2019 strain was provided by the Wuhan Institute of Virology, Chinese Academy of Sciences. The preservation number is CSTR: 16533.06. IVCAS 6.7512.

Vero E6 cells were seeded at a density of 1×10^4 cells per well in a black 96-well plate and incubated at 37°C and 5% CO₂ overnight. The next day, the supernatant was replaced with medium containing serially diluted compounds (6 points, 3-fold dilutions, in duplicate wells) and 2 μ M CP-100356. Cells were then infected with the SARS-CoV-2 β CoV/Wuhan/WIV04/2019 strain at a multiplicity of infection (MOI) of 0.005. The

final concentration of DMSO in the cell culture was 0.5%. The resulting cultures were incubated at 37°C and 5% CO₂ for an additional 4 days until virus infection in the virus control (cells infected with the virus, without compound treatment) displays significant CPE. The cell control (without virus infection or compound treatment) and virus control (with virus infection, without compound treatment) were tested in parallel. The CPE was measured using CellTiter Glo, following the manual of the manufacturer. The antiviral activity of compounds was calculated based on the protection of the virus-induced CPE at each concentration, normalized by the virus control.

The cytotoxicity of compounds was assessed under the same conditions but without virus infection, in parallel. Cell viability was measured using CellTiter Glo, following the manual of the manufacturer.

The antiviral activity and cytotoxicity of compounds were expressed as % Inhibition and % Viability, respectively, and calculated using the formulas below:

Inhibition (%) = $(Raw\ data\ _{CPD}$ - $Average\ _{VC})$ / $(Average\ _{CC}$ - $Average\ _{VC})*100$ Viability (%) = $(Raw\ data\ _{CPD}$ - $Average\ _{MC})$ / $(Average\ _{CC}$ - $Average\ _{MC})*100$ Where:

Raw data CPD is the values of the sample-treated wells.

Average v_C is the average value of virus control.

Average cc is the average value of cell control.

 EC_{50} and CC_{50} values were calculated using GraphPad Prism software (Version 8.0) with the equation log(inhibitor) vs. response with variable slope.

4.2 Mechanistic studies of the target compounds against SASR-CoV-2 Mpro

4.2.1 X-ray crystal structure of SARS-CoV-2 M^{pro} in complex with MC12

To elucidate the mechanism of inhibition of SARS-CoV-2 M^{pro} by MC compounds, the crystal structure of the M^{pro}-inhibitor complex was determined. Figure 4.1A depicts compound MC12 bound in the substrate-binding pocket of SARS-CoV-2 M^{pro} and the specific interactions. The crystal structure showed that MC12 formed a covalent bound to Cys145. The π - π stacking interactions of the thiazole ring with His41 and His164 are crucial for the stabilization of the complex. Meanwhile, the N atom of the thiazole of MC12 engage in hydrogen bonding with the main chain of His164. Additionally, the terminal phenyl group of MC12 engages in hydrophobic interactions with Met165 and Met49, which further stabilize its binding. Figure 4.1B indicated that the binding mode of MC12 within the SARS-CoV-2 M^{pro} complex structure exhibits similarities to that of MAC-5576 in the SARS-CoV M^{pro} complex, as previously reported. However, the primary distinctions are observed in the interactions of the terminal phenyl ring of MC12 with Met165 and Met49.

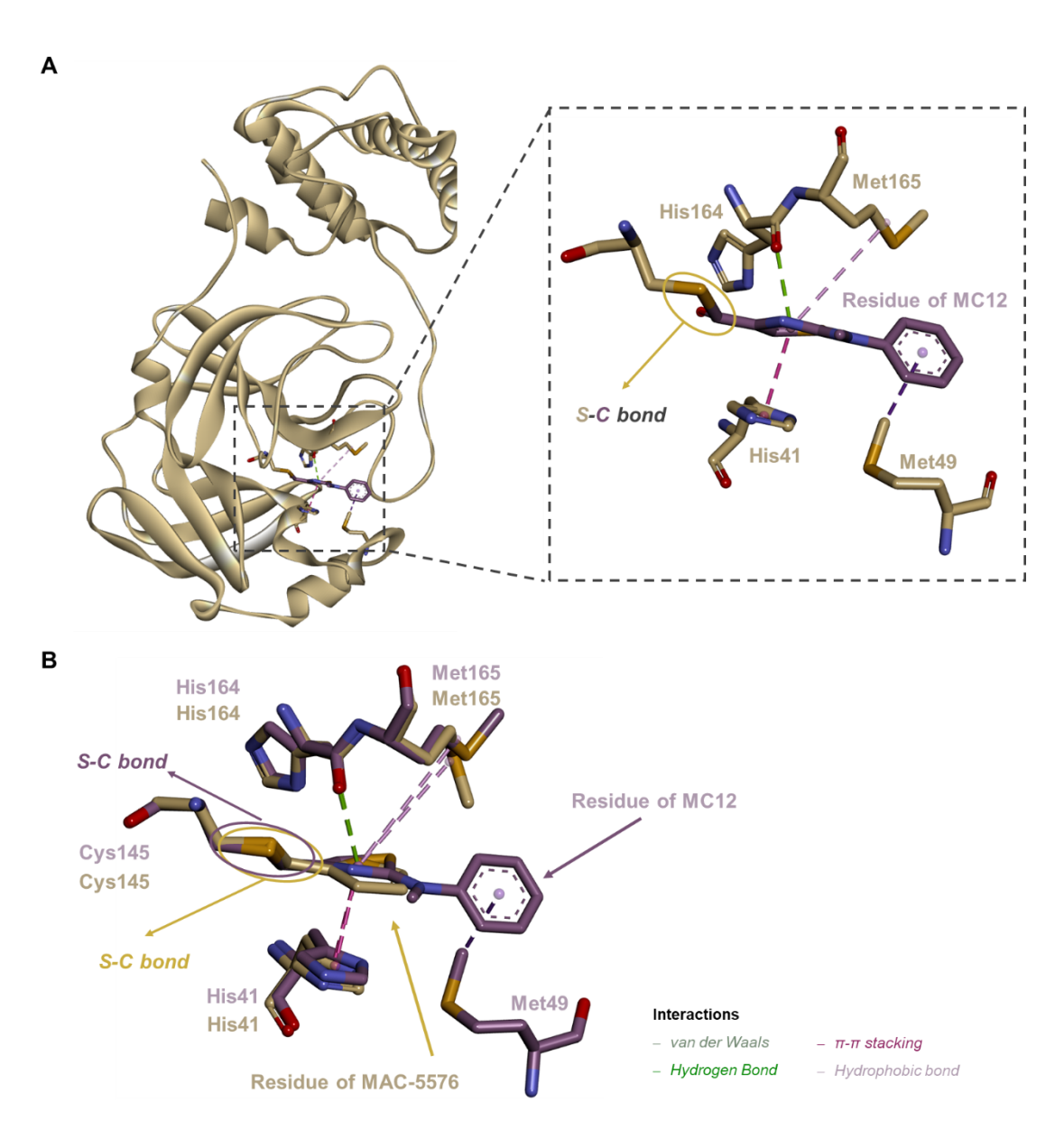


Figure 4.1 A) X-ray crystal structure of MC12 binding to SARS-CoV-2 M^{pro} (PDB ID 9M2V) and B) Comparison of the binding mode of MC12 with MAC-5576 (PDB ID 7JT0). Carbons of MC12 and MAC-5575 are shown as purple and yellow, respectively.

4.2.2 Mass Spectrometry of MC04-SASR-CoV-2 M^{pro} complex formation

Mass Spectrometry was employed to elucidate the inhibitory mechanism of the designed compounds against SARS-CoV-2 M^{pro} (details in section 4.1.2). Figure 4.2A presents the mass spectrum of the wild-type SARS-CoV-2 M^{pro} without any inhibitor, showing a molecular ion peak at 33,795.37 Da, corresponding to its mass of the purified enzyme plus a proton (33,794 ± 1 Da). Figures 4.2B and 4.2C illustrate the ion peak changes following treatment of the purified SARS-CoV-2 Mpro with MC04 over a period of 0 to 40 minutes. In Figure 4.2B, the emergence of a new set of ion peaks signifies the initial interaction of SARS-CoV-2 M^{pro} with MC04, with a new molecular ion peak observed at 33,997.38 Da. Figure 4.2B indicated that the molecular ion peak of new forming complex, when the mass of the purified SARS-CoV-2 M^{pro} was subtracted, yielded an anticipated difference of approximately 202 Da. After a 40minute incubation with MC04, as shown in Figure 4.2C, the intensity of these new ion peaks increased, while the peaks corresponding to the untreated SARS-CoV-2 M^{pro} diminished compared to those in Figure 4.2B. This finding from the mass spectral analysis substantiated the hypothesis that the designed compounds bind covalently to SARS-CoV-2 M^{pro}. This detailed mass spectrometry analysis confirms the covalent binding mechanism of MC04 to SARS-CoV-2 M^{pro} as indicated by the appearance and intensification of the new ion peaks, which correspond to the enzyme-inhibitor

complex. The decrease in the original enzyme peaks over time implies a progressive formation of this complex.

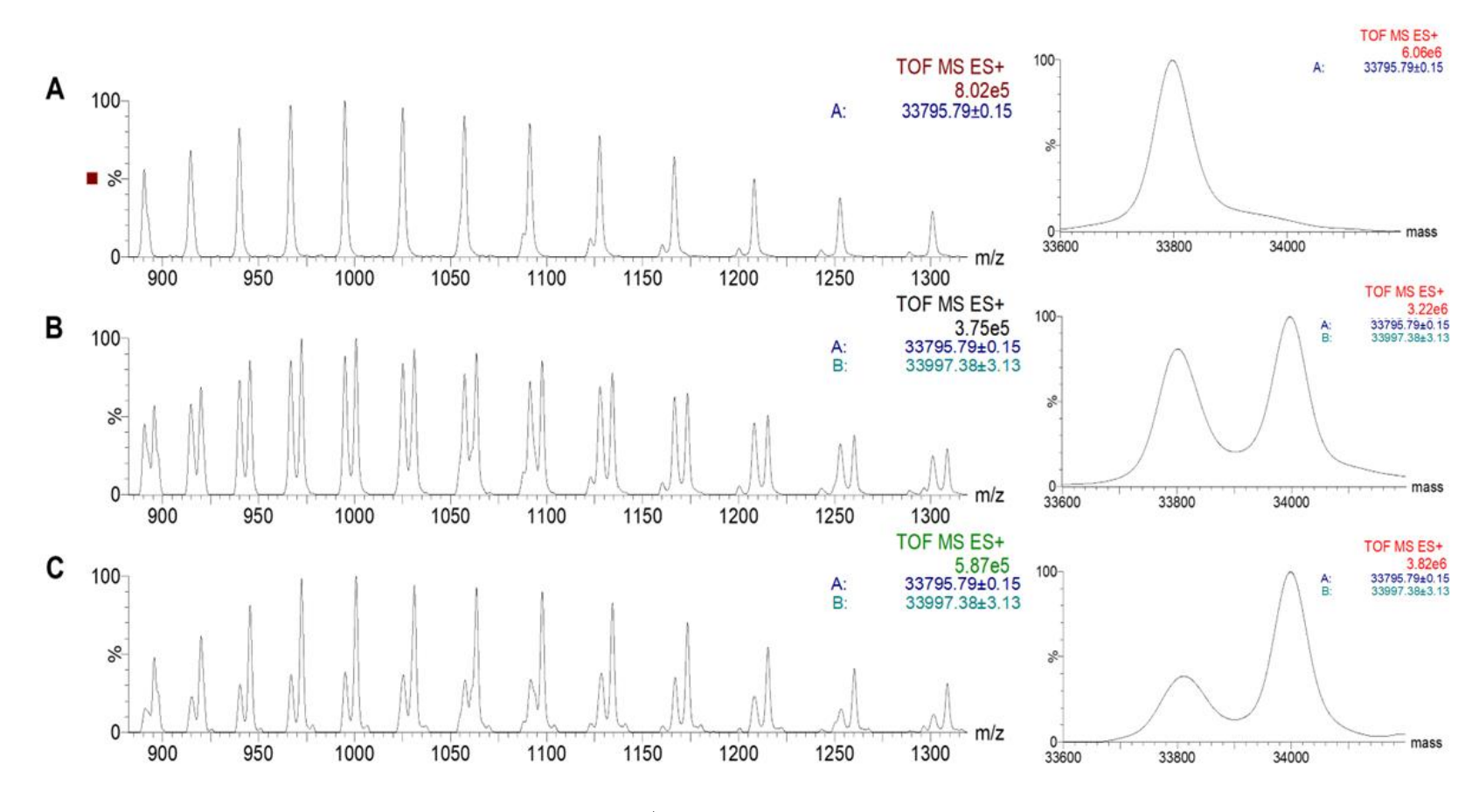


Figure 4.2 A) Mass spectrum of wild type SARS-CoV-2 M^{pro} (M⁺ = 33 795.37 Da), B) and C) Mass spectra of the complex of M^{pro} and MC04 (M⁺ = 33 997.38 Da) with different incubation time (B: without incubation; C: with 40-min incubation).

The proposed mechanism involves the deprotonation of Cys145 in the catalytic site by His41, generating a sulfur anion (the enzyme minus a proton: 33,793 Da = 33,794-1 Da). This anion then attacks the carbonyl carbon of MC04, resulting in the release of the 3-chloropyridin-5-yl group (the fragment weight of 2-(phenylamino)thiazole-4-carbonyl: 203 Da, calculated as 331 Da minus 128 Da for the departing group). Ultimately, a thioester covalent complex is formed, with the molecular weight of the thioester product calculated as 33,996 Da (33,793 Da + 203 Da) (Figure 4.3). The molecular ion peak observed in the mass spectrum is consistent with the molecular weight of the thioester product plus the mass of a proton: 33,997 Da (33,796 Da + 1 Da).

The enzyme minus a proton: 33,793 Da = 33,794 Da - 1 Da

The fragment weight of 2-(phenylamino)thiazole-4-carbonyl: 203 Da = 331 Da - 128 Da for the departing group

The molecular weight of the thioester product plus the mass of a proton: 33,997 Da (33,793 Da + 203 Da + 1 Da)

Figure 4.3 Mechanism of inhibition of SARS-CoV-2 M^{pro} by MC04.

4.2.3 Dilution assay of MC12 against SARS-CoV-2 Mpro

A reversible covalent inhibitor is a molecule that can form a covalent bond with the target, slowing the reaction rate, but without permanently altering the target [99]. The findings in section 4.2.1 and 4.2.2 established that the interaction between the tested compounds and SARS-CoV-2 M^{pro} is covalent. To further delineate the covalent binding characteristics of MC12 with SARS-CoV-2 M^{pro}, a dilution assay was conducted in accordance with the methodologies outlined in references [97, 98]. In this assay (additional details in section 4.1.4), Nirmatrelvir served as a positive control, known to be a reversible covalent inhibitor as references [97, 98]. The dilution of the SARS-CoV-2 M^{pro}-MC12 complex from a concentration of 1000 nM to 50 nM using the enzymatic buffer resulted in the resurgence of enzymatic activity (Figure 4.4). The recovery of enzymatic activity upon dilution confirms the reversible nature of the covalent bond formed by MC12 with the protease. This outcome indicates that MC12, equipped with a pyridinyl ester as its warhead, operates as a reversible covalent inhibitor against SARS-CoV-2 M^{pro}.

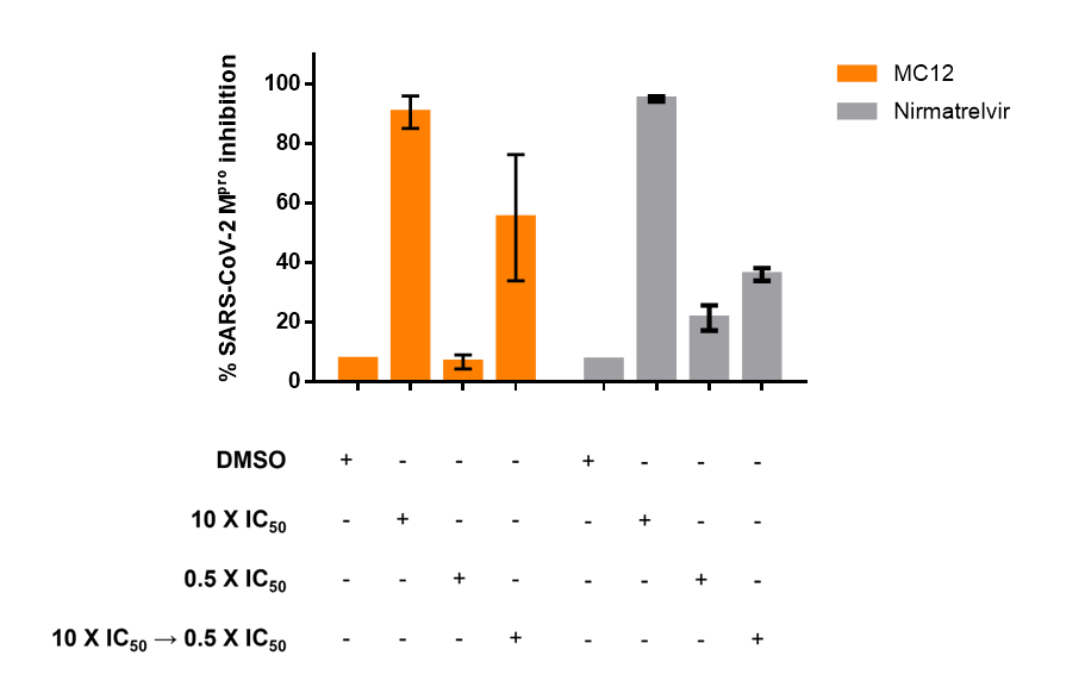


Figure 4.4 Dilution assay of MC12 and Nirmatrelvir against SARS-CoV-2 M^{pro} .

4.2.4 Time-dependent assay of MC12 against SARS-CoV-2 M^{pro}

In the time-dependent assay, SARS-CoV-2 M^{pro} was preincubated with MC12 at five distinct time points to assess the impact of preincubation duration on enzymatic activity. The results demonstrated a significant influence of preincubation time on enzymatic activity. Notably, MC12 exhibited more potent inhibition when preincubated without delay or for an earlier period of 10 minutes, as opposed to longer preincubation times. Specifically, the 10-minute preincubation marked the optimal condition for MC12 to exert its most pronounced inhibitory effect across all tested concentration points. An extension of the preincubation period beyond 10 minutes was correlated with a decline in the inhibitory activity of MC12 (Figure 4.5). This observation suggests that the interaction between MC12 and SARS-CoV-2 M^{pro} may be time-sensitive, with initial binding strength peaking at the 10-minute mark and gradually diminishing thereafter.

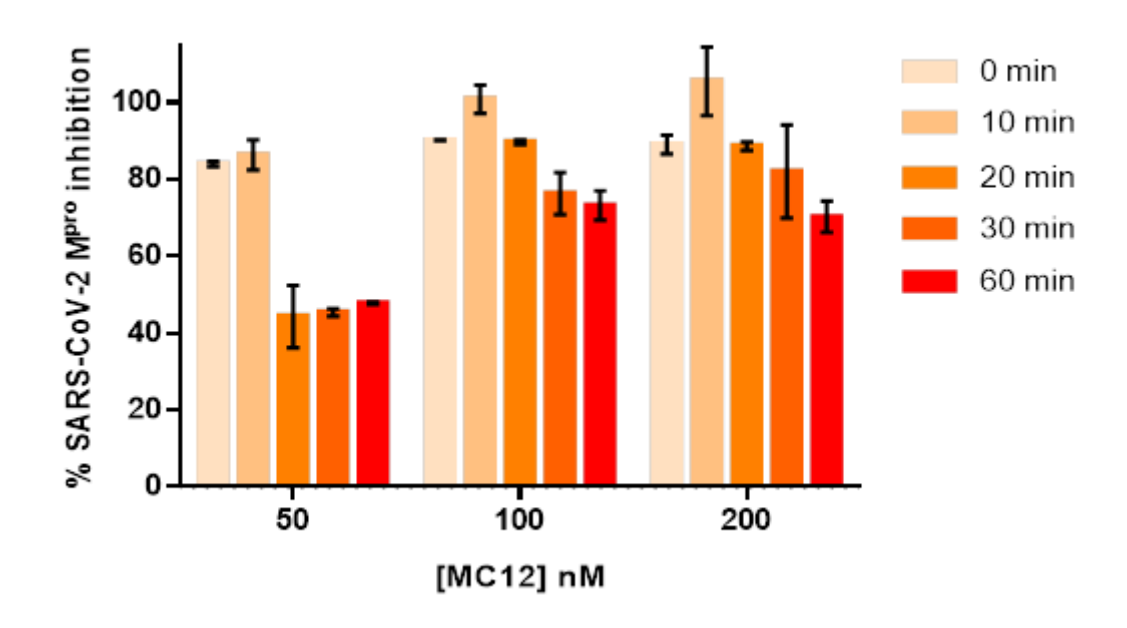
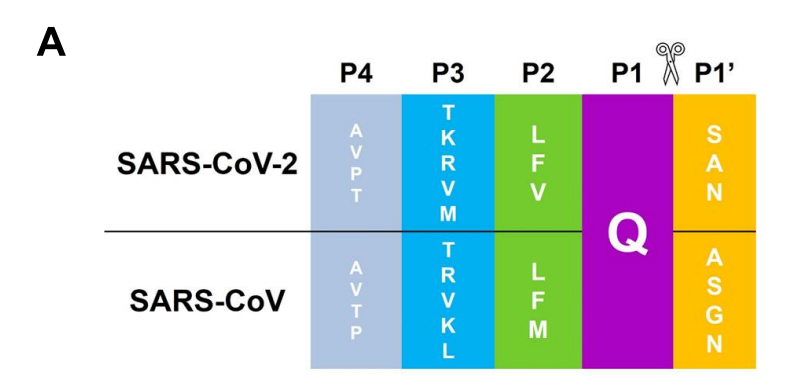


Figure 4.5 Time-dependent inhibition of SARS-CoV-2 M^{pro} by MC12

4.3 Inhibition against SARS-CoV Mpro

As detailed in section 1.3.1, the substrate residues spanning from P4 to P1' are pivotal for the recognition process by both main proteases of SARS-CoV-2 and SARS-CoV [18]. In assays targeting SARS-CoV M^{pro}, the FRET-based biosensor with the structure of MCA-AVLQ\SGFR-K(DNP)K as detailed in section 3.2 was also selected to quantify the enzymatic activity (Figure 4.6).



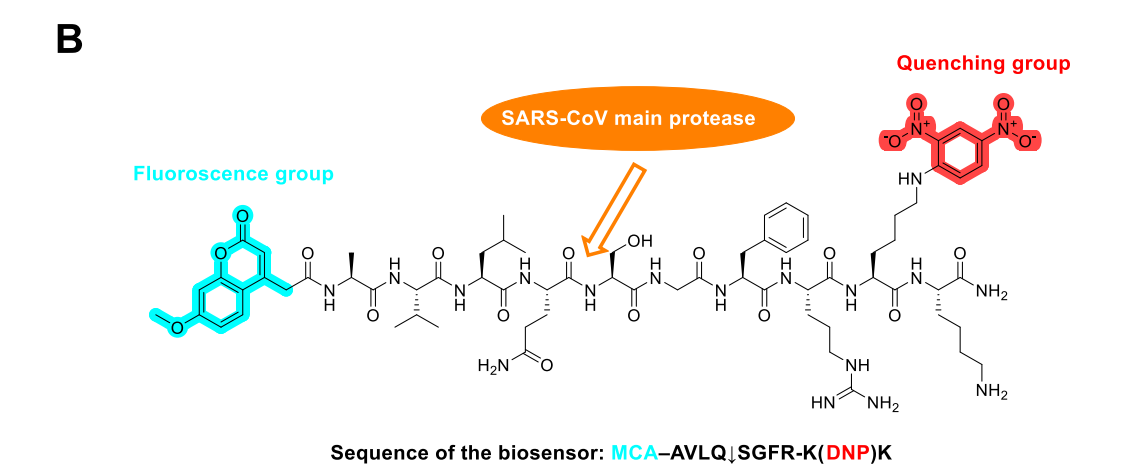


Figure 4.6 A) Peptide sequences covering residues P4 to P1' recognized by SARS-CoV-

2 M^{pro} and SARS-CoV M^{pro}; B) Chemical structure of the employed biosensor.

Table 4.1 demonstrates that at final concentrations of 100 nM for both SARS-CoV-2 M^{pro} and SARS-CoV M^{pro}, and a compound concentration of 200 nM, MC12 and Nirmatrelvir both exhibited inhibitory activities exceeding 80% against each of the main proteases. Notably, the inhibitory effect of MC12 was consistent against both SARS-CoV-2 M^{pro} and SARS-CoV M^{pro}. This result indicates that MC12 possesses potential as a dual inhibitor, effective against both SARS-CoV-2 M^{pro} and SARS-CoV M^{pro} in enzymatic assays.

Table 4.1 Results of inhibition of Nirmatrelvir and MC12 at 200 nM against SARS-CoV-2 M^{pro} and SARS-CoV M^{pro} .

Compounds -	% Inhibition at 200 nM against the enzyme	
	SARS-CoV-2 M ^{pro}	SARS-CoV M ^{pro}
MC12	98.27 ± 4.51 %	93.43 ± 4.49 %
Nirmatrelvir*	94.02 ± 5.55 %	$81.38 \pm 4.49 \%$

^{*}Nirmatrelvir as a positive control

4.4 Cytotoxic studies of the target compounds

The aforementioned results confirmed the efficacy of the designed compounds in inhibiting the enzymatic activity of SARS-CoV-2 M^{pro}. To advance the evaluation of these compounds as potential SARS-CoV-2 M^{pro} inhibitors, their safety profiles in mammalian cells were assessed. This step is crucial for establishing the therapeutic window of the compounds, ensuring that they exhibit significant antiviral activity without causing undue harm to host cells.

4.4.1 Results after 1 day treatment

The outcomes of the 3-(4,5-Dimethylthiazol-2-yl)-2,5-diphenyltetrazolium bromide (MTT) assays following a 1-day exposure to MC04 indicated no cytotoxic effects on HFF-1 and A549 cells, even at a concentration of 500 μ M. However, in HepG2 cells, MC04 displayed concentration-dependent cytotoxicity. The 50% cytotoxic concentration (CC₅₀) of MC04 for HepG2 cells was determined to be approximately 212 μ M in this assay, signifying a relatively low toxicity threshold for this cell line compared to the non-toxic concentrations observed in the other cell types tested (Figure 4.7).

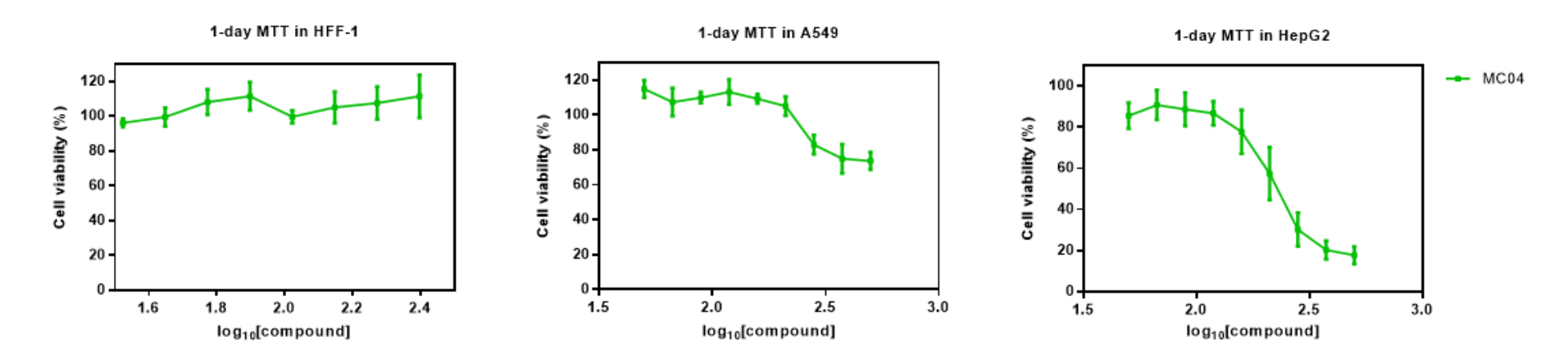


Figure 4.7 Results of MTT assays of MC04 for 1-day treatment to the cells.

4.4.2 Results after 2-day treatment

In the 2-day cytotoxicity assay, the PPAEC cell line was chosen as an alternative to the skin cell line HFF-1 to evaluate the designed compounds. The highest concentration of compounds tested was 200 μM. The findings indicated that all compounds displayed low or negligible cytotoxicity to HepG2 cells, in contrast to MAC-5576. The cytotoxicity to other cell types varied. For PPAEC cells, the CC₅₀ values for MC12, MC1210, and MC10 were within the range of 150 to 200 μM. In A549 cells, with the exception of MC1112, which had a CC₅₀ of approximately 100 μM, the remaining compounds did not exhibit cytotoxic effects (Figure 4.8).

These results underscore the low cytotoxicity of the designed compounds in mammalian cells, regardless of whether they were subjected to a 1-day or 2-day treatment period. This low cytotoxic profile is a promising indicator of the potential safety of compounds for further development as SARS-CoV-2 M^{pro} inhibitors.

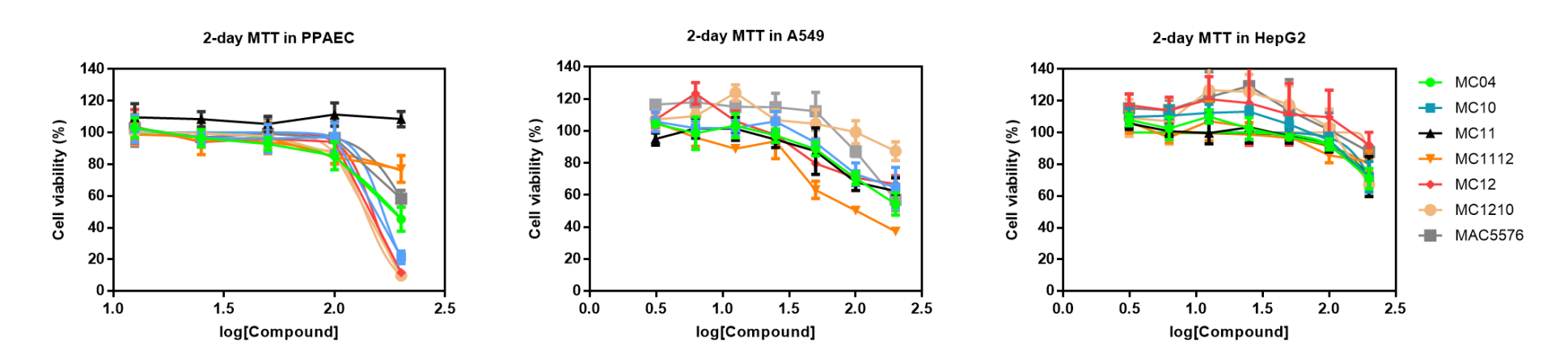


Figure 4.8 Results of MTT assays of MC04, MC10, MC11, MC1112, MC12, MC1210 and MAC-5576 for 2-day treatment to the cells.

4.5 Antiviral assays of the target compounds in Vero E6

4.5.1 Results of the antiviral assays

Antiviral assay was conducted by the collaborator biosafety level 3 (BSL-3) lab of WuXi AppTec (HongKong) Limited. The cytopathic effect (CPE)-based screening is a pivotal assay in drug discovery, utilized to identify compounds with potential antiviral activity against viruses such as Zika and coronaviruses. Virus-infected mammalian cells typically undergo morphological changes characteristic of CPE. In CPE-based assays, cells treated with the tested compounds are assessed against untreated cells, as well as positive (e.g., effective drugs) and negative controls (e.g., vehicle like DMSO). A reduction in CPE in the treated wells indicates potential antiviral compounds [100]. In the CPE experiment (further details can be found in section 4.1.8), the *in vitro* antiviral effects of compounds against the wild-type virus of SARS-CoV-2 were evaluated, with Nirmatrelvir as a positive control. At a concentration of 100 µM, MC04 showed notable antiviral activity, achieving approximately 40% inhibition of the wild type of SARS-CoV-2 virus, which was superior to the other compounds tested (Figure 4.9). Although the EC₅₀ (Half-maximal effective concentration) value of MC04 is projected to be approximately 100 µM, its performance suggests it has potential as a lead compound for further refinement. Additionally, MC04 did not exhibit significant cytotoxicity to Vero E6 cells within the tested concentration range, which is a crucial factor for its consideration as a safe and viable antiviral lead candidate (Table 4.2).

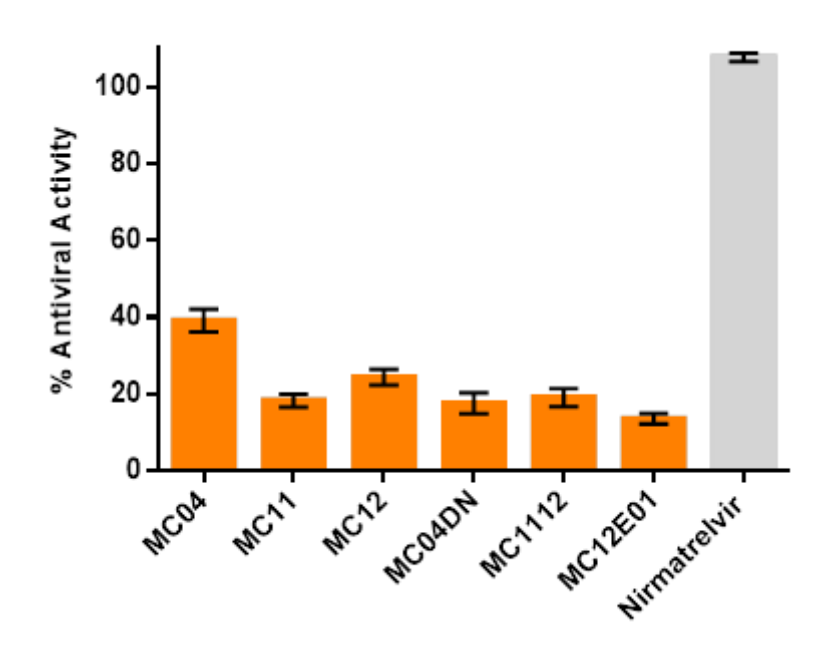


Figure 4.9 Antiviral activities against SARS-CoV-2 β CoV/Wuhan/WIV04/2019 in Vero E6 cells of the selected compounds at 100 μ M.

Table 4.2 Evaluation of cytotoxicity in Vero E6 cells of the selected compounds.

Compounds	CC50 values (µM)	
MC04	> 100	
MC11	73.78	
MC12	41.77	
MC04DN	46.97	
MC1112	> 100	
MC12E01	33.49	
Nirmatrelvir*	> 10	

^{*}Nirmatrelvir as a positive control

^{*}CC50: Median cytotoxic concentration

4.5.2 Discussion on the antiviral results

The confirmed mechanism of inhibition from the mechanistic studies provides a plausible explanation for the observed outcomes in the antiviral assay for the selected compounds. Although the bond formed between the compounds and the Cys145 residue of SARS-CoV-2 M^{pro} is covalent, its reversible nature suggests it can be hydrolyzed. Mechanistic studies have indicated that following the hydrolysis of the thioester bond formed between MC12 and SARS-CoV-2 M^{pro}, the enzymatic activity is restored. This reactivation of the main protease could potentially enable it to carry out its autoproteolysis function, which is essential for completing viral replication within the host cell. As shown in Figure 4.10, the alignment of cocrystal structures of MC12 and Nirmatrelvir revealed that, unlike Nirmatrelvir, MC12 lacks groups extending into the S1 or S3 subsites after the release of the pyridinyl ring. This difference may contribute to the variation in antiviral activity between Nirmatrelvir and MC12 observed. Further optimization may involve the introduction of a moiety to compensate for the loss of pyridine-3-ol or the exploration of alternative warheads to enhance binding affinity. In addition, the observed low antiviral activity could be attributed to the poor solubility of the compounds, which results in limited dissolution in the aqueous phase and consequently reduced cellular uptake. To address this, the future structural optimization should aim to improve the solubility of the compound in aqueous phase, thereby increasing intracellular concentrations to effectively inhibit viral replication.

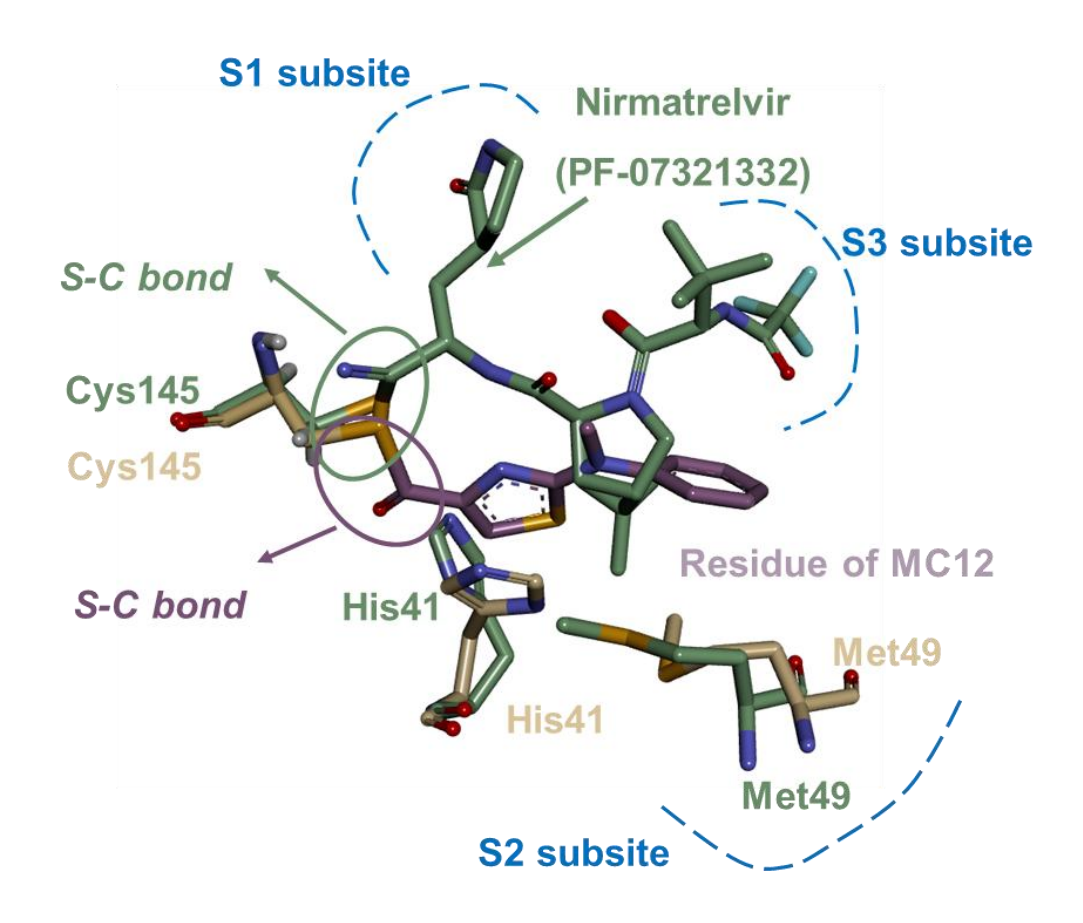


Figure 4.10 Comparison of the binding mode of MC12 with Nirmatrelvir (PDB ID 8DZ2). Carbons of MC12 and Nirmatrelvir are shown as purple and green, respectively.

Chapter 5. Further Optimization on the Structure of Compounds

5.1 Methods

5.1.1 Materials and equipment

All tested compounds were synthesized in the laboratory. The fluorogenic peptide substrate was purchased from GL Biochem (Shanghai). The kinetics of enzymatic activity were measured using TECAN Freedom EVO 100. IC₅₀ values were calculated using GraphPad Prism software (Version 8.0) with the equation log(inhibitor) vs. response with variable slope, where the R^2 values were as follows: 0.9430 for Nirmatrelvir, 0.9507 for MC12, and 0.9339 for MC04BP01. The molecular docking pose was conducted with Discovery Studio 2016 64-bit. MarvinSketch 6.1.0 was used to draw the structure of MC04BP01 for molecular docking. Molegro Virtual Docker (MVD) was used for the calculation of molecular docking. The assays of enzymatic inhibition, time-dependent assays, and molecular docking modes of MC04BP01 were conducted using similar procedures to those of MC04 and MC12 as described in Chapter 4.

5.1.2 Chemistry

Procedures for the chemical synthesis of MC04BP01

5-Chloropyridin-3-yl 2-(((1H-benzo[d][1,2,3]triazol-1-yl)methyl)(benzyl)amino)thia zole-4-carboxylate (MC04BP01)

1-Benzylthiourea (2.00 g, 13.16 mmol) was taken in a round-bottom flask and charged with methanol (45 mL), stirred for 10 minutes, and then methyl bromopyruvate (2.27 g, 12.61 mmol) was slowly added. The reaction solution was heated to 90 °C for 4 hours. Reaction completion was monitored by TLC. After the reaction was complete, the mixture was poured onto ice with vigorous stirring. The resulting solid was collected and washed with H₂O to yield a pale-yellow solid, methyl 2-(benzylamino)thiazole-4-carboxylate, with a yield of 1.59 g (70%) [78].

Methyl 2-(benzylamino)thiazole-4-carboxylate (0.45 g, 9.70 mmol) was added to *N,N*-Dimethylformamide (DMF) (10 mL) at 0 °C, and then sodium hydride (0.065 g, 9.70 mmol) was added to the solution. After 5 minutes of stirring, 1-chloromethyl-1*H*-benzotriazole (0.27 g, 9.70 mmol) was added to the reaction mixture. The reaction solution was then warmed to room temperature and stirred for 1 hour. After the reaction was complete, the reaction solution was added to water, and a solid formed. The resulting solid was collected by filtration. The crude product was collected and washed with water to afford the white solid, Methyl 2-(((1*H*-benzo[*d*][1,2,3]triazol-1-yl)methyl)(benzyl)amino)thiazole-4-carboxylate, with a yield of 1.27 g (80%).

Methyl 2-(((1H-benzo[d][1,2,3]triazol-1-yl)methyl)(benzyl)amino)thiazole-4-carboxy late (1.0 g, 9.70 mmol) was added to a mixture of methanol and 1 M aqueous NaOH (v/v = 1:3, 10 mL) at 0 °C and then warmed to reflux. After 2 hours of stirring, the

reaction solution was cooled to room temperature, and a solid formed. The resulting solid was collected by filtration. The collected solid was dissolved in water, and the pH was adjusted to approximately 3 with 1 N HCl. The crude product was collected and washed with water to afford the pale-yellow solid, 2-(phenylamino)thiazole-4-carboxylic acid, with a yield of 0.65 g (80%).

To a solution of 2-(((1*H*-benzo[*d*][1,2,3]triazol-1-yl)methyl)(benzyl)amino)thiazole-4carboxylic acid (20.0 mg, 0.091 mmol) in N,N-Dimethylformamide (DMF) (10 mL) at 0 °C, 3-Chloro-5-hydroxypyridine (11.7 mg, 0.091 mmol), N,N-Diisopropylethylamine (DIPEA, 11.7 mg, 0.091 mmol), 1-Hydroxybenzotriazole (HOBt, 11.7 mg, 0.087 mmol), and N,N'-Diisopropylcarbodiimide (DIC, 12.2 mg, 0.097 mmol) were added. The resulting solution was stirred overnight, allowing it to warm slowly to room temperature. The reaction mixture was then quenched with water, and a solid formed. The resulting solid was collected by filtration to yield a yellow crude solid product. Purification of the crude product by flash chromatography on silica gel (Dichloromethane: Ethyl acetate = 20:1) afforded 5-chloropyridin-3-yl 2-(((1Hbenzo[d][1,2,3]triazol-1-yl)methyl)(benzyl)amino)thiazole-4-carboxylate (MC04BP01) as a white solid, with a yield of 21 mg (0.063 mmol, 53%). H NMR (600 MHz, DMSO- d_6) δ 8.64 (d, J = 2.1 Hz, 1H), 8.60 (d, J = 2.3 Hz, 1H), 8.27 (d, J = 8.4Hz, 1H), 8.14 (s, 1H), 8.13 (s, 1H), 8.06 (d, J = 8.3 Hz, 1H), 7.55 - 7.51 (m, 1H), 7.43 -7.40 (m, 1H), 7.30 (d, J = 6.7 Hz, 1H), 7.29 (d, J = 5.5 Hz, 1H), 7.27 (d, J = 7.0 Hz,

1H), 7.20 (d, J = 6.5 Hz, 2H), 6.61 (s, 2H), 4.93 (s, 2H). HRMS (ESI) m/z 477.0897 [M + H]⁺; 499.0712 [M + Na]⁺.

Procedures for the chemical synthesis of BP0101

N-((1H-benzo[d][1,2,3]triazol-1-yl)methyl)-N-benzyl-4-(pyridin-3-yl)thiazol-2-amine (BP0101)

1-Benzylthiourea (2.00 g, 13.16 mmol) was taken in a round-bottom flask and charged with methanol (45 mL), stirred for 10 minutes, and then 3-(2-chloroacetyl)pyridine (2.27 g, 12.61 mmol) was slowly added. The reaction solution was heated to 80 °C for 12 hours. Reaction completion was monitored by TLC. After the reaction was complete, the mixture was poured onto ice with vigorous stirring. The resulting solid was collected and washed with H₂O to yield a pale-yellow solid, *N*-benzyl-4-(pyridin-3-yl)thiazol-2-amine, with a yield of 1.59 g (70%) [78].

N-benzyl-4-(pyridin-3-yl)thiazol-2-amine (0.45 g, 9.70 mmol) was added to *N*,*N*-Dimethylformamide (DMF) (10 mL) at 0 °C, and then sodium hydride (0.06 g, 9.70 mmol) was added to the solution. After stirring for 5 minutes, 1-chloromethyl-1*H*-benzotriazole (0.27 g, 9.70 mmol) was added to the reaction mixture. The reaction solution was then warmed to room temperature and stirred for 1 hour. After the reaction was complete, the reaction solution was added to water, and a solid formed. The resulting solid was collected by filtration. The crude product was collected and washed

with water to afford the white solid. Purification of the crude product by flash chromatography on silica gel (Dichloromethane: Ethyl acetate = 20:1) afforded *N*-((1*H*-benzo[d][1,2,3]triazol-1-yl)methyl)-*N*-benzyl-4-(pyridin-3-yl)thiazol-2-amine (BP0101) as a white solid, with a yield of 1.27 g (7.76 mmol, 80%). ¹H NMR (600 MHz, DMSO- d_6) δ 9.13 (d, J = 1.5 Hz, 1H), 8.52 (dd, J = 4.8, 1.6 Hz, 1H), 8.24 (dt, J = 8.0, 1.9 Hz, 1H), 8.11 (d, J = 8.4 Hz, 1H), 8.06 (d, J = 8.3 Hz, 1H), 7.57 - 7.53 (m, 1H), 7.51 (s, 1H), 7.46 (m, J = 8.0, 4.8, 0.8 Hz, 1H), 7.42 - 7.39 (m, 1H), 7.30 (d, J = 7.5 Hz, 1H), 7.29 (d, J = 3.0 Hz, 1H), 7.27 (s, 1H), 7.25 (s, 2H), 6.69 (s, 2H), 4.90 (s, 2H). HRMS (ESI) m/z 399.1383 [M + H] $^+$; 421.1205 [M + Na] $^+$.

Procedures for the chemical synthesis of AD01

2-(Methyl(phenyl)amino)-N-((S)-1-oxo-3-((S)-2-oxopyrrolidin-3-yl)propan-2-yl)thia zole-4-carboxamide (AD01)

Methyl (*S*)-2-((*tert*-butoxycarbonyl)amino)-3-((*S*)-2-oxopyrrolidin-3-yl)propanoate (1.0 g. 3.5 mmol) was dissolved in 10 mL of Dichloromethane, and then HCl (9 mL, 4 M in dioxane) was added. The reaction mixture was stirred at ambient temperature for 12 hours, and the mixture was concentrated under reduced pressure to obtain a white solid, methyl (*S*)-2-amino-3-((*S*)-2-oxopyrrolidin-3-yl)propanoate, which could be used for the following step without further purification.

To a solution of 2-(methyl(phenyl)amino)thiazole-4-carboxylic acid (0.23 g, 1 mmol) in acetonitrile, N,N,N',N'-tetramethylchloroformamidinium hexafluorophosphate (TCFH, 0.27 g, 1 mmol), N-methylimidazole (NMI, 0.32 g, 4 mmol), and methyl (S)-2-amino-3-((S)-2-oxopyrrolidin-3-yl)propanoate (0.18 g, 1 mmol) were added, followed by stirring at room temperature. After stirring overnight, the reaction solution was cooled to room temperature, and a solid formed. The solution was washed with a saturated aqueous NaCl solution and extracted with Ethyl acetate (10 mL \times 3). The organic phase was dried with sodium sulfate and concentrated under reduced pressure to afford the pale-yellow solid, methyl (S)-2-(2-(methyl(phenyl)amino)thiazole-4-carboxamido)-3-((S)-2-oxopyrrolidin-3-yl)propanoate, with a yield of 0.27 g (T0%).

To a solution of Methyl (S)-2-(2-(methyl(phenyl)amino)thiazole-4-carboxamido)-3-((S)-2-oxopyrrolidin-3-yl)propanoate (0.2 g, 0.5 mmol) in dry THF, NaBH₄ (0.18 g, 10 mmol) was added portionwise at 0 °C, and CH₃OH (2 mL) was added dropwise. The reaction mixture was stirred at room temperature for 3 hours. The completion of the reaction was confirmed by TLC, and then the reaction was quenched with a saturated NH₄Cl solution (20 mL). The reaction mixture was extracted with Ethyl acetate (50 mL × 3), and the organic layers were washed with saturated NH₄Cl solution (50 mL × 3) and brine (50 mL × 3). The organic phase was dried over Na₂SO₄ and concentrated under reduced pressure to afford the white solid, N-((S)-1-hydroxy-3-((S)-2-

oxopyrrolidin-3-yl)propan-2-yl)-2-(methyl(phenyl)amino)thiazole-4-carboxamide, with a yield of 0.16 g (90%).

To a solution of N-((S)-1-hydroxy-3-((S)-2-oxopyrrolidin-3-yl)propan-2-yl)-2-(methyl(phenyl)amino)thiazole-4-carboxamide (0.1 g, 0.25 mmol) n Dichloromethane, Dess-Martin periodinane (DMP, 0.11 g, 0.25 mmol) was added slowly, and the reaction mixture was stirred at room temperature. When the reactant was consumed, as confirmed by TLC, the reaction was quenched with a saturated Na₂S₂O₃ solution (50 mL × 3), saturated NaHCO₃ solution (50 mL × 3), and brine (50 mL × 3). The organic phase was dried over Na₂SO₄ and concentrated, and the residue was purified by flash column chromatography (Dichloromethane: CH₃OH, 20:1 v/v) to afford the pure product 2-(methyl(phenyl)amino)-N-((S)-1-oxo-3-((S)-2-oxopyrrolidin-3-yl)propan-2-yl)thiazole-4-carboxamide as white solid, with a yield of 0.07 g (0.19 mmol, 76%). ¹H NMR (600 MHz, DMSO-S) δ 9.65 - 9.27 (m, 1H), 8.89 - 8.19 (m, 1H), 8.15 - 7.66 (m, 1H), 7.53 - 7.44 (m, 4H), 7.40 - 7.27 (m, 2H), 4.53 - 4.04 (m, 1H), 3.61 - 3.47 (m, 3H), 3.31 - 3.06 (m, 2H), 2.38 - 2.10 (m, 2H), 2.08 - 1.77 (m, 1H), 1.74 - 1.54 (m, 1H), 1.53 - 1.29 (m, 1H), 1.27 - 0.79 (m, 1H). HRMS (ESI) m/z 411.0481[M + K]⁺.

Procedures for the chemical synthesis of AD02

Tert-butyl (4-(((S)-4-methyl-1-oxo-1-(((S)-1-oxo-3-((S)-2-oxopyrrolidin-3-yl)propan-2-yl)amino)pentan-2-yl)carbamoyl)thiazol-2-yl)carbamate (AD02)

To a solution of 2-((*tert*-butoxycarbonyl)amino)thiazole-4-carboxylic acid (0.24 g, 1.0 mmol) in *N*,*N*-Dimethylformamide (DMF) (10 mL) at 0 °C, methyl *L*-leucinate (0.14 g, 1.0 mmol), *N*,*N*-Diisopropylethylamine (DIPEA, 0.129 g, 1.0 mmol), and 2-(7-Azabenzotriazol-1-yl)-*N*,*N*,*N'*,*N'*-tetramethyluronium hexafluorophosphate (HATU, 0.38 g, 1.0 mmol) were added. The resulting solution was stirred overnight at room temperature. Then, the reaction mixture was quenched with water, and the resulting solid was collected by filtration to obtain a yellow crude solid, methyl (2-((*tert*-butoxycarbonyl)amino)thiazole-4-carbonyl)-*L*-leucinate, with a yield of 0.25 g (70%).

Methyl (2-((*tert*-butoxycarbonyl)amino)thiazole-4-carbonyl)-L-leucinate (0.19 g, 0.5 mmol) was added to a mixture of THF and 0.8 M aqueous LiOH (v/v = 1:3, 10 mL) at 0 °C and then warmed to room temperature. After stirring for 2 hours, the reaction solution was cooled to 0 °C, and the pH was adjusted to approximately 4 with 1 N HCl. The crude product was collected and washed with water to afford the pale-yellow solid, (2-((*tert*-butoxycarbonyl)amino)thiazole-4-carbonyl)-L-leucine, with a yield of 0.14 g (80%).

Methyl (S)-2-((tert-butoxycarbonyl)amino)-3-((S)-2-oxopyrrolidin-3-yl)propanoate (1.0 g. 3.5 mmol) was dissolved in 10 mL of Dichloromethane, and then HCl (9 mL, 4 M in dioxane) was added. The reaction mixture was stirred at ambient temperature for 12 hours and concentrated under reduced pressure to obtain a white solid, methyl (S)-

2-amino-3-((*S*)-2-oxopyrrolidin-3-yl)propanoate, which could be used for the following step without purification.

To a solution of (2-((tert-butoxycarbonyl)amino)thiazole-4-carbonyl)-L-leucine (0.35) 1 mmol) in acetonitrile, N,N,N',N'-tetramethylchloroformamidinium hexafluorophosphate (TCFH, 0.27 g, 1 mmol), N-methylimidazole (NMI, 0.32 g, 4 mmol), and Methyl (S)-2-amino-3-((S)-2-oxopyrrolidin-3-yl)propanoate (0.18 g, 1 mmol) were added, followed by stirring at room temperature. After stirring overnight, the reaction solution was cooled to room temperature, and a solid formed. The solution was washed with a saturated aqueous NaCl solution and extracted with Ethyl acetate (10 mL × 3). The organic phase was dried with sodium sulfate and concentrated under reduced pressure afford the pale-yellow solid, methyl (S)-2-((S)-2-(2-((tertbutoxycarbonyl)amino)thiazole-4-carboxamido)-4-methylpentanamido)-3-((S)-2-oxopyrrolidin-3-yl)propanoate, with a yield of 0.36 g, (0.7 mmol, 70%).

To a solution of methyl (*S*)-2-((*S*)-2-(2-((*tert*-butoxycarbonyl)amino)thiazole-4-carboxamido)-4-methylpentanamido)-3-((*S*)-2-oxopyrrolidin-3-yl)propanoate (0.26 g, 0.5 mmol) in dry THF, NaBH₄ (0.18 g, 10 mmol) was added portionwise at 0 °C, and CH₃OH (2 mL) was added dropwise. The reaction mixture was stirred at room temperature for 3 hours. The completion of the reaction was confirmed by TLC, and then the reaction was quenched with a saturated NH₄Cl solution (20 mL). The reaction

mixture was extracted with Ethyl acetate (50 mL × 3), and the organic layers were washed with saturated NH₄Cl solution (50 mL × 3) and brine (50 mL × 3). The organic phase was dried over Na₂SO₄ and concentrated under reduced pressure to afford the white solid, *tert*-butyl (4-(((S)-1-(((S)-1-hydroxy-3-((S)-2-oxopyrrolidin-3-yl)propan-2-yl)amino)-4-methyl-1-oxopentan-2-yl)carbamoyl)thiazol-2-yl)carbamate, with a yield of 0.22 g (90%).

To a solution of tert-butyl (4-(((S)-1-(((S)-1-hydroxy-3-((S)-2-oxopyrrolidin-3yl)propan-2-yl)amino)-4-methyl-1-oxopentan-2-yl)carbamoyl)thiazol-2-yl)carbamate (0.13 g, 0.25 mmol) in Dichloromethane, Dess-Martin periodinane (DMP, 0.11 g, 0.25 mmol) was added slowly, and the reaction mixture was stirred at room temperature. When the reactant was consumed, as confirmed by TLC, the reaction was quenched with a saturated Na₂S₂O₃ solution (50 mL × 3), saturated NaHCO₃ solution (50 mL × 3), and brine (50 mL × 3). The organic phase was dried over Na₂SO₄ and concentrated, and the residue was purified by flash column chromatography (Dichloromethane: CH₃OH, 20:1 v/v) to afford the white pure solid product, tert-butyl (4-(((S)-4-methyl-1-oxo-1-(((S)-1-oxo-3-((S)-2-oxopyrrolidin-3-yl)propan-2-yl)amino)pentan-2-yl)carbamoyl)thiazol-2-yl)carbamate, with a yield of 0.09 g, (0.18 mmol, 70%). ¹H NMR (600 MHz, DMSO-d₆) δ 11.69 (s, 1H), 7.77 (s, 1H), 7.68 - 7.60 (m, 1H), 4.79 - 4.46 (m, 1H), 3.20 - 3.06 (m, 2H), 2.32 - 2.15 (m, 1H), 2.12 - 1.96 (m, 1H), 1.92 - 1.74 (m, 1H), 1.69 - 1.55 (m, 2H), 1.54 - 1.50 (m, 2H), 1.49 - 1.46 (m, 9H), 1.40 - 1.30 (m, 1H), 1.26 - 1.18 (m, 2H), 0.94 - 0.88 (m, 6H), 0.85 - 0.73 (m, 2H). HRMS (ESI) m/z 496.2280 [M + H]⁺.

Procedures for the chemical synthesis of AD04

(S)-4-methyl-N-((S)-1-oxo-3-((S)-2-oxopyrrolidin-3-yl)propan-2-yl)-2-((S)-3-phenyl-2-(2-(thiophen-2-yl)acetamido)propanamido)pentanamide (AD04)

To a solution of 2-(thiophen-2-yl)acetic acid (0.28 g, 2.0 mmol) in *N,N*-Dimethylformamide (DMF) (10 mL) at 0 °C, methyl *L*-phenylalaninate (0.36 g, 2.0 mmol), *N,N*-Diisopropylethylamine (DIPEA, 0.25 g, 2.0 mmol), and 2-(7-Azabenzotriazol-1-yl)-*N,N,N',N'*-tetramethyluronium hexafluorophosphate (HATU, 0.76 g, 2.0 mmol) were added. The resulting solution was stirred overnight at room temperature. Then, the reaction mixture was quenched with water, and the resulting solid was collected by filtration to obtain a yellow crude solid, methyl (2-(thiophen-2-yl)acetyl)-*L*-phenylalaninate, with a yield of 0.24 g (70%).

Methyl (2-(thiophen-2-yl)acetyl)-L-phenylalaninate (0.2 g, 1.2 mmol) was added to a mixture of THF and 0.8 M aqueous LiOH (v/v = 1:3, 10 mL) at 0 °C and then warmed to room temperature. After stirring for 2 hours, the reaction solution was cooled to 0 °C, and the pH was adjusted to about 4 with 1 N HCl. The crude product was collected and washed with water to afford the pale-yellow solid, (2-(thiophen-2-yl)acetyl)-L-phenylalanine, with a yield of 0.15 g (80%).

To a solution of (2-(thiophen-2-yl)acetyl)-*L*-phenylalanine (0.29 g, 1 mmol) in *N,N*-Dimethylformamide (DMF) (10 mL) at 0 °C, methyl L-leucine (0.14 g, 1.0 mmol), *N,N*-Diisopropylethylamine (DIPEA, 0.129 g, 1.0 mmol), and 2-(7-Azabenzotriazol-1-yl)-*N,N,N',N'*-tetramethyluronium hexafluorophosphate (HATU, 0.38 g, 1.0 mmol) were added. The resulting solution was stirred overnight at room temperature. Then, the reaction mixture was quenched with water, and the resulting solid was collected by filtration to obtain a yellow crude solid, methyl (2-(thiophen-2-yl)acetyl)-*L*-phenylalanyl-*L*-leucinate, with a yield of 0.32 g (70%).

Methyl (2-(thiophen-2-yl)acetyl)-L-phenylalanyl-L-leucinate (0.21 g, 0.5 mmol) was added to a mixture of THF and 0.8 M aqueous LiOH (v/v = 1:3, 10 mL) at 0 °C and then warmed to room temperature. After stirring for 2 hours, the reaction solution was cooled to 0 °C, and the pH was adjusted to about 4 with 1 N HCl. The crude product was collected and washed with water to afford the pale-yellow solid, (2-(thiophen-2-yl)acetyl)-L-phenylalanyl-L-leucine, with a yield of 0.17 g (80%).

Methyl (S)-2-((tert-butoxycarbonyl)amino)-3-((S)-2-oxopyrrolidin-3-yl)propanoate (1.0 g. 3.5 mmol) was dissolved in 10 mL of Dichloromethane, and then HCl (9 mL, 4 M in dioxane) was added. The reaction mixture was stirred at ambient temperature for 12 hours and concentrated under reduced pressure to obtain a white solid, methyl (S)-

2-amino-3-((S)-2-oxopyrrolidin-3-yl)propanoate, which could be used for the following step without further purification.

To a solution of (2-(thiophen-2-yl)acetyl)-L-phenylalanyl-L-leucine (0.2 g, 0.5 mmol) in acetonitrile, N,N,N',N'-tetramethylchloroformamidinium hexafluorophosphate (TCFH, 0.14 g, 0.5 mmol), N-methylimidazole (NMI, 0.16 g, 2 mmol), and Methyl (S)-2-amino-3-((S)-2-oxopyrrolidin-3-yl)propanoate (0.09 g, 0.5 mmol) were added, followed by stirring at room temperature. After stirring overnight, the reaction solution was cooled to room temperature, and a solid formed. The solution was washed with a saturated aqueous NaCl solution and extracted with Ethyl acetate (10 mL \times 3). The organic phase was dried with sodium sulfate and concentrated under reduced pressure to afford the pale-yellow solid, methyl (S)-2-((S)-4-methyl-2-((S)-3-phenyl-2-(2-(thiophen-2-yl)acetamido)propanamido)pentanamido)-3-((S)-2-oxopyrrolidin-3-yl)propanoate, with a yield of 0.21 g (70%).

To a solution of methyl (*S*)-2-((*S*)-4-methyl-2-((*S*)-3-phenyl-2-(2-(thiophen-2-yl)acetamido)propanamido)pentanamido)-3-((*S*)-2-oxopyrrolidin-3-yl)propanoate (0.2 g, 0.5 mmol) in dry THF, NaBH₄ (0.18 g, 10 mmol) was added portionwise at 0 °C, and CH₃OH (2 mL) was added dropwise. The reaction mixture was stirred at room temperature for 3 hours. The completion of the reaction was confirmed by TLC, and then the reaction was quenched with a saturated NH₄Cl solution (20 mL). The reaction

mixture was extracted with Ethyl acetate (50 mL × 3), and the organic layers were washed with saturated NH₄Cl solution (50 mL × 3) and brine (50 mL × 3). The organic phase was dried over Na₂SO₄ and concentrated under reduced pressure to afford the crude (*S*)-*N*-((*S*)-1-hydroxy-3-((*S*)-2-oxopyrrolidin-3-yl)propan-2-yl)-4-methyl-2-((*S*)-3-phenyl-2-(2-(thiophen-2-yl)acetamido)propanamido)pentanamide, with a yield of 0.24 g (90%).

To a solution of (S)-N-((S)-1-hydroxy-3-((S)-2-oxopyrrolidin-3-yl)propan-2-yl)-3phenyl-2-(2-(thiophen-2-yl)acetamido)propanamide (0.13 0.25 mmol) g, Dichloromethane, Dess-Martin periodinane (DMP, 0.11 g, 0.25 mmol) was added slowly, and the reaction mixture was stirred at room temperature. When the reactant was consumed, as confirmed by TLC, the reaction was quenched with a saturated $Na_2S_2O_3$ solution (50 mL × 3), saturated NaHCO₃ solution (50 mL × 3), and brine (50 mL × 3). The organic phase was dried over Na₂SO₄ and concentrated, then the residue was purified by flash column chromatography (Dichloromethane: CH₃OH, 20:1 v/v) to afford the white pure solid product, (S)-4-methyl-N-((S)-1-oxo-3-((S)-2-oxopyrrolidin-3-yl)propan-2-yl)-2-((S)-3-phenyl-2-(2-(thiophen-2-yl)acetamido)propanamido)pentanamide, with a yield of 0.09 g (0.17 mmol, 70%). ¹H NMR (600 MHz, DMSO- d_6) δ 13.15 (s, 1H), 8.57 - 8.10 (m, 1H), 8.04 - 7.69 (m, 3H), 7.68 - 7.40 (m, 2H), 7.39 - 7.26 (m, 1H), 7.26 - 7.22 (m, 2H), 7.22 - 7.14 (m, 2H), 6.95 - 6.70 (m, 1H), 5.05 - 4.34 (m, 1H), 4.32 - 3.81 (m, 1H), 3.78 - 3.46 (m, 1H), 3.25 - 2.87 (m, 2H), 2.86 - 2.54 (m, 1H),

2.39 - 2.02 (m, 1H), 2.01 - 1.66 (m, 1H), 1.65 - 1.29 (m, 3H), 1.27 - 0.94 (m, 2H), 0.87 - 0.44 (m, 6H). HRMS (ESI) *m*/z 541.2488 [M + H]⁺.

Procedures for the chemical synthesis of AD05

2-Chloro-N-((S)-4-methyl-1-oxo-1-(((S)-1-oxo-3-((S)-2-oxopyrrolidin-3-yl)propan-2-yl)amino)pentan-2-yl)thiazole-4-carboxamide (AD05)

To a solution of 2-chlorothiazole-4-carboxylic acid (0.16 g, 1 mmol) in N,N-Dimethylformamide (DMF) (10 mL) at 0 °C, methyl L-leucine (0.14 g, 1.0 mmol), N,N-Diisopropylethylamine (DIPEA, 0.129 g, 1.0 mmol), and 2-(7-Azabenzotriazol-1-yl)-N,N,N',N'-tetramethyluronium hexafluorophosphate (HATU, 0.38 g, 1.0 mmol) were added. The resulting solution was stirred overnight at room temperature. Then, the reaction mixture was quenched with water, and the resulting solid was collected by filtration to obtain a yellow crude solid, methyl (2-chlorothiazole-4-carbonyl)-L-leucinate, with a yield of 0.19 g (70%).

Methyl (2-chlorothiazole-4-carbonyl)- L-leucinate (0.15 g, 0.5 mmol) was added to a mixture of THF and 0.8 M aqueous LiOH (v/v = 1:3, 10 mL) at 0 °C and then warmed to room temperature. After stirring for 2 hours, the reaction solution was cooled to 0 °C, and the pH was adjusted to about 4 with 1 N HCl. The crude product was collected and washed with water to afford the pale-yellow solid, (2-chlorothiazole-4-carbonyl)- L-leucine, with a yield of 0.22 g (80%).

Methyl (*S*)-2-((*tert*-butoxycarbonyl)amino)-3-((*S*)-2-oxopyrrolidin-3-yl)propanoate (1.0 g. 3.5 mmol) was dissolved in 10 mL of Dichloromethane, and then HCl (9 mL, 4 M in dioxane) was added. The reaction mixture was stirred at ambient temperature for 12 hours and concentrated under reduced pressure to obtain a white solid, methyl (*S*)-2-amino-3-((*S*)-2-oxopyrrolidin-3-yl)propanoate, which could be used for the following step without further purification.

To a solution of (2-chlorothiazole-4-carbonyl)-L-leucine (0.14 g, 0.5 mmol) in acetonitrile, N,N,N',N'-tetramethylchloroformamidinium hexafluorophosphate (TCFH, 0.14 g, 0.5 mmol), N-methylimidazole (NMI, 0.16 g, 2 mmol), and Methyl (S)-2-amino-3-((S)-2-oxopyrrolidin-3-yl)propanoate (0.09 g, 0.5 mmol) were added, followed by stirring at room temperature. After stirring overnight, the reaction solution was cooled to room temperature, and a solid formed. The solution was washed with a saturated aqueous NaCl solution and extracted with Ethyl acetate ($10 \text{ mL} \times 3$). The organic phase was dried with sodium sulfate and concentrated under reduced pressure to afford the pale-yellow solid, methyl (S)-2-((S)-2-(2-chlorothiazole-4-carboxamido)-4-methyl-pentanamido)-3-((S)-2-oxopyrrolidin-3-yl)propanoate, with a yield of 0.31 g (T0%).

To a solution of methyl (S)-2-((S)-2-(2-chlorothiazole-4-carboxamido)-4-methyl-pentanamido)-3-((S)-2-oxopyrrolidin-3-yl)propanoate (0.22 g, 0.5 mmol) in dry THF,

NaBH₄ (0.18 g, 10 mmol) was added portionwise at 0 °C, and CH₃OH (2 mL) was added dropwise. The reaction mixture was stirred at room temperature for 3 hours. The completion of the reaction was confirmed by TLC, and then the reaction was quenched with a saturated NH₄Cl solution (20 mL). The reaction mixture was extracted with Ethyl acetate (50 mL × 3), and the organic layers were washed with saturated NH₄Cl solution (50 mL × 3) and brine (50 mL × 3). The organic phase was dried over Na₂SO₄ and concentrated under reduced pressure to afford the crude 2-chloro-*N*-((*S*)-1-(((*S*)-1-hydroxy-3-((*S*)-2-oxopyrrolidin-3-yl)propan-2-yl)amino)-4-methyl-1-oxo-pentan-2-yl)thiazole-4-carboxamide, with a yield of 0.37 g (90%).

To a solution of 2-chloro-*N*-((*S*)-1-(((*S*)-1-hydroxy-3-((*S*)-2-oxopyrrolidin-3-yl) propan-2-yl)amino)-4-methyl-1-oxopentan-2-yl)thiazole-4-carboxamide, (0.11 g, 0.25 mmol) in Dichloromethane, Dess-Martin periodinane (DMP, 0.11 g, 0.25 mmol) was added slowly, and the reaction mixture was stirred at room temperature. When the reactant was consumed, as confirmed by TLC, the reaction was quenched with a saturated Na₂S₂O₃ solution (50 mL × 3), saturated NaHCO₃ solution (50 mL × 3), and brine (50 mL × 3). The organic phase was dried over Na₂SO₄ and concentrated, then the residue was purified by flash column chromatography (Dichloromethane: CH₃OH, 20:1 v/v) to afford the white pure solid product, *2-chloro-N*-((*S*)-4-methyl-1-oxo-1-(((*S*)-1-oxo-3-((*S*)-2-oxopyrrolidin-3-yl)propan-2-yl)amino)pentan-2-yl)thiazole-4-carboxamide, with a yield of 0.14 g (0.17 mmol, 70%). ¹H NMR (600 MHz, DMSO-

*d*₆) δ 8.35 - 8.24 (m, 1H), 8.23 - 8.02 (m, 1H), 7.77 - 7.39 (m, 1H), 5.77 (s, 1H), 4.82 - 4.11 (m, 2H), 3.20 - 2.91 (m, 2H), 2.34 - 1.95 (m, 2H), 1.94 - 1.69 (m, 1H), 1.68 - 1.60 (m, 1H), 1.58 - 1.44 (m, 2H), 1.39 - 1.17 (m, 2H), 0.90 - 0.84 (m, 6H). HRMS (ESI) *m*/z 415.1203 [M + H]⁺; 437.102 [M + Na]⁺, 453.0763 [M + K]⁺

Procedures for the chemical synthesis of AD06

2-Chloro-N-((S)-3-methyl-1-(((S)-4-methyl-1-oxo-1-(((S)-1-oxo-3-((S)-2-oxopyrolidin-3-yl)propan-2-yl)amino)pentan-2-yl)amino)-1-oxobutan-2-yl)thiazole-4-carboxamide (AD06)

To a solution of 2-chlorothiazole-4-carboxylic acid (0.33 g, 2.0 mmol) in N,N-Dimethylformamide (DMF) (10 mL) at 0 °C, methyl L-valinate (0.36 g, 2.0 mmol), N,N-Diisopropylethylamine (DIPEA, 0.25 g, 2.0 mmol), and 2-(7-Azabenzotriazol-1-yl)-N,N,N',N'-tetramethyluronium hexafluorophosphate (HATU, 0.76 g, 2.0 mmol) were added. The resulting solution was stirred overnight at room temperature. Then, the reaction mixture was quenched with water, and the resulting solid was collected by filtration to obtain a yellow crude solid, methyl (2-chlorothiazole-4-carbonyl)-L-valinate, with a yield of 0.38 g (70%).

Methyl (2-chlorothiazole-4-carbonyl)-L-valinate (0.27 g, 1.0 mmol) was added to a mixture of THF and 0.8 M aqueous LiOH (v/v = 1:3, 10 mL) at 0 °C and then warmed to room temperature. After stirring for 2 hours, the reaction solution was cooled to 0

°C, and the pH was adjusted to about 4 with 1 N HCl. The crude product was collected and washed with water to afford the pale-yellow solid, (2-chlorothiazole-4-carbonyl)-L-valine, with a yield of 0.21 g (80%).

To a solution of (2-chlorothiazole-4-carbonyl)-L-valine (0.27 g, 1 mmol) in N,N-Dimethylformamide (DMF) (10 mL) at 0 °C, methyl L-leucine (0.14 g, 1.0 mmol), N,N-Diisopropylethylamine (DIPEA, 0.129 g, 1.0 mmol), and 2-(7-Azabenzotriazol-1-yl)-N,N,N',N'-tetramethyluronium hexafluorophosphate (HATU, 0.38 g, 1.0 mmol) were added. The resulting solution was stirred overnight at room temperature. Then, the reaction mixture was quenched with water, and the resulting solid was collected by filtration to obtain a yellow crude solid, methyl (2-chlorothiazole-4-carbonyl)-L-valyl-L-leucinate, with a yield of 0.28 g (70%).

Methyl (2-chlorothiazole-4-carbonyl)-L-valyl-L-leucinate (0.18 g, 0.5 mmol) was added to a mixture of THF and 0.8 M aqueous LiOH (v/v = 1:3, 10 mL) at 0 °C and then warmed to room temperature. After stirring for 2 hours, the reaction solution was cooled to 0 °C, and the pH was adjusted to about 4 with 1 N HCl. The crude product was collected and washed with water to afford the pale-yellow solid, (2-chlorothiazole-4-carbonyl)-L-valyl-L-leucine, with a yield of 0.15 g (80%).

Methyl (S)-2-((tert-butoxycarbonyl)amino)-3-((S)-2-oxopyrrolidin-3-yl)propanoate (1.0 g. 3.5 mmol) was dissolved in 10 mL of Dichloromethane, and then HCl (9 mL, 4 M in dioxane) was added. The reaction mixture was stirred at ambient temperature for 12 hours and concentrated under reduced pressure to obtain a white solid, methyl (S)-2-amino-3-((S)-2-oxopyrrolidin-3-yl)propanoate, which could be used for the following step without further purification.

To a solution of (2-chlorothiazole-4-carbonyl)-L-valyl-L-leucine (0.19 g, 0.5 mmol) in acetonitrile, N,N,N',N'-tetramethylchloroformamidinium hexafluorophosphate (TCFH, 0.14 g, 0.5 mmol), N-methylimidazole (NMI, 0.16 g, 2 mmol), and Methyl (S)-2-amino-3-((S)-2-oxopyrrolidin-3-yl)propanoate (0.09 g, 0.5 mmol) were added, followed by stirring at room temperature. After stirring overnight, the reaction solution was cooled to room temperature, and a solid formed. The solution was washed with a saturated aqueous NaCl solution and extracted with Ethyl acetate (10 mL \times 3). The organic phase was dried with sodium sulfate and concentrated under reduced pressure to afford the pale-yellow solid, methyl (S)-2-((S)-2-((S)-2-(2-chlorothiazole-4-carboxamido)-3-methylbutanamido)-4-methylpentanamido)-3-((S)-2-oxopyrrolidin-3-yl)propanoate, with a yield of 0.19 g (70%).

To a solution of methyl (S)-2-((S)-2-((S)-2-(2-chlorothiazole-4-carboxamido)-3-methylbutanamido)-4-methylpentanamido)-3-((S)-2-oxopyrrolidin-3-yl)propanoate

(0.27 g, 0.5 mmol) in dry THF, NaBH₄ (0.18 g, 10 mmol) was added portionwise at 0 °C, and CH₃OH (2 mL) was added dropwise. The reaction mixture was stirred at room temperature for 3 hours. The completion of the reaction was confirmed by TLC, and then the reaction was quenched with a saturated NH₄Cl solution (20 mL). The reaction mixture was extracted with Ethyl acetate (50 mL × 3), and the organic layers were washed with saturated NH₄Cl solution (50 mL × 3) and brine (50 mL × 3). The organic phase was dried over Na₂SO₄ and concentrated under reduced pressure to afford the crude (*S*)-*N*-((*S*)-1-hydroxy-3-((*S*)-2-oxopyrrolidin-3-yl)propan-2-yl)-4-methyl-2-((*S*)-3-phenyl-2-(2-(thiophen-2-yl)acetamido)propanamido)pentanamide, with a yield of 0.23 g (90%).

To a solution of 2-chloro-N-((S)-1-(((S)-1-(((S)-1-hydroxy-3-((S)-2-oxopyrrolidin-3-yl)propan-2-yl)amino)-4-methyl-1-oxopentan-2-yl)amino)-3-methyl-1-oxobutan-2-yl)thiazole-4-carboxamide (0.13 g, 0.25 mmol) in Dichloromethane, Dess-Martin periodinane (DMP, 0.11 g, 0.25 mmol) was added slowly, and the reaction mixture was stirred at room temperature. When the reactant was consumed, as confirmed by TLC, the reaction was quenched with a saturated Na₂S₂O₃ solution (50 mL \times 3), saturated NaHCO₃ solution (50 mL \times 3), and brine (50 mL \times 3). The organic phase was dried over Na₂SO₄ and concentrated, then the residue was purified by flash column chromatography (Dichloromethane: CH₃OH, 20:1 v/v) to afford the white pure solid product, 2-chloro-N-((S)-3-methyl-1-(((S)-4-methyl-1-oxo-1-(((S)-1-oxo-3-((S)-2-oxo

pyrrolidin-3-yl)propan-2-yl)amino)pentan-2-yl)amino)-1-oxobutan-2-yl)thiazole-4-carboxamide, with a yield of 0.09 g (0.17 mmol, 70%). ¹H NMR (600 MHz, DMSO-d₆) δ 8.60 - 8.39 (m, 1H), 8.35 - 8.29 (m, 1H), 8.07 - 7.95 (m, 1H), 7.68 - 7.45 (m, 1H), 6.05 - 5.57 (m, 1H), 4.80 - 4.37 (m, 2H), 4.36 - 4.10 (m, 1H), 3.18 - 2.93 (m, 2H), 2.27 - 2.15 (m, 1H), 2.12 - 2.03 (m, 2H), 1.65 - 1.53 (m, 2H), 1.52 - 1.37 (m, 3H), 1.31 - 1.17 (m, 2H), 0.91 - 0.86 (m, 6H), 0.86 - 0.81 (m, 6H). HRMS (ESI) *m*/z 514.2899 [M + H]⁺; 536.1716 [M + Na]⁺.

 $2-Chloro-N-((S)-1-(((S)-1-(((S)-1-cyano-2-((S)-2-oxopyrrolidin-3-yl)ethyl)amino)-4-\\methyl-1-oxopentan-2-yl)amino)-3-methyl-1-oxobutan-2-yl)thiazole-4-carboxamide (AD06CN01)$

(*S*)-2-Amino-3-((*S*)-2-oxopyrrolidin-3-yl)propanenitrile hydrochloride was chosen to replace methyl (*S*)-2-amino-3-((*S*)-2-oxopyrrolidin-3-yl)propanoate. AD06CN01 was prepared by following a similar procedure to that used for AD06. White solid (34 mg, 0.068 mmol, 70%, $R_f = 0.33$, Dichloromethane: Methol = 20:1). ¹H NMR (600 MHz, DMSO- d_6) δ 8.96 - 8.78 (m, 1H), 8.61 - 8.35 (m, 1H), 8.34 - 8.27 (m, 1H), 8.08 - 7.95 (m, 1H), 7.76 - 7.70 (m, 1H), 5.00 - 4.89 (m, 1H), 4.41 - 4.34 (m, 1H), 4.34 - 4.20 (m, 1H), 3.19 - 3.04 (m, 2H), 2.39 - 2.21 (m, 1H), 2.18 - 2.08 (m, 2H), 2.07 - 2.02 (m, 1H), 1.80 - 1.63 (m, 2H), 1.55 - 1.26 (m, 3H), 0.90 - 0.83 (m, 12H). HRMS (ESI) m/z 511.18922 [M + H]⁺; 533.1716 [M + Na]⁺.

 $Tert-Butyl \ (4-(((S)-1-(((S)-1-cyano-2-((S)-2-oxopyrrolidin-3-yl)ethyl)amino)-1-oxo-3-phenylpropan-2-yl) carbamoyl) thiazol-2-yl) carbamate \ (CN01)$

(*S*)-2-Amino-3-((*S*)-2-oxopyrrolidin-3-yl)propanenitrile hydrochloride was chosen to replace methyl (*S*)-2-amino-3-((*S*)-2-oxopyrrolidin-3-yl)propanoate. *L*-Phenylalanine was chosen to replace methyl *L*-valinate. CN01 was prepared by following a similar procedure to that used for AD02. White solid (34 mg, 0.065 mmol, 70%, $R_f = 0.33$, Dichloromethane: Methol = 20:1). ¹H NMR (600 MHz, DMSO-*d*₆) δ 11.74 (s, 1H), 9.11 (d, J = 7.7 Hz, 1H), 7.79 - 7.72 (m, 3H), 7.28 - 7.24 (m, 2H), 7.22 - 7.20 (m, 1H), 7.19 - 7.17 (m, 2H), 4.98 - 4.93 (m, 1H), 4.74 - 4.70 (m, 1H), 3.16 - 3.11 (m, 2H), 3.10 - 3.02 (m, 2H), 2.32 - 2.26 (m, 1H), 2.14 - 2.08 (m, 2H), 1.79 (ddd, J = 13.5, 9.1, 7.0 Hz, 1H), 1.72 - 1.66 (m, 1H), 1.48 (s, 9H). HRMS (ESI) m/z 527.2072 [M + H]⁺; 549.1909 [M + Na]⁺.

 $Tert-Butyl \ (4-(((S)-1-(((S)-1-cyano-2-((S)-2-oxopyrrolidin-3-yl)ethyl)amino)-1-oxo-3-phenylpropan-2-yl) carbamoyl) oxazol-2-yl) carbamate \ (CN02)$

2-((*Tert*-butoxycarbonyl)amino)oxazole-4-carboxylic acid was chosen to replace 2-((*tert*-butoxycarbonyl)amino)thiazole-4-carboxylic acid. CN02 was prepared by following a similar procedure to that used for CN01. White solid (34 mg, 0.065 mmol, 70%, $R_f = 0.33$, Dichloromethane: Methol = 20:1). ¹H NMR (600 MHz, DMSO- d_6) δ 10.88 (s, 1H), 9.03 - 9.00 (m, 1H), 8.32 (s, 1H), 7.90 - 7.87 (m, 1H), 7.73 (s, 1H), 7.27 - 7.24 (m, 2H), 7.23 - 7.22 (m, 1H), 7.22 - 7.18 (m, 2H), 4.98 - 4.94 (m, 1H), 4.71 -

4.66 (m, 1H), 3.16 - 3.11 (m, 2H), 3.10 - 3.06 (m, 2H), 2.34 - 2.29 (m, 1H), 2.15 - 2.10 (m, 2H), 1.82 - 1.76 (m, 1H), 1.73 - 1.66 (m, 1H), 1.48 - 1.45 (m, 9H). HRMS (ESI) *m*/z 511.2305 [M + H]⁺; 533.2145 [M + Na]⁺.

N-((5-Chloropyridin-3-yl)methyl)-2-(2-(methyl(phenyl)amino)thiazol-4-yl)-2-oxo-acetamide (MC12D01)

The preparation of MC12D01 took one of the intermediates of MC12, methyl 2-(methyl(phenyl)amino)thiazole-4-carboxylate, as the starting material. To a solution of methyl 2-(methyl(phenyl)amino)thiazole-4-carboxylate (0.5 g, 1.0 mmol) in dry THF, NaBH₄ (0.36 g, 10 mmol) was added portionwise at 0 °C, and CH₃OH (2 mL) was added dropwise. The reaction mixture was stirred at room temperature for 3 hours. The completion of the reaction was confirmed by TLC, and then the reaction was quenched with a saturated NH₄Cl solution (20 mL). The reaction mixture was extracted with Ethyl acetate (50 mL × 3), and the organic layers were washed with saturated NH₄Cl solution (50 mL × 3) and brine (50 mL × 3). The organic phase was dried over Na₂SO₄ and concentrated under reduced pressure to afford the crude (2-(methyl(phenyl)-amino)thiazol-4-yl)methanol, with a yield of 0.46 g (90%).

To a solution of (2-(methyl(phenyl)amino)thiazol-4-yl)methanol (0.14 g, 0.25 mmol) in Dichloromethane, Dess-Martin periodinane (DMP, 0.11 g, 0.25 mmol) was added slowly, and the reaction mixture was stirred at room temperature. When the reactant

was consumed, as confirmed by TLC, the reaction was quenched with a saturated Na₂S₂O₃ solution (50 mL × 3), saturated NaHCO₃ solution (50 mL × 3), and brine (50 mL × 3). The organic phase was dried over Na₂SO₄ and concentrated to afford the crude 2-(methyl(phenyl)amino)thiazole-4-carbaldehyde, with a yield of 0.13 g (90%).

Acetic acid (0.029 g, 0.50 mmol) and 3-chloro-5-(isocyanomethyl)pyridine (0.038 g, 0.25 mmol) were added to the solution of 2-(methyl(phenyl)amino)thiazole-4-carbaldehyde (0.14 g 0.25 mmol) in DCM (15 mL). The mixture was stirred at 20 °C for 24 h. The reaction was concentrated to afford the crude *N*-((5-chloropyridin-3-yl)methyl)-2-hydroxy-2-(2-(methyl(phenyl)amino)thiazol-4-yl)acetamide, with a yield of 0.36 g (90%).

To a solution of *N*-((5-chloropyridin-3-yl)methyl)-2-hydroxy-2-(2-(methyl(phenyl)-amino)thiazol-4-yl)acetamide (0.1 g, 0.25 mmol) in Dichloromethane, Dess-Martin periodinane (DMP, 0.11 g, 0.25 mmol) was added slowly, and the reaction mixture was stirred at room temperature. When the reactant was consumed, as confirmed by TLC, the reaction was quenched with a saturated Na₂S₂O₃ solution (50 mL × 3), saturated NaHCO₃ solution (50 mL × 3), and brine (50 mL × 3). The organic phase was dried over Na₂SO₄ and concentrated. Then the residue was purified by flash column chromatography (Dichloromethane: CH₃OH, 40:1 v/v) to afford the white pure solid product, *N*-((5-chloropyridin-3-yl)methyl)-2-(2-(methyl(phenyl)amino)thiazol-4-yl)-

2-oxoacetamide, with a yield of 0.07 g (0.17 mmol, 70%). ¹H NMR (600 MHz, DMSO- d_6) δ 9.46 (s, 1H), 8.55 (s, 2H), 8.18 (s, 1H), 7.87 (s, 1H), 7.50 (d, 4H), 7.38 - 7.34 (m, 1H), 4.47 (d, J = 6.1 Hz, 2H), 3.49 (s, 3H). HRMS (ESI) m/z 387.0685 [M + H]⁺; 409.0507 [M - H]⁻.

The NMR and mass spectra of the synthesized compounds are given in the A3 of Appendices.

5.1.3 Crystallization, data collection and structure determination

The protein-substrate complexes were generated by mixing SARS-CoV-2 M^{pro} with the AD05 and AD06, respectively, in a 1:10 molar ratio overnight at 4 °C. The complexes were then concentrated to 10 mg/mL and crystallized by hanging drop vapor diffusion method at 20 °C. Plate-like crystal of SARS-CoV-2 M^{pro} in complex with AD05 was grown with well buffer containing 0.1 M Bis-Tris pH 5.8, 30% (v/v) polyethylene glycol (PEG) 3350 at a 1:2 ratio. For the complex with AD06, plate-like crystal appeared in the crystallization condition comprised of 0.1 M Bis-Tris pH 6.5, 18% (v/v) PEG 3350 at a 1:2 ratio. The crystals were cryoprotected in the same crystallization buffer with an additional 10% DMSO.

The diffraction data were collected inhouse on a Rigaku MicroMax-007 HK generator with a Dectris PILATUS3 R 200K detector at 100 K. The diffraction images were

processed with IMOSFLM [90], and data were reduced by AIMLESS [91] from the CCP4 suite [92]. The structure was determined by molecular replacement with Phaser [93] in CCP4 using the native SARS-CoV-2 M^{pro} structure (PDB ID: 7K3T) [94] as a search model. The output model was subsequently subjected to iterative cycles of manual adjustment with Coot [95] and refinement with REFMAC [96]. The inhibitors were built according to the omit map along with the refinement cycle.

5.1.4 Antiviral assay

Antiviral assay was conducted by the collaborator biosafety level 3 (BSL-3) lab of WuXi AppTec (HongKong) Limited. Vero E6 cells were provided by the Wuhan Institute of Virology and maintained in Dulbecco's Modified Eagle Medium (DMEM, Gibco#C11995500BT) supplemented with 10% fetal bovine serum (FBS) and 1% penicillin-streptomycin (PS). DMEM supplemented with 2% FBS and 1% PS was used as the assay medium. The SARS-CoV-2 βCoV/Wuhan/WIV04/2019 strain was provided by the Wuhan Institute of Virology, Chinese Academy of Sciences. The preservation number is CSTR: 16533.06. IVCAS 6.7512.

Vero E6 cells were seeded at a density of 1×10^4 cells per well, in a black 96-well plate, and incubated at 37°C and 5 % CO₂ overnight. Next day, the supernatant was replaced with medium containing serially diluted compounds (8 points, 2 or 2.5-fold dilutions, in duplicate wells) and 2 μ M CP-100356, and incubated at 37°C and 5 % CO₂ for 1

hour. Cells were then infected with SARS-CoV-2 βCoV/βCoV/Wuhan/WIV04/2019 strain at a multiplicity of infection (MOI) of 0.01. At 1 h post infection, the inoculum was removed, and cells were washed three times and further incubated in an assay medium containing the serially diluted compounds and 2 μM CP-100356. The final concentration of DMSO in the cell culture was 0.5%. The resulting cultures were incubated at 37°C and 5 % CO₂ for an additional 3 days until virus infection in the virus control (cells infected with virus, without compound treatment) displays significant CPE. The cell control (without virus infection or compounds treatment) and virus control (with virus infection, without compounds treatment) were tested in parallel. The CPE was measured by CellTiter Glo following the manufacturer's manual. The antiviral activity of compounds was calculated based on the protection of the virus-induced CPE at each concentration normalized by the virus control.

The cytotoxicity of compounds was assessed under the same conditions but without virus infection, in parallel. Cell viability was measured using CellTiter Glo, following the manual of the manufacturer.

The antiviral activity and cytotoxicity of compounds were expressed as % Inhibition and % Viability, respectively, and calculated using the formulas below:

Inhibition (%) = (Raw data CPD - Average VC) / (Average CC - Average VC)*100

Viability (%) = $(Raw\ data\ _{CPD}$ - $Average\ _{MC})$ / $(Average\ _{CC}$ - $Average\ _{MC})*100$

Where:

Raw data CPD is the values of the sample-treated wells.

Average vc is the average value of virus control.

Average *cc* is the average value of cell control.

EC₅₀ and CC₅₀ values were calculated using GraphPad Prism software (Version 8.0) with the equation log(inhibitor) vs. response with variable slope.

5.2 Strategy I of the structural modification

It is hypothesized that the release of 3-chloro-5-hydroxypyridine could result in reduced recognition of the S1 subsite and diminished binding affinity for the catalytic pocket. Consequently, the first direction of structural optimization is the incorporation of an additional group that can effectively occupy the S1 subsite following the departure of 3-chloro-5-hydroxypyridine. This strategic modification aims to enhance the overall binding of the compounds.

5.2.1 Direction of the structural modification

Our findings indicated that extending the linker between Parts A and B did not diminish the inhibitory activity against SARS-CoV-2 M^{pro}. This was evidenced by MC04BP and MC12E01 showing comparable enzymatic inhibition to MC04 and MC12, respectively, at equivalent concentrations. Additionally, MC04DN investigated in section 3.4.3, a derivative lacking the amino group of MC04, displayed reduced activity. Based on these results, we hypothesize that the amino group of the 2-aminothiazole could be a key site for further structural optimization to enhance the inhibitory potential of the compound (Figure 5.1).

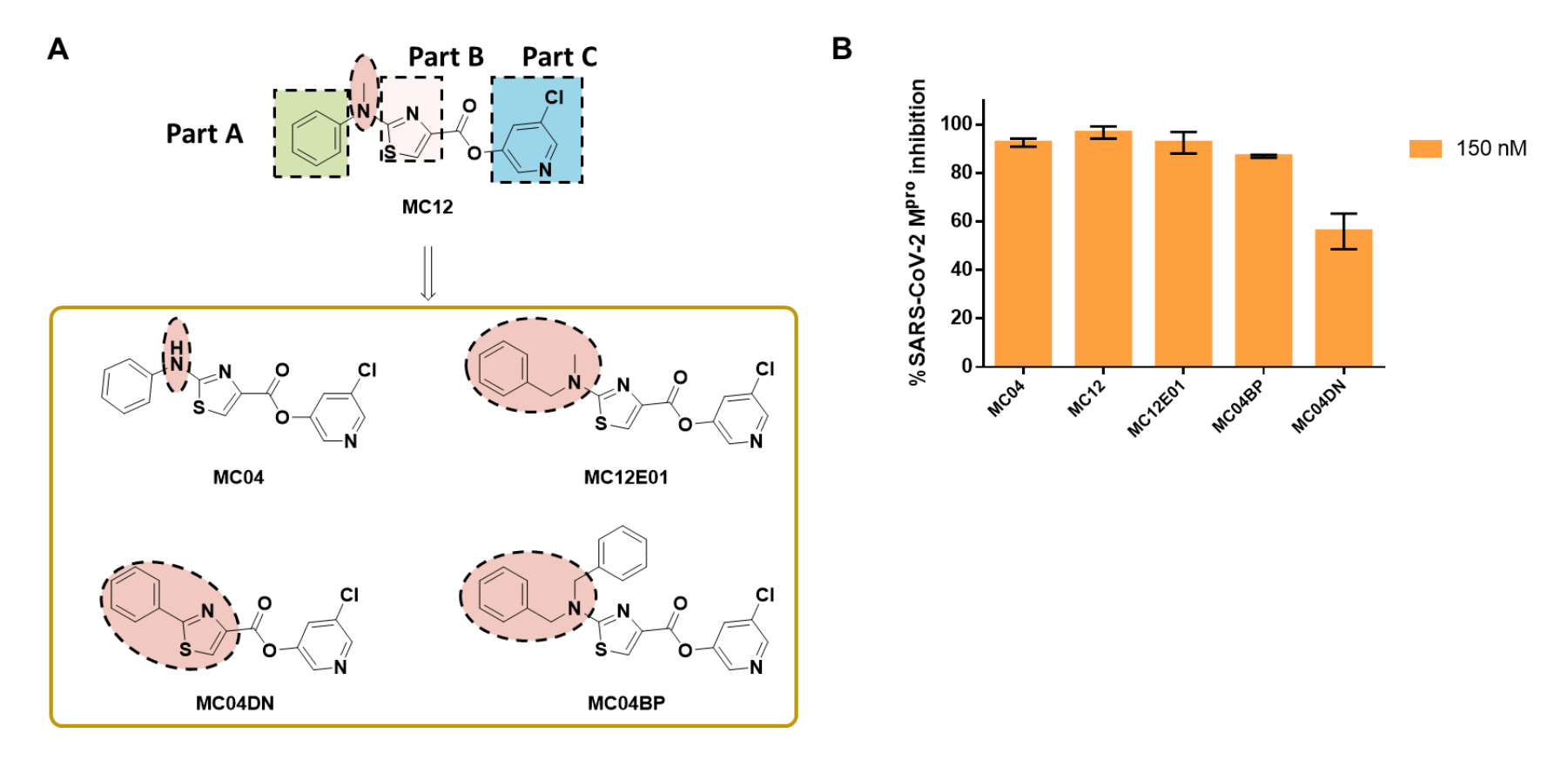


Figure 5.1 A) Structures of MC04, MC12, MC12E01 and MC04BP; B) Results of inhibition of MC04, MC12, MC12E01 and MC04BP01 at 150 nM against SARS-CoV-2 M^{pro} and structures of MC04, MC12, MC12E01, MC04BP and MC04DN.

5.2.2 Strategy of the structural modification

CCF981 (CCF0058981) serves as a noncovalent M^{pro} inhibitor probe, employing a distinct binding mode with SARS-CoV-2 M^{pro} compared to peptidomimetic inhibitors ^[101]. It features two moieties targeting the S2 subsite, with its 1*H*-benzotriazole group capable of fitting into the S1 subsite. As posited in section 5.2.1, incorporating an additional group to enhance S1 subsite recognition could potentially restore the affinity of the compound to the catalytic pocket of SARS-CoV-2 M^{pro}. Leveraging the structural attributes of MC04BP and CCF981, the 1*H*-benzotriazole group from CCF981 was integrated to replace one of the phenyl groups in MC04BP, resulting in the creation of MC04BP01 (Figure 5.2). This modification also aimed to assess the significance of the ester warhead within the structure of the compound, leading to the design of BP0101.

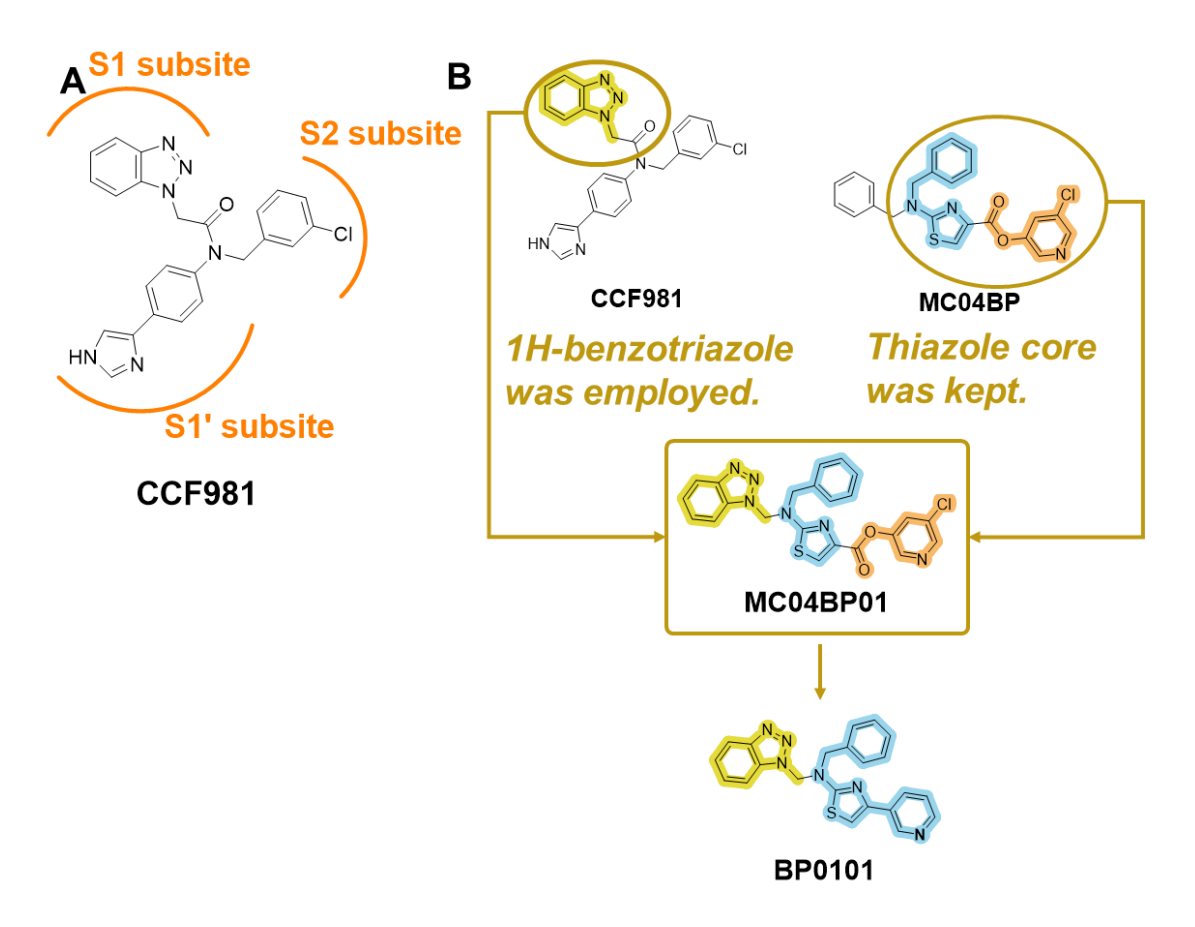


Figure 5.2 A) Schematic of the binding mode of CCF981 (CCF0058981) orienting the binding site; B) Strategy of the structural modification.

5.2.3 Synthetic route of new compounds

The synthetic pathway for MC04BP01 was modeled after that of MC12E01. Commencing with benzyl thiourea as the initial compound, the process involved its cyclization with methyl bromopyruvate to yield methyl 2-(benzylamine)thiazole-4-carboxylate. This intermediate was then coupled with 1-chloromethyl-1*H*-benzotriazole in the presence of sodium hydride as a catalyst. Subsequent hydrolysis of the product led to the formation of the requisite carboxylic acid, which was subsequently employed in the synthesis of the final ester compound (Scheme 5.1).

The synthesis of BP0101 initiated with benzyl thiourea, similar to the approach for MC04BP01. Benzyl thiourea underwent cyclization with 3-(2-chloroacetyl)pyridine to produce *N*-benzyl-4-(pyridin-3-yl)thiazol-2-amine. This intermediate was then reacted with 1-chloromethyl-1*H*-benzotriazole, employing sodium hydride as a catalyst, to achieve the final product, BP0101 (Scheme 5.2).

Scheme 5.1 Synthetic route to MC04BP01: (i) methyl bromopyruvate, methanol, 80 °C, 30 min, 70%; (ii) NaH, *N*,*N*-Dimethylformamide (DMF), -20 °C to room temperature, 1 h, 80%; (iii) 1 M aqueous NaOH/MeOH, room temperature, 1 h, 80%; (iv) 3-chloro-5-hydroxypyridine, HOBt, DIC, DIPEA, *N*,*N*-Dimethylformamide (DMF), room temperature, 24h, 53%.

Scheme 5.2 Synthetic route to BP0101: (i) 3-(2-chloroacetyl)pyridine, methanol, 80 °C, 12 h, 70%; (ii) NaH, *N*,*N*-Dimethylformamide (DMF), -20 °C to room temperature, 1 h, 80%.

5.2.4 Evaluation of the inhibitory activity against SASR-CoV-2 M^{pro}

In this series of assays, the operational concentration of SARS-CoV-2 M^{pro} was set at 200 nM to evaluate the inhibitory activities of MC12, MC12E01, MC04BP, MC04BP01, and BP0101 (Figure 5.3). At a final concentration of 150 nM, MC04BP01 exhibited significant inhibitory effects against the protease. Except for BP0101, all other compounds demonstrated over 90% inhibition against SARS-CoV-2 M^{pro}. Notably, BP0101 showed substantially reduced inhibitory activity compared to the other compounds. These results suggest that the amino group of the aminothiazole ring is a promising site for structural modifications, potentially enhancing inhibitory activity. Furthermore, the ester warhead retains its importance as a key pharmacophore for this class of compounds, indicating that modifications to this group may impact the overall efficacy against SARS-CoV-2 M^{pro}.

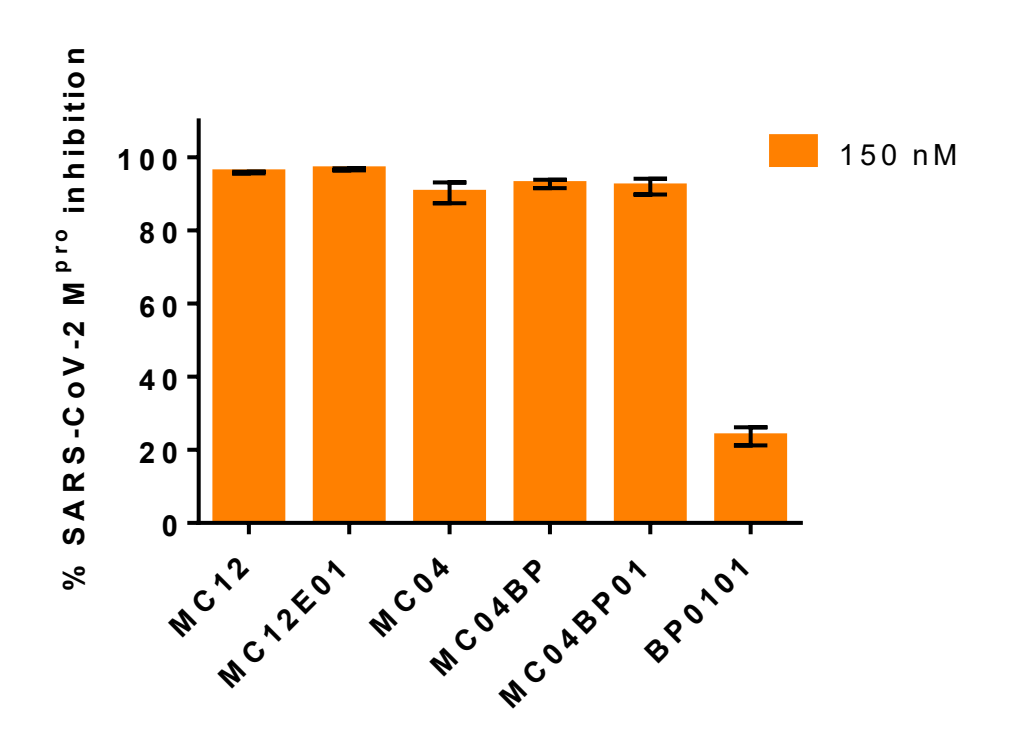


Figure 5.3 Results of inhibition of MC12, MC12, MC04, MC04BP, MC04BP01 and BP0101 against SARS-CoV-2 M^{pro}.

5.2.5 Determination on the IC₅₀ values against SASR-CoV-2 M^{pro}

MC04BP01, MC12, and Nirmatrelvir were selected for the assessment of their IC₅₀ values, as depicted in Figure 5.4. The IC₅₀ values for MC04BP01 and MC12 were found to be in close proximity to that of Nirmatrelvir, with measured values of 12.13 nM and 12.38 nM, respectively, compared to 10.33 nM of Nirmatrelvir (Figure 5.4). This IC₅₀ determination confirmed that the introduction of a methyl-1*H*-benzotriazole group at the amino position of the aminothiazole ring does not compromise the inhibitory potency against SARS-CoV-2 M^{pro}, thus validating the effectiveness of this structural modification.

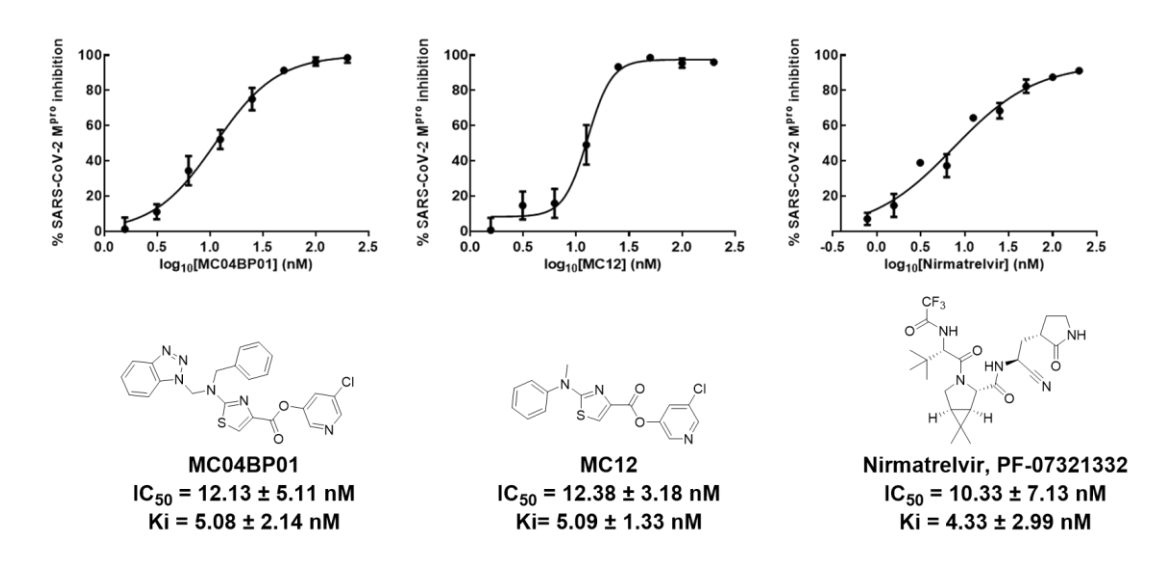


Figure 5.4 Results of the evaluation of SARS-CoV-2 M^{pro} IC₅₀ and structures of MC04BP01, MC12 and Nirmatrelvir.

5.2.6 Mechanistic studies of the target compounds against SASR-CoV-2 M^{pro}

1) Molecular docking of MC04BP01 with SARS-CoV-2 Mpro

Semi-flexible molecular docking was utilized to predict the binding mode of MC04BP01 to SARS-CoV-2 M^{pro} prior to the formation of a covalent bond. As illustrated in Figure 5.5, the predicted binding pose of MC04BP01 closely resembled those of MC04 and MC12. The complete structure of MC04BP01 fits into three subsites within the enzymatic catalytic site. The carbonyl group forms two hydrogen bonds with Ser144 and Cys145. Additionally, the pyridinyl group partakes in π -anion stacking with Glu166 at the S1 subsite. The phenyl ring at the benzyl group, akin to MC04, occupies the S2 subsite and engages in π - π stacking with His41. The 1*H*-benzotriazole group forms an additional π - π stacking with His41. Molegro Virtual Docker (MVD) was applied to estimate the binding affinity, with the rerank score serving as an indicator for ranking virtual screening results [102]. A high negative Rerank Score in MVD docking results indicates strong binding affinity. The lowest Rerank scores for MC04BP01, MC04, and MC12 were -124.048, -93.83, and -94.35, respectively (Table 5.1).

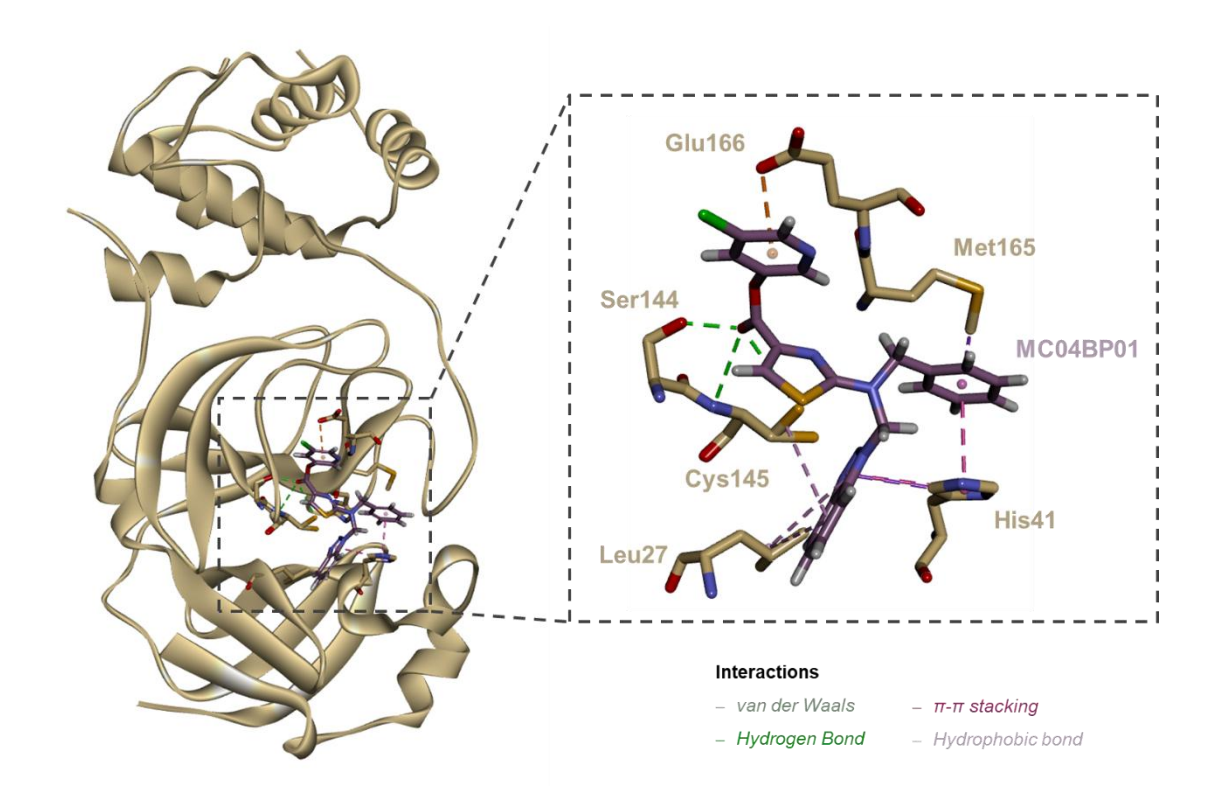


Figure 5.5 The predicted binding poses of MC04BP01 (carbons colored in purple) with the catalytic site of SARS-CoV-2 M^{pro} (PDB ID 7VTH).

Table 5.1 The lowest Rerank scores for MC04BP01, MC04, and MC12 calculated through Molegro Virtual Docker (MVD) docking.

Compounds	The lowest Rerank scores
MC04BP01	-124.048
MC04	-93.83
MC12	-94.35

2) Time-dependent assay of MC04BP01 against SARS-CoV-2 Mpro

Following the same time-dependent assay methodology applied to MC12, the assay for MC04BP01 evaluated the impact of five different preincubation time points on the enzymatic activity of SARS-CoV-2 M^{pro}. The findings indicated that the duration of preincubation significantly influenced the enzymatic activity (Figure 5.6). Notably, after a 10-minute preincubation period with MC04BP01, the compound exhibited the most potent inhibitory effect against the enzyme at all tested concentration points. Without preincubation or with preincubation times longer than 10 minutes, the inhibitory activity of MC04BP01 was comparatively weaker. Furthermore, when the preincubation duration exceeded 10 minutes, the inhibitory activity of MC04BP01 remained relatively stable across all tested concentrations. These observations suggest that the covalent bond formed with Cys145 may undergo gradual hydrolysis, which could explain the sustained inhibitory activity of MC04BP01 even after extended preincubation times. This insight underscores the reversible nature of the covalent bond and its implications for the mechanism of action of the compound against SARS-CoV-2 M^{pro}.

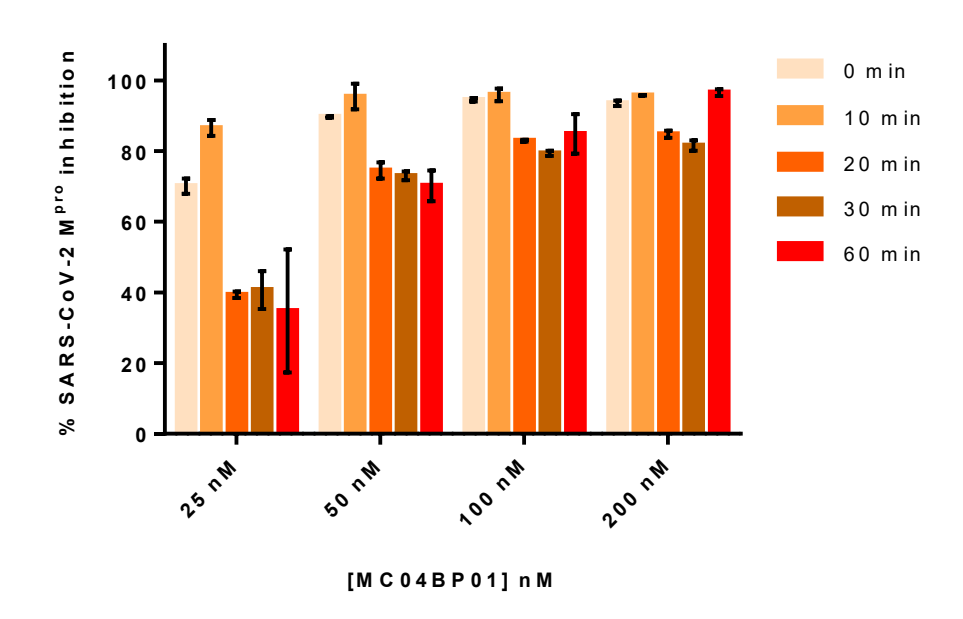


Figure 5.6 Time-dependent inhibition of SARS-CoV-2 M^{pro} by MC04BP01.

5.3 Alternative strategy on the structural modification

5.3.1 Direction of the structural modification

Alternative strategies have focused on modification of the ester warhead of the M^{pro} inhibitors, exploring three distinct modifications: conversion to amide and aldehyde groups. The ester group of MC12 was transformed into a ketone, giving rise to MC12D01. AD01, derived from MC12, incorporates a new moiety in place of the pyridinyl ester. This moiety is designed to mimic glutamine, enabling it to recognize and bind within the S1 subsite. By altering the warhead, we explored the impact of different functional groups on the binding affinity and specificity of the inhibitors for the target enzyme (Figure 5.7).

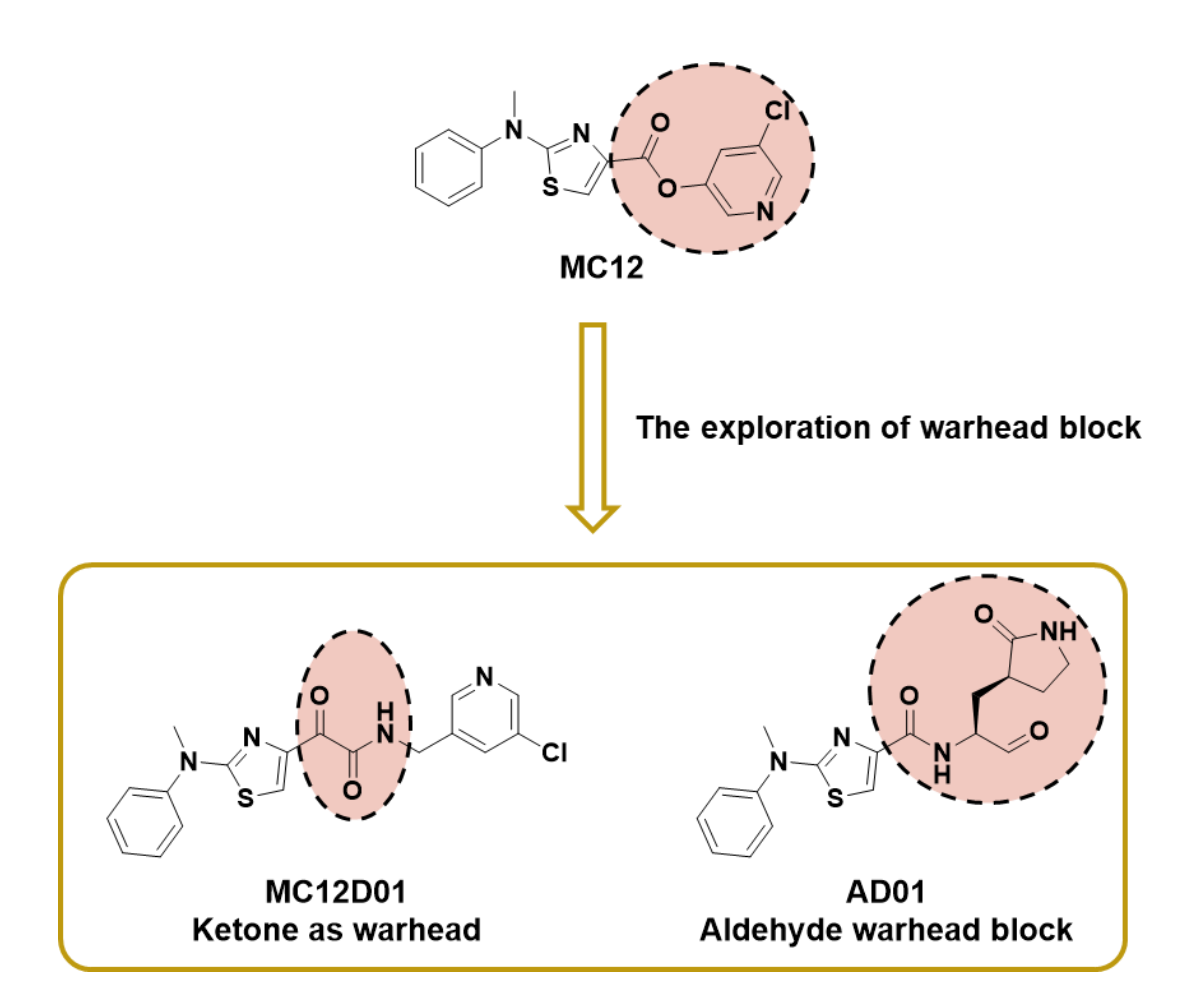


Figure 5.7 Alternative strategies for structural modification.

5.3.2 Synthetic route of new compounds

1) Synthetic route to AD01

The synthesis of AD01 leveraged an intermediate from the MC12 preparation process, specifically 2-(methyl(phenyl)amino)thiazole-4-carboxylic acid, as the starting material. For the amide synthesis with methyl (*S*)-2-amino-3-((*S*)-2-oxopyrrolidin-3-yl)propanoate, *N*,*N*,*N*',*N*'-tetramethylchloroformamidinium hexafluorophosphate (TCFH) was used with *N*-methylimidazole (NMI) as the catalyst [103]. The intermediates were reduced to alcohols and subsequently oxidized using Dess-Martin Periodinane [45] to obtain the final aldehydes (Scheme 5.3).

Scheme 5.3 Synthetic routes to AD01: (i) 6 M HCl in 1,4-dioxane, room temperature, overnight; (ii) *N,N,N',N'*-tetramethylchloroformamidinium hexafluorophosphate (TCFH), *N*-methylimidazole (NMI), acetonitrile, room temperature, overnight, 70%; (iii) NaBH₄, THF, room temperature, overnight, 90%; (iv) Dess-Martin Periodinane, room temperature, overnight, 76%.

2) Synthetic route to AD02, AD04, AD05 and AD06

The synthetic routes for AD02, AD04, AD05 and AD06 share initial steps, particularly in the synthesis of certain intermediates. The deprotection of (*S*)-2-((*tert*-butoxycarbonyl)amino)-3-((*S*)-2-oxopyrrolidin-3-yl)propanoate was facilitated by 6 M HCl in 1,4-dioxane. Except preparation of the amide with methyl (*S*)-2-amino-3-((*S*)-2-oxopyrrolidin-3-yl)propanoate, other amides were synthesized under the catalysis of *N*,*N*-Diisopropylethylamine (DIPEA) and 2-(7-Azabenzotriazol-1-yl)-*N*,*N*,*N*',*N*'-tetramethyluronium hexafluorophosphate (HATU). The products were then hydrolyzed to yield the corresponding carboxylic acids. For the amide synthesis with methyl (*S*)-2-amino-3-((*S*)-2-oxopyrrolidin-3-yl)propanoate, *N*,*N*,*N*',*N*'-tetramethylchloroformamidinium hexafluorophosphate (TCFH) was used with *N*-methylimidazole (NMI) as the catalyst [105]. The intermediates were reduced to alcohols and subsequently oxidized using Dess-Martin Periodinane [45] to obtain the final aldehydes (Scheme 5.4).

Scheme 5.4 Synthetic routes to AD02, AD04, AD05 and AD06: (i) 6 M HCl in 1,4-dioxane, room temperature, overnight; (ii) 2-(7-Azabenzotriazol-1-yl)-*N*,*N*,*N*',*N*'-tetramethyluronium hexafluorophosphate (HATU), Triethylamine (TEA), room temperature, overnight, 70%; (iii) 0.8 M aqueous LiOH, THF, room temperature, 2 h, 80%; (iv) *N*,*N*,*N*',*N*'-tetramethylchloroformamidinium hexafluorophosphate (TCFH), *N*-methylimidazole (NMI), acetonitrile, room temperature, overnight, 70%; (v) NaBH₄, THF, room temperature, overnight, 90%; (vi) Dess-Martin Periodinane, room temperature, overnight, 70%.

5.3.3 Evaluation of the inhibitory activity against SASR-CoV-2 M^{pro}

The results of inhibitory evaluation indicated that the substitution of the ester with a ketone, as observed in the creation of MC12D01 from MC12, led to a significant decrease in inhibitory activity against SARS-CoV-2 M^{pro}. Among the modified compounds, despite showing lower inhibitory effects compared to MC12, AD01 demonstrated the most potent inhibition against SARS-CoV-2 M^{pro} (Figure 5.8).

This modification suggests direction for future structural refinements, highlighting the importance of the warhead group in the inhibitory activity of compounds against SARS-CoV-2 M^{pro}. AD01 provides guidance for the subsequent structural modifications, indicating that the introduction of moieties that can specifically target the enzymatic subsites may be a promising approach to enhance the inhibitory potency of the compounds.

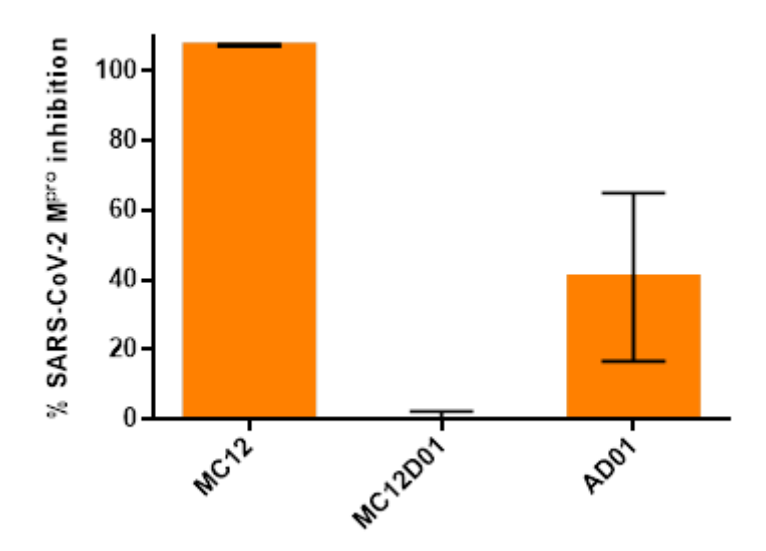


Figure 5.8 Evaluation of the inhibitory activity of MC12, MC12D01 and AD01 against SARS-CoV-2 M^{pro} .

Further modifications have been directed towards the thiazole core with the goal of optimizing the peptidomimetic scaffold. In alignment with the substrate sequence profile for SARS-CoV-2 M^{pro}, *L*-leucine was selected for the P2 position to interact with the S2 subsite. Thiazole or the equivalent thiophene was utilized as the terminal group, designed to fit into the S3/4 subsite. Peptidomimetics, due to their inherent flexibility, typically exhibit greater solubility in aqueous environments than their nonpeptidic small molecule counterparts (Figure 5.9). The evaluation of inhibitory activity indicated that AD04 exhibited reduced inhibitory activity compared to AD02, highlighting the importance of proper accommodation within the S3/4 subsite. Among these modified compounds, AD02 demonstrated the most potent inhibition against SARS-CoV-2 M^{pro}, suggesting that the specific structural features at the P2 position contribute to enhanced binding and inhibitory efficacy. These insights are instrumental for the continued structural optimization of M^{pro} inhibitors.

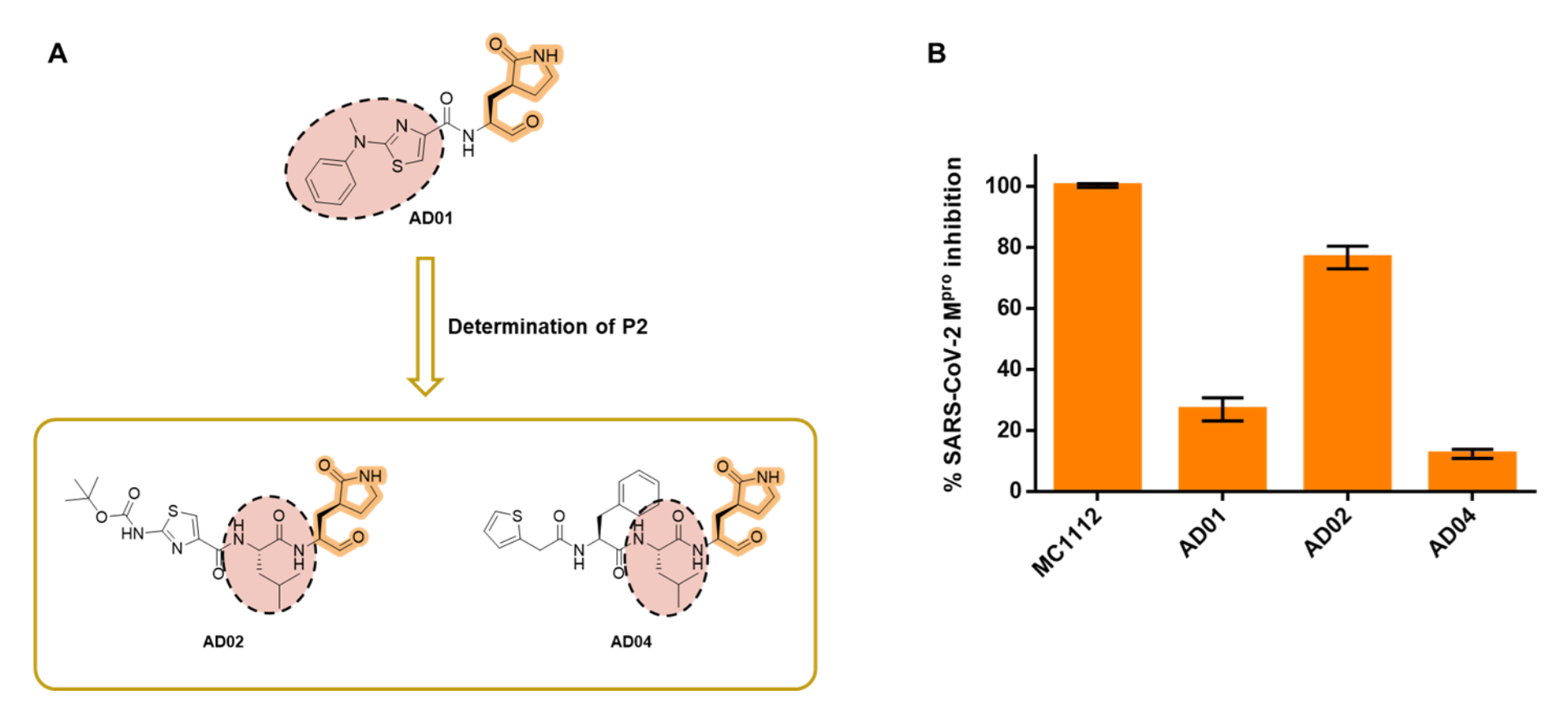


Figure 5.9 Structural modification of AD01 and evaluation of their inhibitory activity against SARS-CoV-2 M^{pro}.

5.3.4 Structural optimization of AD02

Enhancements have been focused on the thiazole core with the aim of refining the peptidomimetic framework. In accordance with the substrate sequence profile for SARS-CoV-2 M^{pro}, the *N-tert*-BOC-2-aminothiazole in AD02 was substituted with 2-chlorothiazole to yield AD05. Additionally, *L*-valine was chosen for the P3 position, and the *N-tert*-BOC-2-aminothiazole was replaced by 2-chlorothiazole to obtain AD06 (Figure 5.10). The assessment of inhibitory activity revealed that the size of the substituent at the second position on the thiazole ring greatly impacts the inhibitory potency. This was demonstrated by comparing AD02 and AD05, with AD05 showing superior inhibitory activity, underscoring the significance of the appropriate size of the thiazole moiety. Among the modified compounds, AD06 exhibited the strongest inhibition against SARS-CoV-2 M^{pro}, indicating that the *L*-valine at P3 position contributes significantly to improved binding affinity and inhibitory effectiveness.

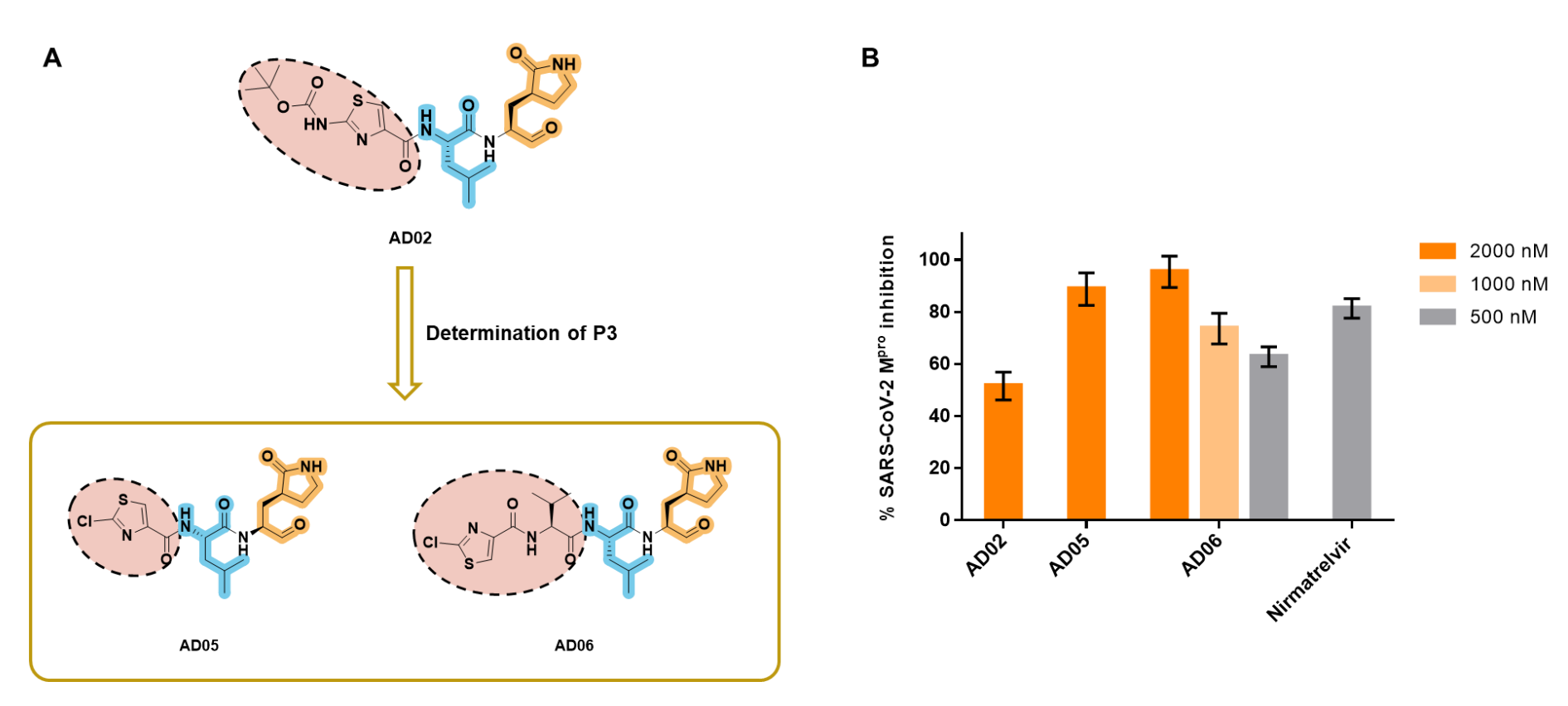


Figure 5.10 Structural modification of AD02 and evaluation of their inhibitory activity against SARS-CoV-2 M^{pro}.

5.3.5 Determination on the IC₅₀ values against SASR-CoV-2 M^{pro}

Among the modified compounds with alternative strategies, AD02 and AD06 were selected to determine their IC₅₀ values against SARS-CoV-2 M^{pro}. The assay was conducted with a final concentration of 200 nM for SARS-CoV-2 M^{pro}. AD02 showed an IC₅₀ value of approximately $1.252 \pm 0.195 \mu M$. In contrast, AD06 exhibited a significantly lower IC₅₀ value of $175.2 \pm 43.5 nM$, which is comparable to the $160.2 \pm 15.1 nM$ of Nirmatrelvir, serving as a positive control. This quantitative assessment of inhibitory efficacy of AD06 highlights its potential as a promising candidate for further research, despite having a slightly higher IC₅₀ value than the positive control (Figure 5.11 and Table 5.2).

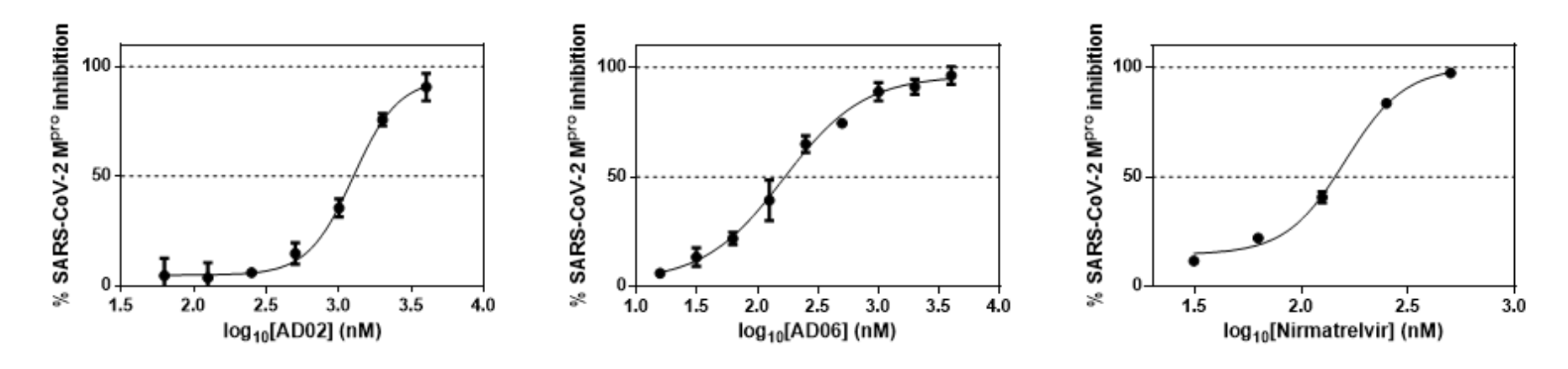


Figure 5.11 Results of the evaluation of IC₅₀ of the selected compounds against SARS-CoV-2 M^{pro}

Table 5.2 The IC_{50} values of the selected compounds against SARS-CoV-2 M^{pro}

Compounds	IC ₅₀ values (nM)	
AD02	1252 ± 113	
AD06	175.2 ± 43.5	
Nirmatrelvir*	160.2 ± 15.1	

^{*}Nirmatrelvir as a positive control

5.3.6 Types of warheads and the effects of thiazole/oxazole

To assess the influence of warhead type on inhibitory activity, the aldehyde group in AD06 was substituted with a nitrile group, which is the warhead of AD06CN01. The thiazole ring was replaced with an oxazole ring to detect their effects on the inhibitory activity. The analysis of the inhibitory activity revealed that both the aldehyde and nitrile groups are effective as warheads, exhibiting comparable inhibitory effects. However, the replacement of the thiazole ring with an oxazole ring resulted in a significant reduction in inhibitory activity. This suggests that the specific chemical nature of the warhead and the heterocyclic ring system are critical determinants of the interaction of AD compounds with SARS-CoV-2 M^{pro} (Figure 5.12).

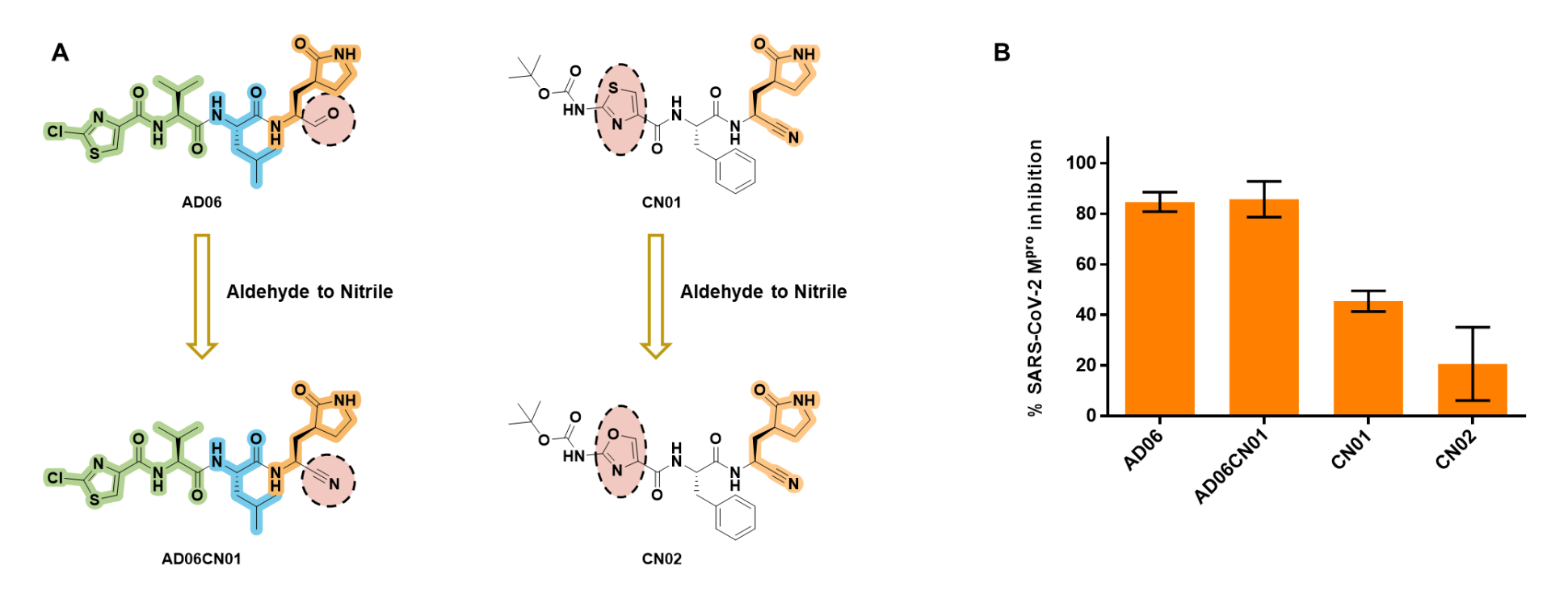


Figure 5.12 Evaluation of the effects of warhead and thiazole on inhibitory activity against SARS-CoV-2 M^{pro}.

5.3.7 X-ray crystal structures of SARS-CoV-2 M^{pro} in complex with AD05 and AD06

To elucidate the mechanism of inhibition of SARS-CoV-2 M^{pro} by AD compounds, we determined the crystal structure of the M^{pro}-inhibitor complex. Figure 5.13 and Figure 5.14 depict compound AD05 and AD06 bound in the substrate-binding pocket of SARS-CoV-2 M^{pro} and the specific interaction specifics. The crystal structures showed that AD05 and AD06 shared same covalent bound to Cys145 and interaction with S1 and S2 subsites. The cocrystal structures reveal a standard C-S covalent bond between the C atom of the aldehyde groups of AD05/AD06 and the catalytic-site Cys145 of SARS-CoV-2 M^{pro}. The oxygen atom of the aldehyde group is crucial for stabilizing the conformation of the inhibitor, forming a hydrogen bond with the backbone of Cys145. The (S)-γ-lactam ring at P1 of AD05/AD06 snugly fits into the S1 site, with the main chain of Phe140 and the side chain of Glu166 contributing to its stabilization through hydrogen bonds with the NH group, respectively. Furthermore, the amide bonds along the chain of AD05/AD06 engage in hydrogen bonding with the main chain of His164. The tert-Butyl group at P2 of AD05/AD06 extends deeply into the S2 site, stacking with the imidazole ring of His41 and is encircled by Met49 and Met165, leading to significant hydrophobic interactions. The distinct P3 moieties in AD05 and AD06 result in varied binding affinities with SARS-CoV-2 M^{pro}. In AD05, the P3 position features a 2-chlorothiazole group that is solvent-exposed within the S4 subsite

(Figure 5.13A). This moiety is stabilized by a hydrogen bond with the amino group of the main chain of Glu166. Conversely, in AD06, both the amino and carbonyl groups of Glu166 contribute to the anchoring of the P3 moiety, enhancing its fit within the pocket (Figure 5.14A). Additionally, the terminal 2-chlorothiazole group of AD06 engages in hydrophobic interactions with Pro168, which further stabilizes its binding. These differences in molecular interactions suggest that AD06 has a more favorable conformation and binding affinity to SARS-CoV-2 M^{pro} compared to AD05. AD05 and AD06 share the same mechanism of inhibition as depicted in Figure 5.13B and Figure 5.14B.

Figure 5.15A indicated that the binding mode of AD06 within the SARS-CoV-2 M^{pro} complex structure exhibits similarities to that of nirmatrelvir in the SARS-CoV-2 M^{pro} complex, as previously reported. However, the primary distinctions are observed in the interactions at the S1', S2, and S3/4 subsites (Figure 5.15B). These variations are likely attributable to the different warhead types and the sizes of the P2 and P3 moieties present in the inhibitors, which can significantly influence the specific binding interactions and overall affinity for the enzyme.

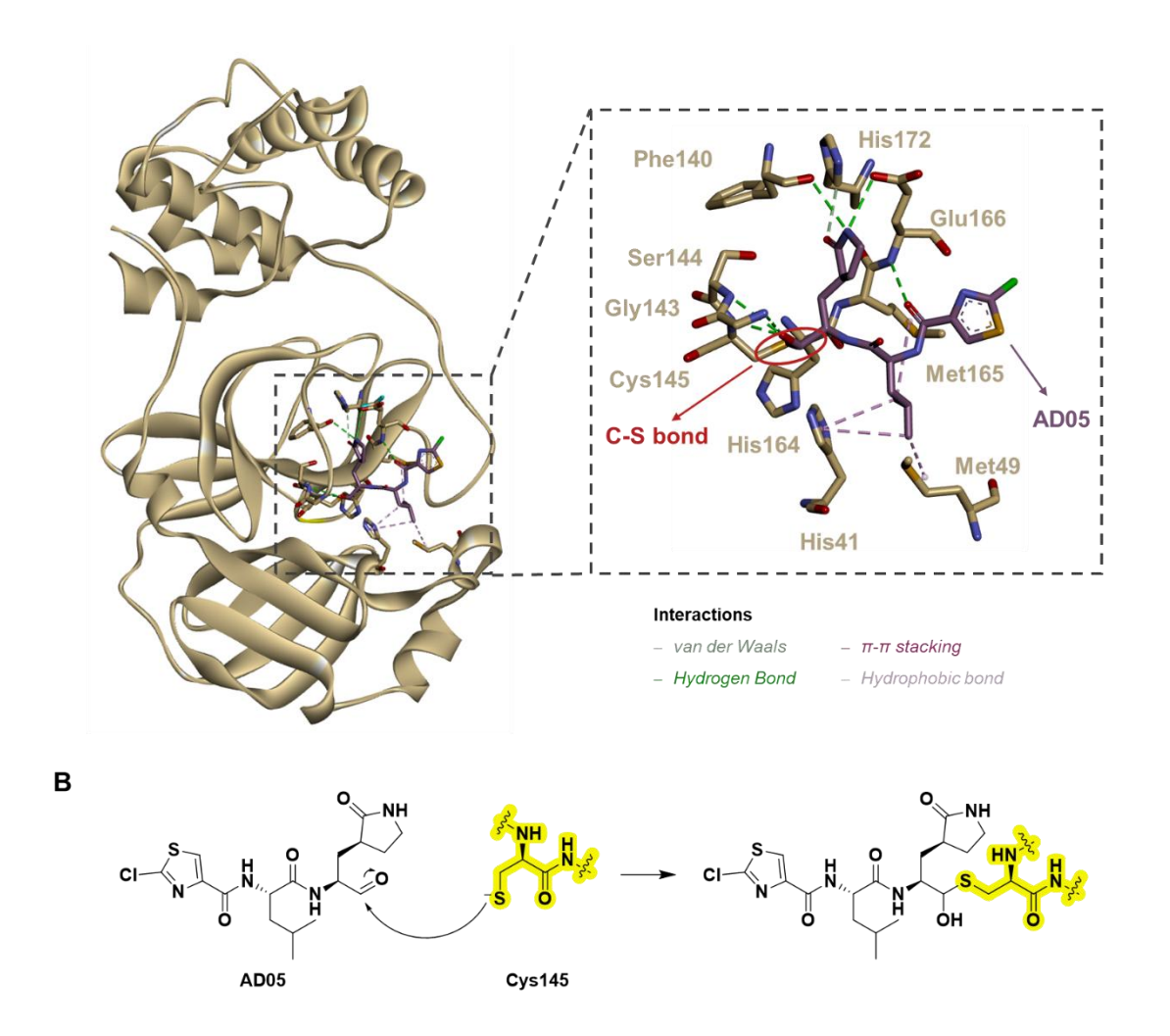


Figure 5.13 A) X-ray crystal structure of AD05 (carbons colored in purple) binding to SARS-CoV-2 M^{pro} (PDB ID 9M29). B) Mechanism of inhibition of SARS-CoV-2 M^{pro} by AD05.

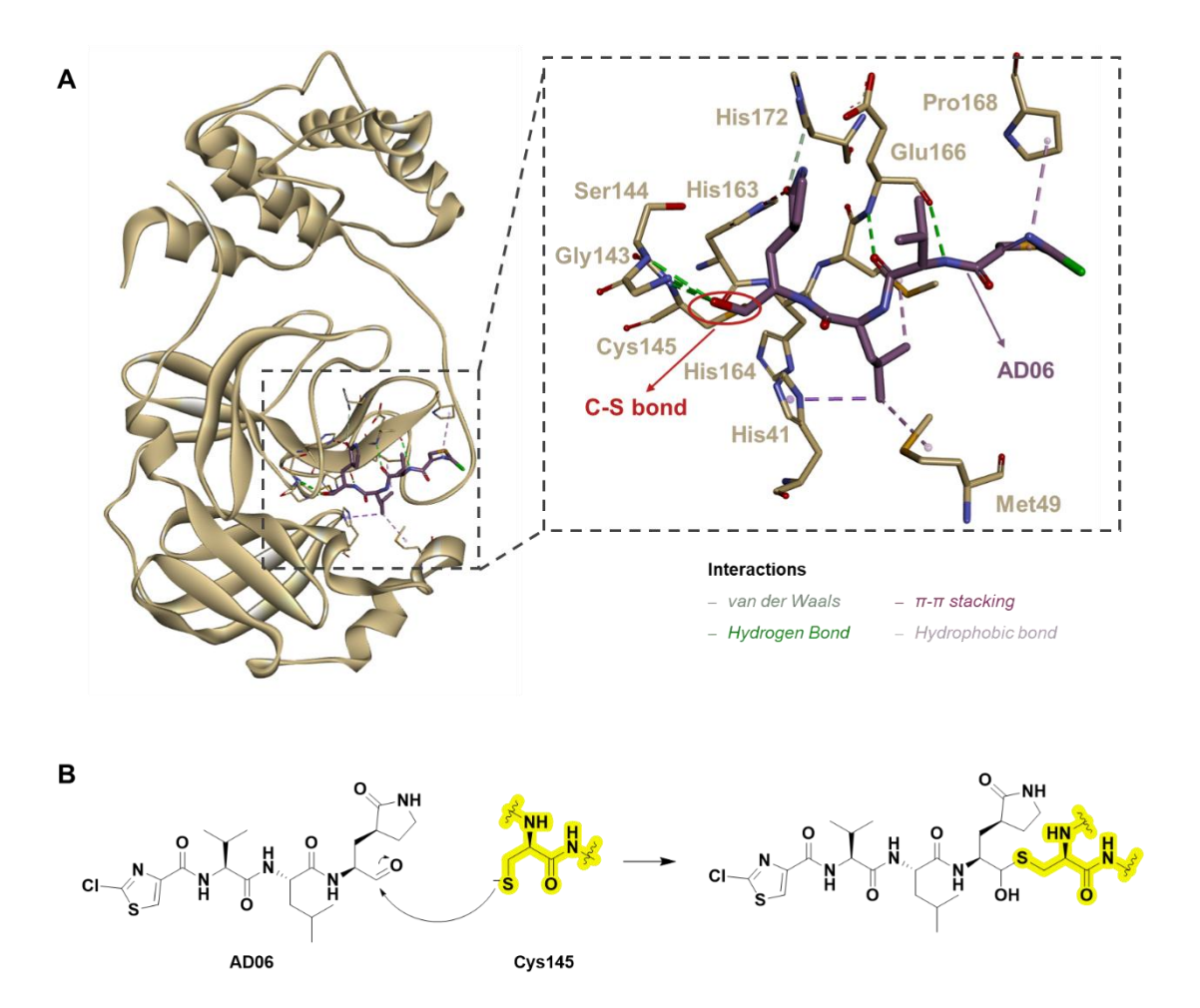


Figure 5.14 A) X-ray crystal structure of AD06 (carbons colored in purple) binding to SARS-CoV-2 M^{pro} (PDB ID 9M2U). B) Mechanism of inhibition of SARS-CoV-2 M^{pro} by AD06.

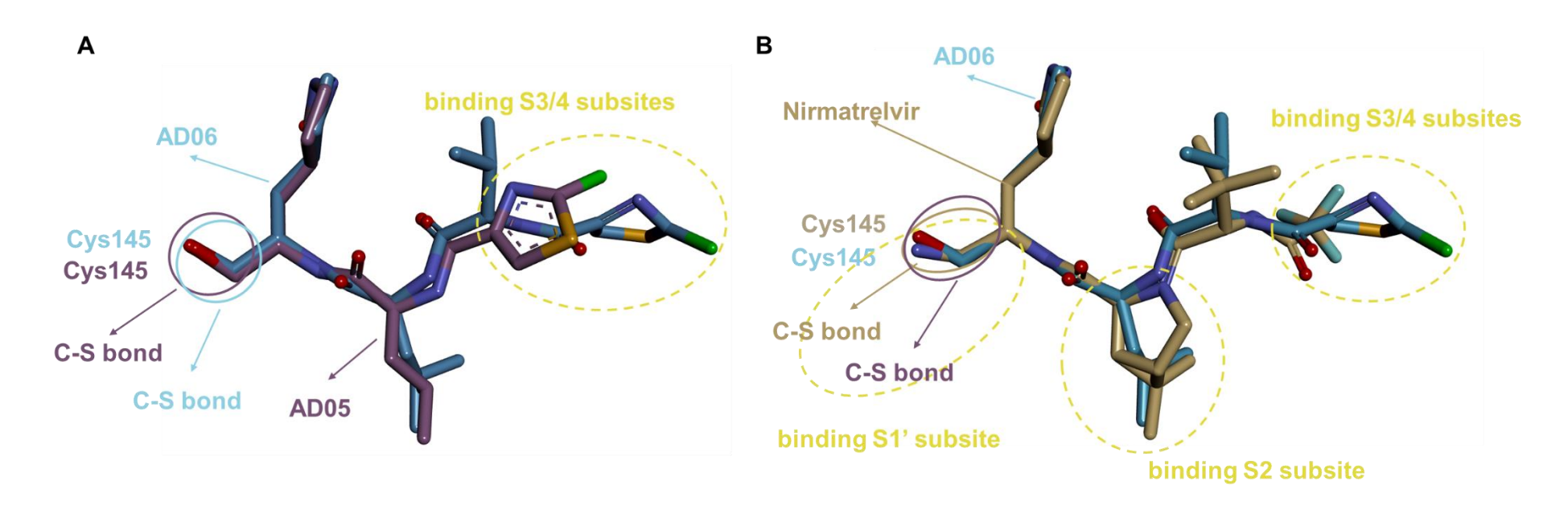


Figure 5.15 Comparison of the binding modes of A) AD06 with Nirmatrelvir (PDB ID 8DZ2) and B) AD06 with AD05 in SARS-CoV-2 M^{pro}. The major differences of AD06 from Nirmatrelvir and AD05 are marked with a dashed circle.

5.3.8 Summary of Structure Activity Relationship

The chemical structure depicted in Figure 5.16 is dissected into five key components: warhead, P1, P2, P3 and P4. The subsequent summary consolidates the structureactivity relationship (SAR) findings for AD components, highlighting how each element contributes to the overall inhibitory effect on SARS-CoV-2 M^{pro}. The aldehyde group, acting as a warhead, can form a covalent bond with Cys145. However, replacing the aldehyde warhead with a nitrile group preserves the inhibitory activity against SARS-CoV-2 M^{pro}. A lactam ring at the P1 position is crucial for recognition by the S1 subsite. The moiety at the P2 position is responsible for occupying the S2 subsite. Besides, P2 prefers hydrophobic groups for optimal interaction. The carbonyl group at the P3 position is essential for binding to the main chain of Glu166, stabilizing the active conformation of the small molecule. The inhibitory activity can be maintained when compound has a non-amino acid residue at the P3 position. The thiazole ring at the P3 position exhibits higher inhibitory potency compared to the oxazole ring. A valine residue at P3 can enhance solubility compared to a thiazole ring. The P4 position can be tailored for integration with additional technologies. In addition, the replacement of the thiazole ring with an oxazole ring in AD compounds has resulted in a significant reduction in inhibitory activity against SARS-CoV-2 M^{pro}, underscoring the critical role of the heterocyclic ring system in the interaction of these compounds with SARS-CoV-2 M^{pro}.

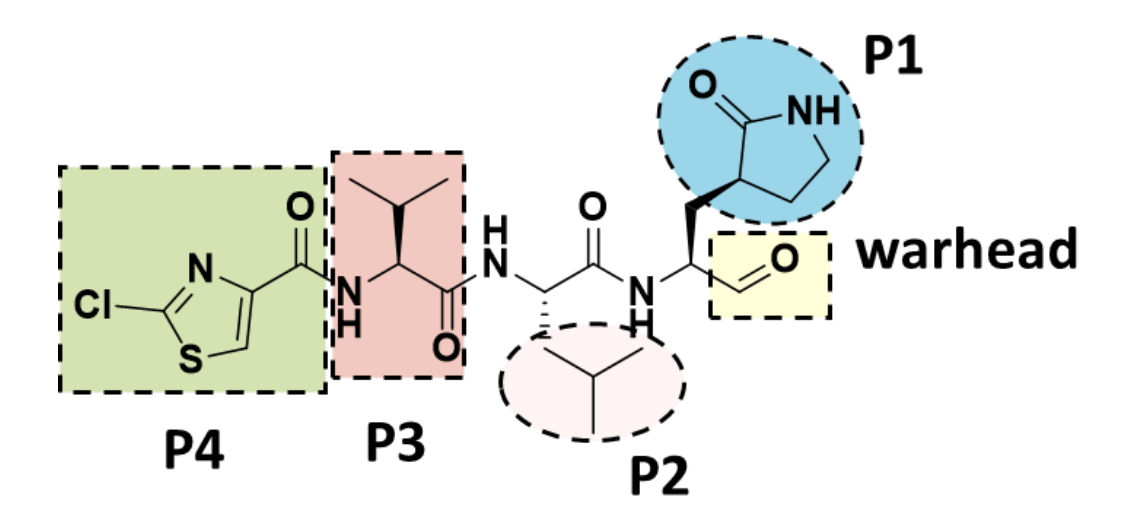


Figure 5.16 Five components of AD compounds.

5.3.9 Antiviral assays of the target compounds in Vero E6

1) Results of the antiviral assays

The antiviral assay was conducted by the collaborator biosafety level 3 (BSL-3) lab of WuXi AppTec (Hong Kong) Limited. In the CPE experiment, the in vitro antiviral effects of compounds against the wild-type SARS-CoV-2 virus were evaluated to determine their EC50 values. AD05 and AD06 were selected for EC50 evaluation. The structure-activity relationship (SAR) analysis of enzymatic inhibition highlighted that replacing the aldehyde warhead with a nitrile group preserves inhibitory activity against SARS-CoV-2 M^{pro}. Consequently, AD06CN was also chosen for EC₅₀ evaluation. Nirmatrelvir was used as positive control. As shown in Table 5.3, the positive control Nirmatrelvir exhibited the strongest inhibition against the SARS-CoV-2 virus. Interestingly, although AD05 showed lower inhibition than AD06, its EC50 value (3.264 μM) was lower than that of AD06 (25.830 μM). Additionally, although AD06CN (with a nitrile warhead) demonstrated comparable enzymatic inhibitory activity to AD06 (with an aldehyde warhead), its antiviral activity (EC₅₀ = $9.43 \mu M$) was nearly three times stronger than that of AD06 (EC₅₀ = 25.83 μ M). Cytotoxicity of the compounds was assessed under the same conditions but without virus infection. None of AD05, AD06, or AD06CN exhibited significant cytotoxicity to Vero E6 cells within the tested concentration range ($CC_{50} > 100 \mu M$). The selectivity index (SI) was used to evaluate the selectivity of a ligand towards its target. The SI value is calculated as the ratio of CC₅₀ (the concentration at which 50% of normal cells are affected) to IC₅₀ (the

concentration at which 50% of the target is inhibited). A higher SI indicates greater selectivity of the ligand for the target, with reduced toxicity to normal cells^[104]. The combination of potent antiviral activity and low cytotoxicity positions AD05 as a promising lead candidate for the development of effective and safe antiviral agents against SARS-CoV-2.

Table 5.3 Results of CPE assay of AD05, AD06, and AD06CN against SARS-CoV-2 $$\rm M^{pro}.$

Compound	EC ₅₀ (μM)	CC50 (µM)	SI (CC50/EC50)
AD05	3.264	> 100	>30.64
AD06	25.830	> 100	>3.87
AD06CN	9.429	> 100	>10.61
Nirmatrelvir*	0.072	> 5	>1393.34

^{*} Nirmatrelvir as a positive control

^{*} EC50: Half-maximal effective concentration

^{*} CC₅₀: Median cytotoxic concentration

^{*} SI: Selectivity Index

2) Discussion on the results of the antiviral assays

To elucidate the factors contributing to the different antiviral potencies, LogP values were calculated using software. A drug needs to possess amphiphilic properties to some extent (LogP = $0 \sim 5$) so that it can be both hydrophilic enough to dissolve in blood (mainly water) and lipophilic enough to pass through lipid membranes. The LogP value for a compound is the logarithm (base 10) of the ratio between the concentration of the compound in the organic (oil) and aqueous (water) phases. A higher LogP value indicates better solubility in organic phases and improved lipid membrane permeability. The calculated LogP values for AD06, AD06CN, and AD05 were 0.95, 1.67, and 0.72, respectively. The higher LogP value of AD06CN suggests better membrane permeability, leading to higher intracellular concentrations in Vero E6 cells and more efficient blocking of the SARS-CoV-2 replication cycle. Conversely, the lower LogP value of AD05 (0.72) indicates higher hydrophilicity, which may result in a higher effective concentration in the media. Therefore, AD05 displayed the strongest potency against the SARS-CoV-2 virus.

Chapter 6. Conclusion and Future Direction

In this project, Masitinib and MAC-5576 were utilized as lead compounds. A novel series of thiazole-based SARS-CoV-2 M^{pro} inhibitors were developed. The design features a pyridinyl ester as the warhead for covalent binding to Cys145 and a thiazole core for S2 subsite interaction. SAR analysis revealed that the pyridinyl ester is an essential pharmacophore for potent inhibitory activity. The thiazole core demonstrated superior SARS-CoV-2 M^{pro} inhibition compared to the oxazole core. The presence of a 2-amino group on the thiazole ring significantly enhanced inhibitory potency. Furthermore, *meta* substituents on the phenyl ring were more effective in boosting inhibitory activity than other positions. Notably, MC12 and MC10 exhibited SARS-CoV-2 M^{pro} inhibitory effects comparable to Nirmatrelvir.

Mass spectrometry analysis revealed new ion peaks for recombinant SARS-CoV-2 M^{pro} after treatment with MC04, indicating covalent acylation post-departure of the pyridinyl group. The X-ray crystal structure of SARS-CoV-2 M^{pro} in complex with MC12 revealed the covalent binding mode of MC12 to Cys145 of SARS-CoV-2 M^{pro}. Dilution and time-dependent inhibition assays confirmed the reversibility of covalent binding of MC12 to SARS-CoV-2 M^{pro}.

The inhibitory effects of the compounds on SARS-CoV M^{pro} were assessed, with both MC12 and Nirmatrelvir exhibiting inhibitory activity against the main proteases of both

SARS-CoV and SARS-CoV-2. Cytotoxicity assays indicated that MC12 and the other tested compounds did not significantly impact cell viability. In Vero E6 cells infected with SARS-CoV-2, MC04 displayed antiviral activity against the wild-type virus but the other tested compounds did not exhibit significant antiviral activity against the wild-type virus. The loss of the 3-chloro-5-hydroxypyridine group and the low solubility may be factors contributing to the low antiviral activity.

Various modification strategies were explored. MC04BP01 was synthesized and exhibited inhibitory activity against SARS-CoV-2 M^{pro} comparable to that used for MC12. Additionally, the mechanism of action for MC04BP01 has been elucidated. Another modified compounds, AD compounds feature an aldehyde warhead block. Among those, AD06 showed the strongest inhibitory activity against the SARS-CoV-2 M^{pro} and demonstrated an IC₅₀ value comparable to Nirmatrelvir, marking it as a promising lead candidate for further research and development. The mechanism of the modified was elucidated by the crystal structures of SARS-CoV-2 M^{pro} in complex with AD05 and AD06, respectively. The binding modes of both AD05 and AD06 to SARS-CoV-2 M^{pro} are covalent. Besides, both AD05 and AD06 can well accommodate into the active pocket of SARS-CoV-2 M^{pro}. Although the structure-activity relationship of the enzymatic screening assays highlights that AD05 showed lower inhibition against the enzyme of SARS-CoV-2 M^{pro} than AD06, AD05 (EC₅₀ = 3.264 μ M) showed higher antiviral activity than AD06 (EC₅₀ = 25.830 μ M) against the wild-type virus of SARS-and activity than AD06 (EC₅₀ = 25.830 μ M) against the wild-type virus of SARS-and activity than AD06 (EC₅₀ = 25.830 μ M) against the wild-type virus of SARS-

CoV-2. In addition, all selected compounds displayed low cytotoxicity in Vero E6 cell line.

In future work, structural optimization should focus on improving the solubility of compound to facilitate oral administration. Crystal structures of AD05 and AD06 in complex with SARS-CoV-2 M^{pro} revealed that the chlorine atom of thiazole ring extends to the solvent region of the protease. This suggests that the thiazole ring could be a target for solubility optimization through the introduction of soluble moieties such as piperazine or amino groups, which may enhance aqueous solubility. Chemical stability of compound should also be a focus of structural optimization in the future. Crystal structures of AD05 and AD06 with SARS-CoV-2 M^{pro} suggest that P2 position might be modified through "Ring-Closing" strategy to make the scaffold of the peptidomimetic more rigid and increase the chemical stability. In addition, the findings from this study provide a solid foundation for the continued optimization of AD compounds as potent inhibitors of SARS-CoV-2 Mpro. Future work should focus on exploring modifications on the warhead type based on the structure of AD05 to further enhance the inhibitory potency, selectivity, and pharmacokinetic properties of these compounds. Furthermore, given that MC04BP01 has demonstrated comparable inhibitory activity to MC12 and MC04 against SARS-CoV-2 Mpro, chemical stability and solubility of MC04BP01 should also be optimized. The strategy of optimization will involve the replacement of the ester linkage with a more stable amide bond to

bolster the overall chemical stability of the compound. Additionally, the incorporation of flexible bonds within MC04BP01 is expected to improve solubility.

Appendices

Declaration

Kimi AI was utilized only for grammar checking.

A1 Purification of recombinant SARS-CoV-2 Mpro

The recombinant SARS-CoV-2 M^{pro} was expressed in *E. coli* and purified as described in section 3.1.2. SDS-PAGE analysis confirmed the purity of the preparation, which was over 95% (Figure A.1).

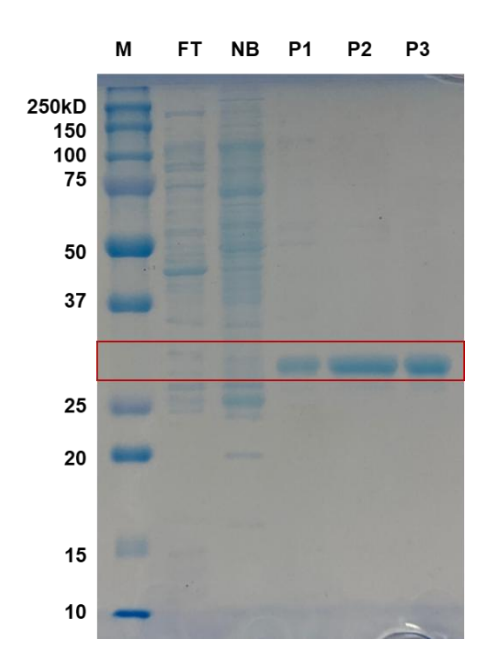


Figure A.1 Result of the purified recombinant SARS-CoV-2 M^{pro} on SDS-PAGE (M: marker, FT: flow through, NB: nonspecific binding, P1-P3: triple lanes of the same purified recombinant SARS-CoV-2 M^{pro}).

A2 List of the structures of final compounds

Through the strategies conducted in Chapter 2 and Chapter 5, compounds synthesized via the routes in in Chapter 2 and Chapter 5 were shown in Table A.1.

Table A.1 List of the structures of the synthesized compounds

NO.	Compound ID	Chemical Structures	Chemical Names
01	MC02	CI H N O CI N MC02	5-chloropyridin-3-yl 2-((4-chloropyridin-2-yl)amino)thiazole-4- carboxylate
02	MC04	H N O CI N N O N	5-chloropyridin-3-yl 2-(phenylamino)thiazole-4-carboxylate
03	MC05	F H N O CI N MC05	5-chloropyridin-3-yl 2-((2,4-difluorophenyl)amino)thiazole-4-carboxylate

04	MC06	MC06	5-chloropyridin-3-yl 2-((3,5-dimethylphenyl)amino)thiazole-4-carboxylate
05	MC07	H_3CO S OCH_3 $MC07$	5-chloropyridin-3-yl 2-((3,5-dimethoxyphenyl)amino)thiazole-4- carboxylate
06	MC08	MC08	5-chloropyridin-3-yl 2-((4-methylpyridin-2-yl)amino)thiazole-4- carboxylate
07	MC09	H N O CI N S O N	5-chloropyridin-3-yl 2-((4-methylpyridin-3-yl)amino)thiazole-4- carboxylate

08	MC10	$ \begin{array}{c c} & H \\ & N \\ & S \\ & O \\ & N \end{array} $ $ \begin{array}{c} & CI \\ & N \\ & N \\ & N \end{array} $ $ \begin{array}{c} & CI \\ & N \\ $	5-chloropyridin-3-yl 2-((3-methoxyphenyl)amino)thiazole-4- carboxylate
09	MC11	MC11	5-chloropyridin-3-yl 2-(phenylamino)oxazole-4-carboxylate
10	MC12	N N N N N N N N N N	5-chloropyridin-3-yl 2-(methyl(phenyl)amino)thiazole-4- carboxylate
11	MC13	F_3C N	5-chloropyridin-3-yl 2-((3- (trifluoromethyl)phenyl)amino)thiazole-4-carboxylate
12	MC14	CI N	5-chloropyridin-3-yl 2-((3-chlorophenyl)amino)thiazole-4- carboxylate

13	MC15	H N O CI	5-chloropyridin-3-yl 2-(pyridin-2-ylamino)thiazole-4-carboxylate
14	MC16	MC15 H N N N N N N N	5-chloropyridin-3-yl 2-((2-methyl-5-nitrophenyl)amino)thiazole- 4-carboxylate
15	MC17	F H N O CI S N O N	5-chloropyridin-3-yl 2-((2-fluorophenyl)amino)thiazole-4- carboxylate
16	MC19	MC19	5-chloropyridin-3-yl 2-((2-chlorophenyl)amino)thiazole-4- carboxylate

17	MC12S02	MC12S02	5-chloropyridin-3-yl 2-(isopropyl(phenyl)amino)thiazole-4- carboxylate
18	MC12S03	MC12S03	5-chloropyridin-3-yl 2-(phenyl(propyl)amino)thiazole-4- carboxylate
19	MC12S04	N N O CI	5-chloropyridin-3-yl 2-(butyl(phenyl)amino)thiazole-4- carboxylate
20	MC1112	MC12S04 N N N O CI N MC1112	5-chloropyridin-3-yl 2-(methyl(phenyl)amino)oxazole-4- carboxylate

21	MC1210	$ \begin{array}{c c} O & & & & & & & & & & & & & & & & & & &$	5-chloropyridin-3-yl 2-((3-methoxyphenyl)(methyl)amino)thiazole-4-carboxylate
22	MC1210S01	HO N N O CI N S O N	5-chloropyridin-3-yl 2-((3-hydroxyphenyl)(methyl)amino)thiazole-4-carboxylate
23	MC10S01	HO N N O CI S N O N	5-chloropyridin-3-yl 2-((3-hydroxyphenyl)amino)thiazole-4- carboxylate
24	MC04DN	N O CI S O N	5-chloropyridin-3-yl 2-phenylthiazole-4-carboxylate

25	MC04DN02	CI S N O CI N	5-chloropyridin-3-yl 2-(2,4-dichlorophenyl)thiazole-4- carboxylate
26	MC12E01	MC04DN02 CI N S MC12E01	5-chloropyridin-3-yl 2-(benzyl(methyl)amino)thiazole-4- carboxylate
27	MC04AM	NH N O CI S O N	5-chloropyridin-3-yl 2-benzamidothiazole-4-carboxylate
28	MC12F	MC12F	5-chloro-6-fluoropyridin-3-yl 2-(methyl(phenyl)amino)thiazole- 4-carboxylate

29	MC04F	MC04F	5-chloro-6-fluoropyridin-3-yl 2-(phenylamino)thiazole-4- carboxylate
30	MC04DNF	N O CI S O N F MC04DNF	5-chloro-6-fluoropyridin-3-yl 2-phenylthiazole-4-carboxylate
31	MC04BP	MC04BP	5-chloropyridin-3-yl 2-(dibenzylamino)thiazole-4-carboxylate

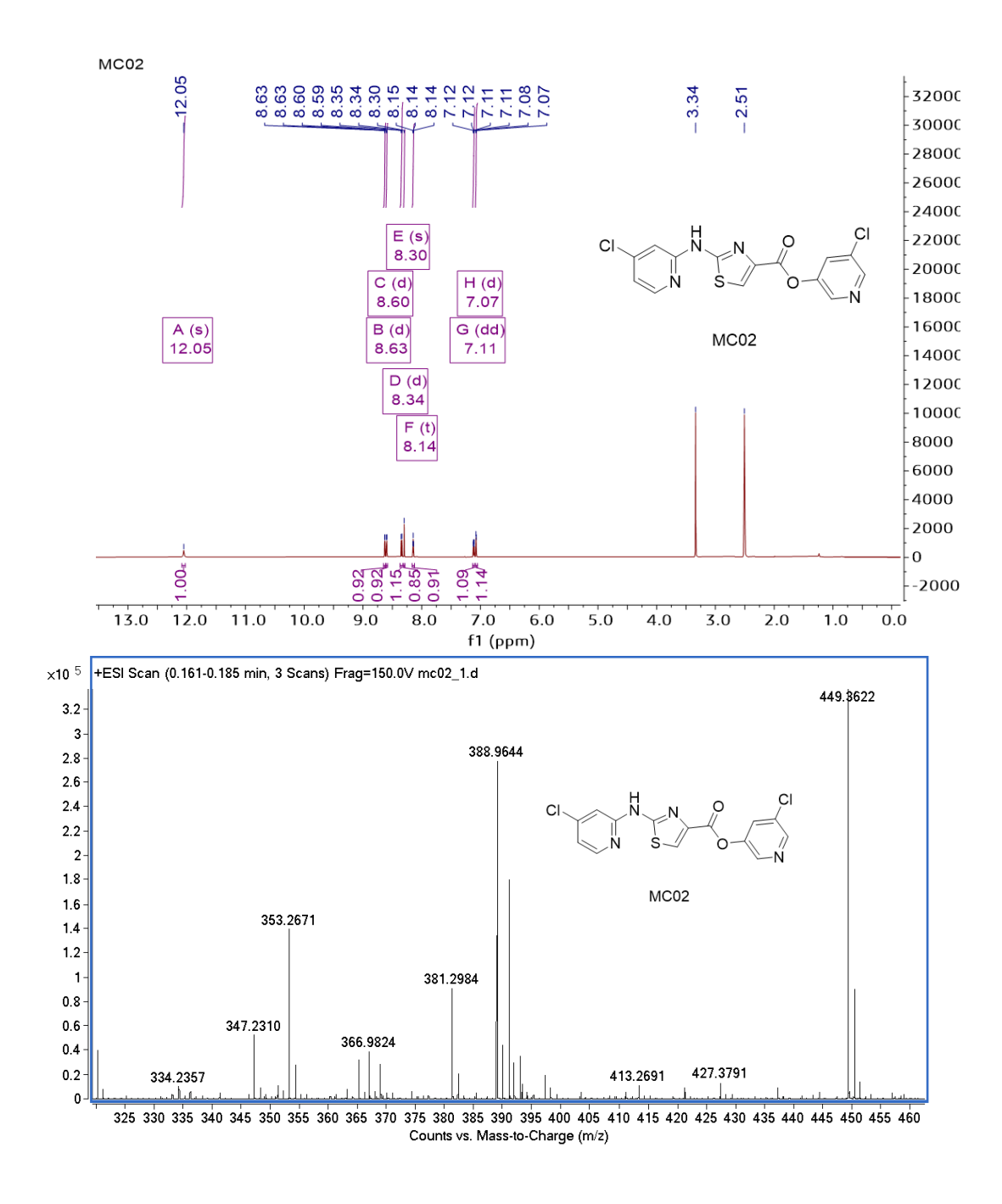
32	MC04BP01	MC04BP01	5-chloropyridin-3-yl 2-(((1 <i>H</i> -benzo[<i>d</i>][1,2,3]triazol-1-yl)methyl)(benzyl)amino)thiazole-4-carboxylate
33	BP0101	BP0101	N-((1 H -benzo[d][1,2,3]triazol-1-yl)methyl)- N -benzyl-4-(pyridin-3-yl)thiazol-2-amine
34	MC12D01	MC12D01	N-((5-chloropyridin-3-yl)methyl)-2-(2-(methyl(phenyl)amino)thiazol-4-yl)-2-oxoacetamide

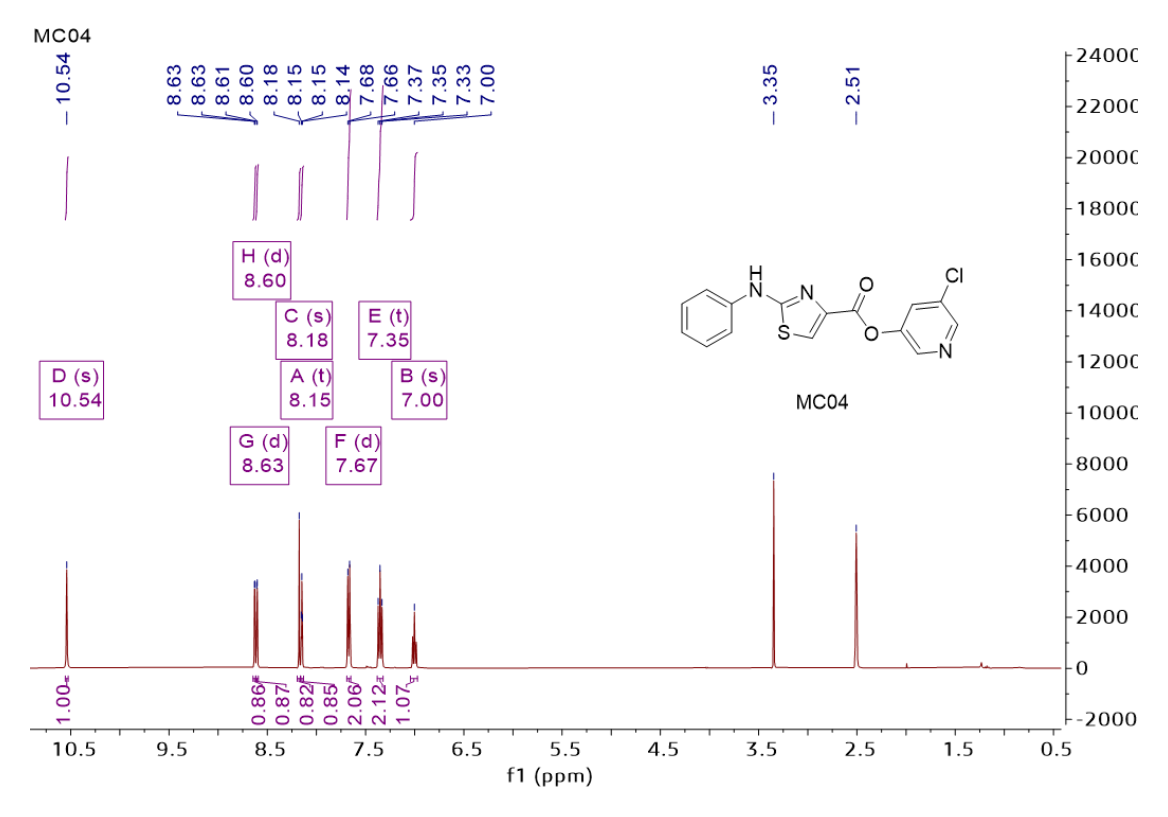
35	AD01	AD01	2-(methyl(phenyl)amino)- <i>N</i> -((<i>S</i>)-1-oxo-3-((<i>S</i>)-2-oxopyrrolidin-3-yl)propan-2-yl)thiazole-4-carboxamide
36	AD02	AD02	tert-butyl (4-(((S)-4-methyl-1-oxo-1-(((S)-1-oxo-3-((S)-2-oxopyrrolidin-3-yl)propan-2-yl)amino)pentan-2-yl)carbamoyl)thiazol-2-yl)carbamate
37	AD04	S O NH N O NH AD04	$(S)\hbox{-}4\hbox{-methyl-}N\hbox{-}((S)\hbox{-}1\hbox{-}oxo\hbox{-}3\hbox{-}((S)\hbox{-}2\hbox{-}oxopyrrolidin-}3\hbox{-}yl)propan-2-$ $yl)\hbox{-}2\hbox{-}((S)\hbox{-}3\hbox{-}phenyl\hbox{-}2\hbox{-}(2\hbox{-}(thiophen-2\hbox{-}yl)acetamido)propanamido)pentanamide}$

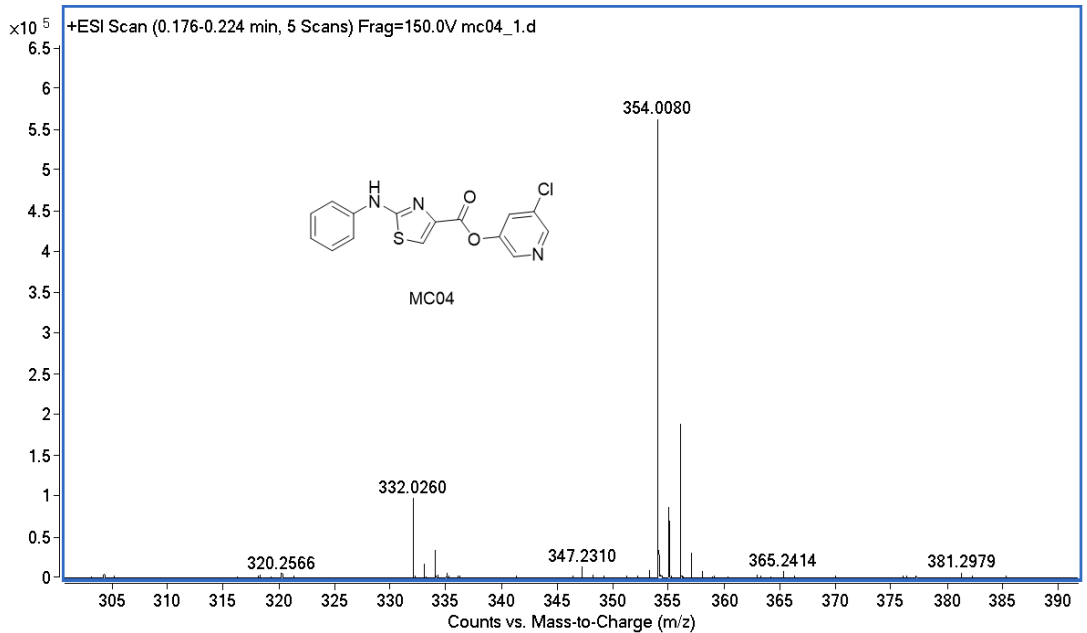
38	AD05	CI N N N N N N N N N N N N N N N N N N N	2-chloro- N -((S)-4-methyl-1-oxo-1-(((S)-1-oxo-3-((S)-2-oxopyrrolidin-3-yl)propan-2-yl)amino)pentan-2-yl)thiazole-4-carboxamide
39	AD06	CI N H O N H	$ 2\text{-chloro-}N\text{-}((S)\text{-}3\text{-methyl-}1\text{-}(((S)\text{-}4\text{-methyl-}1\text{-}oxo\text{-}1\text{-}(((S)\text{-}1\text{-}oxo\text{-}3\text{-}((S)\text{-}2\text{-}oxopyrrolidin-}3\text{-}yl)propan-}2\text{-}yl)amino)pentan-}2\text{-}yl)amino)-1\text{-}oxobutan-}2\text{-}yl)thiazole-}4\text{-}carboxamide $
40	AD06CN01	AD06CN01	$ 2\text{-chloro-}N\text{-}((S)\text{-}1\text{-}(((S)\text{-}1\text{-}(((S)\text{-}1\text{-}cyano\text{-}2\text{-}((S)\text{-}2\text{-}oxopyrrolidin-}3\text{-}yl)\text{ethyl})amino)\text{-}4\text{-}methyl\text{-}1\text{-}oxopentan\text{-}2\text{-}yl)amino)\text{-}3\text{-}methyl\text{-}1\text{-}oxobutan\text{-}2\text{-}yl)thiazole\text{-}4\text{-}carboxamide} $

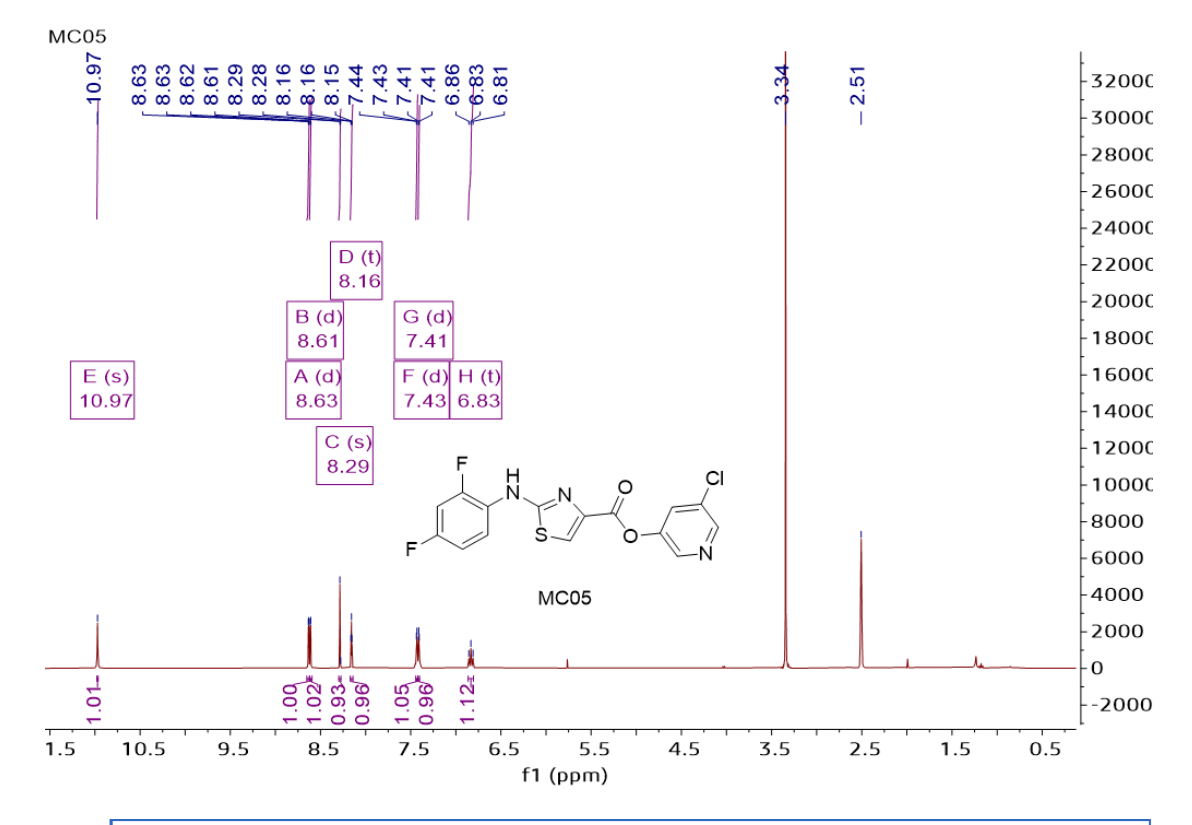
A3 ¹H NMR and mass spectra

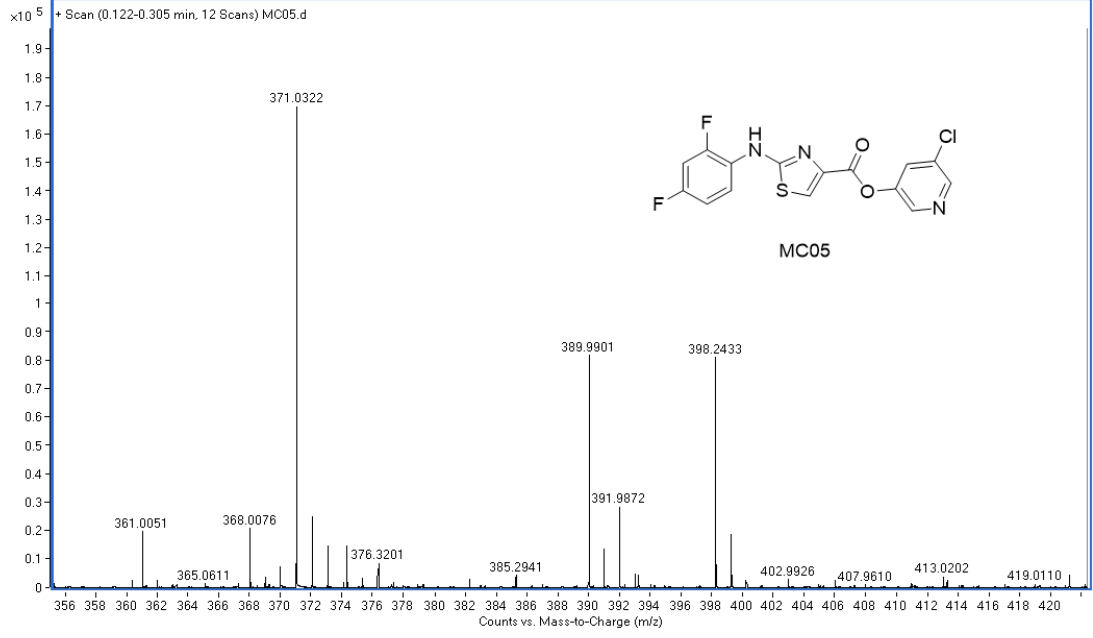
The ¹H NMR and mass spectra of synthesized compounds synthesized shown in Table A.1 are shown as follows.

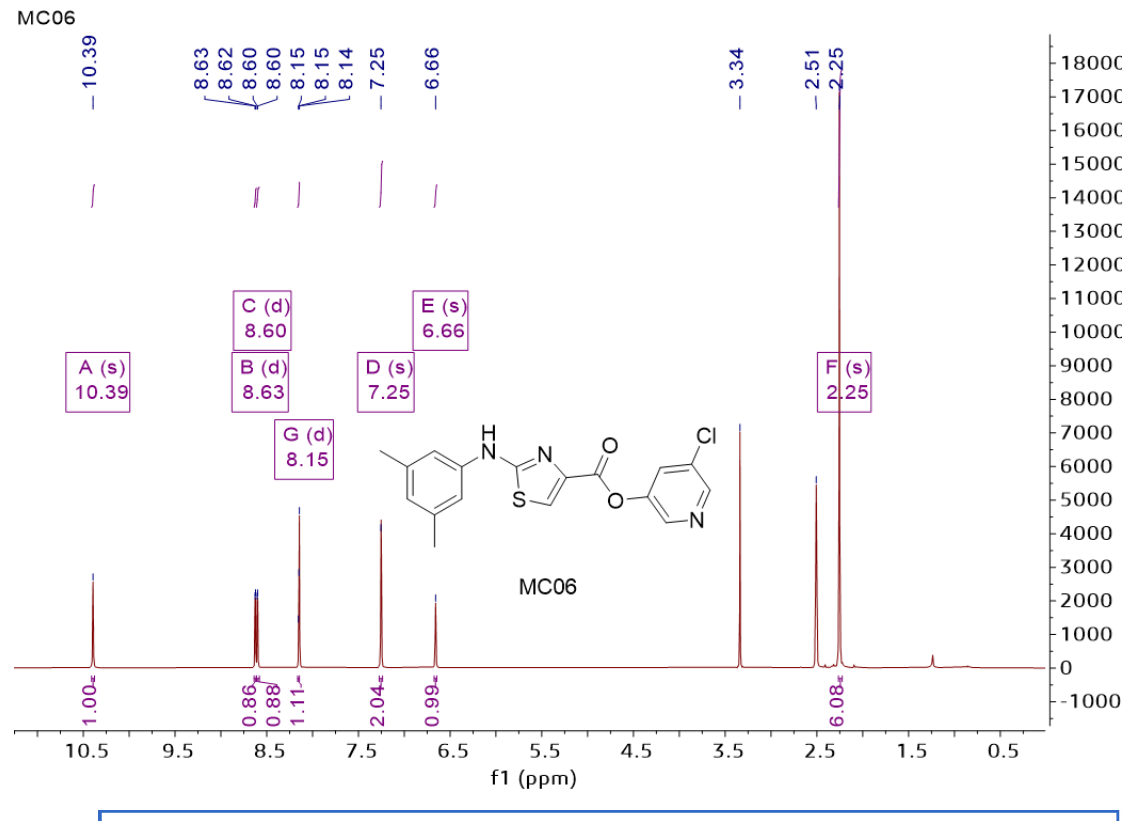


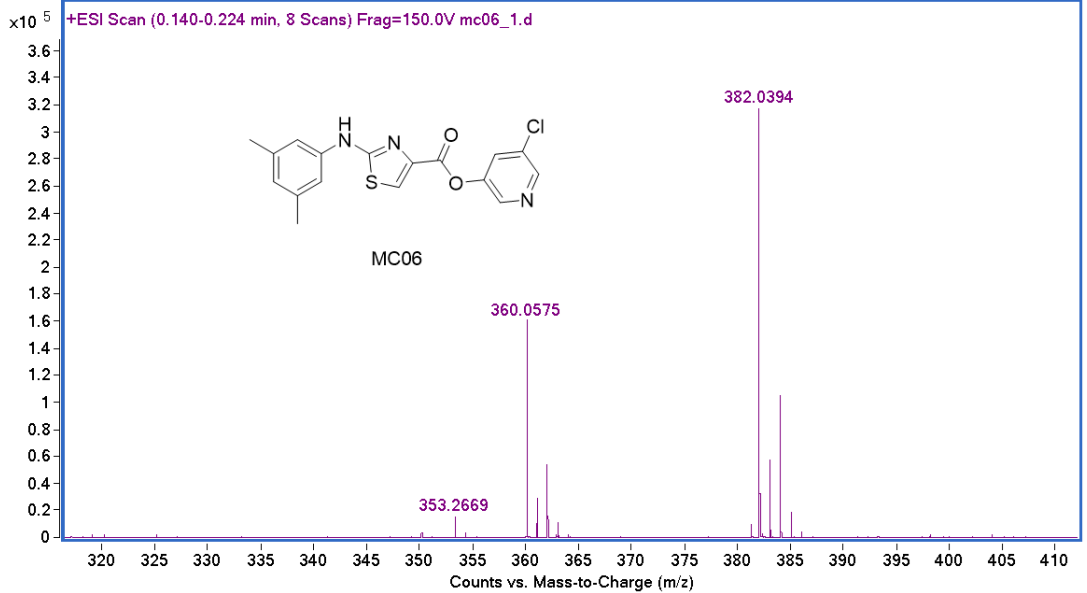


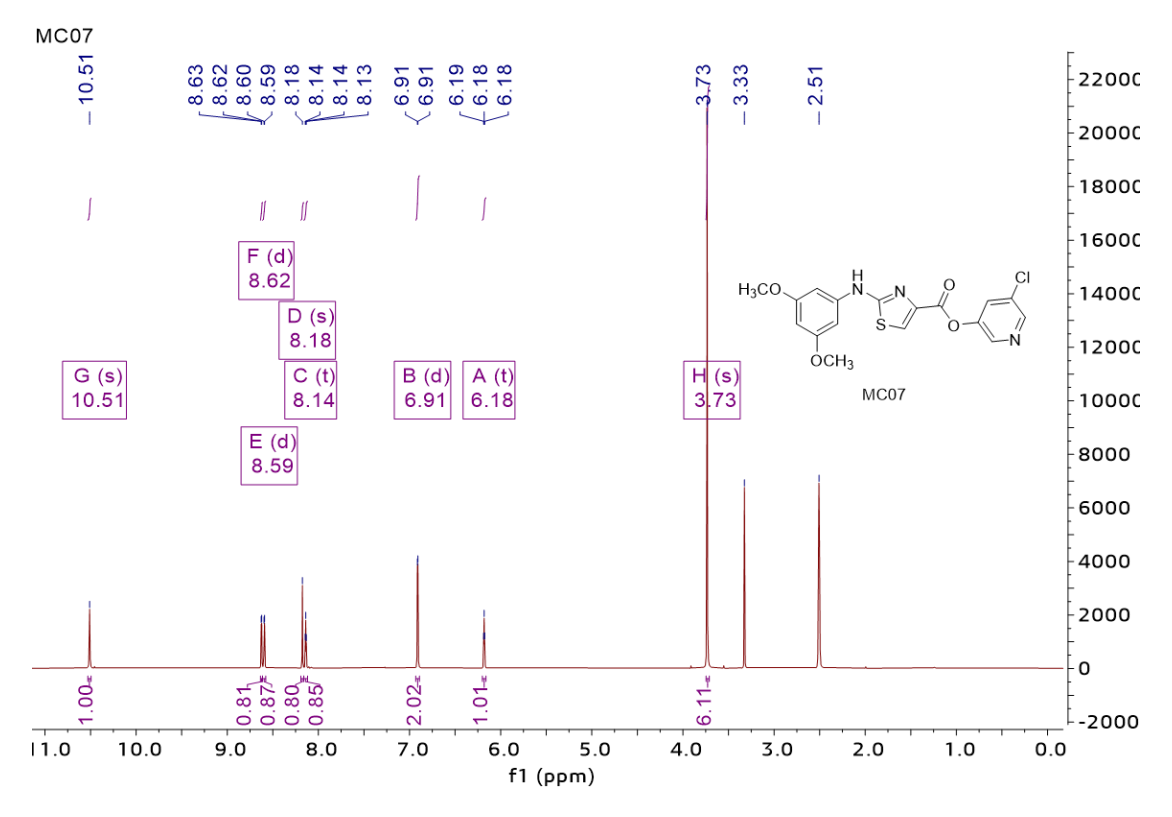


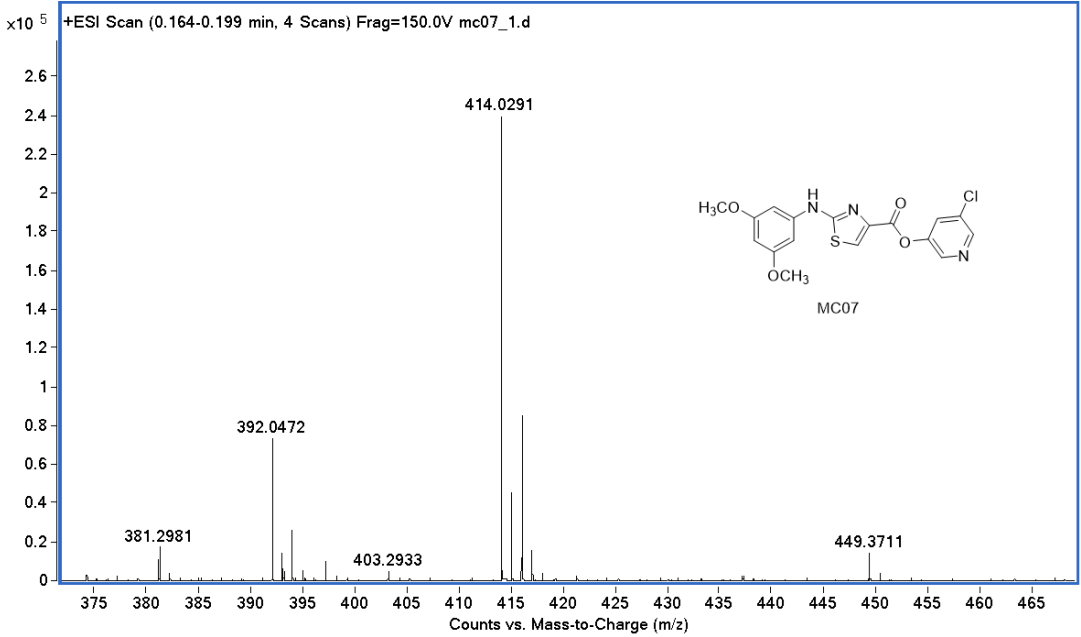


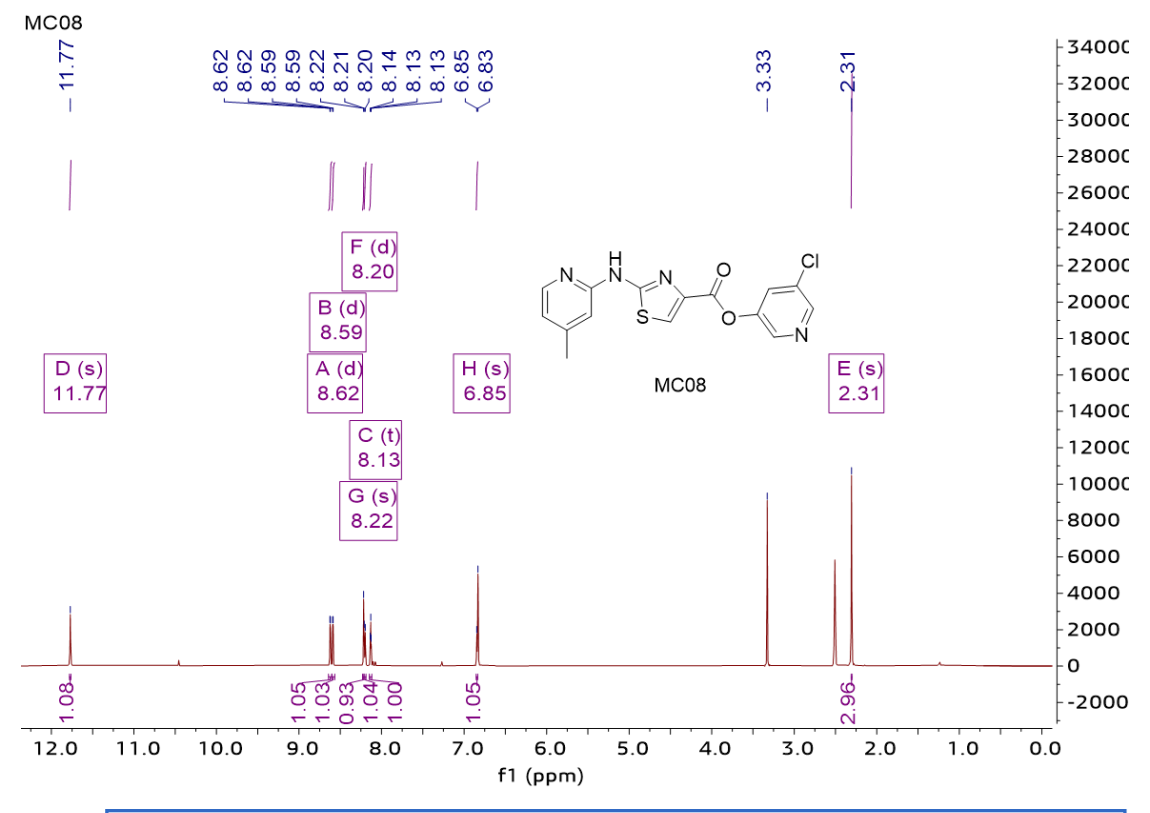


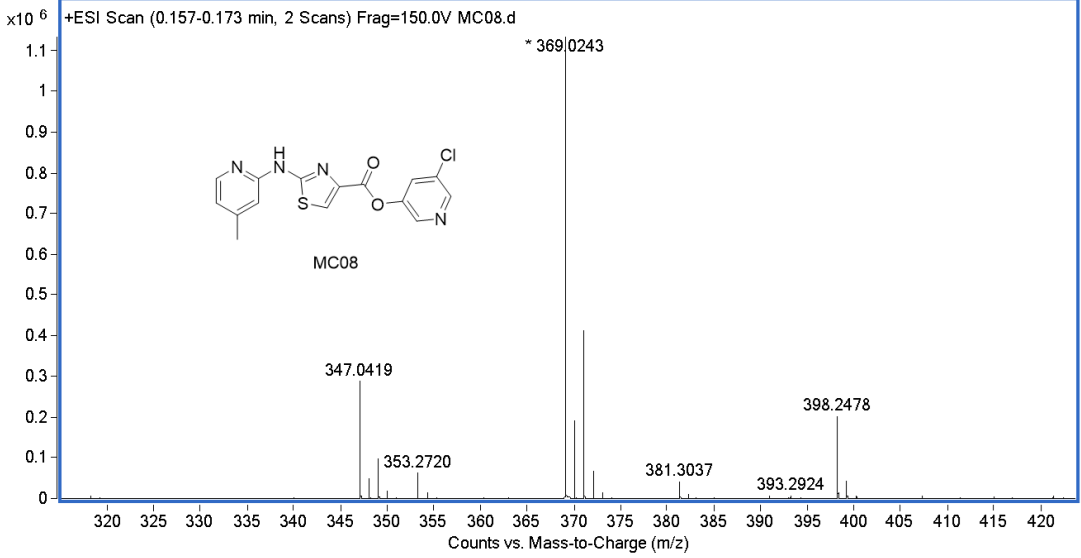


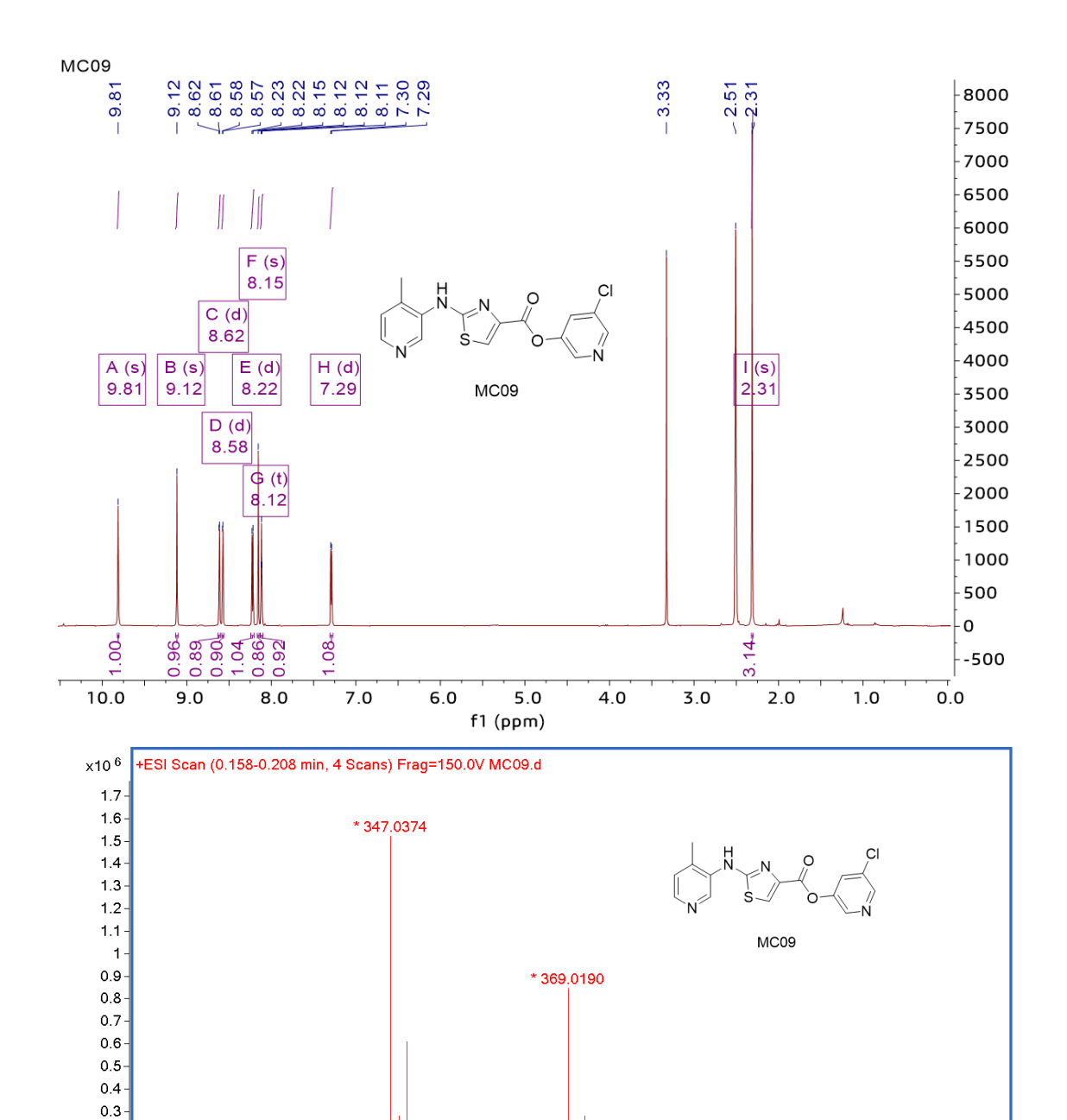












398.2421

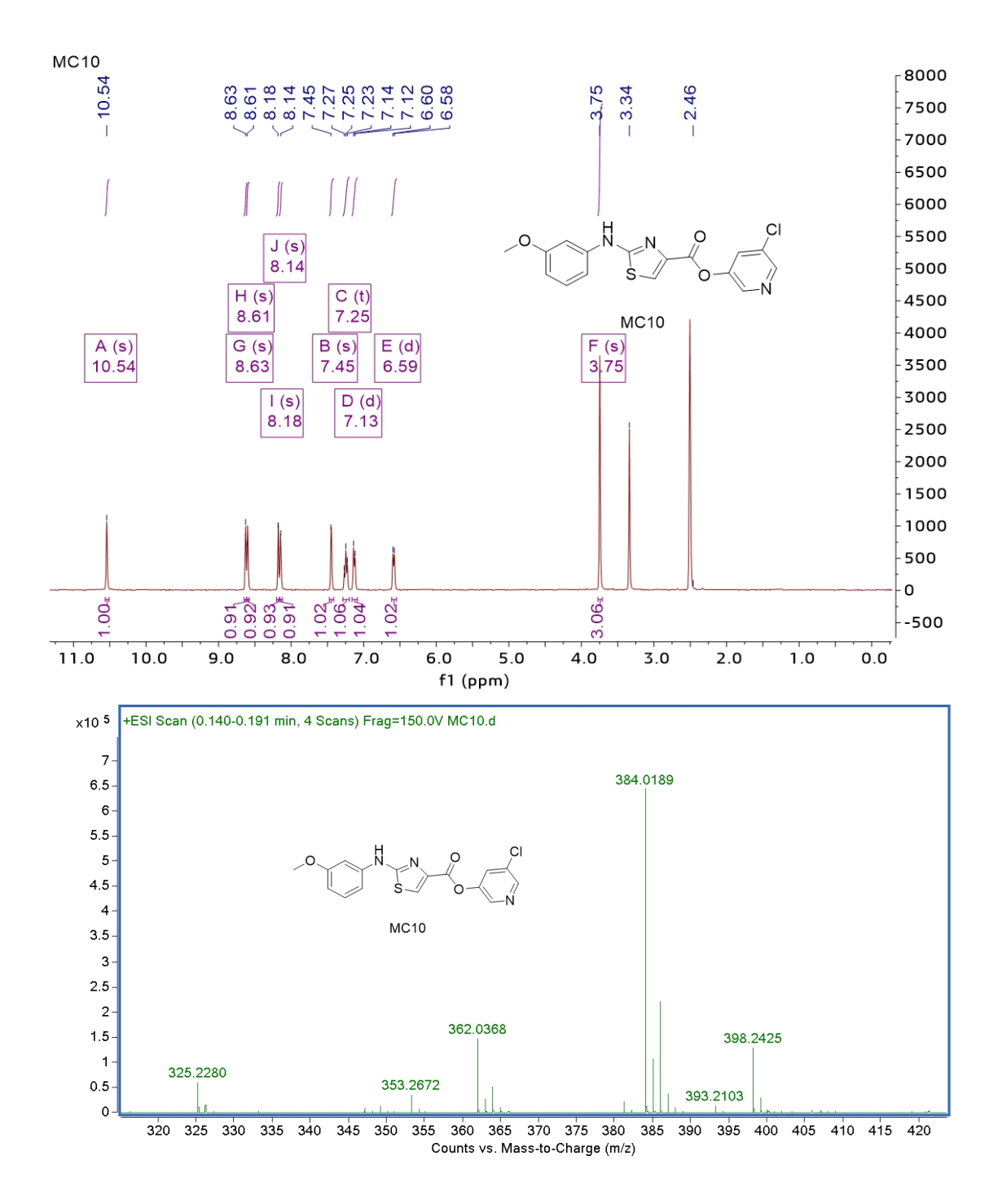
381.2983

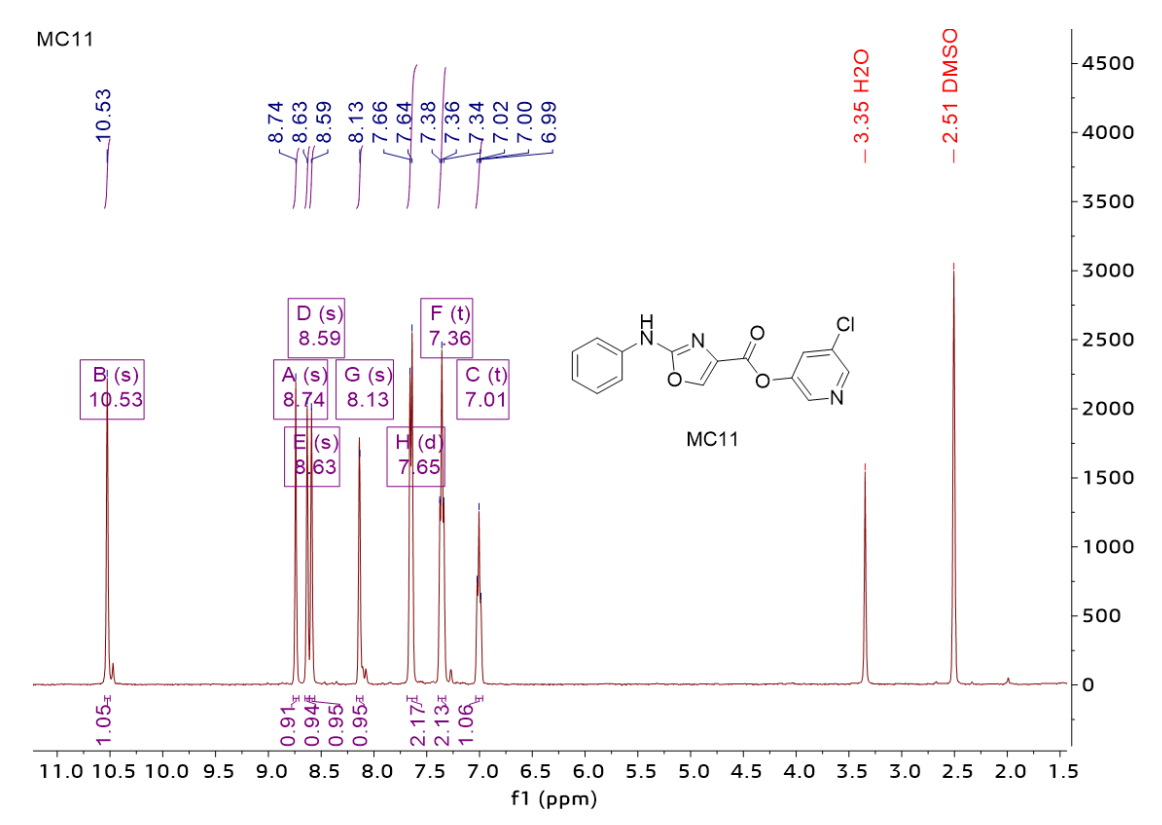
320 325 330 335 340 345 350 355 360 365 370 375 380 385 390 395 400 405 410 415 420 Counts vs. Mass-to-Charge (m/z)

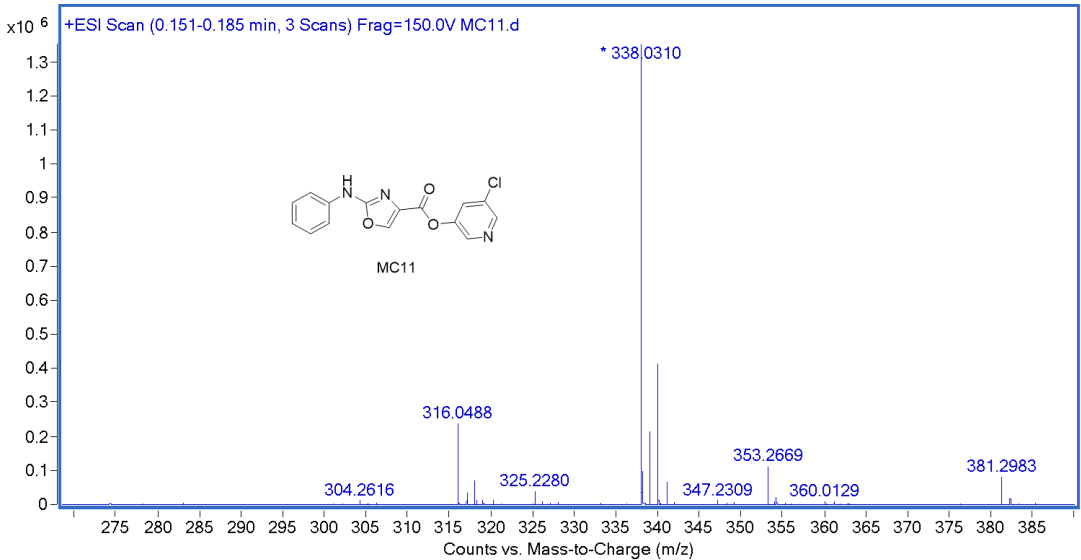
0.2

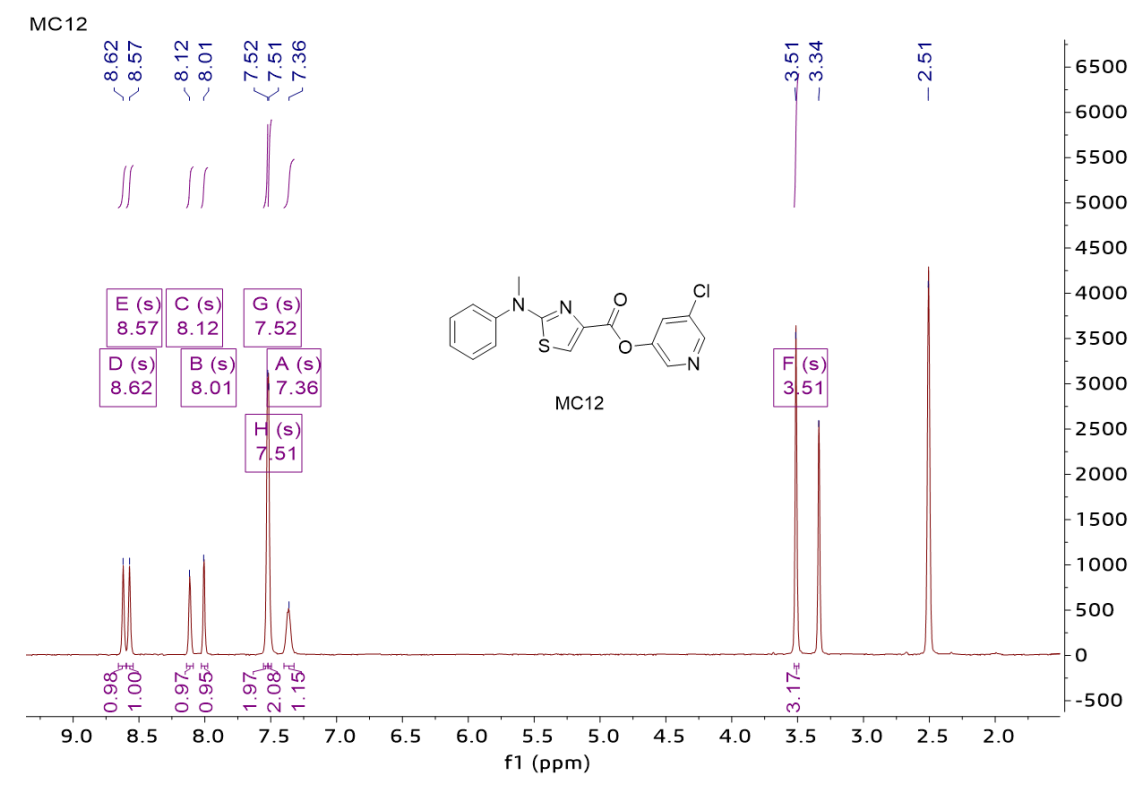
0.1

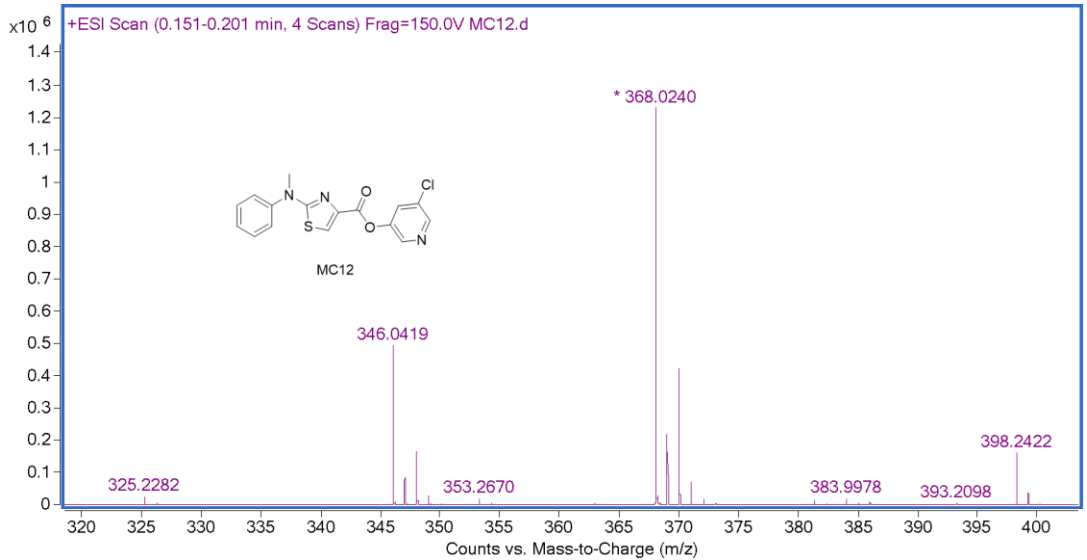
0-

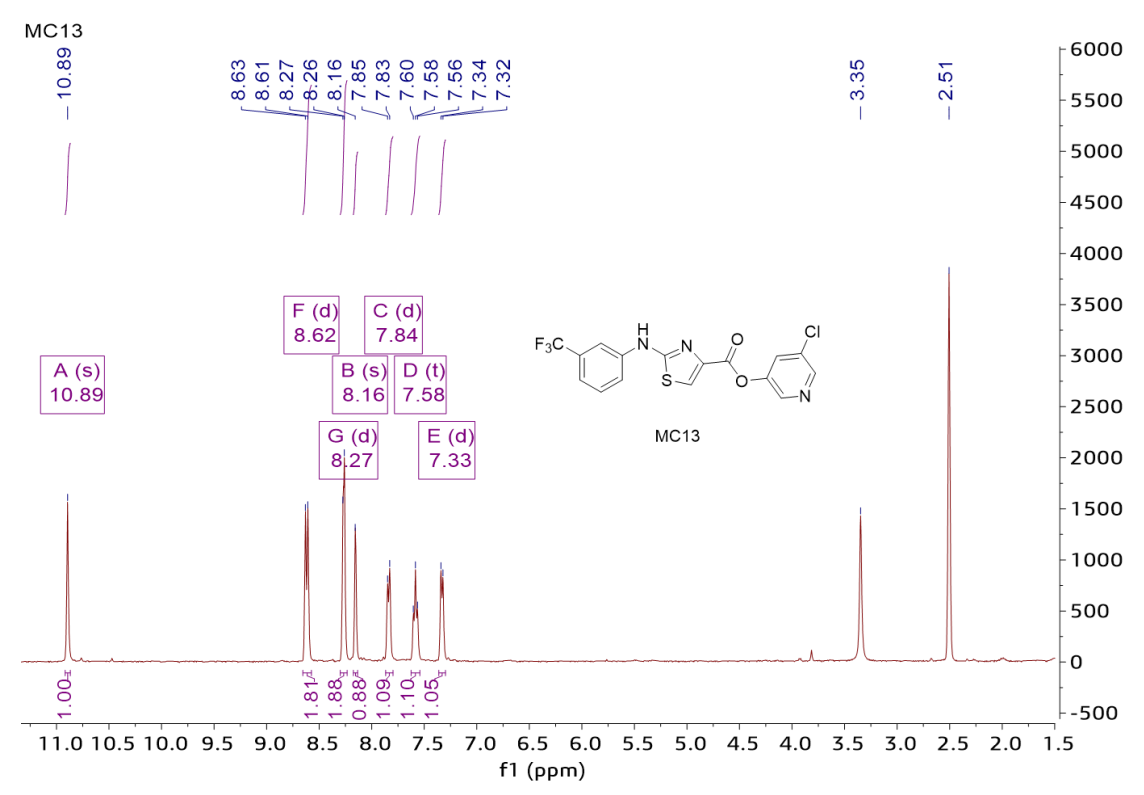


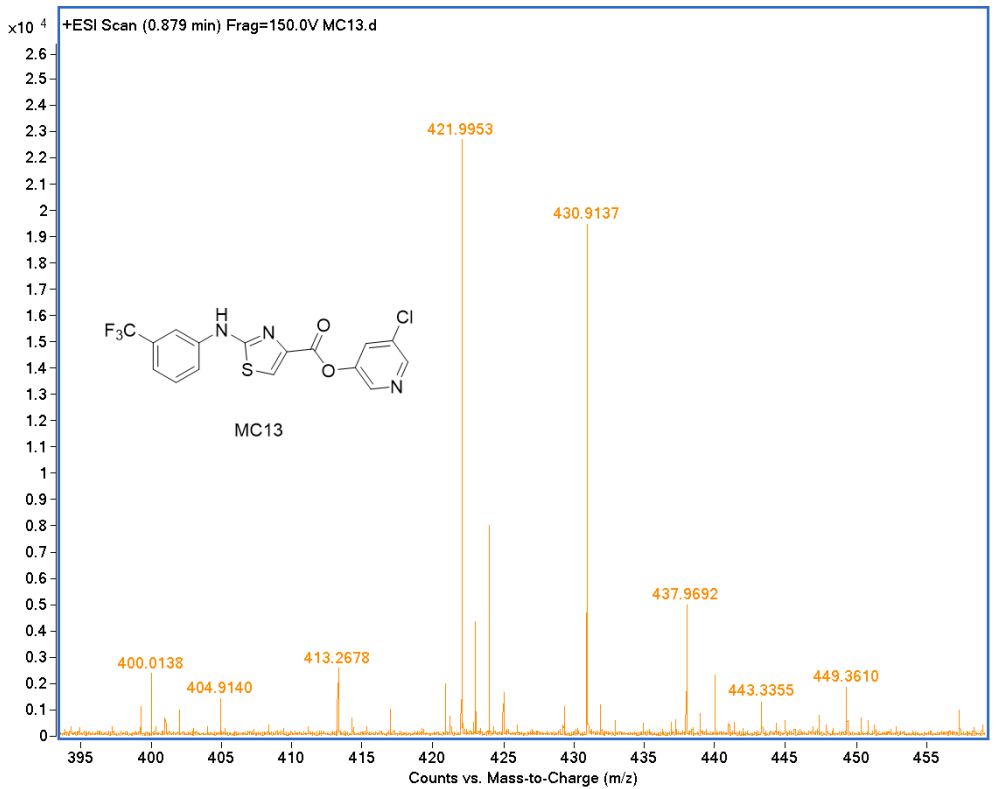


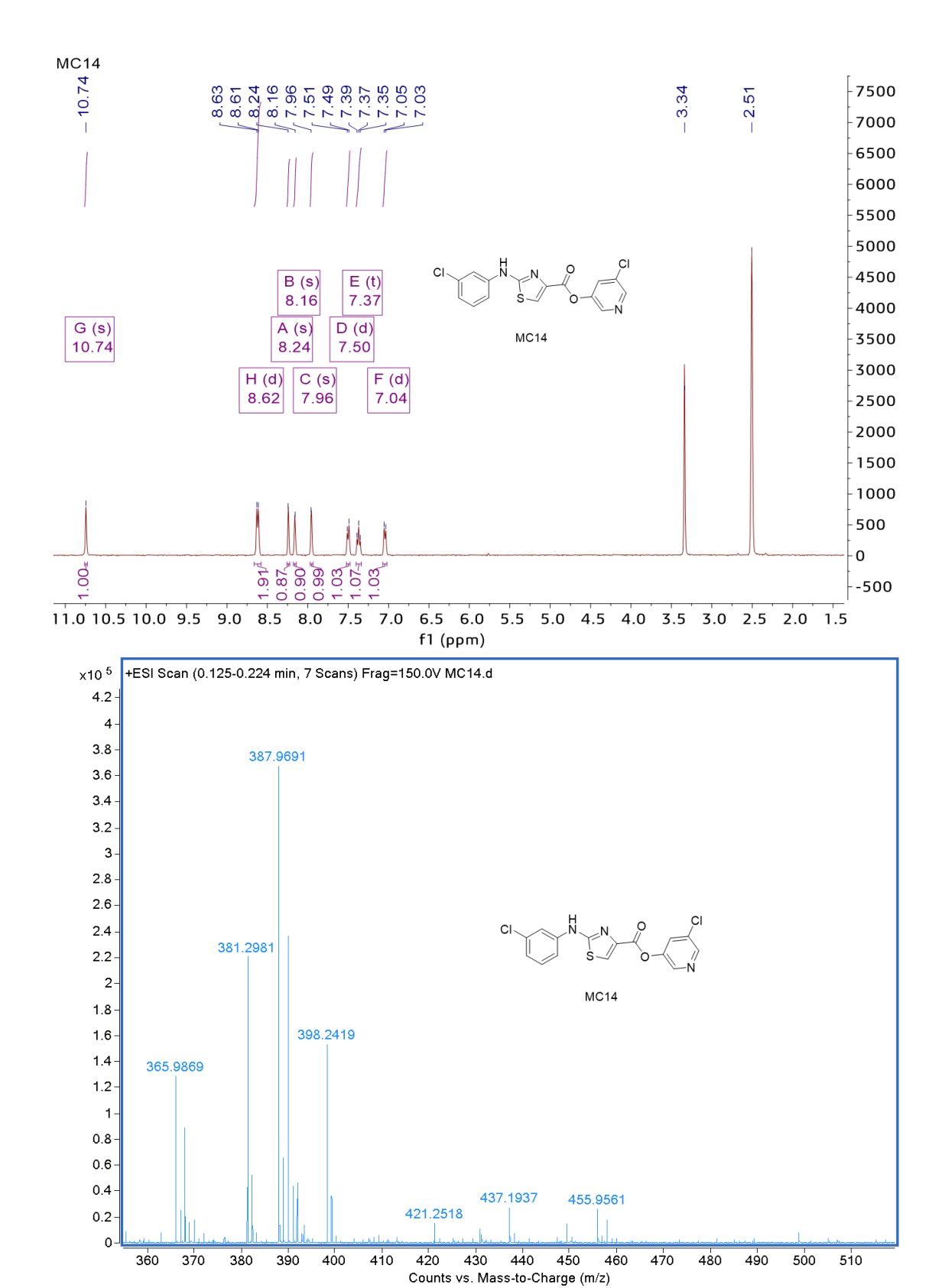


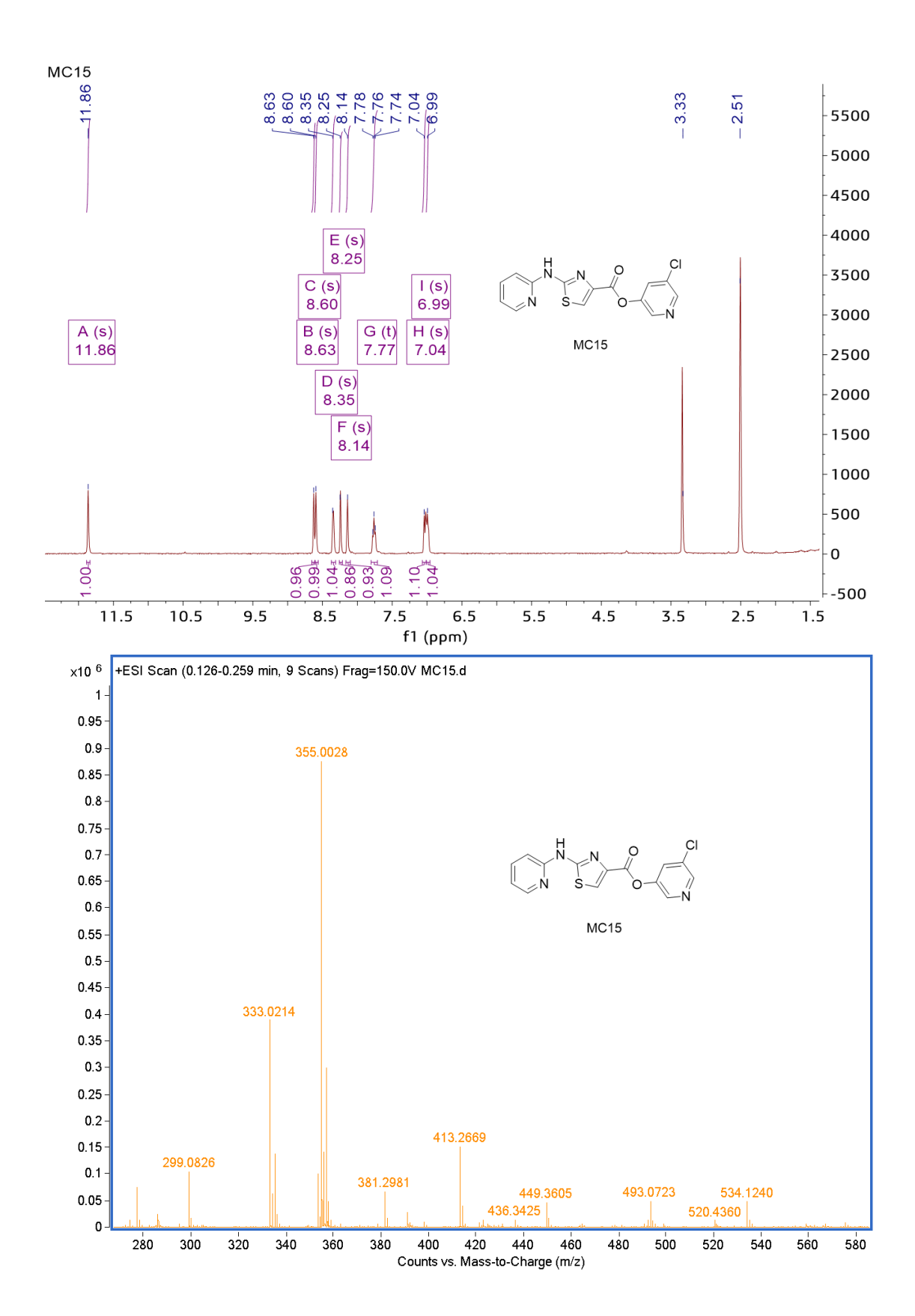


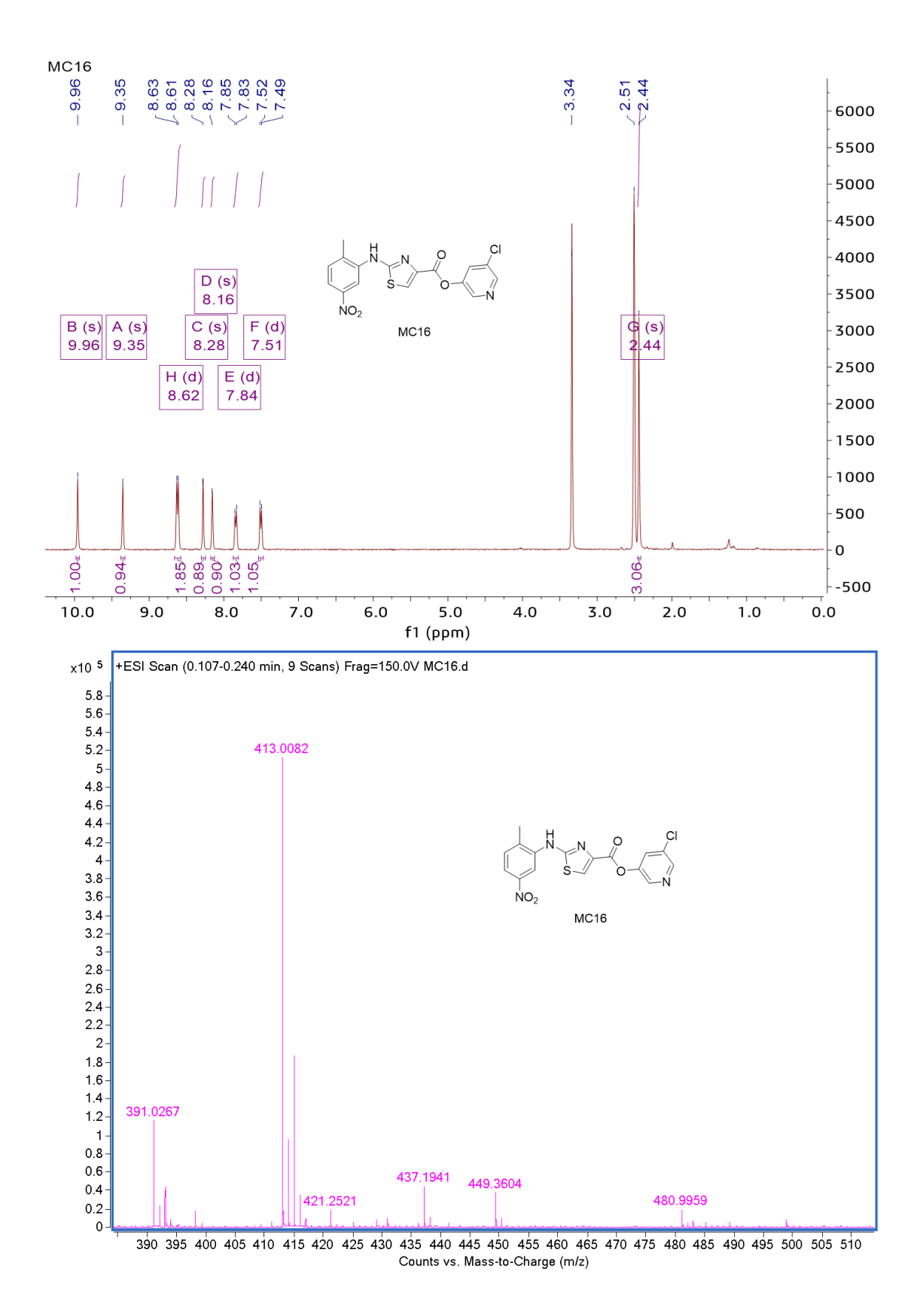


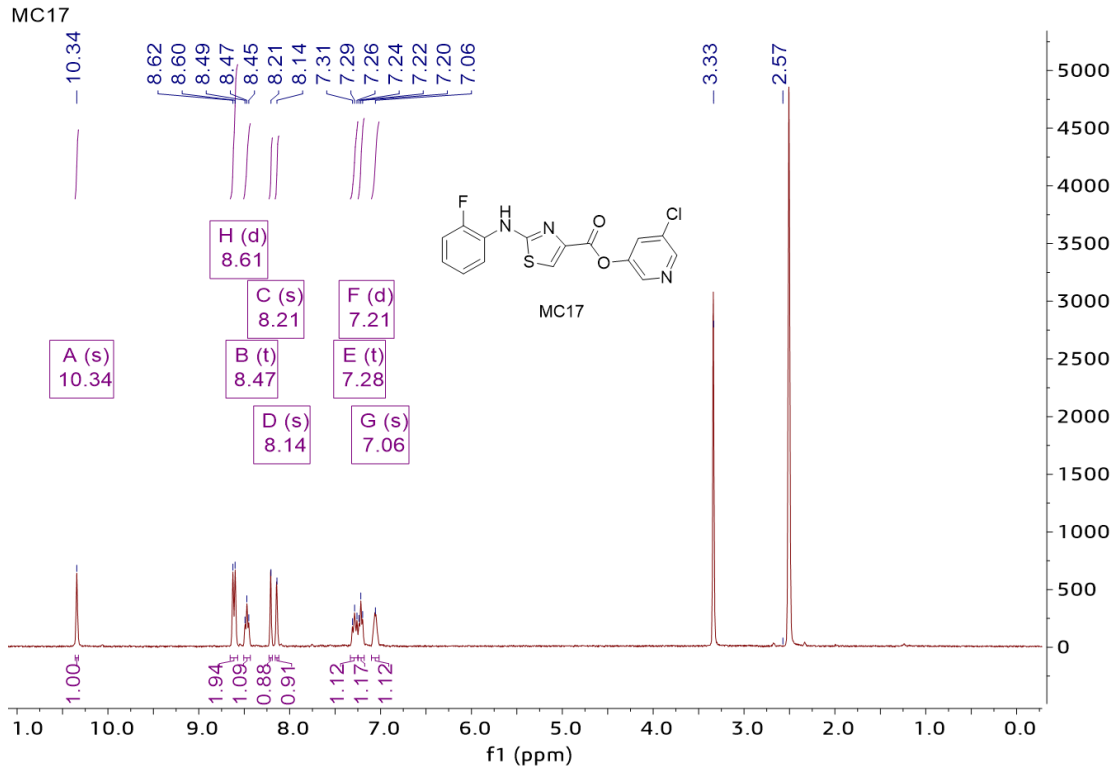


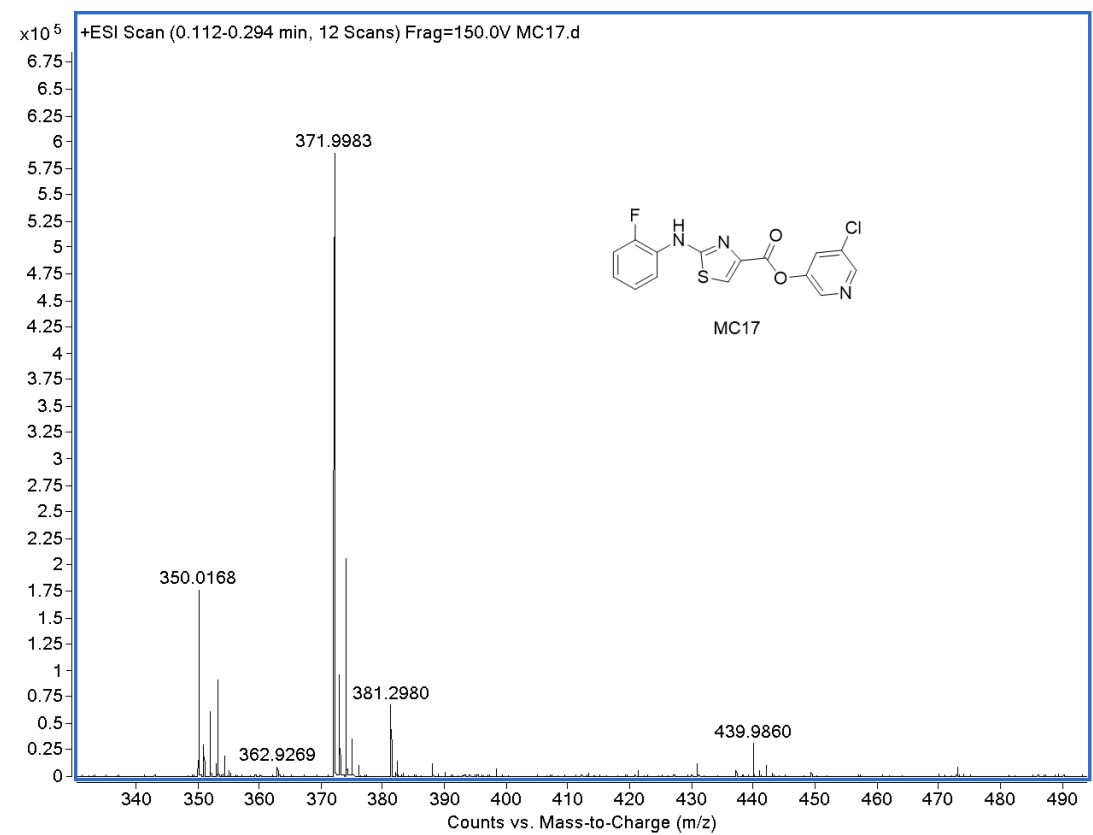


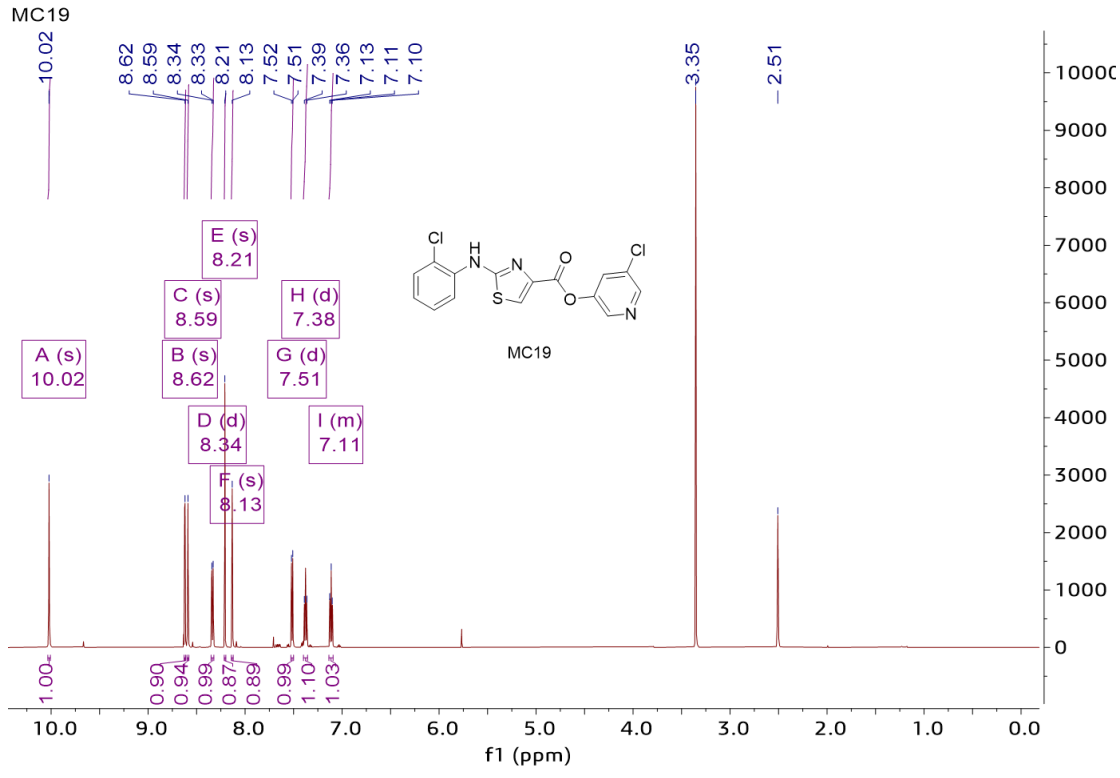


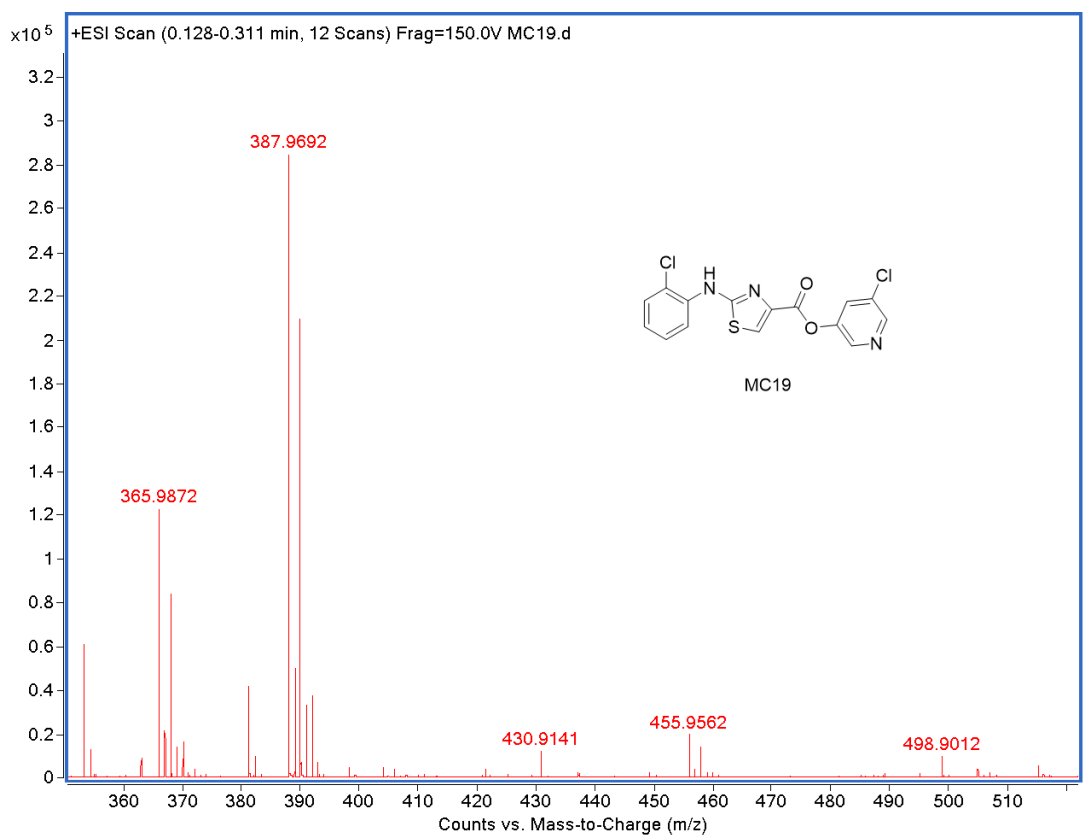


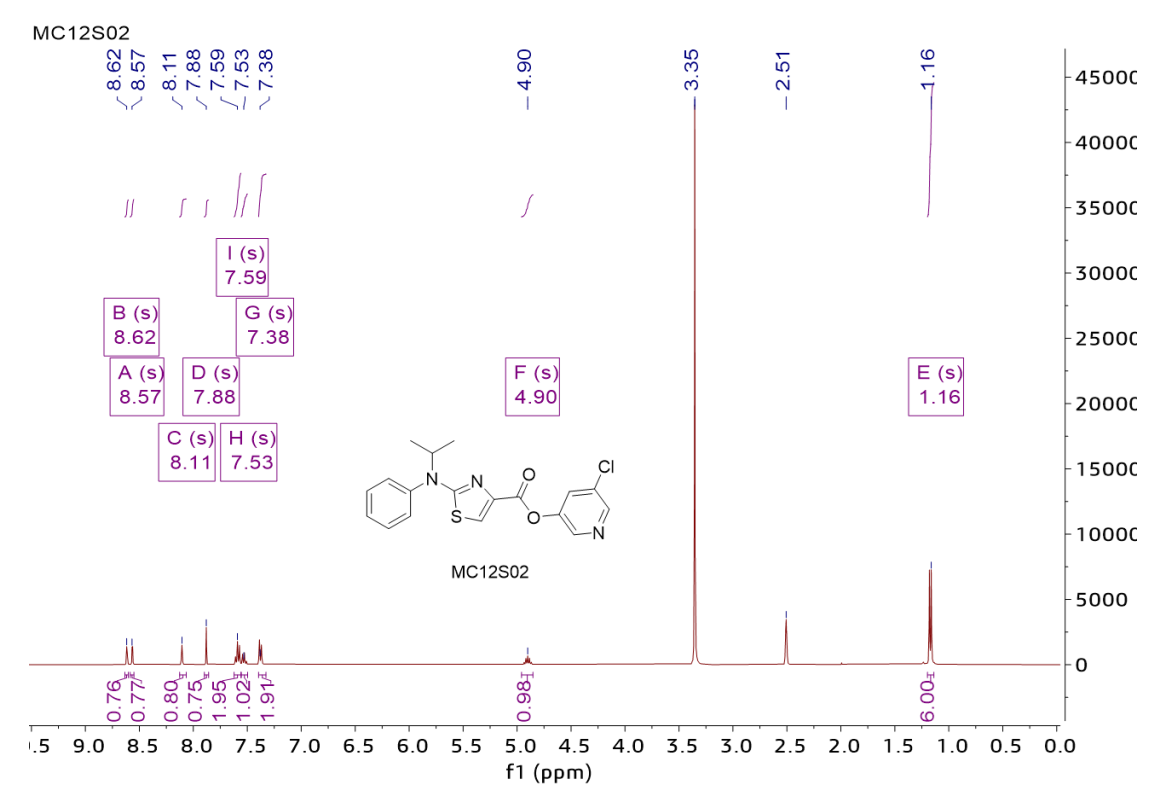


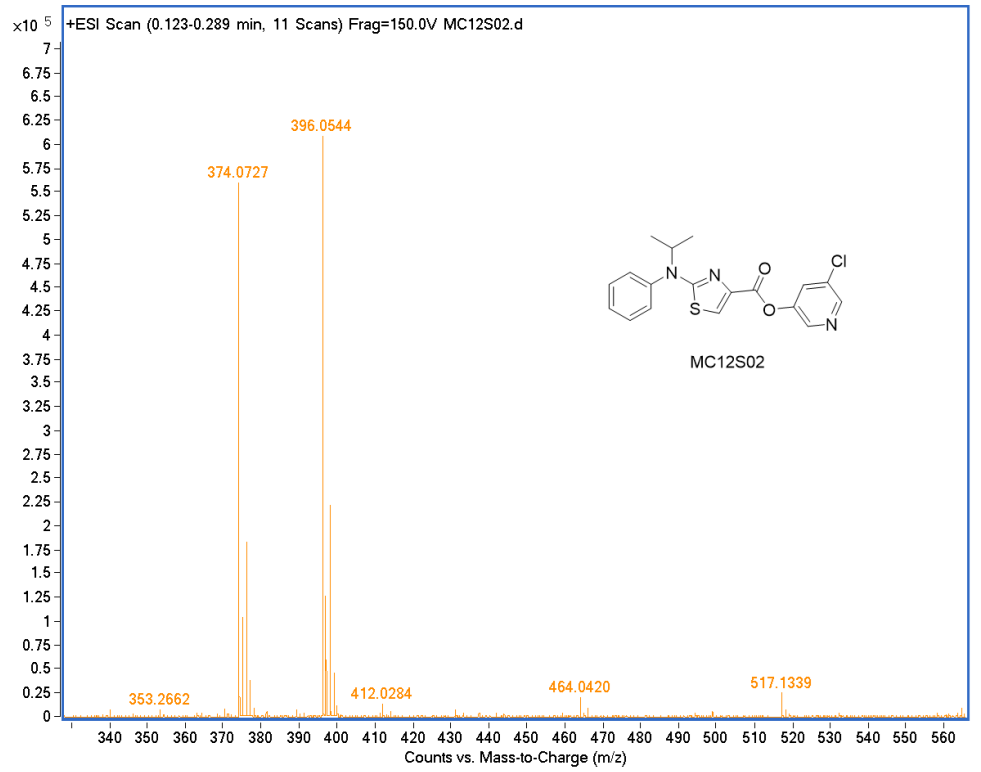


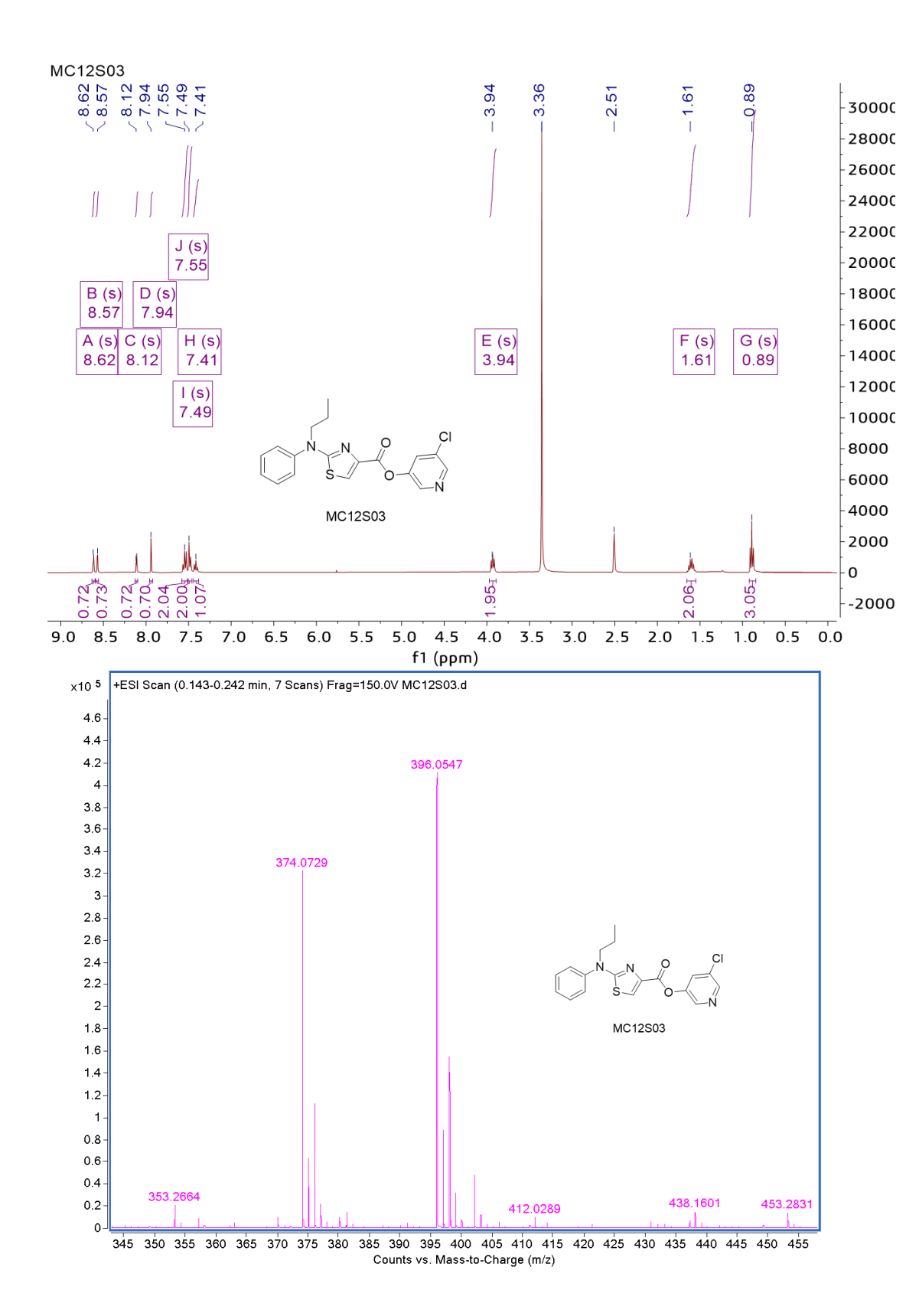


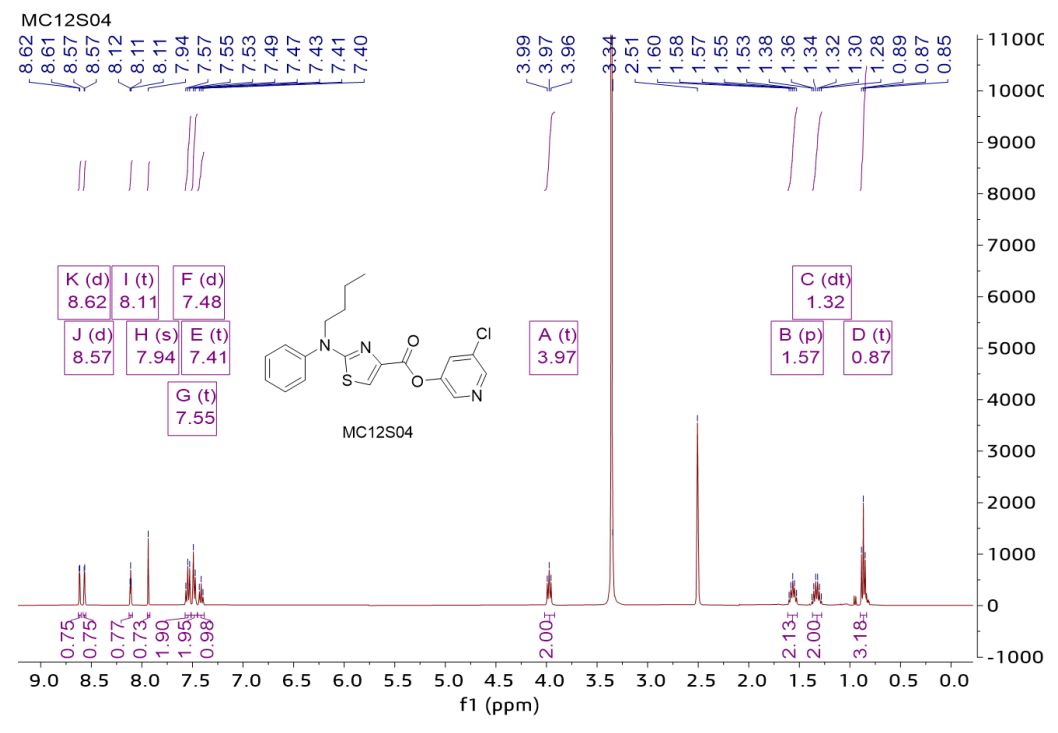


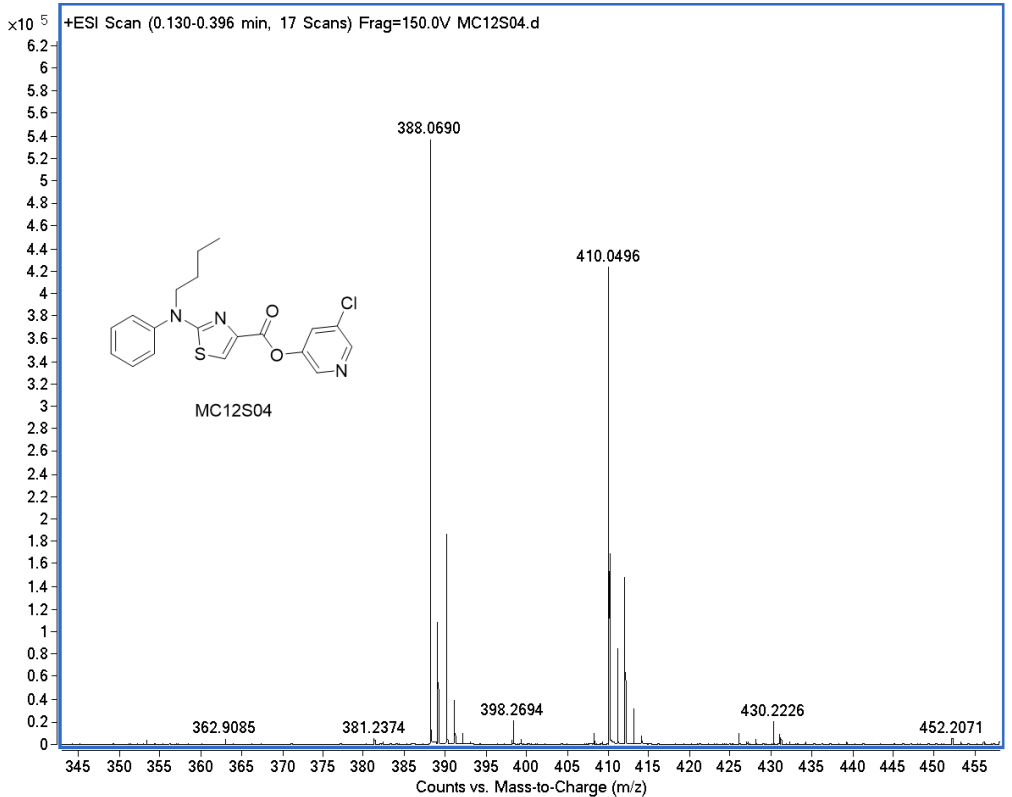


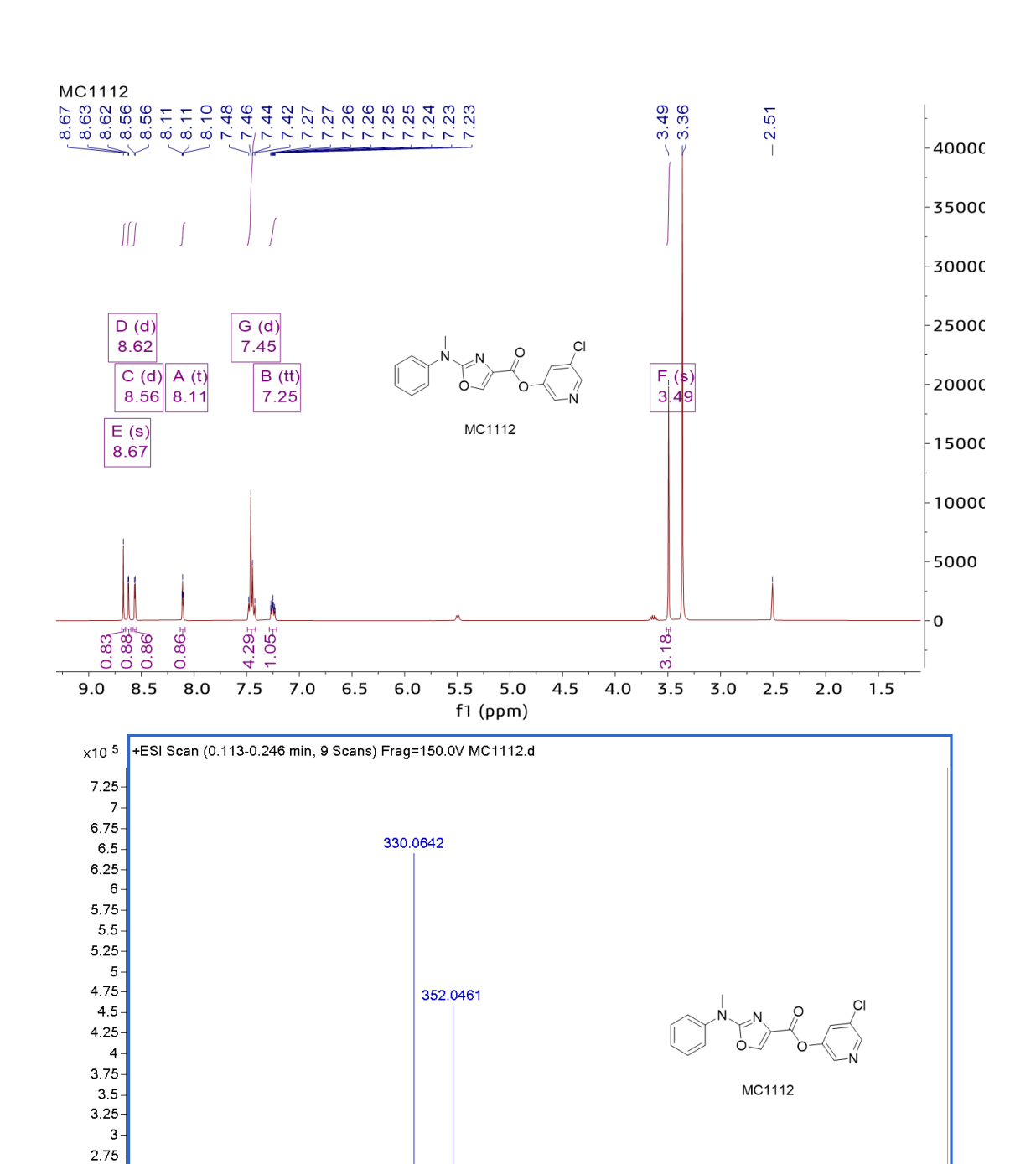












180 200 220 240 260 280 300 320 340 360 380 400 420 440 460 480 500 520 540 560 580 600 620 Counts vs. Mass-to-Charge (m/z)

451.2821

570.1154

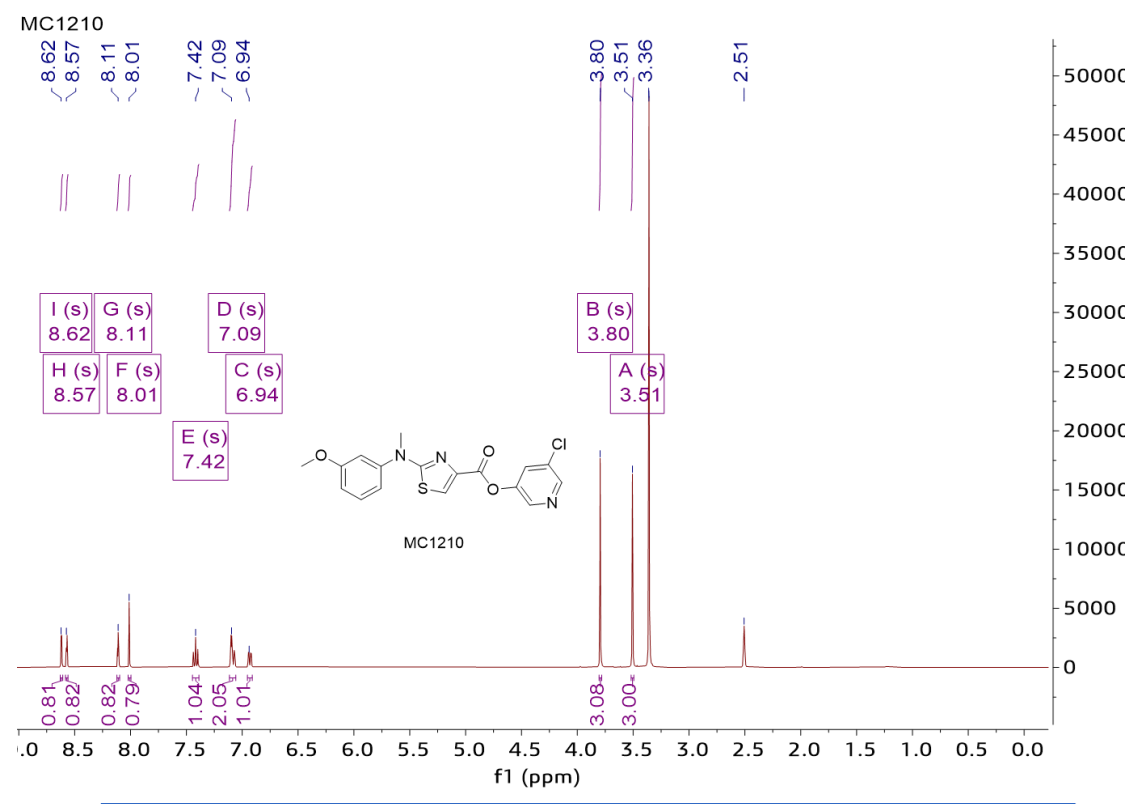
2.5 -2.25 -2 -1.75 -1.5 -

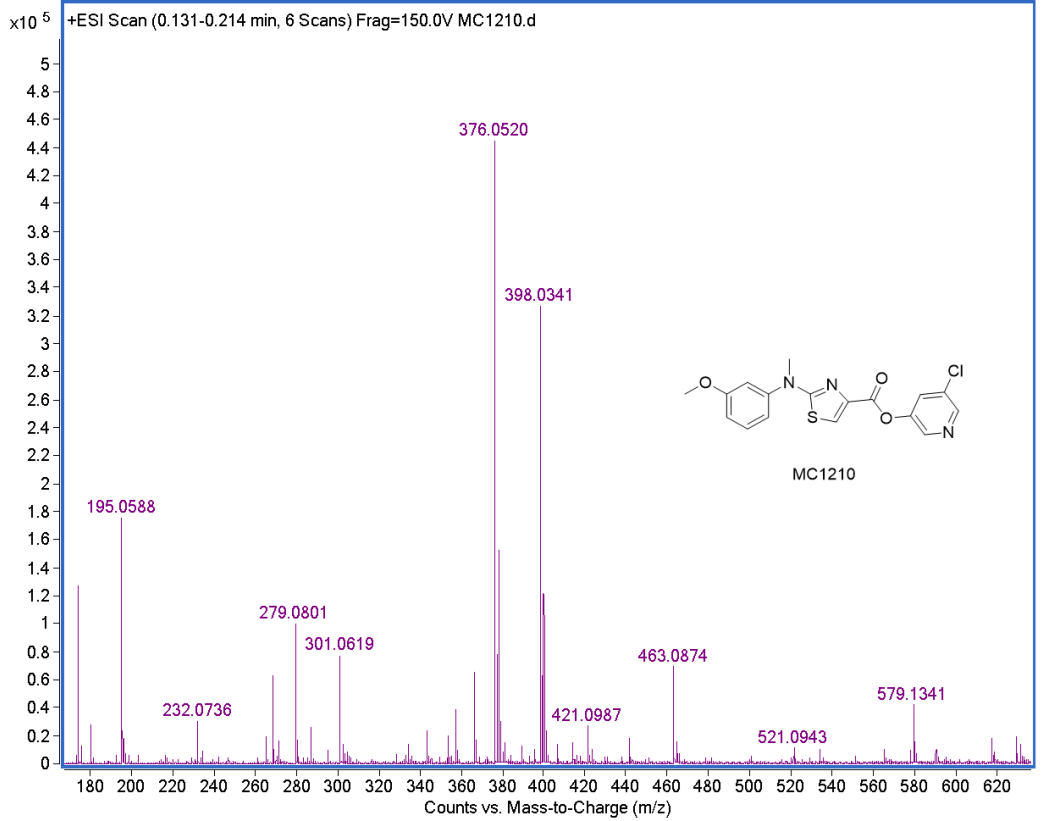
1.25 1-

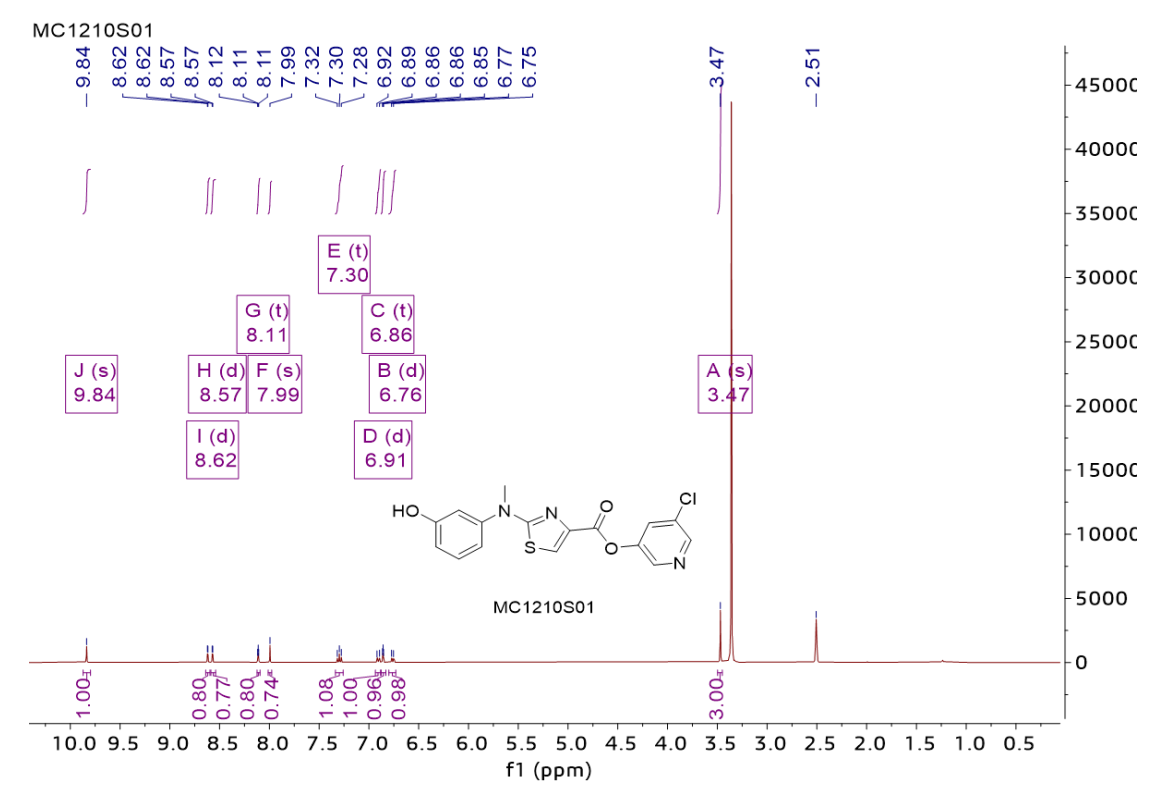
0.75 0.5

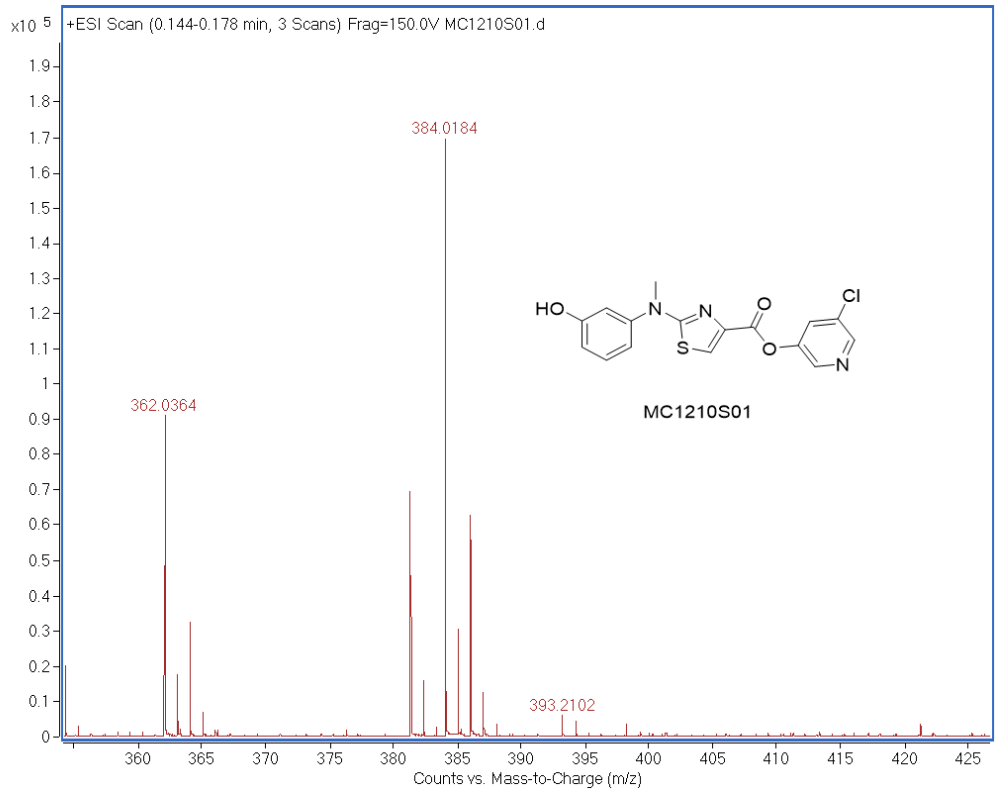
0.25

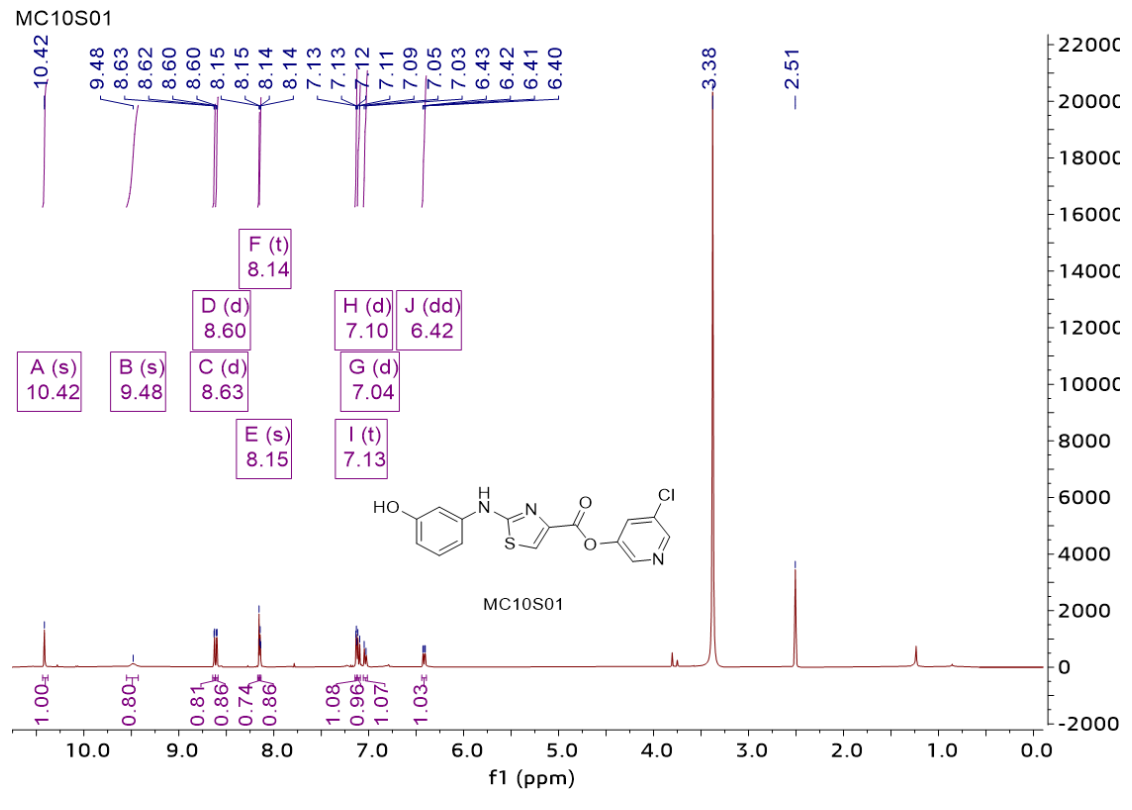
241.0586

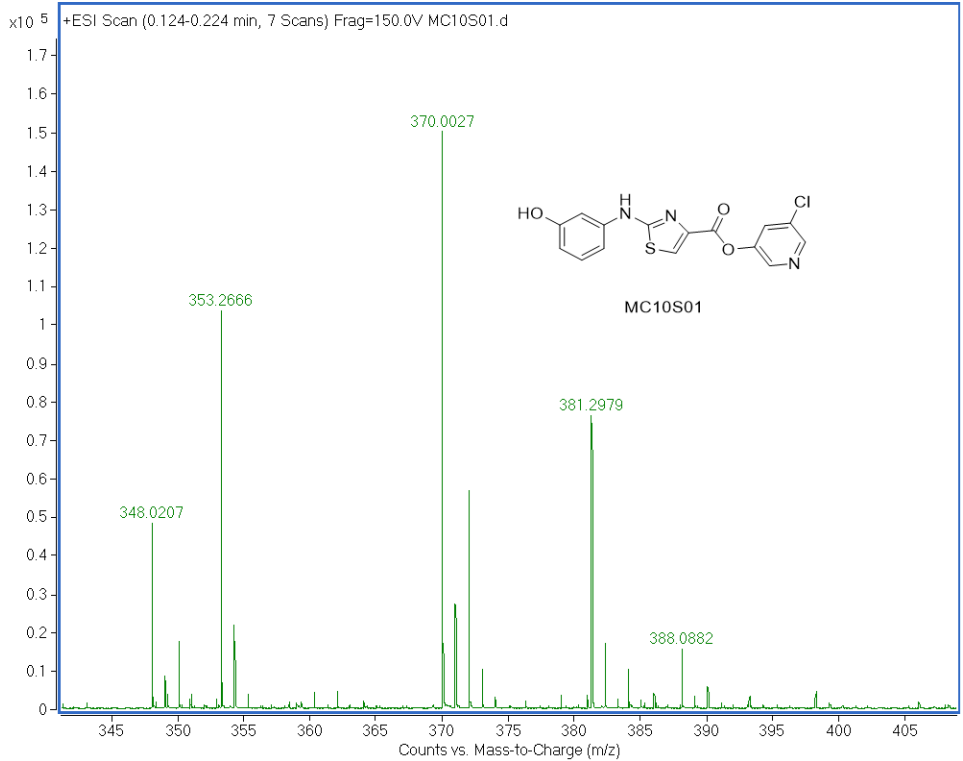


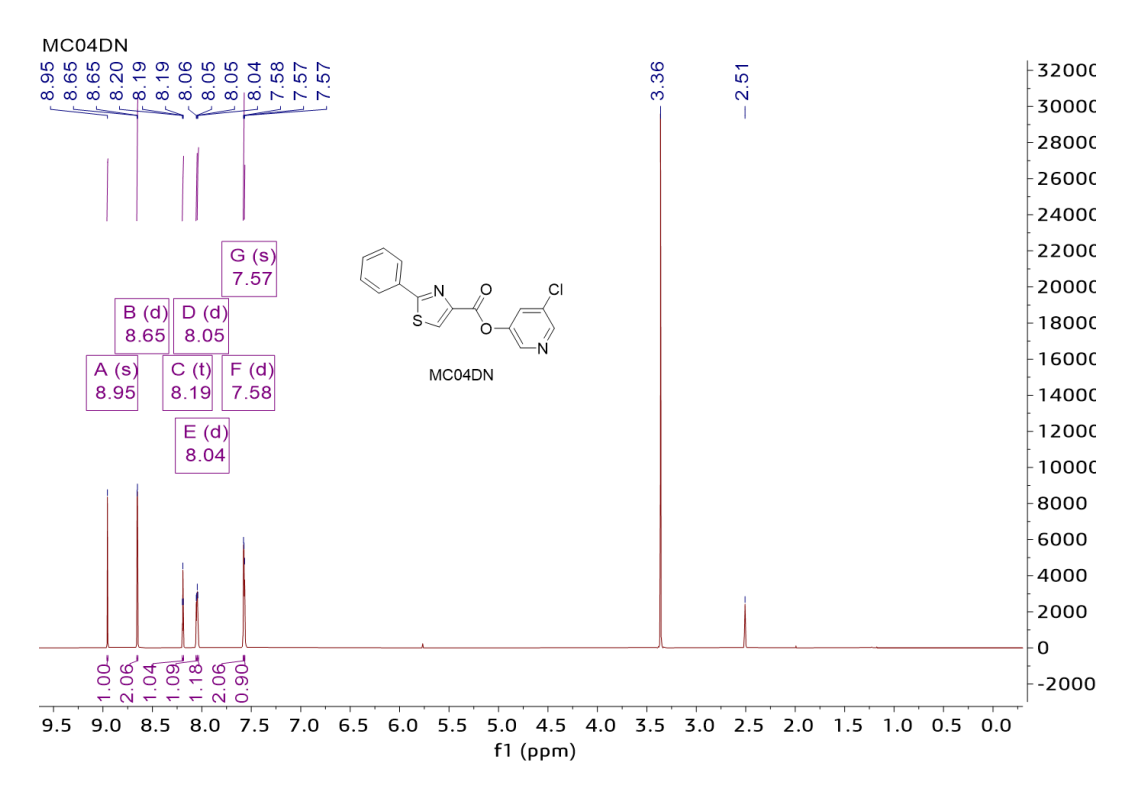


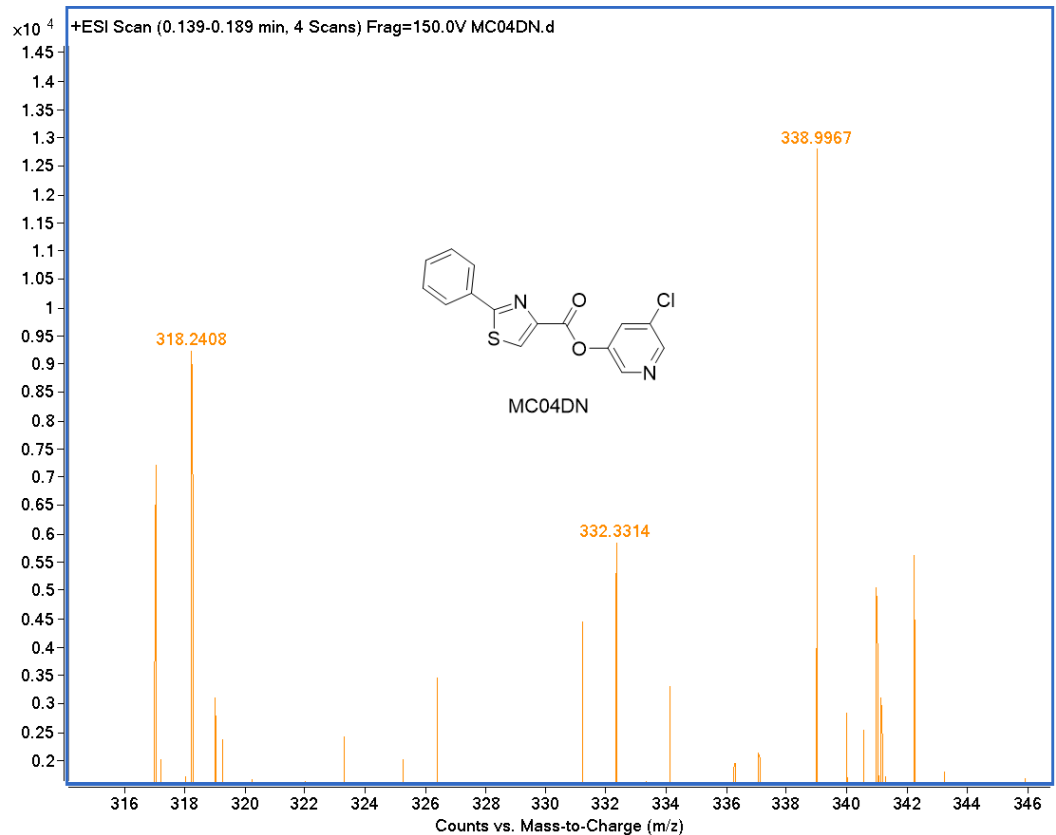


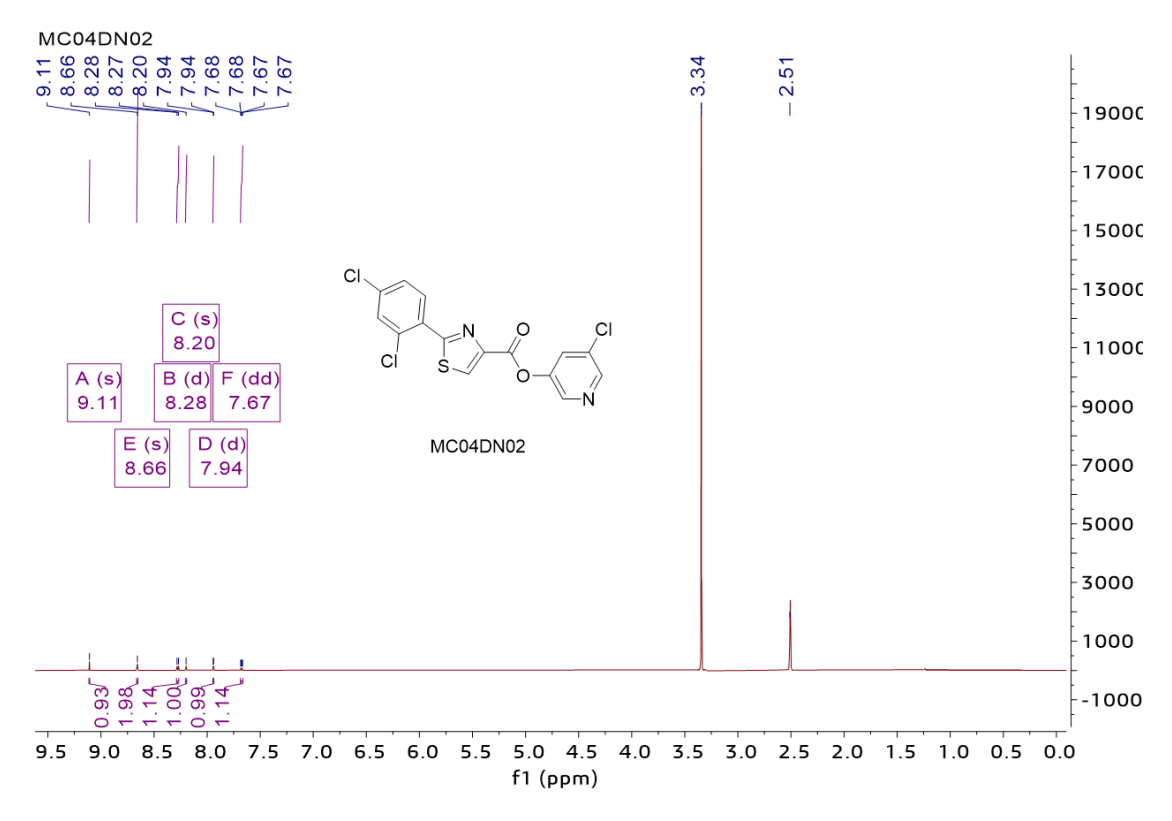


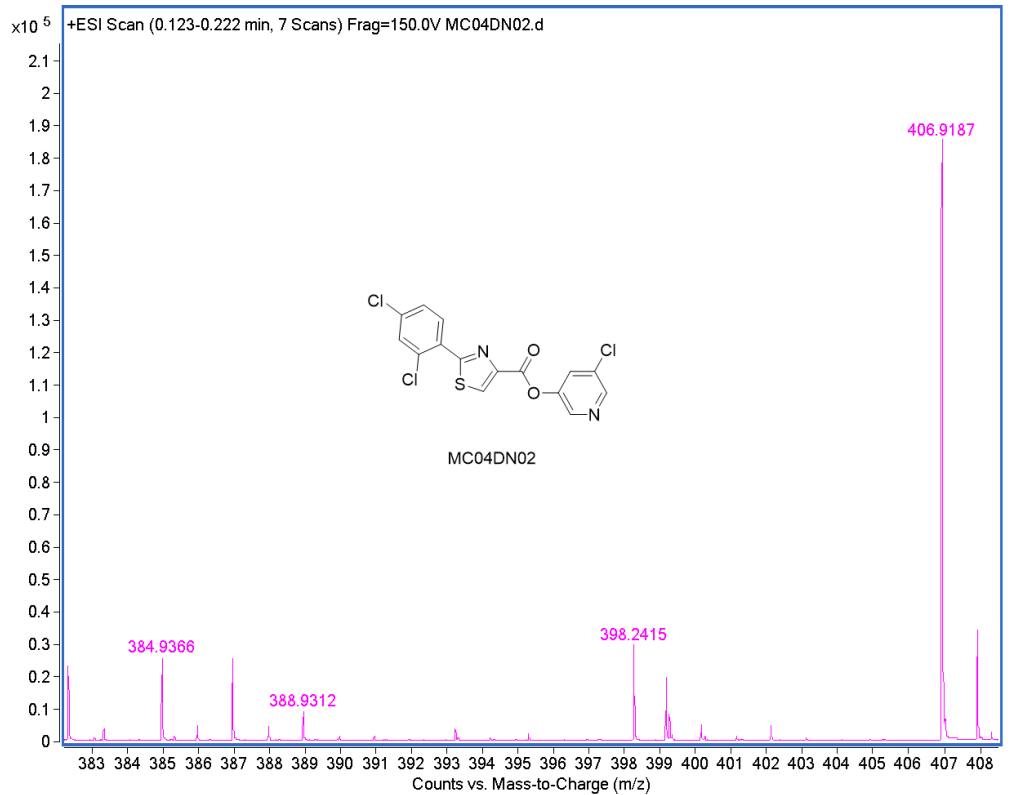


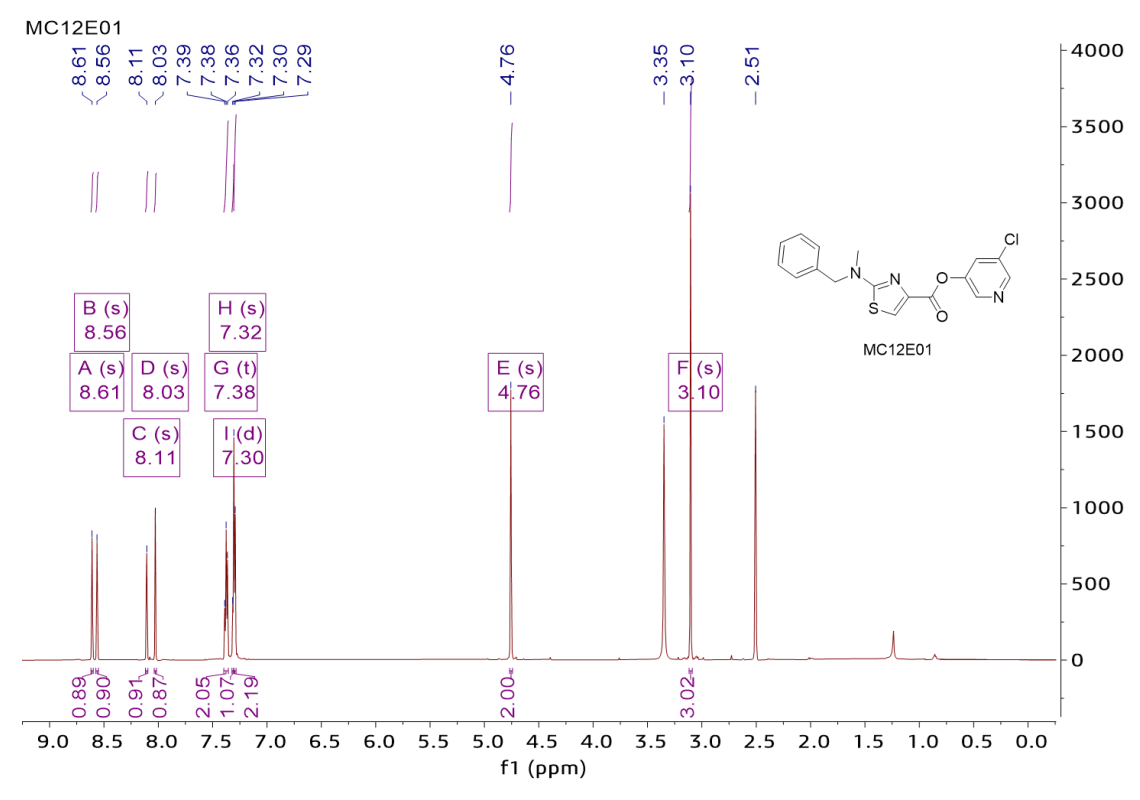


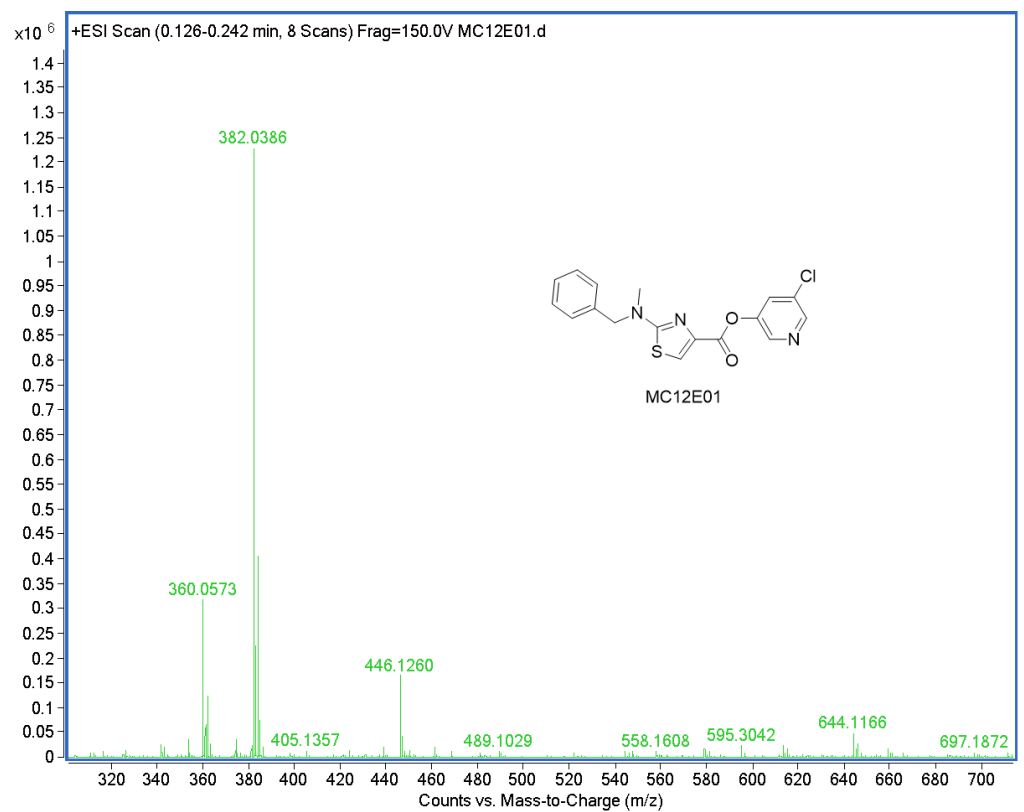


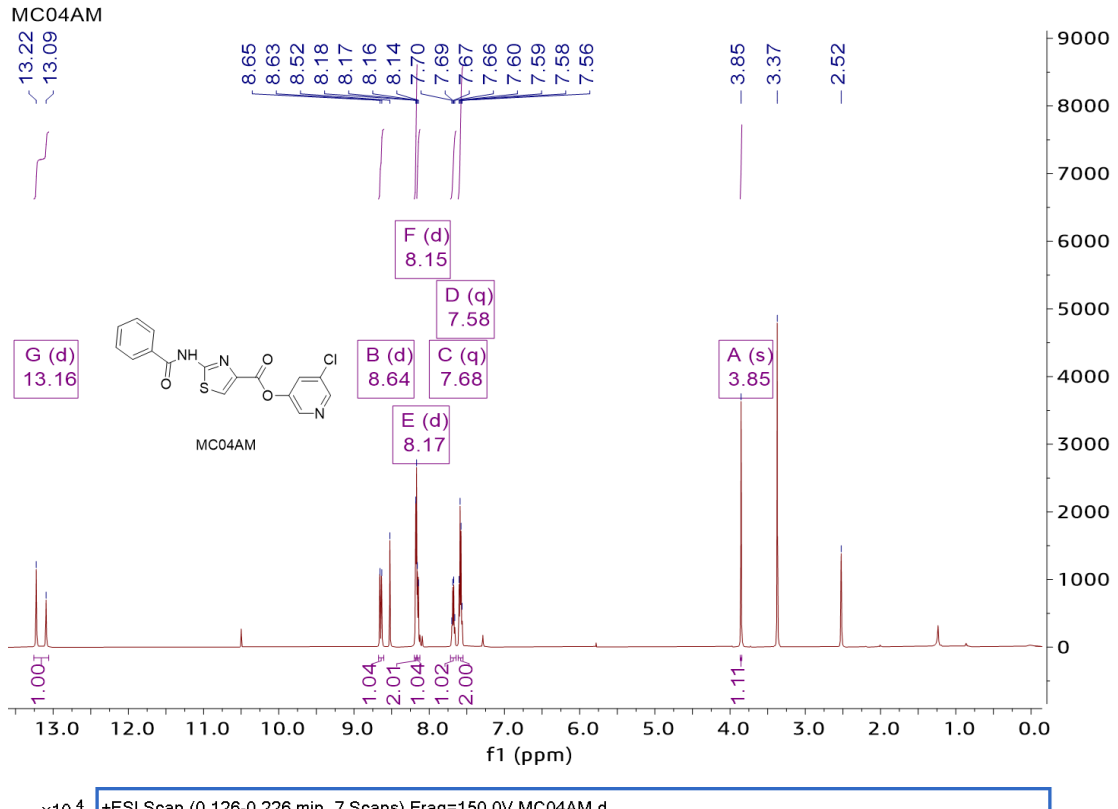


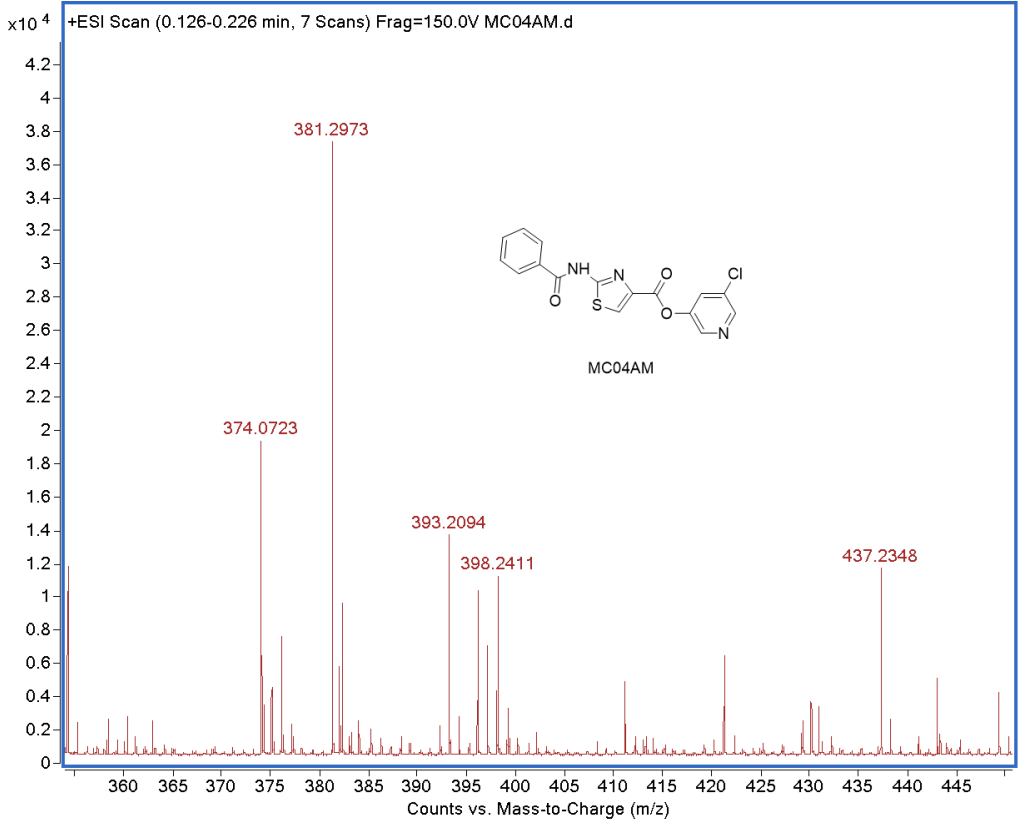


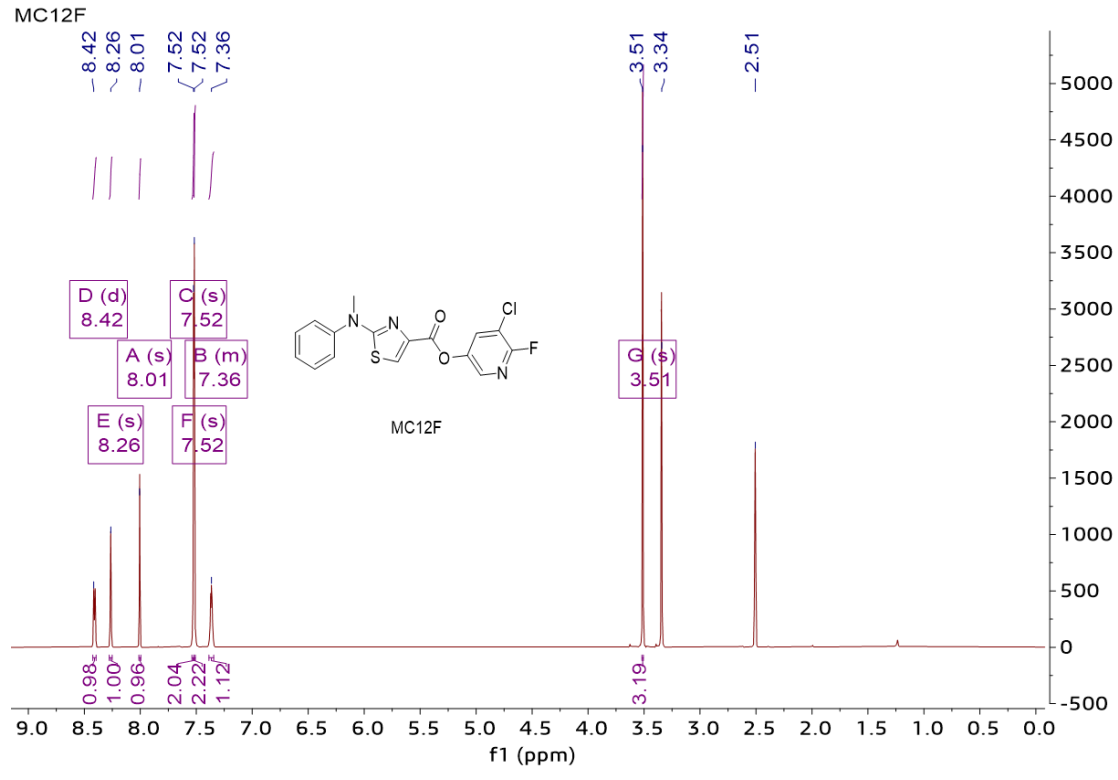


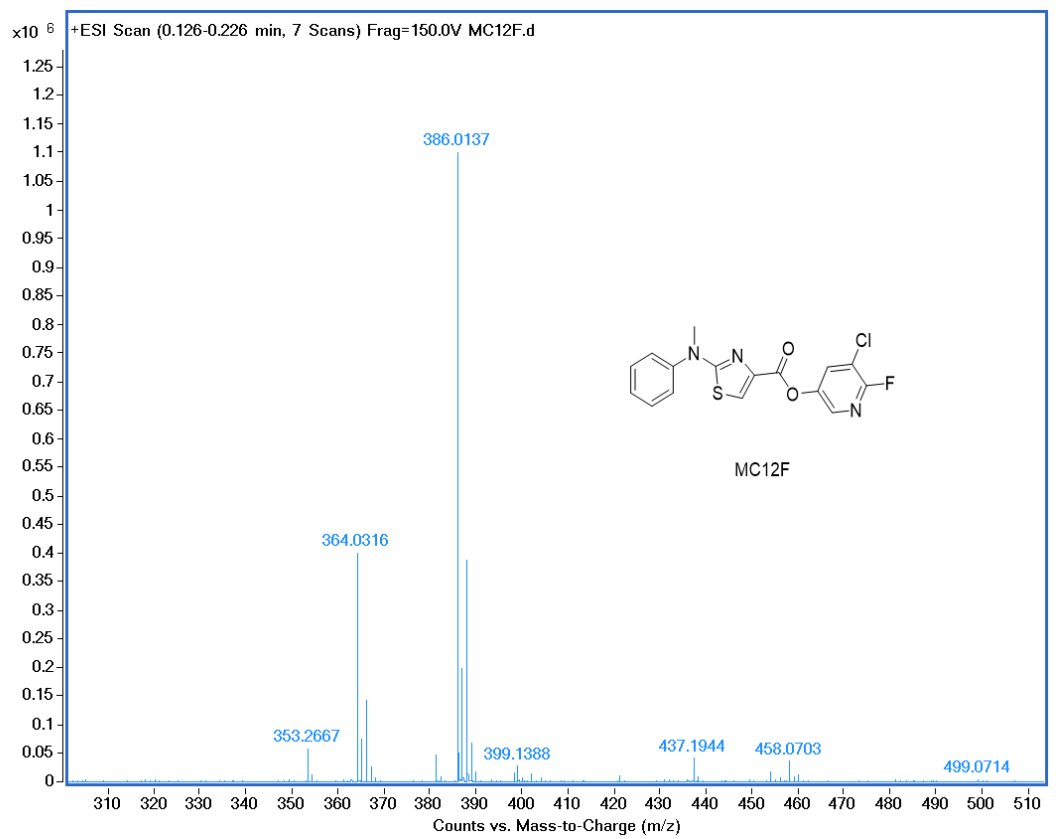


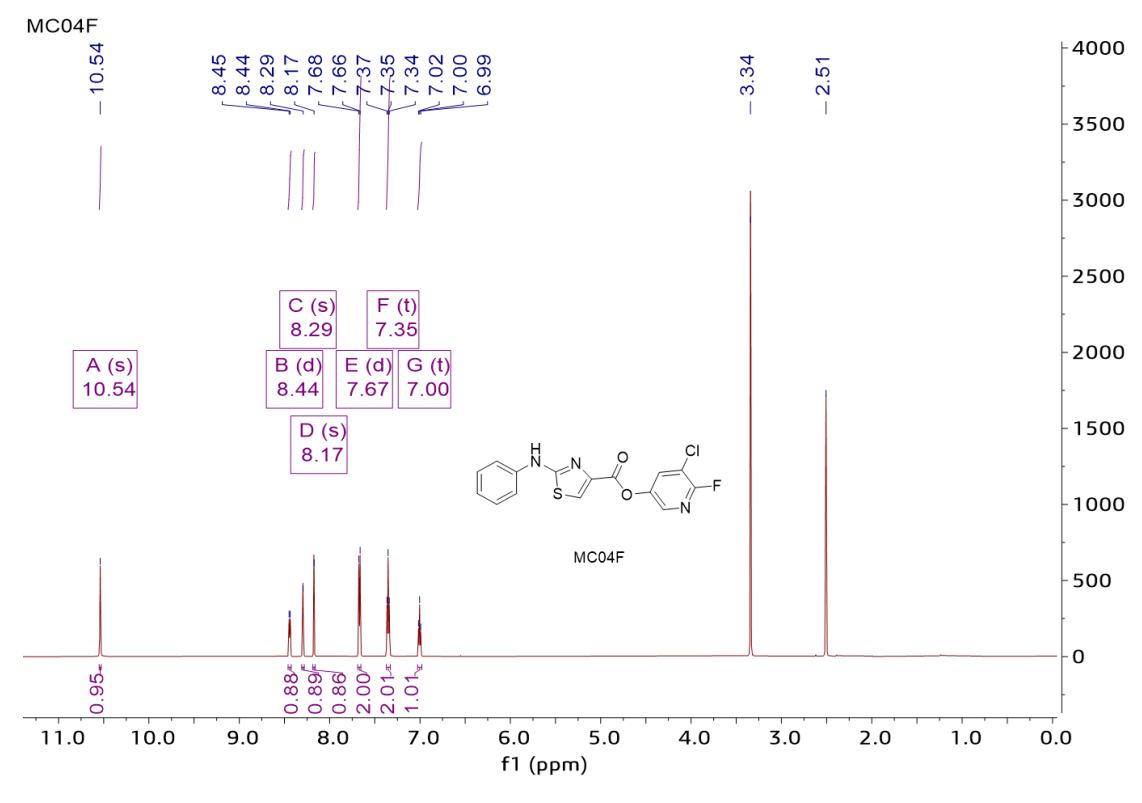


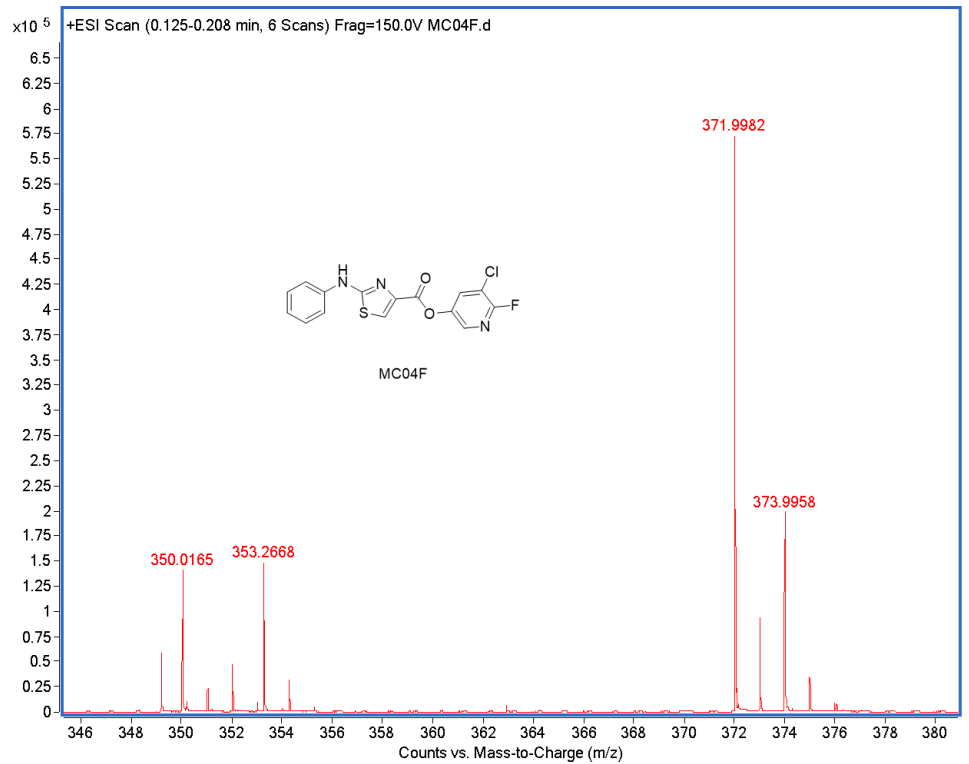


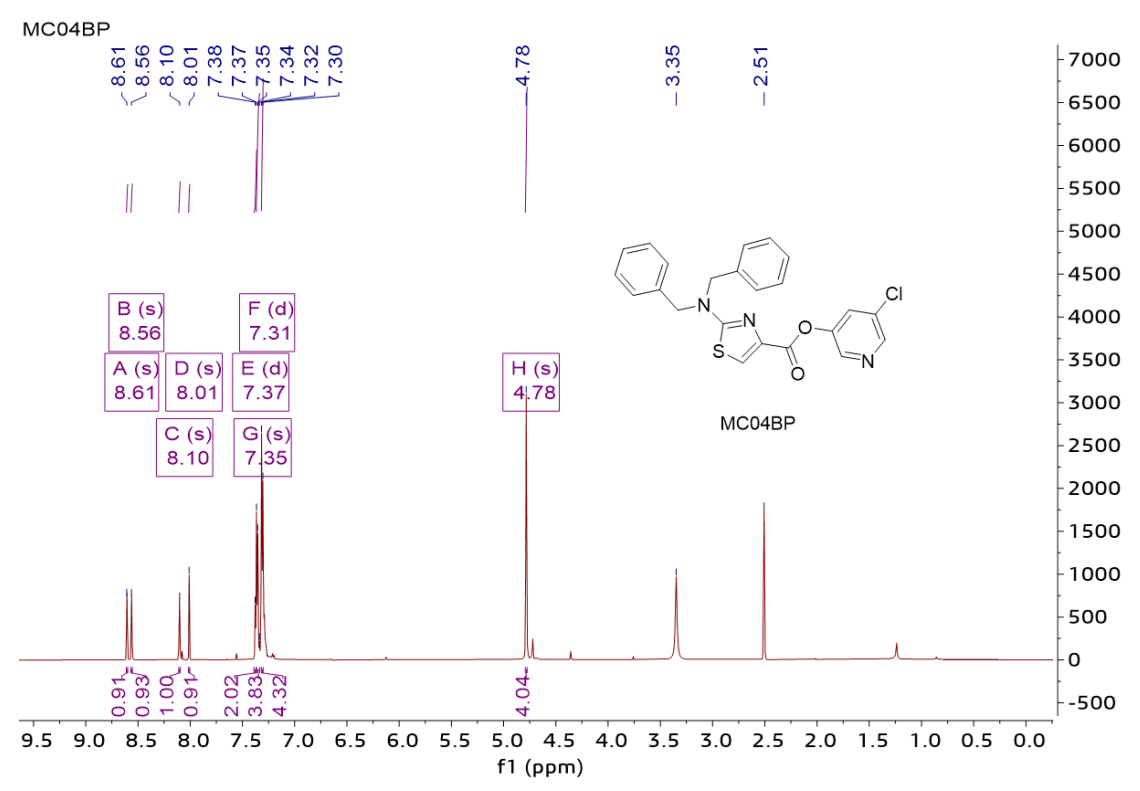


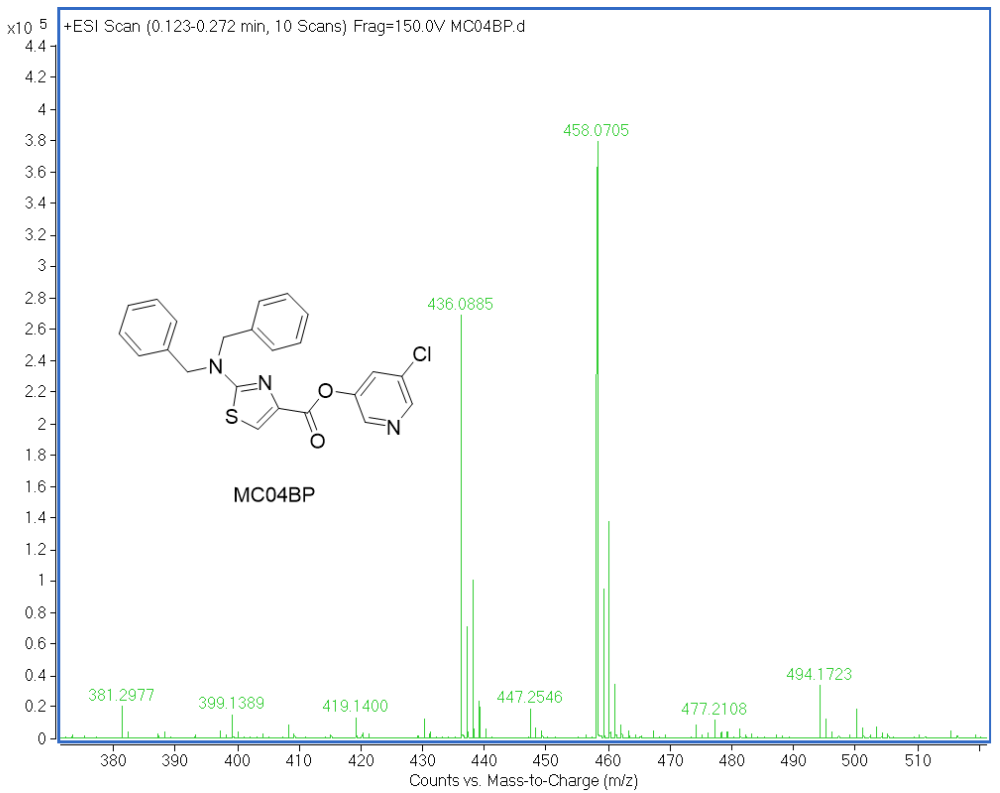


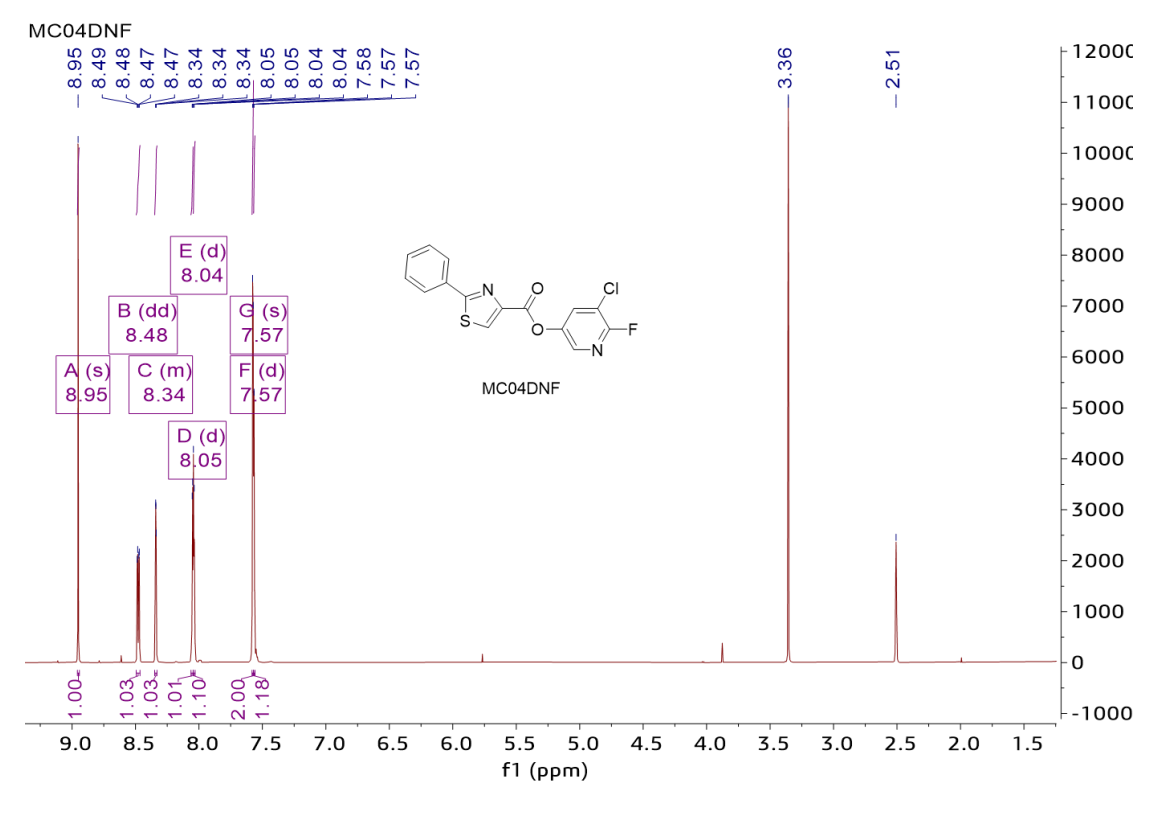


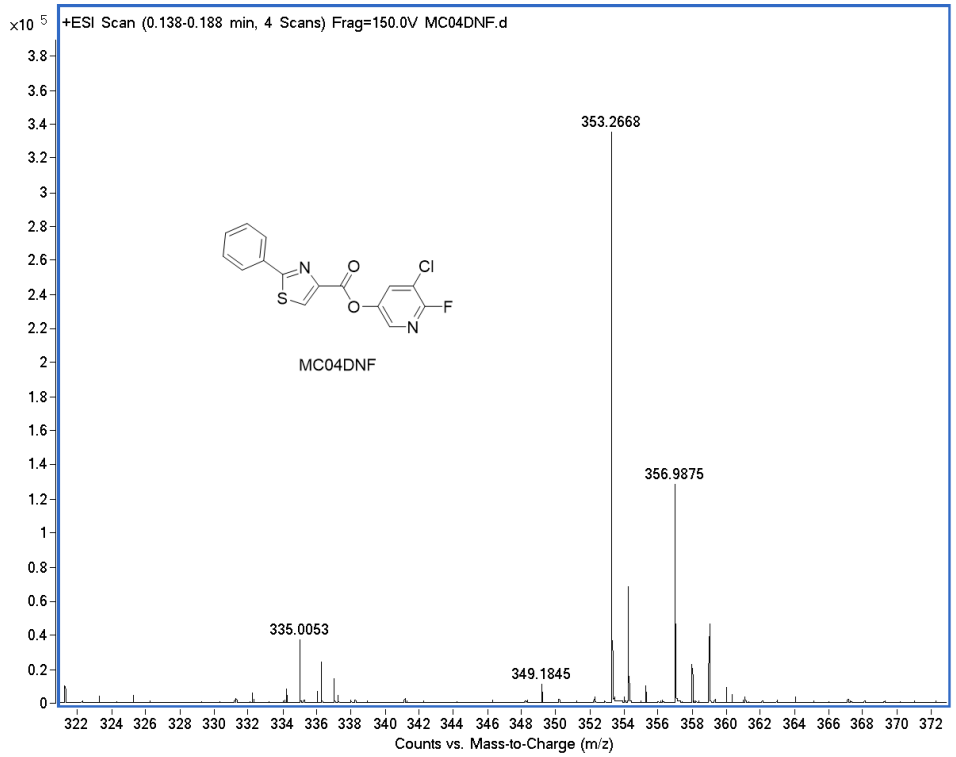


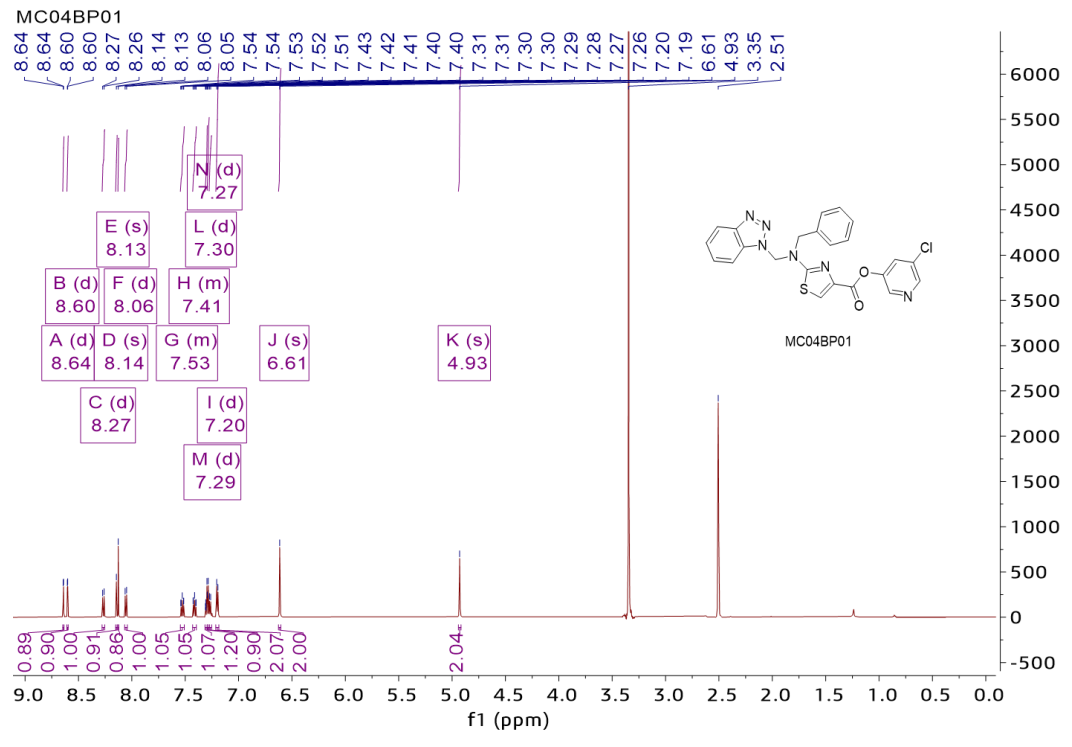


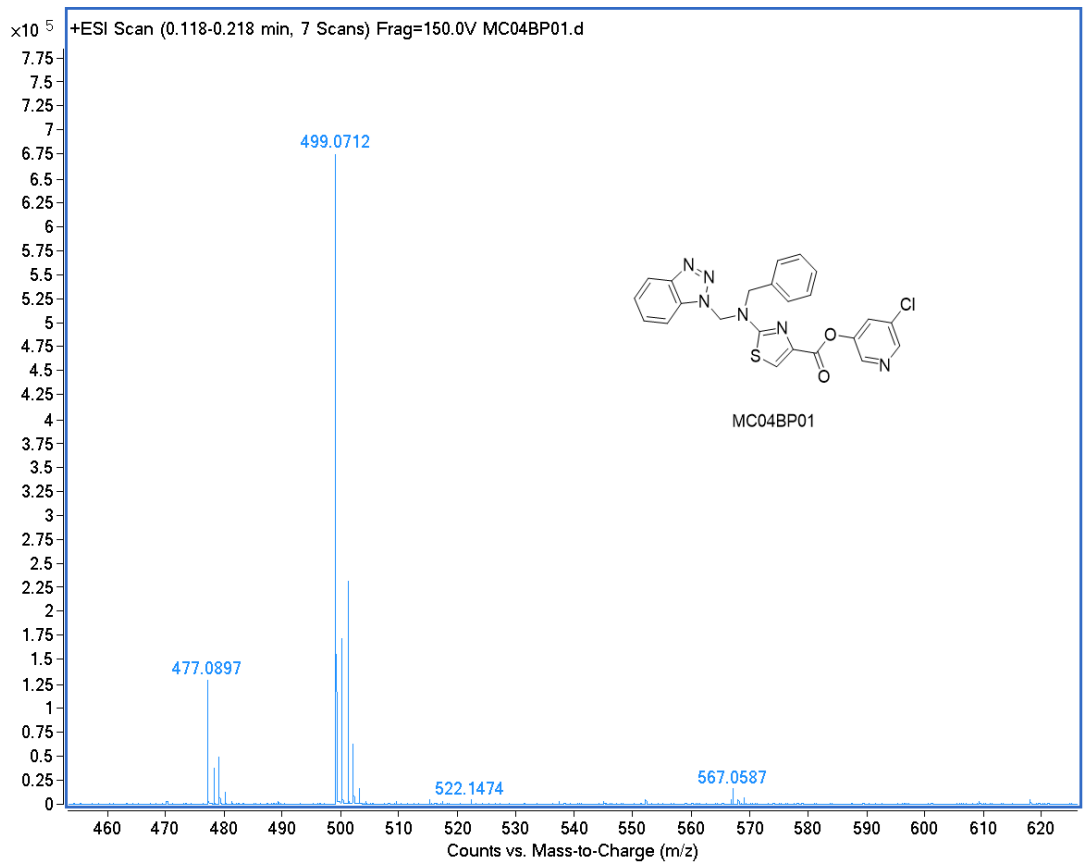


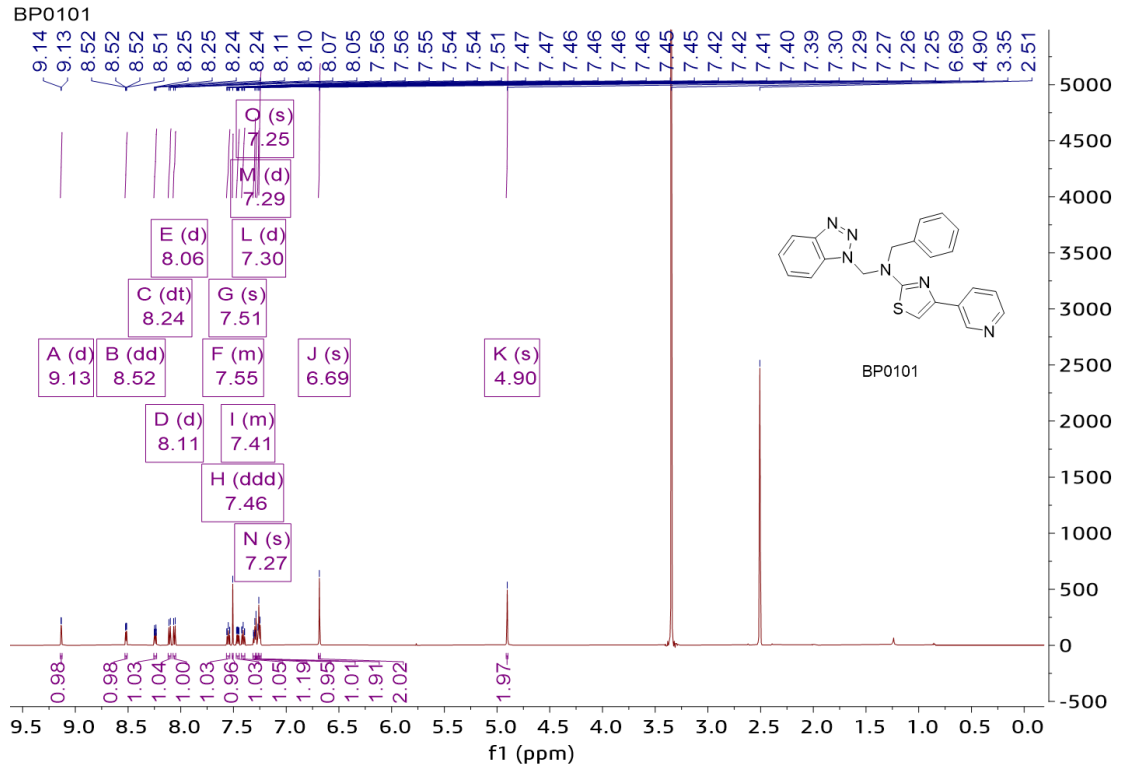


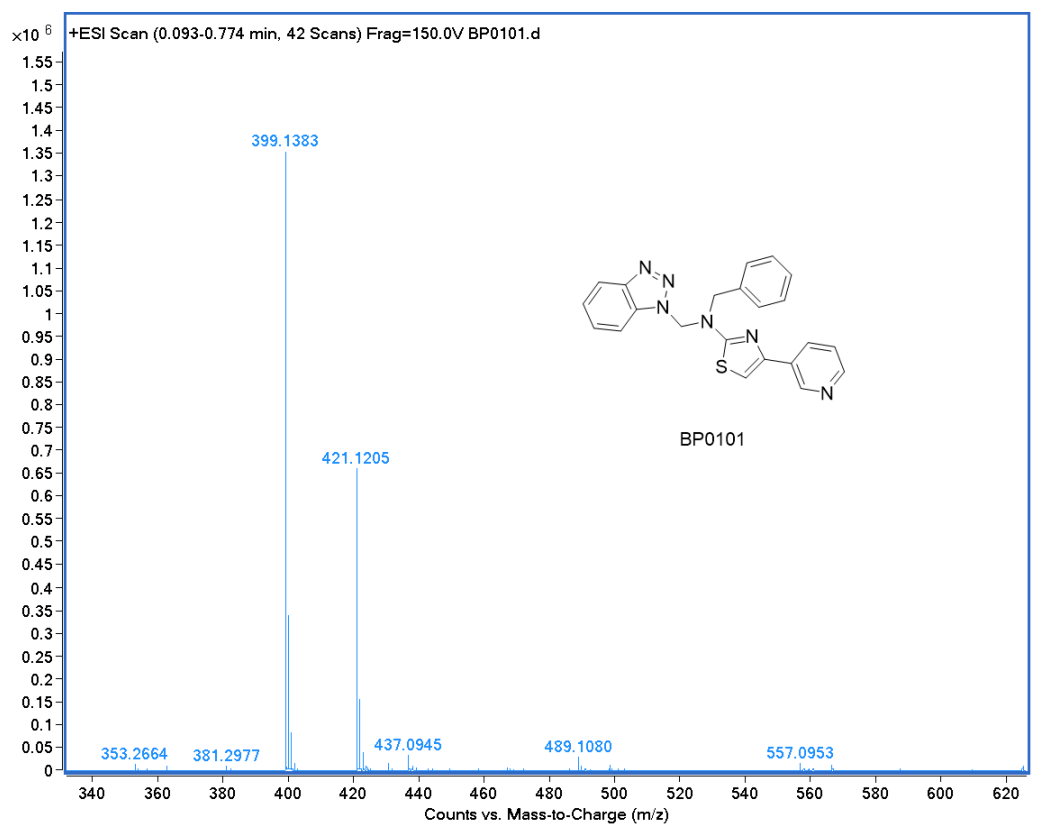


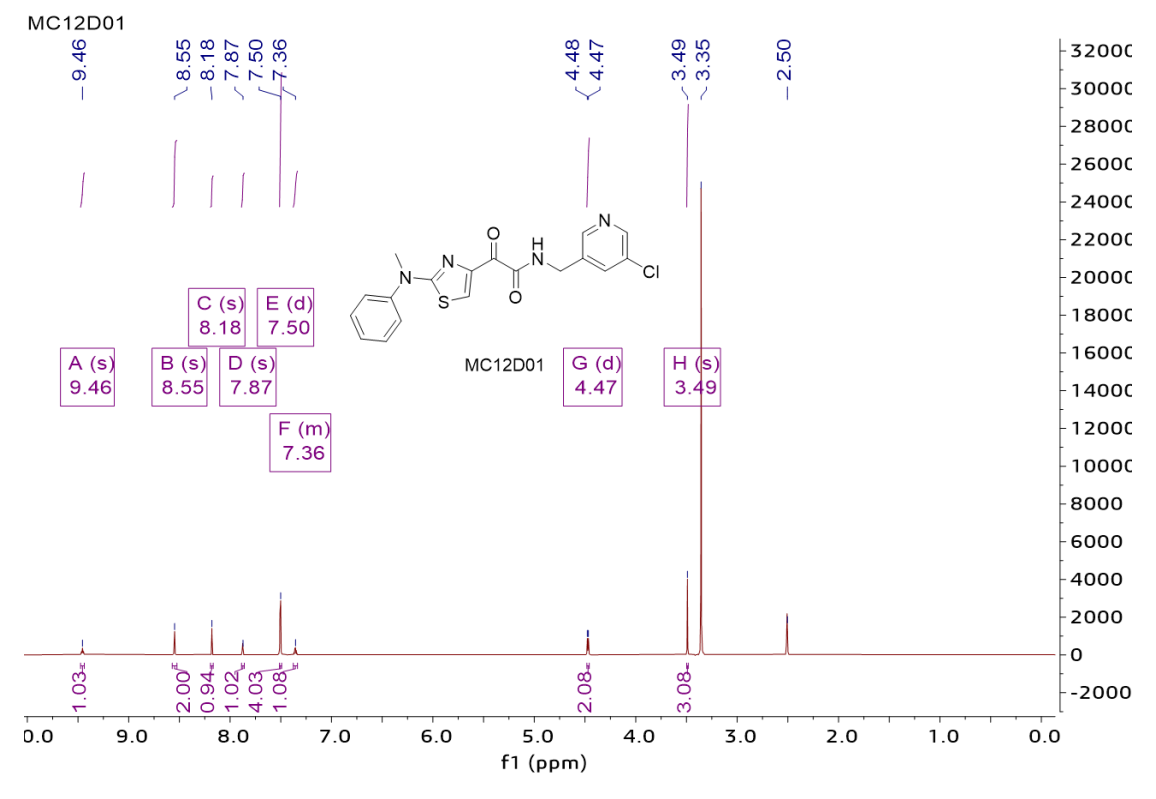


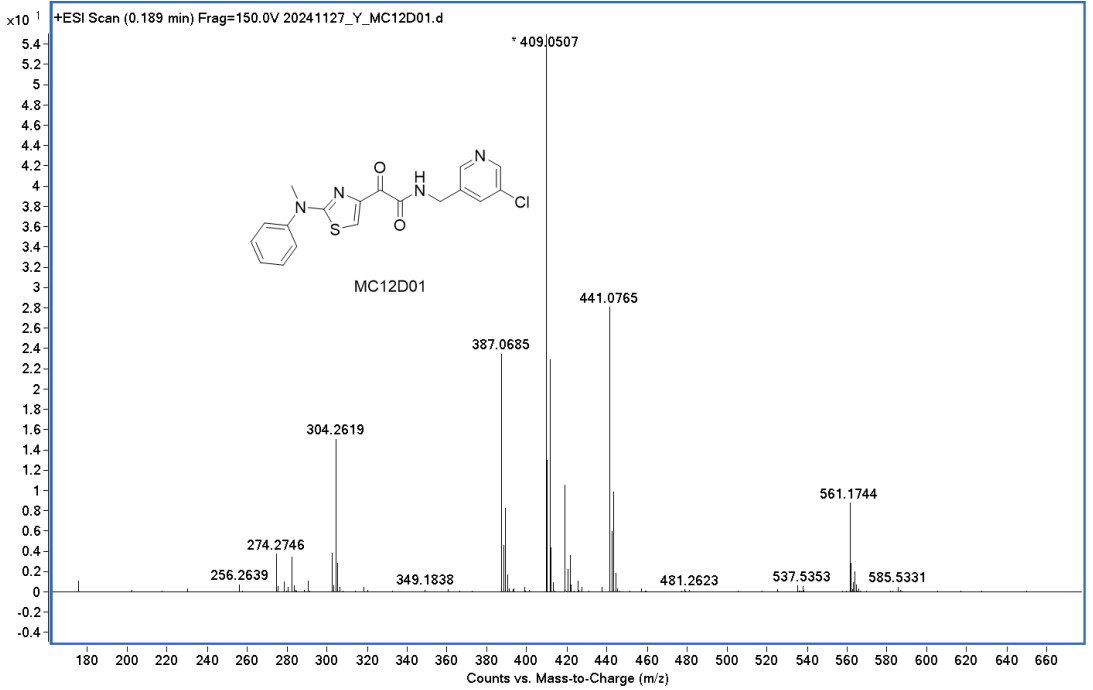


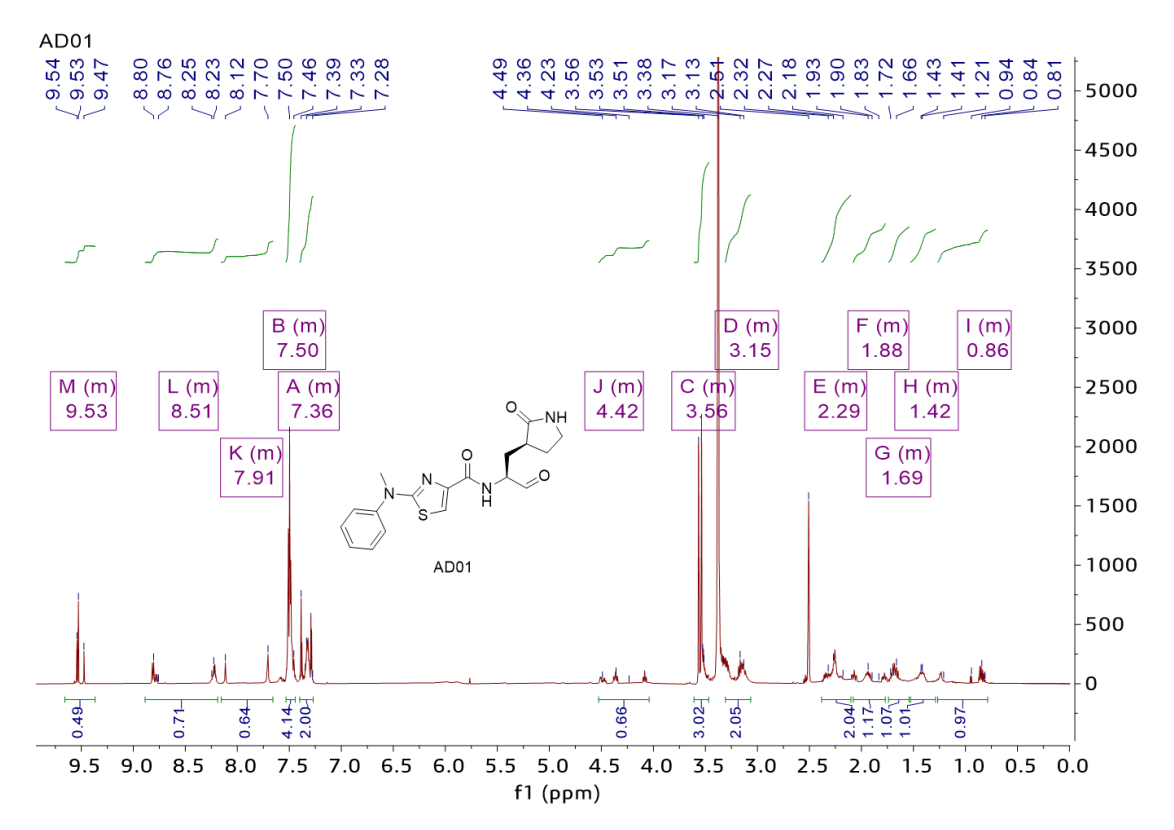


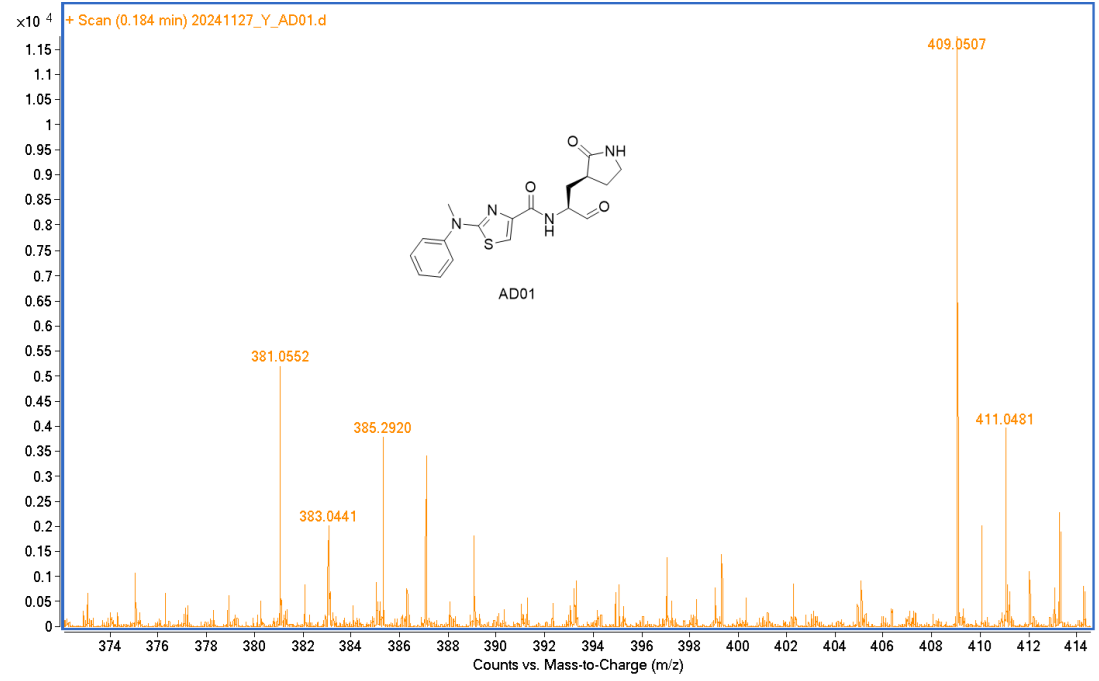


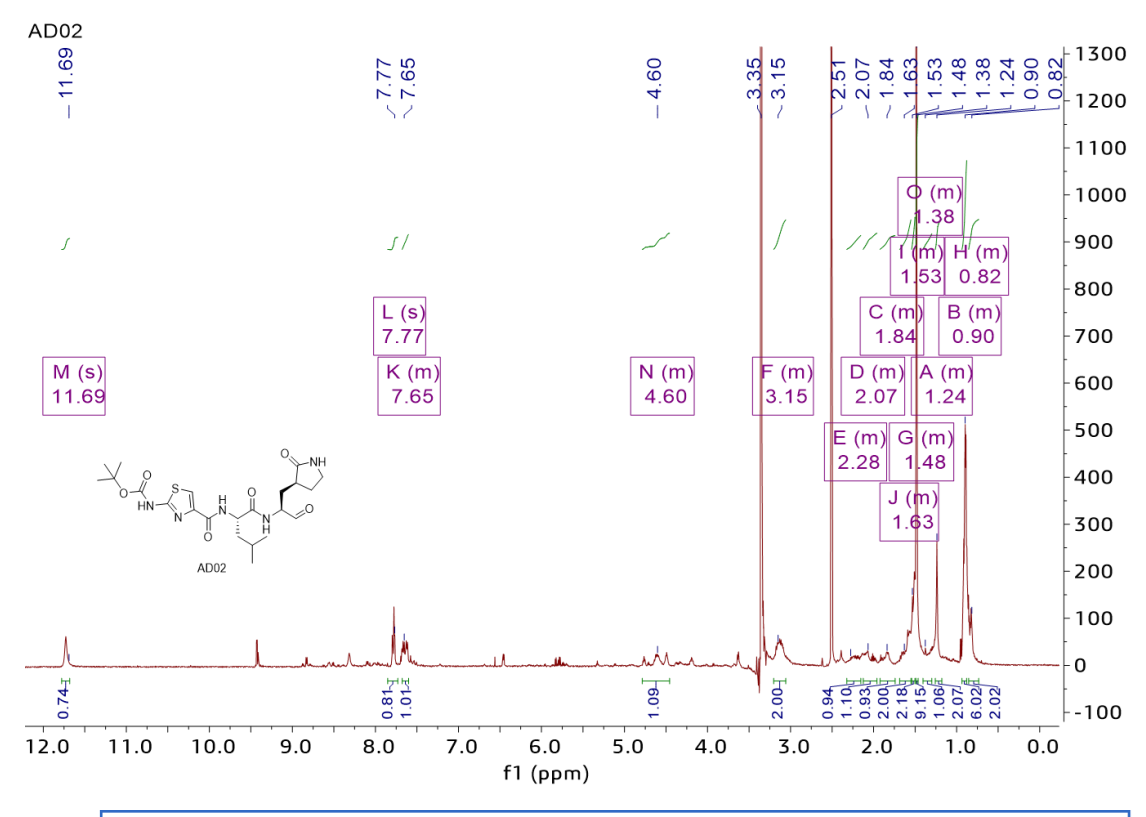


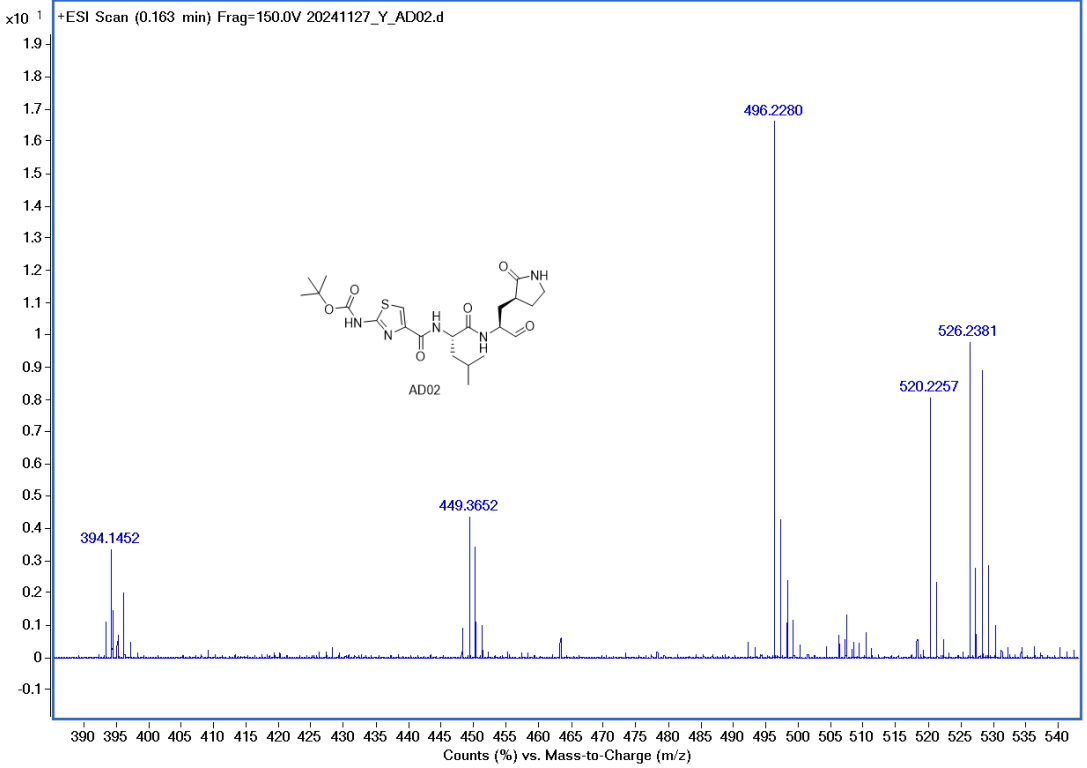


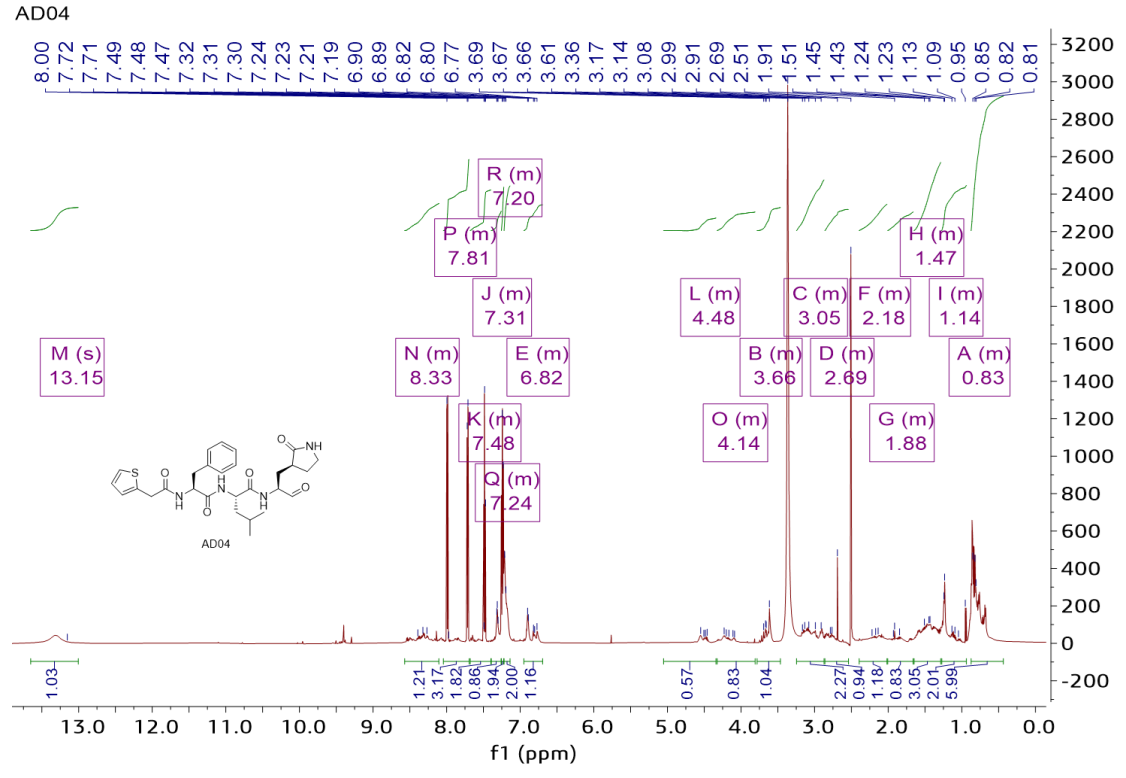


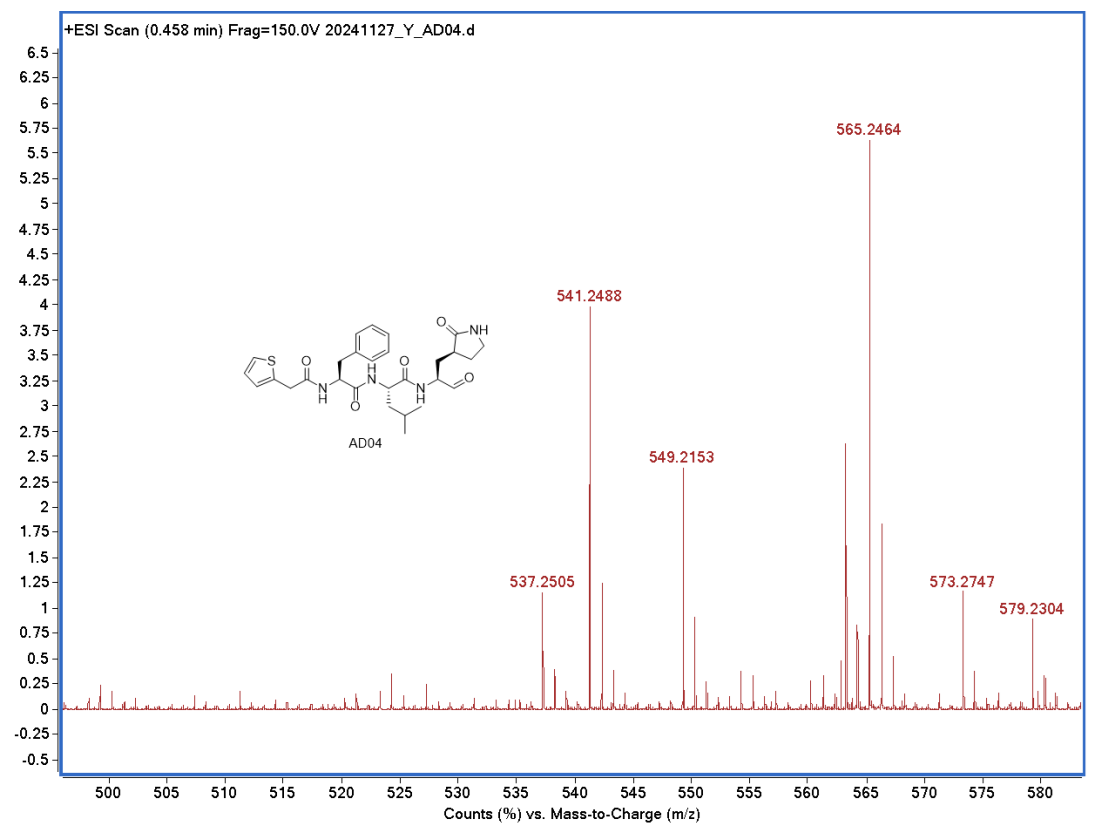


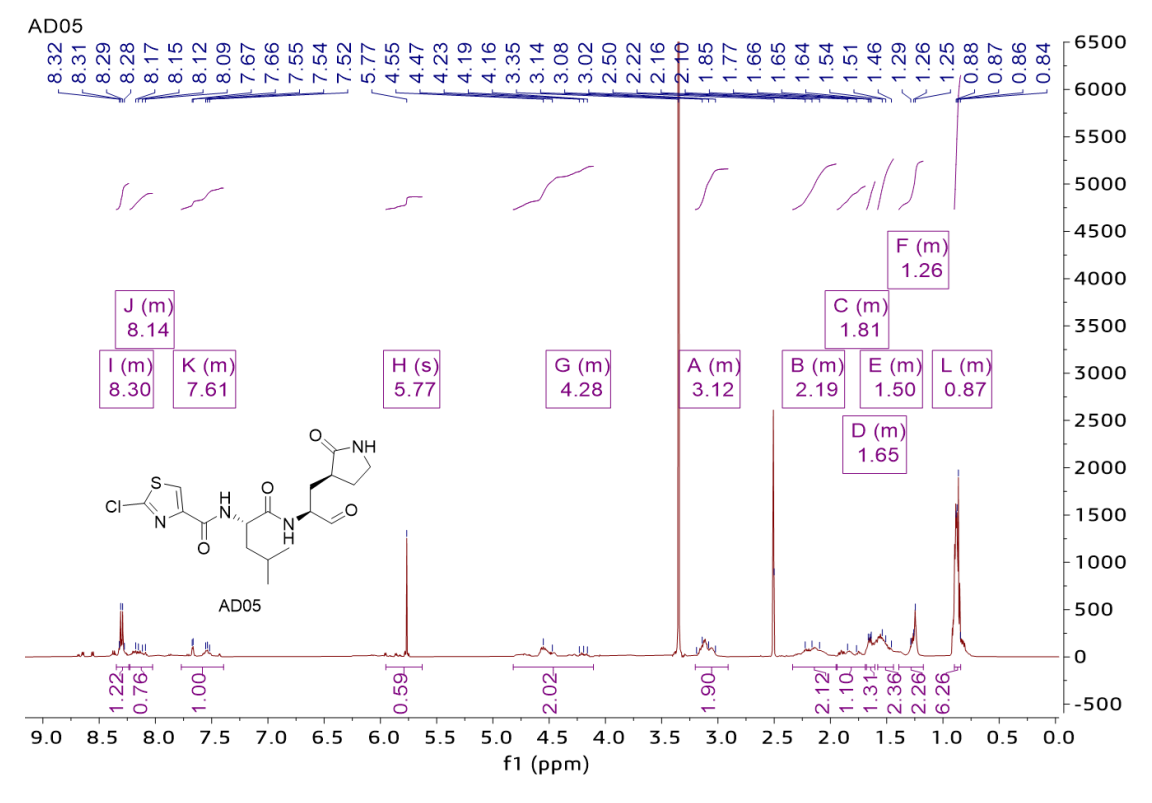


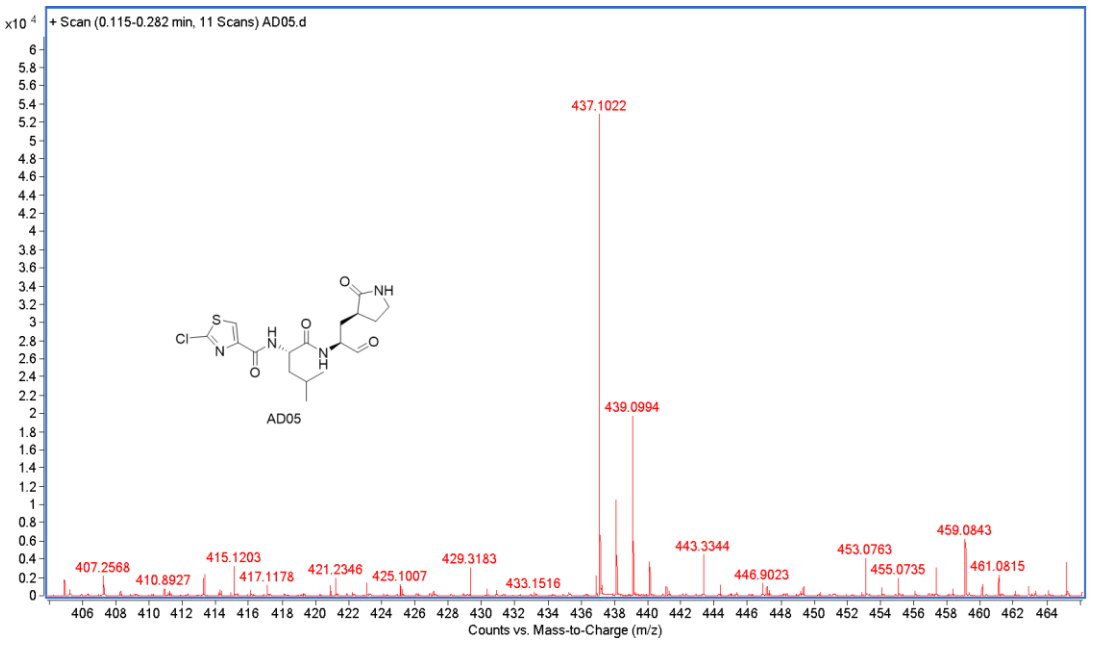


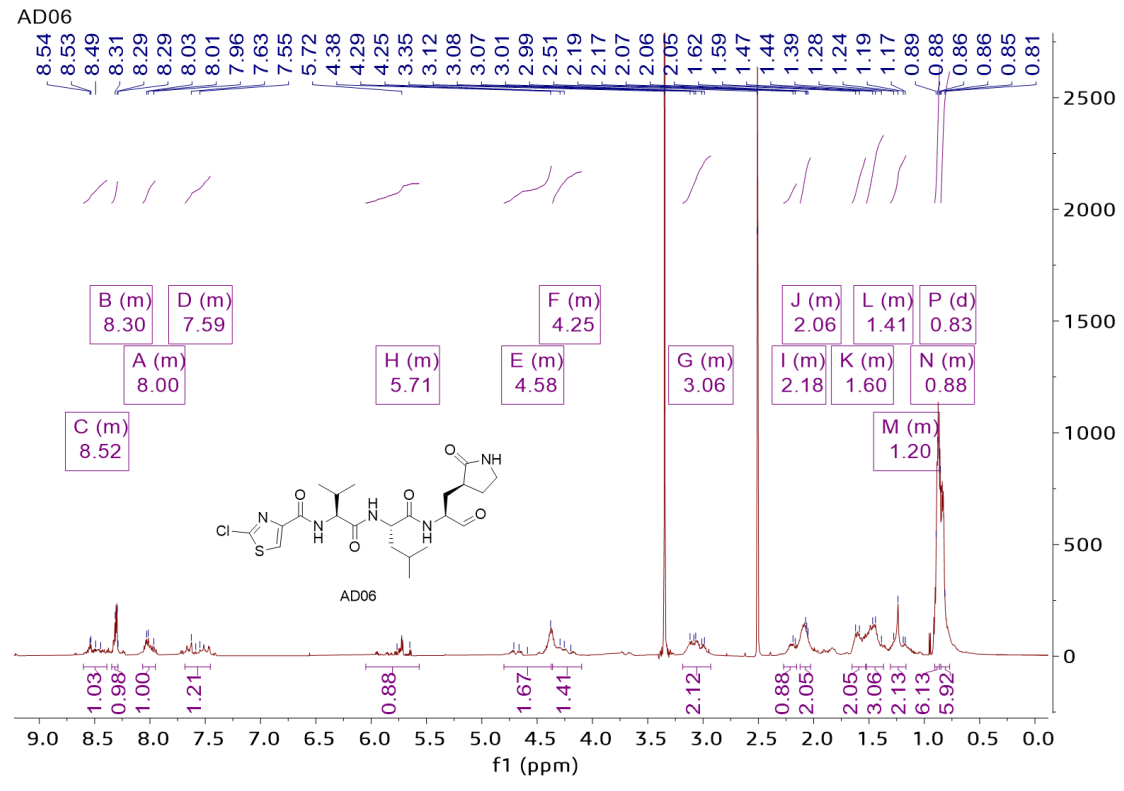


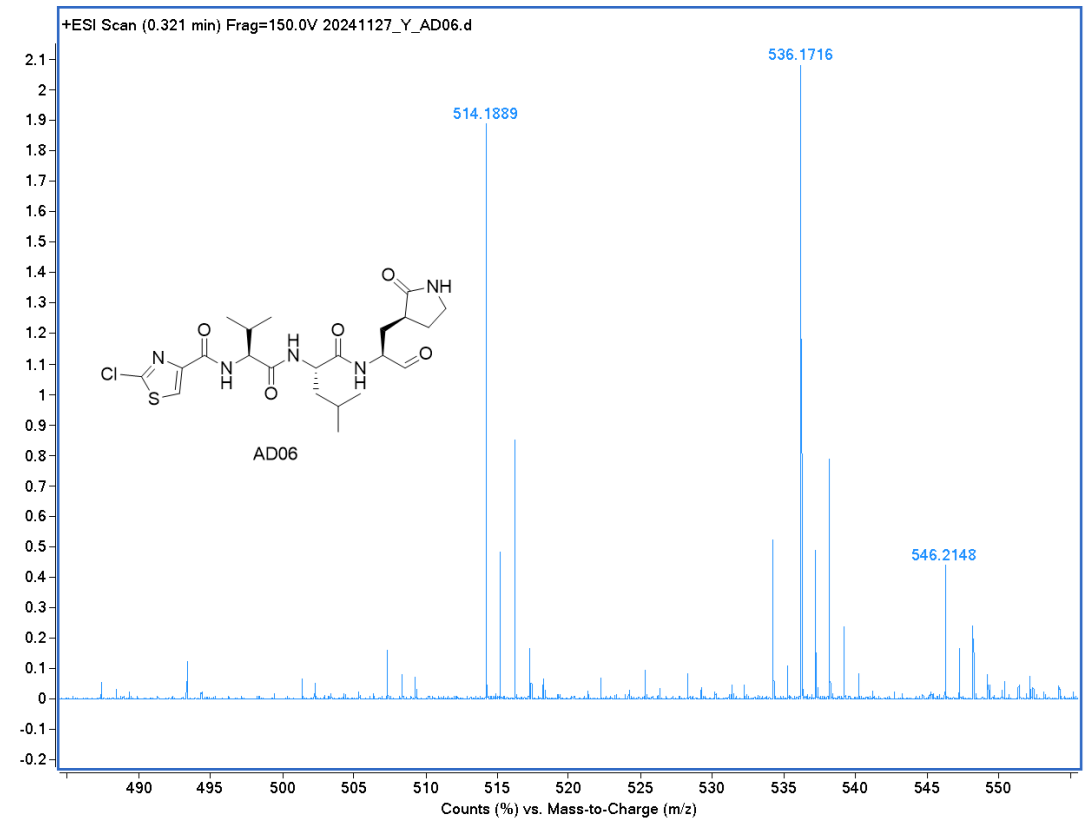


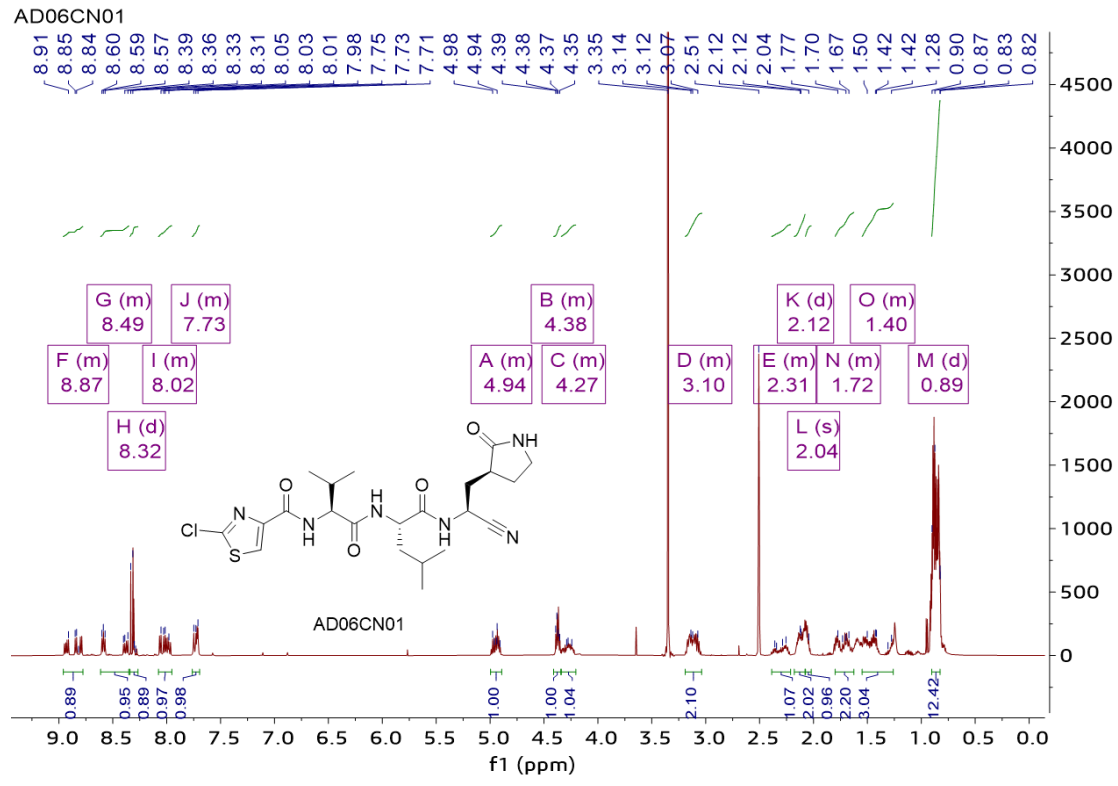


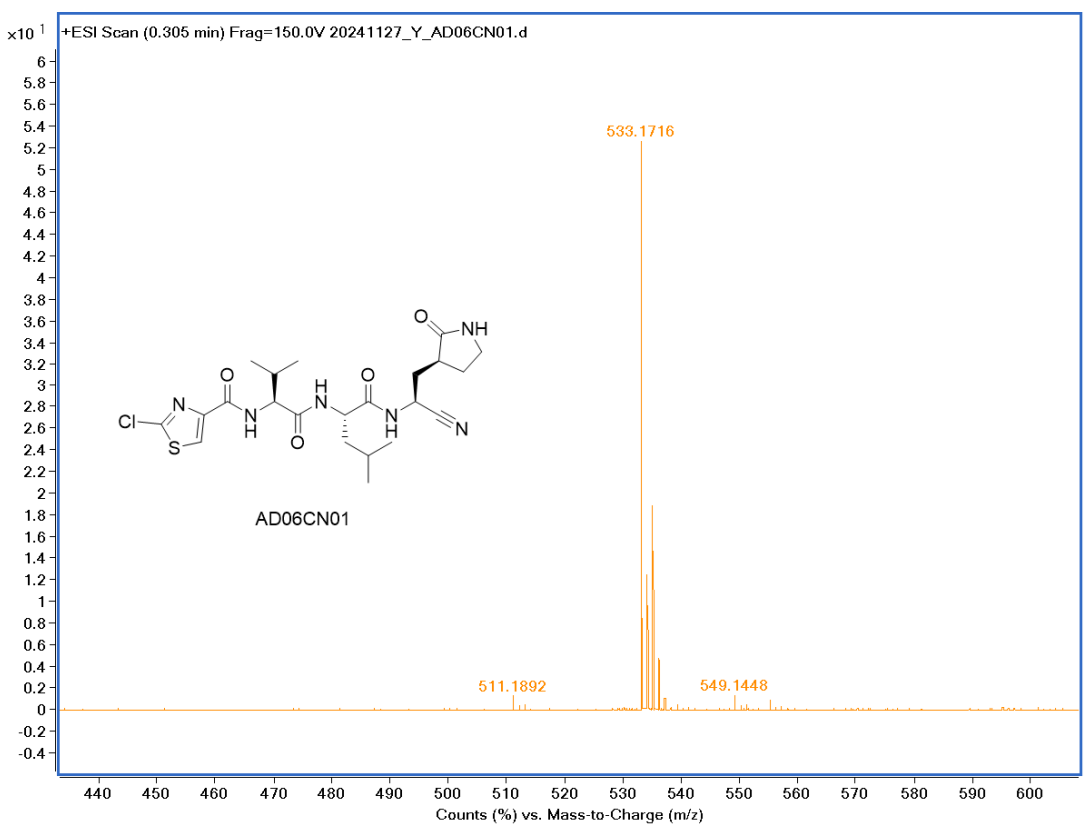


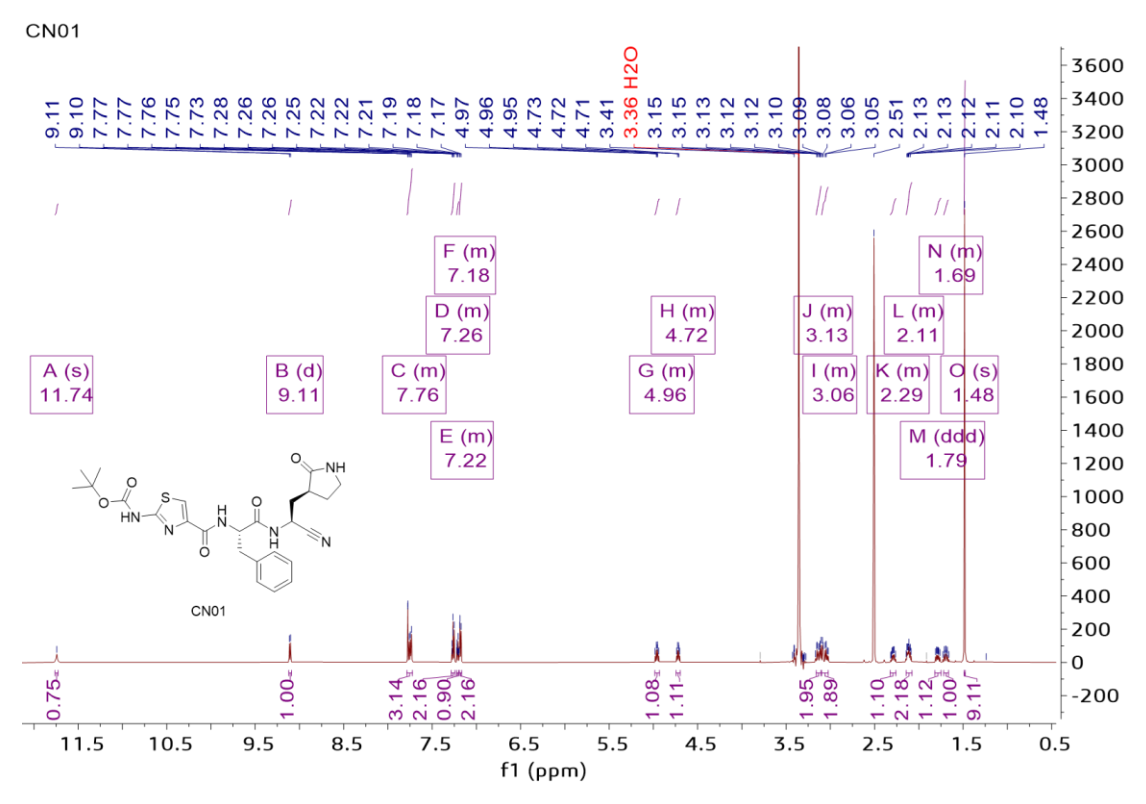


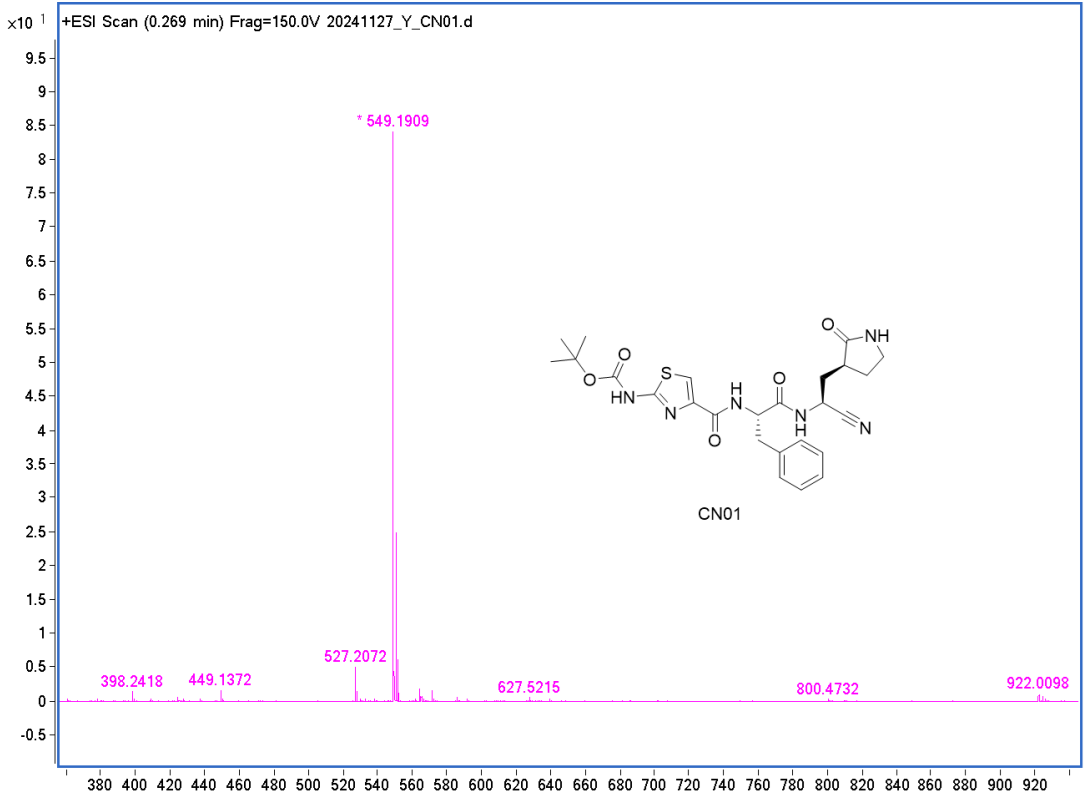






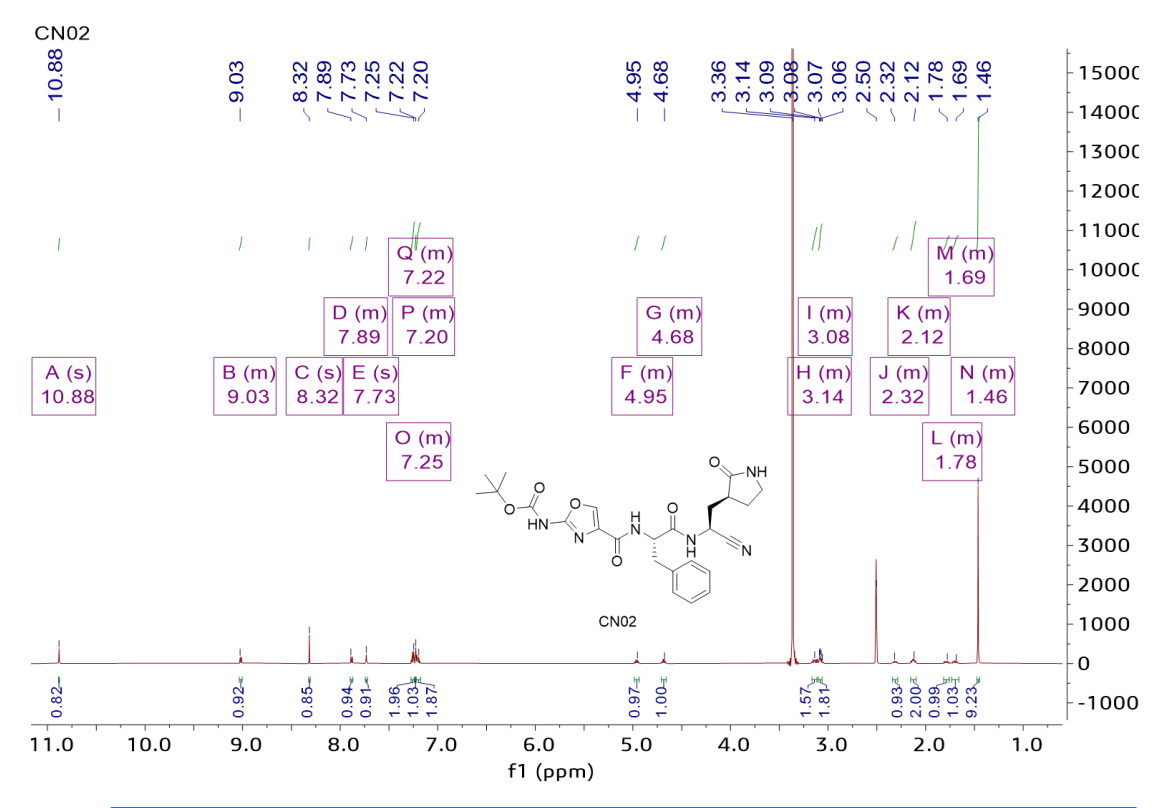


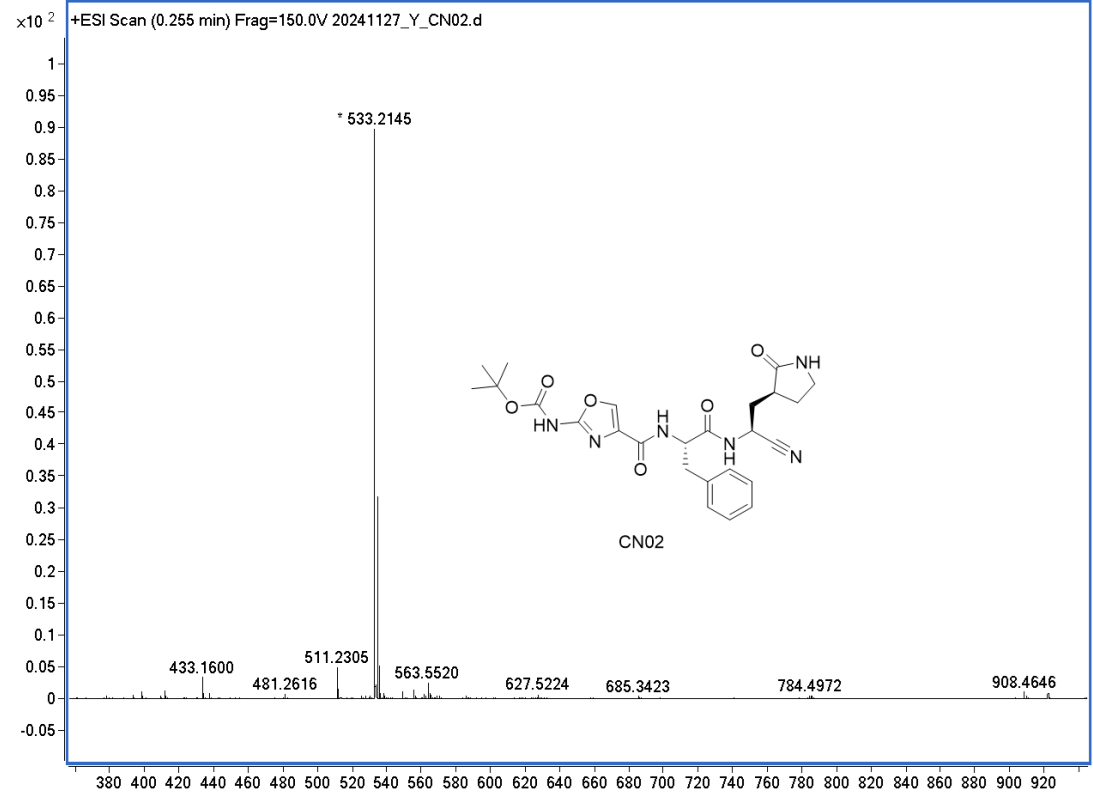




303

Counts (%) vs. Mass-to-Charge (m/z)





Counts (%) vs. Mass-to-Charge (m/z)

References

- 1. Abdelrahman, Z., M. Li, and X. Wang, Comparative Review of SARS-CoV-2, SARS-CoV, MERS-CoV, and Influenza A Respiratory Viruses. Front Immunol, 2020. 11: p. 552909.
- 2. Koreans move out of pandemic's shadow after nearly 3 years of battling COVID-19. 2022; Available from: https://www.koreatimes.co.kr/www/nation/2022/11/113_338813.html.
- 3. Spain to move from treating COVID-19 as a pandemic to an endemic illness.

 2022; Available from: https://www.euronews.com/2022/01/18/spain-to-move-from-treating-covid-19-as-a-pandemic-to-an-endemic.
- 4. WHO declares end to COVID global health emergency. 2023; Available from:

 https://www.reuters.com/business/healthcare-pharmaceuticals/covid-is-no-longer-global-health-emergency-who-2023-05-05/.
- 5. Zhang, L., et al., alpha-Ketoamides as Broad-Spectrum Inhibitors of Coronavirus and Enterovirus Replication: Structure-Based Design, Synthesis, and Activity Assessment. J Med Chem, 2020. **63**(9): p. 4562-4578.
- 6. Yang, H., et al., The crystal structures of severe acute respiratory syndrome virus main protease and its complex with an inhibitor. Proc Natl Acad Sci U S A, 2003. **100**(23): p. 13190-5.

- 7. Cho, E., et al., *Dynamic Profiling of beta-Coronavirus 3CL M(pro) Protease Ligand-Binding Sites.* J Chem Inf Model, 2021. **61**(6): p. 3058-3073.
- 8. Anand, K., et al., Structure of coronavirus main proteinase reveals combination of a chymotrypsin fold with an extra alpha-helical domain. EMBO J, 2002. **21**(13): p. 3213-24.
- 9. Haque, S.M., et al., *A comprehensive review about SARS-CoV-2*. Future Virol, 2020. **15**(9): p. 625-648.
- 10. Shamsi, A., et al., Potential drug targets of SARS-CoV-2: From genomics to therapeutics. Int J Biol Macromol, 2021. 177: p. 1-9.
- 11. Muramatsu, T., et al., SARS-CoV 3CL protease cleaves its C-terminal autoprocessing site by novel subsite cooperativity. Proc Natl Acad Sci U S A, 2016. 113(46): p. 12997-13002.
- 12. Jin, Z., et al., Structure of M(pro) from SARS-CoV-2 and discovery of its inhibitors. Nature, 2020. **582**(7811): p. 289-293.
- 13. Hoffman, R.L., et al., Discovery of Ketone-Based Covalent Inhibitors of Coronavirus 3CL Proteases for the Potential Therapeutic Treatment of COVID-19. J Med Chem, 2020. **63**(21): p. 12725-12747.
- 14. Cannalire, R., et al., Targeting SARS-CoV-2 Proteases and Polymerase for COVID-19 Treatment: State of the Art and Future Opportunities. J Med Chem, 2020.

- 15. Abe, K., et al., Pro108Ser mutation of SARS-CoV-2 3CL(pro) reduces the enzyme activity and ameliorates the clinical severity of COVID-19. Sci Rep, 2022. 12(1): p. 1299.
- 16. Rut, W., et al., Activity profiling and crystal structures of inhibitor-bound SARS-CoV-2 papain-like protease: A framework for anti-COVID-19 drug design. Sci Adv, 2020. **6**(42): p. eabd4596.
- 17. Shin, D., et al., *Papain-like protease regulates SARS-CoV-2 viral spread and innate immunity.* Nature, 2020. **587**(7835): p. 657-662.
- 18. Ullrich, S. and C. Nitsche, *The SARS-CoV-2 main protease as drug target*.

 Bioorg Med Chem Lett, 2020. **30**(17): p. 127377.
- 19. Hilgenfeld, R., From SARS to MERS: crystallographic studies on coronaviral proteases enable antiviral drug design. FEBS J, 2014. **281**(18): p. 4085-96.
- 20. Zhou, Z., et al., *Influenza A virus polymerase: an attractive target for next-generation anti-influenza therapeutics*. Drug Discov Today, 2018. **23**(3): p. 503-518.
- 21. Machitani, M., et al., RNA-dependent RNA polymerase, RdRP, a promising therapeutic target for cancer and potentially COVID-19. Cancer Sci, 2020. **111**(11): p. 3976-3984.
- Jacome, R., et al., Structural Analysis of Monomeric RNA-Dependent
 Polymerases: Evolutionary and Therapeutic Implications. PLoS One, 2015.
 10(9): p. e0139001.

- 23. Sexton, N.R., et al., Homology-Based Identification of a Mutation in the Coronavirus RNA-Dependent RNA Polymerase That Confers Resistance to Multiple Mutagens. J Virol, 2016. **90**(16): p. 7415-7428.
- 24. Imran, M., et al. *Discovery, Development, and Patent Trends on Molnupiravir:*A Prospective Oral Treatment for COVID-19. Molecules, 2021. **26**, DOI: 10.3390/molecules26195795.
- 25. Kabinger, F., et al., *Mechanism of molnupiravir-induced SARS-CoV-2 mutagenesis*. Nat Struct Mol Biol, 2021. **28**(9): p. 740-746.
- 26. Pereira, D.A. and J.A. Williams, *Origin and evolution of high throughput screening*. Br J Pharmacol, 2007. **152**(1): p. 53-61.
- 27. Wu, L., et al., Forster resonance energy transfer (FRET)-based small-molecule sensors and imaging agents. Chem Soc Rev, 2020. **49**(15): p. 5110-5139.
- 28. Didenko, V.V., *DNA Probes Using Fluorescence Resonance Energy Transfer*(FRET): Designs and Applications. BioTechniques, 2001. **31**(5): p. 1106-1121.
- 29. La Monica, G., et al., Targeting SARS-CoV-2 Main Protease for Treatment of COVID-19: Covalent Inhibitors Structure-Activity Relationship Insights and Evolution Perspectives. J Med Chem, 2022. 65(19): p. 12500-12534.
- 30. Pillaiyar, T., et al., An Overview of Severe Acute Respiratory Syndrome-Coronavirus (SARS-CoV) 3CL Protease Inhibitors: Peptidomimetics and Small Molecule Chemotherapy. J Med Chem, 2016. **59**(14): p. 6595-628.

- 31. Ghosh, A.K., et al., *Drug Development and Medicinal Chemistry Efforts toward*SARS-Coronavirus and Covid-19 Therapeutics. ChemMedChem, 2020. **15**(11):
 p. 907-932.
- 32. Ghosh, A.K., et al., *Design, synthesis and antiviral efficacy of a series of potent chloropyridyl ester-derived SARS-CoV 3CLpro inhibitors.* Bioorg Med Chem Lett, 2008. **18**(20): p. 5684-8.
- 33. Unoh, Y., et al., Discovery of S-217622, a Noncovalent Oral SARS-CoV-2 3CL

 Protease Inhibitor Clinical Candidate for Treating COVID-19. J Med Chem,
 2022. 65(9): p. 6499-6512.
- 34. Zhang, L., et al., Crystal structure of SARS-CoV-2 main protease provides a basis for design of improved alpha-ketoamide inhibitors. Science, 2020.

 368(6489): p. 409-412.
- 35. Kitamura, N., et al., Expedited Approach toward the Rational Design of Noncovalent SARS-CoV-2 Main Protease Inhibitors. J Med Chem, 2022. **65**(4): p. 2848-2865.
- 36. Owen, D.R., et al., An oral SARS-CoV-2 M(pro) inhibitor clinical candidate for the treatment of COVID-19. Science, 2021. **374**(6575): p. 1586-1593.
- 37. Vankadara, S., et al., A Warhead Substitution Study on the Coronavirus Main Protease Inhibitor Nirmatrelvir. ACS Med Chem Lett, 2022. **13**(8): p. 1345-1350.

- 38. Ren, Z., et al., The newly emerged SARS-like coronavirus HCoV-EMC also has an "Achilles' heel": current effective inhibitor targeting a 3C-like protease.

 Protein Cell, 2013. 4(4): p. 248-50.
- 39. Hirose, Y., et al., Discovery of Chlorofluoroacetamide-Based Covalent Inhibitors for Severe Acute Respiratory Syndrome Coronavirus 2 3CL Protease.

 J Med Chem, 2022. 65(20): p. 13852-13865.
- 40. Ma, C., et al., Boceprevir, GC-376, and calpain inhibitors II, XII inhibit SARS-CoV-2 viral replication by targeting the viral main protease. Cell Res, 2020. **30**(8): p. 678-692.
- 41. Rathnayake, A.D., et al., 3C-like protease inhibitors block coronavirus replication in vitro and improve survival in MERS-CoV-infected mice. Sci Transl Med, 2020. 12(557): p. eabc5332.
- 42. Perera, K.D., et al., *Protease inhibitors broadly effective against feline, ferret and mink coronaviruses*. Antiviral Res, 2018. **160**: p. 79-86.
- 43. Dampalla, C.S., et al., Postinfection treatment with a protease inhibitor increases survival of mice with a fatal SARS-CoV-2 infection. Proc Natl Acad Sci U S A, 2021. 118(29): p. e2101555118.
- 44. Sacco, M.D., et al., Structure and inhibition of the SARS-CoV-2 main protease reveal strategy for developing dual inhibitors against M(pro) and cathepsin L. Sci Adv, 2020. **6**(50): p. eabe0751.

- 45. Dai, W., et al., Structure-based design of antiviral drug candidates targeting the SARS-CoV-2 main protease. Science, 2020. **368**(6497): p. 1331-1335.
- 46. Dai, W.H., et al., Structure-based design of antiviral drug candidates targeting the SARS-CoV-2 main protease. Science, 2020. **368**(6497): p. 1331-+.
- 47. Dai, W., et al., Design, Synthesis, and Biological Evaluation of Peptidomimetic Aldehydes as Broad-Spectrum Inhibitors against Enterovirus and SARS-CoV-2.

 J Med Chem, 2022. 65(4): p. 2794-2808.
- 48. Wang, H., et al., The structure-based design of peptidomimetic inhibitors against SARS-CoV-2 3C like protease as Potent anti-viral drug candidate. Eur J Med Chem, 2022. 238: p. 114458.
- 49. Qiao, J., et al., SARS-CoV-2 M(pro) inhibitors with antiviral activity in a transgenic mouse model. Science, 2021. **371**(6536): p. 1374-1378.
- 50. Niu, C., et al., Molecular docking identifies the binding of 3-chloropyridine moieties specifically to the S1 pocket of SARS-CoV Mpro. Bioorg Med Chem, 2008. **16**(1): p. 293-302.
- 51. Zhang, J., et al., Design, synthesis, and evaluation of inhibitors for severe acute respiratory syndrome 3C-like protease based on phthalhydrazide ketones or heteroaromatic esters. J Med Chem, 2007. **50**(8): p. 1850-64.
- 52. Blanchard, J.E., et al., *High-throughput screening identifies inhibitors of the SARS coronavirus main proteinase*. Chem Biol, 2004. **11**(10): p. 1445-53.

- 53. Iketani, S., et al., Lead compounds for the development of SARS-CoV-2 3CL protease inhibitors. Nat Commun, 2021. 12(1): p. 2016.
- 54. Ghosh, A.K., et al., Indole Chloropyridinyl Ester-Derived SARS-CoV-2 3CLpro
 Inhibitors: Enzyme Inhibition, Antiviral Efficacy, Structure-Activity
 Relationship, and X-ray Structural Studies. J Med Chem, 2021. 64(19): p.
 14702-14714.
- 55. Pillaiyar, T., et al., Small-Molecule Thioesters as SARS-CoV-2 Main Protease
 Inhibitors: Enzyme Inhibition, Structure-Activity Relationships, Antiviral
 Activity, and X-ray Structure Determination. J Med Chem, 2022. 65(13): p.
 9376-9395.
- 56. Malla, T.R., et al., *Penicillin Derivatives Inhibit the SARS-CoV-2 Main Protease*by Reaction with Its Nucleophilic Cysteine. Journal of Medicinal Chemistry,

 2022. **65**(11): p. 7682-7696.
- 57. Dou, X., et al., Discovery of 2-(furan-2-ylmethylene)hydrazine-1-carbothioamide derivatives as novel inhibitors of SARS-CoV-2 main protease.

 Eur J Med Chem, 2022. 238: p. 114508.
- 58. Huff, S., et al., Discovery and Mechanism of SARS-CoV-2 Main Protease Inhibitors. J Med Chem, 2022. **65**(4): p. 2866-2879.
- 59. Jin, Z., et al., Structural basis for the inhibition of SARS-CoV-2 main protease by antineoplastic drug carmofur. Nat Struct Mol Biol, 2020. **27**(6): p. 529-532.

- 60. Kuhl, N., et al., *Discovery of potent benzoxaborole inhibitors against SARS- CoV-2 main and dengue virus proteases.* Eur J Med Chem, 2022. **240**: p. 114585.
- 61. Dubreuil, P., et al., *Masitinib (AB1010), a potent and selective tyrosine kinase inhibitor targeting KIT.* PLoS One, 2009. **4**(9): p. e7258.
- 62. Drayman, N., et al., *Masitinib is a broad coronavirus 3CL inhibitor that blocks* replication of SARS-CoV-2. Science, 2021. **373**(6557): p. 931-936.
- 63. Su, H., et al., Discovery of baicalin and baicalein as novel, natural product inhibitors of SARS-CoV-2 3CL protease in vitro. bioRxiv, 2020: p. 2020.04.13.038687.
- 64. Su, H.X., et al., Anti-SARS-CoV-2 activities in vitro of Shuanghuanglian preparations and bioactive ingredients. Acta Pharmacol Sin, 2020. **41**(9): p. 1167-1177.
- 65. Stille, J.K., et al., *Design, synthesis and in vitro evaluation of novel SARS-CoV-*2 3CL(pro) covalent inhibitors. Eur J Med Chem, 2022. **229**: p. 114046.
- 66. Tan, B., et al., *Exploring diverse reactive warheads for the design of SARS-CoV- 2 main protease inhibitors.* Eur J Med Chem, 2023. **259**: p. 115667.
- 67. Gao, S., et al., Discovery and Crystallographic Studies of Trisubstituted

 Piperazine Derivatives as Non-Covalent SARS-CoV-2 Main Protease Inhibitors

 with High Target Specificity and Low Toxicity. J Med Chem, 2022. 65(19): p.

 13343-13364.

- 68. Gao, S., et al., Discovery and Crystallographic Studies of Nonpeptidic Piperazine Derivatives as Covalent SARS-CoV-2 Main Protease Inhibitors. J Med Chem, 2022. **65**(24): p. 16902-16917.
- 69. Liang, J., et al., *Acriflavine and proflavine hemisulfate as potential antivirals by targeting M(pro)*. Bioorg Chem, 2022. **129**: p. 106185.
- 70. Zhu, W., et al., *Identification of SARS-CoV-2 3CL Protease Inhibitors by a Quantitative High-Throughput Screening*. ACS Pharmacol Transl Sci, 2020. **3**(5): p. 1008-1016.
- 71. Shcherbakov, D., et al., *Design and Evaluation of Bispidine-Based SARS-CoV- 2 Main Protease Inhibitors*. ACS Med Chem Lett, 2022. **13**(1): p. 140-147.
- 72. Liu, P., et al., *Potent inhibitors of SARS-CoV-2 3C-like protease derived from*N-substituted isatin compounds. Eur J Med Chem, 2020. **206**: p. 112702.
- 73. Liu, Y., et al., *The development of Coronavirus 3C-Like protease (3CL(pro)) inhibitors from 2010 to 2020.* Eur J Med Chem, 2020. **206**: p. 112711.
- 74. He, J., et al., Potential of coronavirus 3C-like protease inhibitors for the development of new anti-SARS-CoV-2 drugs: Insights from structures of protease and inhibitors. Int J Antimicrob Agents, 2020. **56**(2): p. 106055.
- 75. Tuttle, J.B., et al., Discovery of Nirmatrelvir (PF-07321332): A Potent, Orally Active Inhibitor of the Severe Acute Respiratory Syndrome Coronavirus 2 (SARS CoV-2) Main Protease. J Med Chem, 2025. **68**(7): p. 7003-7030.

- 76. Wamser, R., et al., A Critical Study on Acylating and Covalent Reversible

 Fragment Inhibitors of SARS-CoV-2 Main Protease Targeting the S1 Site with

 Pyridine. ChemMedChem, 2023. 18(9): p. e202200635.
- 77. Rodl, C.B., et al., *Multi-dimensional target profiling of N,4-diaryl-1,3-thiazole-*2-amines as potent inhibitors of eicosanoid metabolism. Eur J Med Chem, 2014.

 84: p. 302-11.
- 78. Karuvalam, R.P., et al., Design, synthesis of some new (2-aminothiazol-4-yl)methylester derivatives as possible antimicrobial and antitubercular agents.

 Eur J Med Chem, 2012. **49**: p. 172-82.
- 79. science, A. *MASITINIB GENERAL OVERVIEW*. 2023; Available from: https://www.ab-science.com/masitinib-general-overview/.
- 80. AB Science today announced that a new clinical trial with masitinib in patients with symptomatic mild and moderate COVID-19 has been approved by the Regulatory Authorities of Russia and South Africa. 2021.
- 81. Jayashree, B.S., P.S. Nikhil, and S. Paul, *Bioisosterism in Drug Discovery and Development An Overview.* Med Chem, 2022. **18**(9): p. 915-925.
- 82. Brown, N., *Bioisosteres and Scaffold Hopping in Medicinal Chemistry*. Mol Inform, 2014. **33**(6-7): p. 458-62.
- 83. Pola, S., Significance of Thiazole-based Heterocycles for Bioactive Systems, in Scope of Selective Heterocycles from Organic and Pharmaceutical Perspective, V. Ravi, Editor. 2016, IntechOpen: Rijeka. p. Ch. 1.

- 84. Guerrero-Pepinosa, N.Y., et al., Antiproliferative activity of thiazole and oxazole derivatives: A systematic review of in vitro and in vivo studies. Biomed Pharmacother, 2021. **138**: p. 111495.
- 85. Chan, D.M.T., et al., *New N- and O-arylations with phenylboronic acids and cupric acetate*. Tetrahedron Letters, 1998. **39**(19): p. 2933-2936.
- 86. Qiao, J.X. and P.Y.S. Lam, Recent Advances in Chan-Lam Coupling Reaction:

 Copper-Promoted C-Heteroatom Bond Cross-Coupling Reactions with Boronic

 Acids and Derivatives, in Boronic Acids. 2011. p. 315-361.
- 87. Lauer-Fields, J.L., et al., *Kinetic analysis of matrix metalloproteinase activity using fluorogenic triple-helical substrates.* Biochemistry, 2001. **40**(19): p. 5795-803.
- 88. Yang, H., et al., *Design of wide-spectrum inhibitors targeting coronavirus main proteases*. PLoS Biol, 2005. **3**(10): p. e324.
- 89. Qiao, Z., et al., *The Mpro structure-based modifications of ebselen derivatives*for improved antiviral activity against SARS-CoV-2 virus. Bioorg Chem, 2021.

 117: p. 105455.
- 90. Battye, T.G., et al., *iMOSFLM: a new graphical interface for diffraction-image processing with MOSFLM.* Acta Crystallogr D Biol Crystallogr, 2011. **67**(Pt 4): p. 271-81.
- 91. Evans, P.R. and G.N. Murshudov, *How good are my data and what is the resolution?* Acta Crystallographica Section D, 2013. **69**(7): p. 1204-1214.

- 92. Potterton, L., et al., *CCP4i2: the new graphical user interface to the CCP4 program suite.* Acta Crystallogr D Struct Biol, 2018. **74**(Pt 2): p. 68-84.
- 93. McCoy, A.J., et al., *Phaser crystallographic software*. J Appl Crystallogr, 2007. **40**(Pt 4): p. 658-674.
- 94. Andi, B., et al., Hepatitis C virus NS3/4A inhibitors and other drug-like compounds as covalent binders of SARS-CoV-2 main protease. Scientific Reports, 2022. 12(1): p. 12197.
- 95. Emsley, P. and K. Cowtan, *Coot: model-building tools for molecular graphics*.

 Acta Crystallogr D Biol Crystallogr, 2004. **60**(Pt 12 Pt 1): p. 2126-32.
- 96. Vagin, A.A., et al., *REFMAC5 dictionary: organization of prior chemical knowledge and guidelines for its use.* Acta Crystallogr D Biol Crystallogr, 2004. **60**(Pt 12 Pt 1): p. 2184-95.
- 97. Previti, S., et al., Structure-based lead optimization of peptide-based vinyl methyl ketones as SARS-CoV-2 main protease inhibitors. Eur J Med Chem, 2023.

 247: p. 115021.
- 98. Zhang, F.M., et al., Discovery of highly potent covalent SARS-CoV-2 3CL(pro) inhibitors bearing 2-sulfoxyl-1,3,4-oxadiazole scaffold for combating COVID-19. Eur J Med Chem, 2023. **260**: p. 115721.
- 99. Patel, D., Z.E. Huma, and D. Duncan, *Reversible Covalent Inhibition horizontal*line Desired Covalent Adduct Formation by Mass Action. ACS Chem Biol, 2024.

 19(4): p. 824-838.

- 100. Ng, Y.L., C.K. Mok, and J.J.H. Chu, Cytopathic Effect (CPECytopathic effects (CPE))-Based Drug Screening AssayDrug screening assay for SARS-CoV-2, in SARS-CoV-2: Methods and Protocols, J.J.H. Chu, B.A. Ahidjo, and C.K. Mok, Editors. 2022, Springer US: New York, NY. p. 379-391.
- 101. Han, S.H., et al., Structure-Based Optimization of ML300-Derived, Noncovalent
 Inhibitors Targeting the Severe Acute Respiratory Syndrome Coronavirus 3CL
 Protease (SARS-CoV-2 3CL(pro)). J Med Chem, 2022. 65(4): p. 2880-2904.
- 102. Thomsen, R. and M.H. Christensen, *MolDock: a new technique for high-accuracy molecular docking*. J Med Chem, 2006. **49**(11): p. 3315-21.
- 103. Beutner, G.L., et al., TCFH-NMI: Direct Access to N-Acyl Imidazoliums for Challenging Amide Bond Formations. Org Lett, 2018. **20**(14): p. 4218-4222.
- 104. Indrayanto, G., G.S. Putra, and F. Suhud, *Chapter Six Validation of in-vitro bioassay methods: Application in herbal drug research*, in *Profiles of Drug Substances, Excipients and Related Methodology*, A.A. Al-Majed, Editor. 2021, Academic Press. p. 273-307.